Tamaki, K., Pisciotto, K., Allan, J., et al., 1990
Proceedings of the Ocean Drilling Program, Initial Reports, Vol. 127

5. SITE 795[1]

Shipboard Scientific Party[2]

HOLE 795A

Date occupied: 12 July 1989

Date departed: 15 July 1989

Time on hole: 12 days, 15 hr, 45 min

Position: 40.987°N, 138.967°E

Bottom felt (rig floor; m; drill pipe measurement): 3311.2

Distance between rig floor and sea level (m): 11.00

Water depth (drill pipe measurement from sea level, m): 3300.2

Total depth (rig floor; m): 3311.20

Penetration (m): 365.9

Number of cores (including cores with no recovery): 39

Total length of cored section (m): 364.90

Total core recovered (m): 258.26

Core recovery (%): 70

Oldest sediment cored:
Depth sub-bottom (m): 356.40
Nature: silty clay diatom mixed sediment
Earliest age:
Latest age: late Miocene
Measured velocity (km/s): 2.0

Comments: velocity of oldest sediment was measured at Core 25X

HOLE 795B

Date occupied: 15 July 1989

Date departed: 21 July 1989

Time on hole: 6 days, 2 hr, 45 min

Position: 43.987°N, 138.965°E

Bottom felt (rig floor; m; drill pipe measurement): 3310.0

Distance between rig floor and sea level (m): 11.00

Water depth (drill pipe measurement from sea level, m): 3299.0

Total depth (rig floor; m): 3310.00

Penetration (m): 762.2

Number of cores (including cores with no recovery):41

Total length of cored section (m): 397.00

Total core recovered (m): 188.94

Core recovery (%): 47

Oldest sediment cored:
Depth sub-bottom (m): 683.50
Nature: interbedded claystone and tuff
Earliest age:
Latest age: middle Miocene
Measured velocity (km/s): 2.3

Hard rock:
Depth sub-bottom (m):
Nature:
Measured velocity (km/s):

Basement:
Depth sub-bottom (m): 683.50
Nature: brecciated and massive basalt
Measured velocity (km/s): 2.4–3.8

Drill below core (m):

Comments: terminated due to bad hole condition

Principal results: The unifying objective of drilling in the Japan Sea was to assess the style and dynamics of rifting and marginal sea formation in a continental arc setting. The specific objectives of Site 795, located in the northern Japan Basin, were: (1) to determine the age and nature of the basement; (2) to measure the magnitude and direction of the present stress field; and, (3) to characterize the sedimentation, subsidence, and oceanographic evolution of the area. The results at Site 795 are summarized below and in Figure 1A–D. The principal results are:

1. Basalts, basaltic andesites, and basaltic breccias constitute acoustic basement at this locality. Textures, mineralogy, and chemistry indicate that these rocks have calc-alkaline and volcanic arc affinities, quite different from rocks associated with seafloor spreading. They could be associated with either arc volcanism or with initial arc rifting. The sediment which immediately overlies these rocks gives a minimum age of basin initiation in the range 13–15 Ma.

2. The *in-situ* stress field determinations could not be completed because a blockage in the Hole 795B at 230 mbsf prevented downhole logging and packer/hydrofracture experiments needed for the measurements.

3. Lithologic and paleontologic data available indicate a three-stage evolution of this part of the northern Japan Basin: (a) a middle Miocene period beginning with explosive volcanism, resulting in ash falls and submarine, gravity-flow tuffs, coincident with and followed by marine claystone deposition on a well oxygenated to mildly dysoxic slope or basin which subsided from upper middle bathyal (~500–1000 m) to lower middle bathyal depths (~1500 m); then, (b) a gradual increase in hemipelagic diatomaceous sedimentation, beginning in the late Miocene and culminating in the early Pliocene, in cool, well oxygenated waters; and finally, (c) a lively late Pliocene to Recent stage in which diatomaceous sedimentation was episodic and diminished, volcanic ash production and terrigenous input increased, climate cycled from arctic to subarctic conditions, and local tectonism was activated to produce complex interbedding of hemipelagic and terrigenous sediments deposited at nearly twice the rates of coeval sediments found at Site 794. Except for episodes during the middle Miocene, early late Miocene, and late Pliocene through Quaternary, preservation of primary biogenic carbonate within the sediments is poor, indicating a consistently shallow CCD (probably < 1500 m) or dissolution during early diagenesis. Dissolution of siliceous microfossils is also pronounced. The opal-A/opal-CT and opal-CT/quartz diagenetic transitions are well defined by lithology, geochemistry of sediments and interstitial water, and physical properties data. The opal-A/opal-CT boundary corresponds to a widespread bottom-simulating reflector which locally cuts across stratal reflectors.

Location and Approach

Site 795 is located in bathymetric embayment in the northernmost Japan Basin just south of approved location J-1d-2. The site was confirmed by two *JOIDES Resolution* seismic lines, one bearing north, the other east. Both lines are parallel to preexisting multi-

[1] Tamaki, K., Pisciotto, K., Allan, J., et al., 1990. *Proc ODP, Init. Repts.*, 127: College Station, TX (Ocean Drilling Program).

[2] Shipboard Scientific Party is as given in the list of participants preceding the contents.

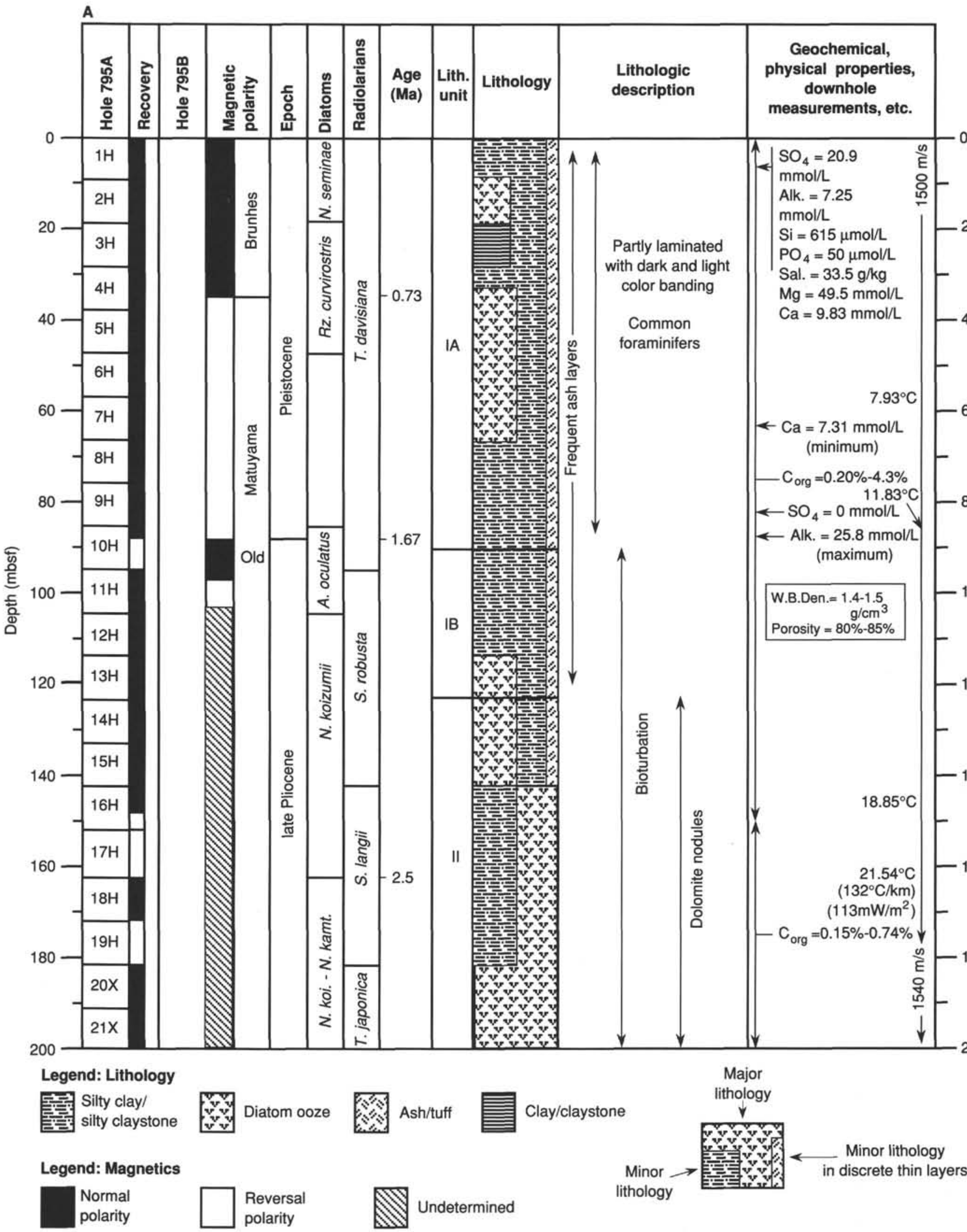

Figure 1. Stratigraphic summary column for Site 795.

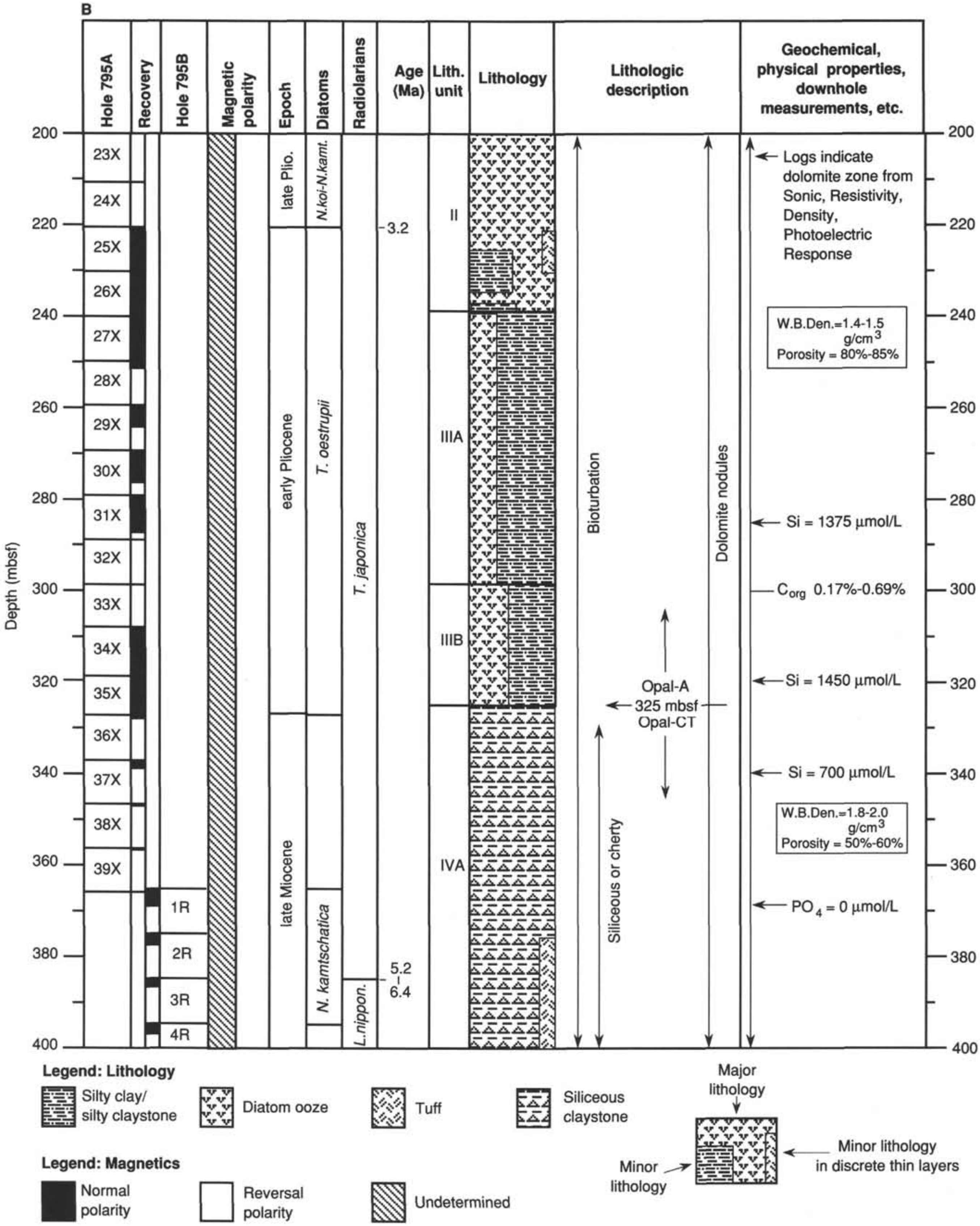

Figure 1 (continued).

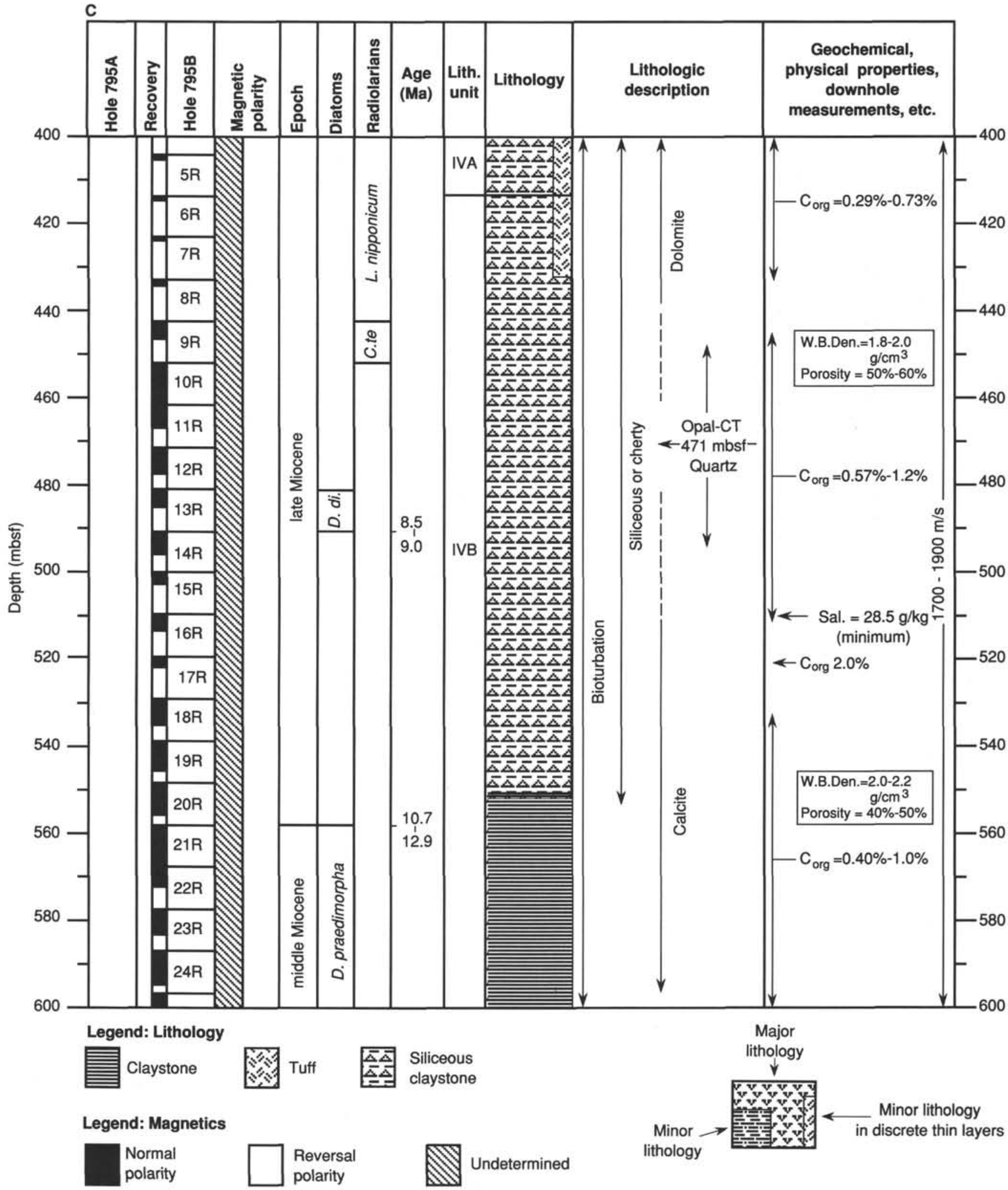

Figure 1 (continued).

channel lines. The beacon was launched on the third pass of the site after reconfirming the location in order to avoid any local closures.

Lithology

The sedimentary section cored in Holes 795A and 795B consists of mostly fine-grained hemipelagic diatomaceous, and terrigenous sediments of middle Miocene to Quaternary age. The division of units is as follows:

Unit I: 0–123.0 mbsf; Quaternary–late Pliocene.
Silty clay and clay. The upper 85 m is color-banded, light and dark silty clay, clay, diatomaceous clay, and minor ash. Subtle size grad-

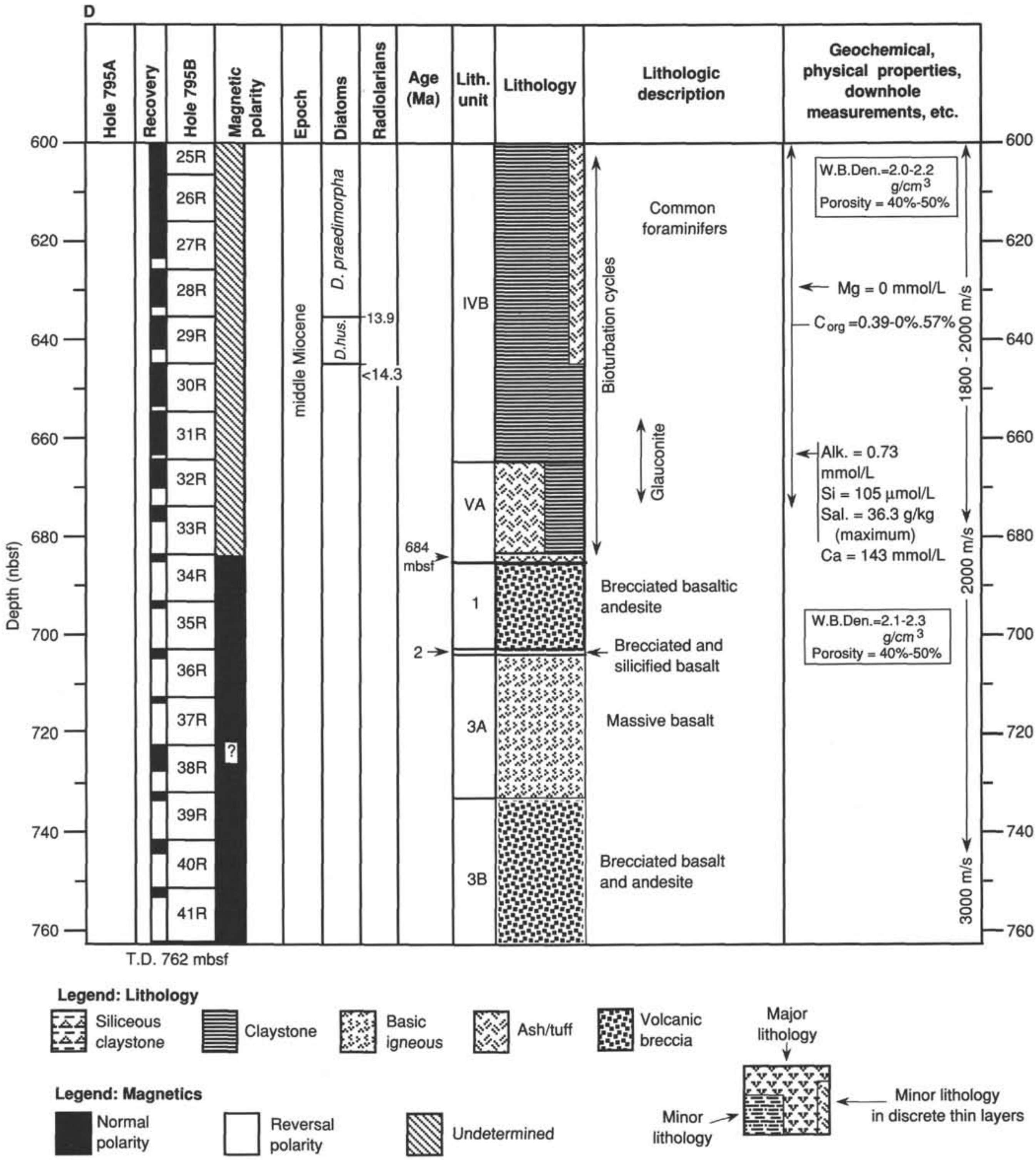

Figure 1 (continued).

ing occurs in the silty clays and ashes. Bioturbation is minimal. The lower 38 m is similar but with increasing diatom content and increased bioturbation.

Unit II: 123.0–239.0 mbsf; 2.1–4.0 Ma, Quaternary–late Pliocene.

Diatom ooze, diatom silty clay, and diatom mixed sediment. This unit is distinguished by a significant increase in diatom content from Unit I. Minor ash layers are present and the unit is moderately to extensively bioturbated.

Unit III: 239.0–325.0 mbsf; early Pliocene–late Miocene.

Silty diatom claystone and diatom-clay-silt mixed sediment. This unit is similar to Unit II but contains a lower diatom content and increased amounts of silt and clay. The lower 50 m of this unit con-

tains slightly less clay than the upper part. Minor calcareous and dolomitic nodules are present. Bioturbation is common.
Unit IV: 325.0–665.0 mbsf; late Miocene–middle Miocene.
Siliceous claystone and silty siliceous claystone. The upper 146 m of this unit comprises opal-CT siliceous silty claystone and siliceous claystone with minor porcellanite, dolomite, and some chert. The lower 194 m consists of burrowed claystone with minor tuff and micrite layers, and pyritic and calcareous nodules. Opal-CT changes to quartz at about 471 mbsf and the claystone becomes less siliceous below 560 mbsf. A cyclicity in style of bioturbation increases with depth as does the abundance of small faults and calcite- and clay-filled fractures. The tuff layers are normally graded with internal laminations and burrowed tops.
Unit V: 665.0–683.5 mbsf; middle Miocene.
Claystone and tuff. This unit overlies the basalt and basaltic breccia and consists of interbedded claystone and altered, fine- to coarse-grained tuff. These strata are commonly graded, laminated, and burrowed in the style of the overlying sediments. Small faults and clay-filled fractures are common in the claystone. Calcite-filled fractures occur in the tuff.

Age and Sediment Accumulation Rates

Sediment ages are well constrained by diatom zones and paleomagnetic reversals in Unit I, and by diatoms in Units II and III (0–325 mbsf). Below this level, all diatoms, except those preserved in calcareous concretions, have been dissolved. Units IV and V are dated using these sporadic samples together with sparse control from foraminifers, radiolarians, and calcareous nannofossils. The oldest paleontologic age occurs at 635.5 mbsf and corresponds to 13.3 Ma. Summarizing all of the age data, compacted sedimentation rates for the three evolutionary stages are: 29–38 m/m.y. for the middle Miocene sediments, 34–78 m/m.y. for the upper Miocene-lower Pliocene interval and 48–56 m/m.y. for the upper Pliocene-Quaternary sediments. The uncompacted accumulation rates show the same relative trends.

Magnetics

The magnetic intensity of the Site 795 sediments are generally quite weak (generally below 1 A/m), except for the upper 100 m of Hole 795A where it reaches values of 10–100 A/m. The polarity pattern is well constrained within this upper 100 m (to the top of the Olduvai subchron), but is not defined below. The magnetic intensity and susceptibility of the basement rocks varied over 2 orders of magnitude, due to widely varying amounts of alteration.

Geochemistry

Sediments from Holes 795A and 795B are characterized by variable organic carbon contents, particularly in the color-banded Pliocene-Pleistocene sediments (TOC: 0.25%–4%). Organic matter type is principally terrestrial, although the Pliocene-Pleistocene contained mixed terrestrial and marine algal sources. Methane occurred in low amounts from the seafloor to 80 mbsf. Below this level, methane increased sharply and ethane appeared, but quantities were still relatively low. Amounts of both gases increased slightly but steadily with depth to the basement. Sporadic traces of propane occurred below about 325 mbsf. No safety problems related to gas were encountered at this site. Interstitial water profiles match observed sediment and organic matter diagenesis. The base of the sulfate reduction zone occurs at 80 mbsf, where methane increases. Dissolved silica increases to a maximum at the opal-A/opal-CT boundary (325 mbsf), then decreases sharply, indicating silica precipitation. Ca and Mg profiles are typical to about 325 mbsf, where the Ca gradient increases sharply to the base of the sediment column suggesting exchange during basement alteration.

Igneous Rocks

Basalt, basaltic andesites, and basaltic breccias comprise acoustic basement at this site. All rocks are moderately to highly altered and vesicular (5%–30%). These are divided into 3 units on the basis of texture and mineralogy as follows:

Unit 1: 683.5–703.3 mbsf.
Brecciated, sparsely plagioclase pyroxene phyric basaltic andesite.
Unit 2: 703.3–704 mbsf.
Silicified brecciated moderately plagioclase phyric basalt.
Unit 3: 704–762.2 mbsf (end of Hole 795B).
Sparsely pyroxene plagioclase phyric basalt. This unit is further divided into two subunits. Unit 3A (704–733.7 mbsf) is predominantly massive basalt. Unit 3B (733.7–762.2 mbsf) is principally brecciated basalt and basaltic andesite.

The igneous rocks are characterized by low amounts of large-ion lithophile elements (LILE; K, Rb, Sr, and Ba), high-field-strength elements (HFSE; Nb, Zr, and Ti), and light rare earth elements (LREE; Ce), and also contain high amounts of Al. They are all evolved, containing low amounts of Cr, Ni, and MgO. Their mineralogy and chemistry indicates that they have calc-alkaline and volcanic arc affinities, yet contain little or no evidence of involvement of continental crust in their genesis. The igneous rocks found at Site 795 were erupted subaqueously. Constraints imposed by the immediately overlying sediments indicate that they were erupted below wavebase (100–200 mbsl); the high vesicularity implies shallow water depth (probably above 1000 mbsl). They represent lavas erupted within a volcanic arc or back-arc setting.

Seismic Stratigraphy

Five distinct seismic intervals occur at this site. From top to bottom these are: (1) an upper weakly stratified interval; (2) a transparent interval with partly hummocky reflectors; (3) a strongly stratified interval; (4) a lower moderately well stratified interval; and, (5) an unstratified, acoustically opaque zone. Interval 1 correlates with Unit I. Interval 2 correlates with the Units II and III. Interval 3 correlates with the upper part of Unit IV. Its top is coincident with the opal-A/opal-CT diagenetic boundary. Reflectors within this interval are parallel with the seafloor but cut across stratal reflectors in places. Interval 4 corresponds with the lower part of Unit IV and all of Unit V. Interval 5 corresponds to acoustic basement (Units 1–3) which was penetrated in Hole 795B.

Heat Flow and Temperature

Successful temperature measurements were made using the Uyeda probe at 5 horizons down to 162.4 mbsf in Hole 795A. The measured temperature gradient is 133°C/km. The calculated heat flow value using this gradient and measured thermal conductivities is 113 mW/m^2. This value is slightly higher than the average value for this part of the Japan Basin (99 mW/m^2).

Logging and Physical Properties

Only a short interval of open hole could be logged at this site due to a blockage caused by swelling clays at about 230 mbsf. A single tool string was run which included the sonic, lithodensity, neutron porosity, resistivity, and gamma ray devices.

The physical properties correlate well with most lithologic changes. Within the sedimentary section, physical properties change most dramatically at the opal/A/opal-CT boundary. Physical properties also delineate variations in alteration, fracturing, and vesicularity in the igneous rocks quite well.

BACKGROUND AND OBJECTIVES

Background

Location and Bathymetry

Site 795 lies in the northern Japan Sea, nearly equidistant from the coasts of Hokkaido and Sikhote-Alin, Siberia (Fig. 2). This site represents the northernmost extent of scientific drilling in the Japan Sea to date. It is situated in 3298 m of water in a bathymetric embayment at the northern extremity of the Japan Basin. This embayment is bounded on three sides by a steep, curvilinear escarpment with up to 1500 m of relief. East of the site, the escarpment marks the westward edge of an extensive system of north-trending offshore ridges, seamounts, escarpments, and closed basins which stretches along much of western Hokkaido and Honshu (Tamaki and Honza, 1985). North of the site the escarpment bifurcates. The shallower arm continues to the north, while the other curves to the west. Above this es-

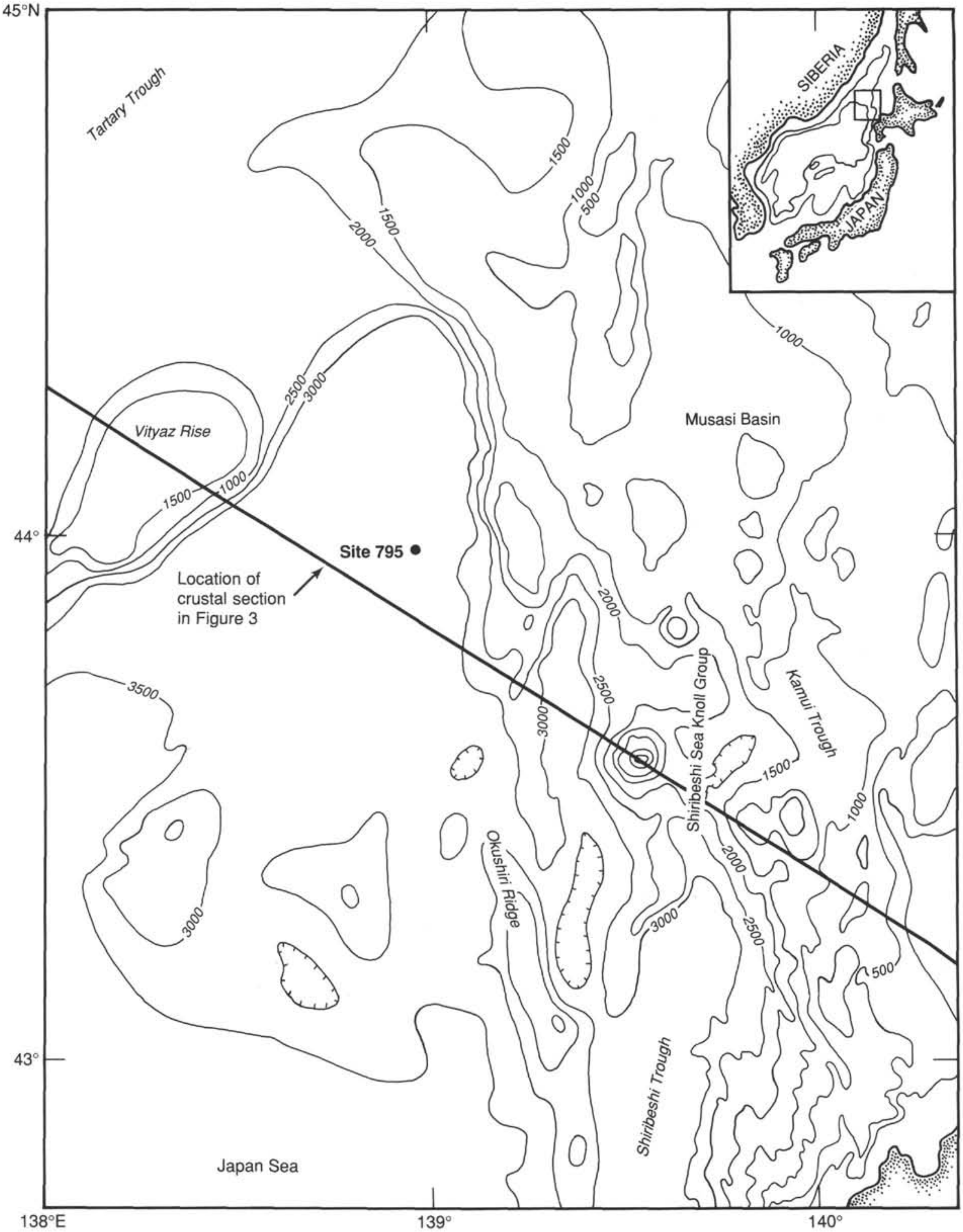

Figure 2. Location map of area surrounding Site 795 showing bathymetric features and locations of seismic reflection and refraction sections. Contour level is 500 m.

carpment to the northwest is a gentle slope leading to a bathymetric sill which separates the Japan Basin embayment from the Tartary Trough. South of the bathymetric sill is the Vityaz Rise, a large, steep-sided bank with a moderately flat top. The southeastern flank of this rise forms part of the curvilinear escarpment which bounds the Japan Basin embayment. Two similar highs occur to the south of Site 795, but these have gentler flanks and sharper tops. Between these two highs and Vityaz Rise is a broad trough which connects the embayment with the deeper Japan Basin.

Locally, Site 795 is situated on the north flank of a small, west-plunging ridge which juts out orthogonally from the escarpment east of the site (Fig. 2). North of this ridge is a closed, rectangular-shaped low which is separated from the deeper Japan Basin by a bathymetric sill. This basin is similar in shape, size, and orientation to other offshore silled basins which occur to the south-southeast along western Hokkaido and Honshu. South of the small, plunging ridge on which the site is situated is a broad, west-dipping trough which leads to the deeper Japan Basin. A number of small canyons and valleys emanate from the escarpment and high blocks on the east and south and converge at the head of this trough.

Crustal Structure

The crustal structure of the northern Japan Basin in the vicinity of Site 795 is inferred principally from seismic refraction data (Gnibidenko, 1979). Figure 3 shows a northwest-southeast crustal section which passes through the site. The key feature of this cross section is the rise in the crust-mantle boundary from a depth of 30–35 km beneath both Sikhote-Alin and Hokkaido to 13–17.5 km beneath the Japan Sea. The crustal thicknesses beneath Siberia and Hokkaido are typical of continental values. In contrast, the crustal thickness beneath the Japan Sea along this profile lies between these values and the range for oceanic crust (5–10 km). Compared to other areas of the Japan Sea, the crustal thickness in the vicinity of Site 795 lies between the observed values for the Yamato Basin (18–19 km) and the Japan Basin (11–12 km) (Ludwig et al., 1975).

At least three layers occur above the Moho in the Site 795 area (Fig. 3). Using oceanic crust terminology, "Layer 3" is 7–10 km thick and has a velocity of 6.6 km/s. This layer thickens and the velocity structure becomes more complex toward Sikhote-Alin and Hokkaido. "Layer 2" is 2–7 km thick with velocities in the range 5.9-6.4 km/s. This layer also thickens and its velocity structure changes toward the continental blocks. The uppermost part of this layer was a principal target at Site 795. Capping this sequence is "Layer 1," the sedimentary section which we planned to continuously core at Site 795. This layer varies from 0–3 km thick with velocities in the range 2–4 km/s.

Heat Flow

The measured heat flow values in the area surrounding Site 795 lie in the range 82–111 mW/m^2 (Fig. 4). The average of these values is 99 mW/m2, which is similar to the measured values in the basinal areas of the Japan Sea (Yoshii and Yamano, 1983; Tamaki, 1986). Using the average heat flow, a first approximation of the age of basin initiation at the Site 795 location is 22.5–25.5 Ma. This estimate is based on a correlation between heat flow and age (Davis and Lister, 1977; Parsons and Sclater, 1977), and assumes that the area is underlain by oceanic crust. It must be considered rather tentative because the correlation between age and heat flow developed for oceanic crust may not apply in this setting.

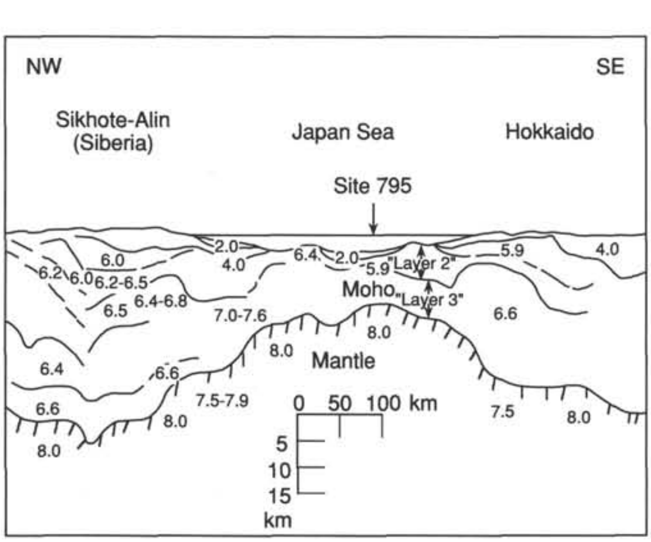

Figure 3. Crustal section for the northern Japan Basin through Site 795 (from Gnibidenko, 1979). Location shown in Figure 2.

Magnetics and Gravity

Magnetic anomaly profiles near Site 795 have peak-to-peak amplitudes of about 100–200 nT and wavelengths on the order of 40 km (Fig. 5). In map view, these anomalies form irregular, blocky patterns which suggest that discrete basement blocks may underlie the area. This signature differs from the high frequency, chaotic patterns found in the Yamato Basin as well as from the short, linear segments found in the eastern Japan Basin (Isezaki, 1986; Tamaki et al., 1988a). It is also distinct from the high amplitude, high frequency anomalies associated with the volcanic terrane off northwestern Hokkaido (Fig. 5; Honza, 1978).

Free-air gravity anomalies in the site area range from -50 to 70 mgal (Fig. 6). The positive values correspond to the ridges and banks, the negative values to the troughs. In addition, a steep gravity gradient is associated with the escarpment. The lowest gravity anomaly (-50 mgal) occurs just north of the site and corresponds to the closed basin in this area. The center of this anomaly lies at the base of the steep escarpment and marks the location of a significant thickness of sediments. The small, west-plunging ridge on which the site is located does not have an associated gravity signature, probably because the station spacing is too great (Honza, 1978).

Basement Rocks

Direct evidence for the types of basement rocks present in the vicinity of Site 795 comes mostly from marine dredge sampling of nearby banks and escarpments, particularly in the areas to the east and north-northeast of the site. Figure 4 summarizes the locations of these samples as reported by Kobayashi (1988) and Honza (1978).

The nearest dredge samples come from the steep escarpment which flanks the northern extension of Okushiri Ridge about 20 km east-northeast of Site 795 (Ishii et al., 1988; Kobayashi, 1988; Sagayama et al., 1988; Miyashita et al., 1987). The recovered material includes angular fragments of basalt and basaltic breccia, shale, and sandy shale in roughly equal proportions. Minor sandstone and some soft clay were also recovered in this dredge. The basalts and basaltic breccias are representative of acoustic basement which underlies the ridge and perhaps much of the surrounding area, including the drill site. Moreover, as Okushiri Ridge is considered to have been uplifted by thrust or reverse faults, it is possible that these basaltic rocks may represent original basinal basement. Based on seismic correlations and paleontology, the age of sedimentary rocks recovered are at least 11 Ma (late middle to early late Miocene), suggesting that the age of the basaltic rocks, and therefore the acoustic basement, may be early late Miocene or older.

Additional dredge samples in the region are located much further from the site. Most of the *in-situ* materials recovered from the dredge sites north and east of Site 795 are Neogene siltstones and sandstones. For the most part, these rocks come from uplifted sedimentary units which overlie acoustic basement. Volcanic rocks have also been recovered in a number of these dredge hauls, but most of these are small pebbles and fragments and thought not to be in place. Only one sample has

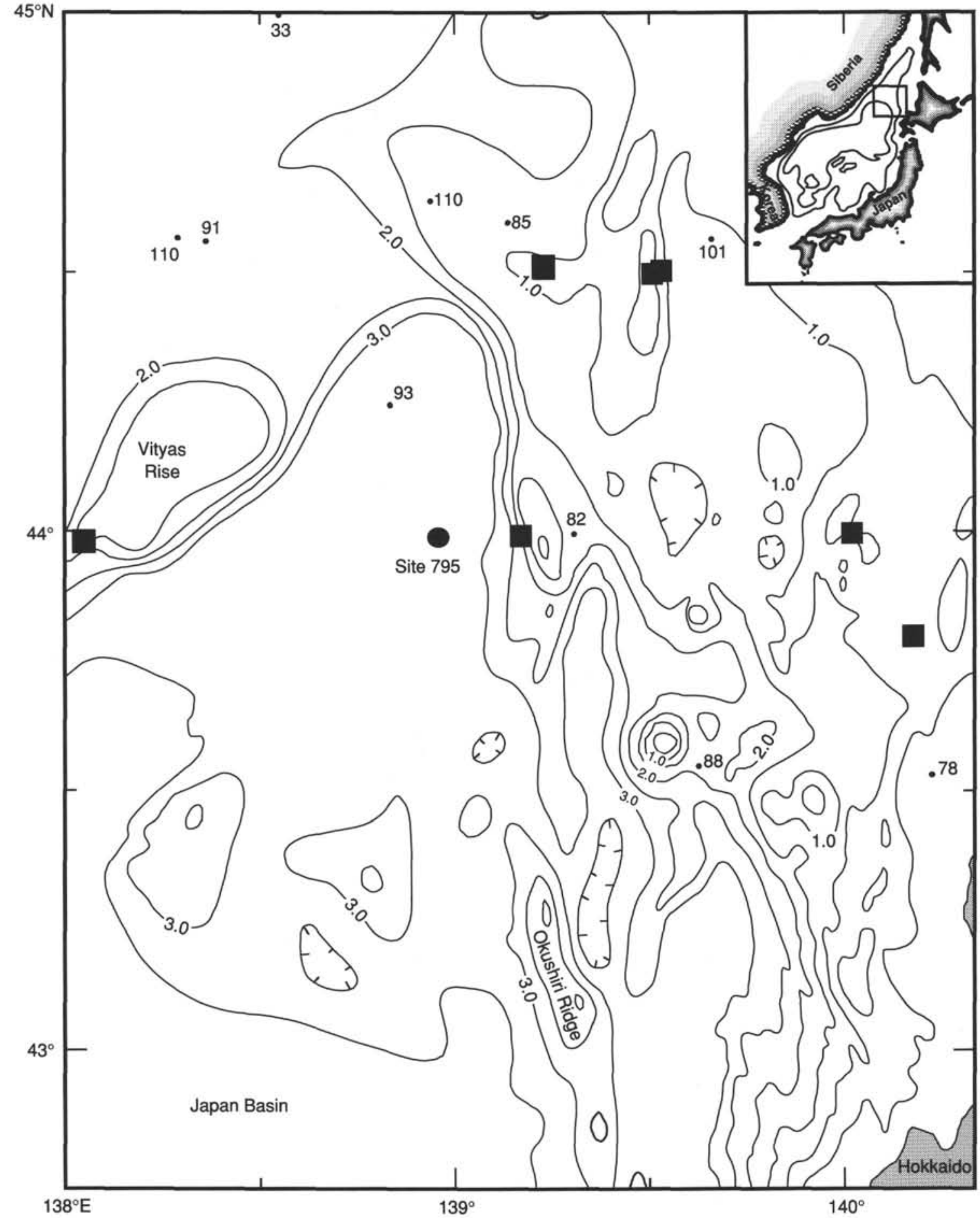

Figure 4. Location map of heat flow values and basement dredge samples. Heat flow values are represented by small dots; units are in mW/m^2 and data are from Yoshii and Yamano (1983). Basement samples are represented by solid squares; see text for descriptions. Bathymetric contours in kilometers.

been dated, a 78 Ma welded tuff boulder from near Musasi Basin which lies over 200 km northeast of Site 795 (Yuasa et al., 1978).

Dredging has also been attempted on Vityaz Rise and a neighboring bank, about 90 km west of Site 795 (Fig. 4). These dredging attempts were largely unsuccessful, recovering only a few pebbles of acidic volcanic and plutonic rocks which may not represent *in-situ* material (Honza, 1978). Based largely on seismic refraction and reflection data, this rise is thought to be a continental block, composed in part of Cretaceous granitic rocks (Melankholina and Kovylin, 1977; Tamaki, 1988).

As for Site 794, onshore geology gives some perspective on basement possibilities, but does not provide a direct tie to Site 795. Hokkaido and Sikhote-Alin are the closest onshore areas and a variety of basement rocks occur there (Melankholina and Kovylin, 1977; Gnibidenko, 1979; Geological Survey of Japan, 1982). These include folded Mesozoic-Paleozoic metamorphic complexes, Cretaceous granitic rocks, and Neogene and Quater-

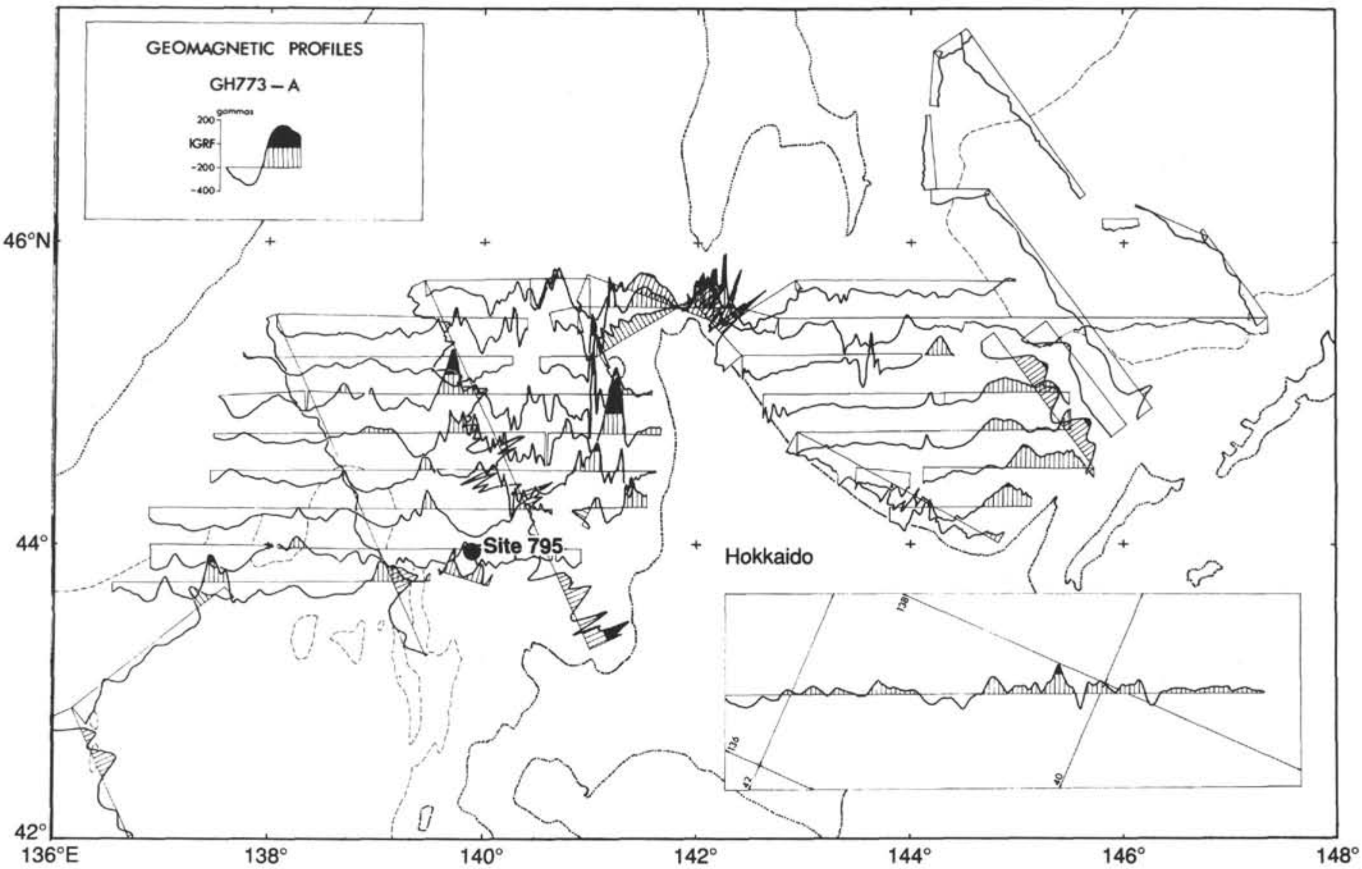

Figure 5. Magnetic anomalies along ship's tracks around Site 795. Data from Honza (1978).

nary basic volcanic rocks. The regional trends of these suites in Hokkaido are north-northwest, while those in Siberia have a northeasterly bearing. The projections of these trends offshore show them converging north and northeast of the Site 795, but because they are poorly constrained, no definite boundaries can be mapped in the northern Japan Sea.

To summarize, the nearest dredge samples to Site 795 contain abundant basalt and basaltic breccia of probable Miocene age and may be representative of acoustic basement in the area. Most other dredge hauls from the surrounding region recovered Neogene shales, mudstones, and sandstones which overlie the basement. The projection of onshore geologic trends in Hokkaido and Sikhote-Alin suggests that they converge north-northeast of Site 795. The range of possible basement types predicted from these trends include Mesozoic-Paleozoic metamorphic suites, Cretaceous granitic rocks, and Cenozoic volcanic rocks.

Tectonic Setting

Bathymetry provides the first clues to the tectonic setting of Site 795 (Fig. 2). The linear complex of north-trending ridges, basins, and escarpments lying east of the site are part of the active tectonic zone which extends along much of western Hokkaido and Honshu (Tamaki and Honza, 1985). Seismic data demonstrate that steep thrust or reverse faults coincide with many of the escarpments, including the one just east of the site, and that fold axes are generally parallel to the ridges (Figs. 7 and 8). Although the dominant structural grain in this area is north-south, other elements are present. Most striking is an escarpment or lineament which begins at Suttu Canyon off southwestern Hokkaido and extends to the northwest behind Siribesi and Kaiyo Seamounts, finally merging with the steep north-south escarpment which lies east and northeast of Site 795 (Fig. 2). The seismic expression of this lineament is shown in Figure 8B. The lineament intersects this profile at an oblique angle and corresponds to a bathymetric and basement low on this northern extension of Okushiri Ridge. The basement reflector does not appear to be offset at this locality, suggesting that if the lineament is a fault, it has no vertical offset. To the southeast, this lineament is represented by an escarpment with considerable vertical offset of basement.

The large compressional earthquakes which have occurred recently in the tectonic zone east of Site 794 have their counterparts to the north. Figure 7 shows the epicenter of a magnitude 7.0 shock that occurred in 1940 along the northern extension of Okushiri Ridge. The epicenter lies about 100 km northeast of Site 795 and the focal depth was at 33 km, which is slightly greater than the estimated thickness of the lithosphere in the Japan Sea (Abe and Kanamori, 1970). The focal mechanism solution indicates that this earthquake occurred on a north-south thrust or reverse fault dipping 45° to the east (Fukao and Furumoto, 1975). Such a fault is observed on a single channel seismic reflection line just south of the epicenter (Fig. 8A). If the focal depth estimate and the lithosphere thickness are correct, then this fault cuts the entire lithosphere. Accordingly, Tamaki and Honza (1985) have suggested that the east Japan Sea tectonic zone is an area of incipient subduction and obduction caused by east-west convergence.

To summarize, the topographic and structural patterns east of Site 795 indicate that this is an area of active compression containing steep reverse faults, some of which cut the entire lithosphere. It also is possible that this area has been affected by oblique transcurrent faulting, where linear ridges represent trans-

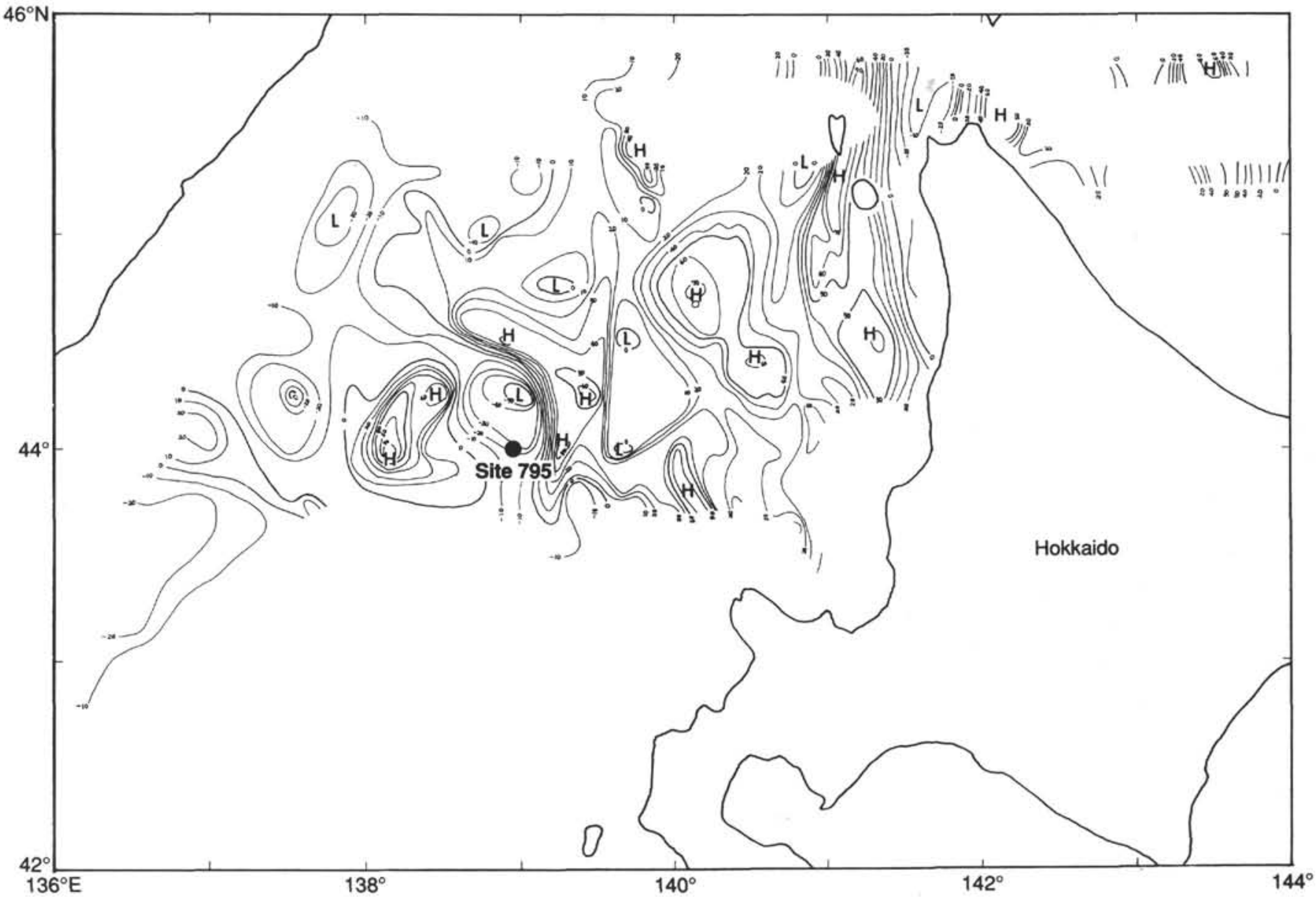

Figure 6. Free-air gravity anomaly map in the vicinity of Site 795. Contour interval is 10 mgal. Data from Honza (1978).

pressional bulges and the associated small basins result from transtension. Low angle thrust faults are not apparent on seismic data or consistent with focal mechanism solutions for the major earthquakes.

North, west, and south of Site 795 the structural style is less dramatic. Vityaz Rise and the two highs south of the site have very little sedimentary cover suggesting that they have stood as high blocks since the Miocene. Their steep flanks appear to be normal faults which formed during rifting of this part of the Japan Sea.

Sedimentation

The sedimentary section which overlies acoustic basement in the vicinity of Site 795 is on the order of 500–800 m thick (Fig. 8). The seismic facies present within this section include: (1) an upper stratified unit characterized by parallel reflectors of moderate amplitude and continuity; (2) an upper transparent interval typified by very low amplitude, parallel reflectors; (3) a lower stratified unit distinguished by moderate to high amplitude, parallel reflectors having fair lateral continuity; and, (4) a lower transparent to moderately stratified interval containing parallel reflectors of moderate to poor amplitude and continuity (Fig. 8). The sedimentary section thickens to the north-northeast, attaining the greatest thickness at the base of the escarpment, coincident with the gravity low. The increase is largely due to a thickening of the upper stratified seismic facies.

Based on character correlations with DSDP Sites 299 and 301 and with Site 794, this interval was thought to represent upper Pliocene to Quaternary hemipelagic and terrigenous sediments. At the site, the expected thickness of this unit was about 100 m. The thickness increase toward the escarpment suggests that terrigenous or redeposited sediments are being derived from the eroded high blocks and dumped into the small closed basin north of Site 795.

Character ties with the other drill sites also shed light on the underlying seismic facies. Accordingly, seismic facies 2 was expected to represent about 170 m of upper Miocene to lower Pliocene hemipelagic diatomaceous ooze and clay; seismic facies 4, approximately 150 m upper Miocene siliceous claystone, also of hemipelagic origin but modified by diagenesis; and seismic facies 3, 150–200 m of mostly middle to upper Miocene hemipelagic claystone with some tuff layers. The reflector at the top of facies 3 cuts across other stratal reflectors in the site area and was thought to represent the opal A-opal CT diagenetic boundary.

Objectives

Style and Dynamics of Back-arc Rifting

As with Site 794, the principal objective of the drilling at Site 795 was to determine the nature and age of acoustic basement at a basinal location in the Japan Sea. Together with the results from additional sites drilled during Legs 127 and 128, these data would permit assessment of the style and dynamics of rifting of the Japan Sea. More specifically, Site 795 constitutes the first basinal test of acoustic basement in the Japan Basin. The pre-

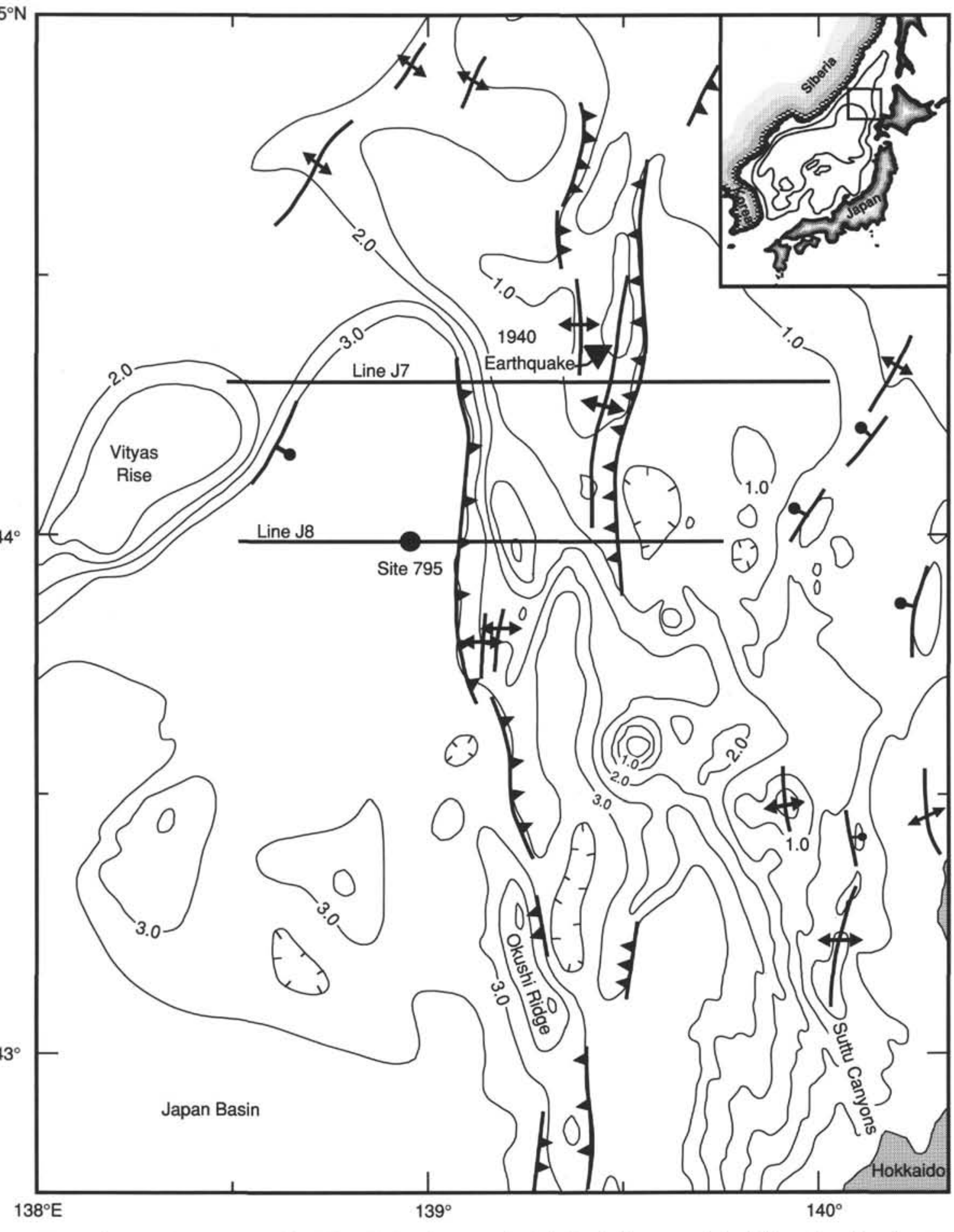

Figure 7. Tectonic map of area surrounding Site 795 showing recognized faults, fold axes, and the 1940 earthquake epicenter (M = 7.0). The location for seismic lines shown in Figure 8 is also noted. Bathymetric contours in kilometers.

vious drilling attempt at DSDP Site 301, in the deeper, central part of the Japan Basin, was stopped by concerns of thermogenic ethane at 497 mbsf, well short of basement. To avoid this potential problem and to be able to reach basement within the time framework of the Leg, Site 795 was situated in a more marginal part of the Japan Basin where we stood the best chance at penetrating oceanic crust. Even if the basement rocks turned out to be something other than spreading ridge basalts, the age and composition would provide valuable constraints on the tectonic development of this part of the Japan Sea.

In-situ Stress Field

An additional objective at Site 795 was the determination and assessment of the present stress field near an incipient convergent plate boundary in the northeastern Japan Sea. This was the second of three sites located near the east Japan Sea tectonic

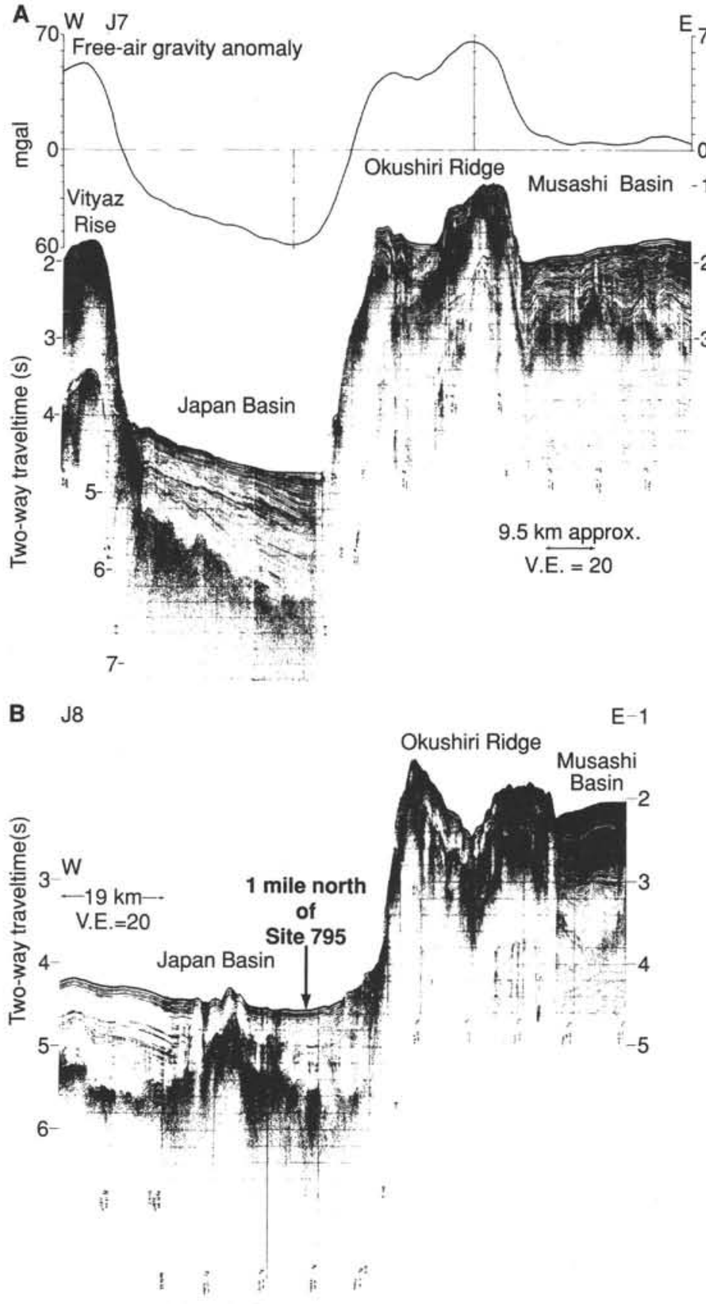

Figure 8. Seismic profiles in vicinity of Site 795. **A.** Single channel reflection profile J7 north of Site 795. **B.** Single channel reflection profile J8 through Site 795. Line locations are on Figure 7. Data from Honza (1978).

zone that was aimed at measuring the magnitude and direction of maximum compressional stress in this region. Following the hole problems at Site 794, a packer/hydrofracture experiment was added to the planned borehole televiewer observations at this site.

Oceanographic and Sedimentation History

The third objective of the drilling at Site 795 was to characterize the history of sedimentation and water mass fluctuations at a northern basinal position in the Japan Sea. Like Site 794, this site was located so as to obtain mostly hemipelagic sediments rather than terrigenous gravity flow deposits; hemipelagic sediments are more likely to contain the microfossils and lithofacies needed for temporal reconstructions of climate, water mass, and subsidence. Except for geographic position, our specific goals were identical to those at Site 794 and included: (1) the history of anoxia, circulation, and sea level in relation to climate and subsidence; (2) fluctuations in the CCD; and, (3) time- and temperature-controlled post-depositional processes, particularly those involving organic matter, biogenic silica, and carbonate. The integration of these results with other regional offshore and onshore data would form the basis for an understanding of the sedimentation and oceanographic history of the Japan Sea and the western Pacific margin.

OPERATIONS

Preamble

Following our departure from Site 794 at 1100 (0200 UTC) on 11 July 1989, we steamed north to Site 795 in the northern Japan Basin. Our destination lay about 420 km north of Site 794 in the northern Japan Sea, and almost equidistant from the coasts of Hokkaido and Sikhote-Alin, Siberia. Of the two approved and closely-spaced sites to choose from in this area, we elected to proceed to the locality where the basement reflector had the lowest amplitude and showed no layering. Based on experience at Site 794, a high amplitude, layered basement reflector could represent igneous sills and we wanted to avoid these and penetrate material more representative of true basement.

Soon after leaving Site 794, we streamed the magnetometer and seismic gear. The seismic records were quite good despite an initial speed of about 9 kt. As we proceeded north, we gradually reduced our speed so that our arrival at the new site would coincide with the best Global Positioning System (GPS) window; navigating by Loran C is much less accurate in this area of the Japan Sea. By 1800 (0900 UTC) on 12 July, we were in a position 3 nautical miles south of the proposed site and ready to begin our seismic survey.

Site Approach

Our survey plan for Site 795 was to obtain several crossings of the site along existing multichannel seismic lines in order to confirm the location and to avoid any local closures. Seismic data were to be acquired using the single channel seismic reflection system aboard the *JOIDES Resolution*. In addition, we planned to acquire magnetic data along all survey lines.

We approached Site 795 from the south along Ocean Research Institute seismic Line 103 at a speed of 6 kt (Figs. 9, 10A, and 11). Our first crossing line began 3 nmi south of the site and proceeded due north for a distance of 4 nmi. At this point, we made a turn to the east, increased our speed slightly, and proceeded southeast to a position about 2 nmi east of the site. We then turned west, reduced our speed and shot a second crossing line parallel to Ocean Research Institute seismic Line MC1 (Fig. 9, 10B, and 11). After crossing the site and confirming the location and the absence of closure, we continued 2 nmi farther on a due west course before turning to a reciprocal course on a bearing of 90°. We launched the beacon on the third pass of the site at 2015 (1115 UTC) on 12 July 1989, then slowed to pull in the gear and position the ship.

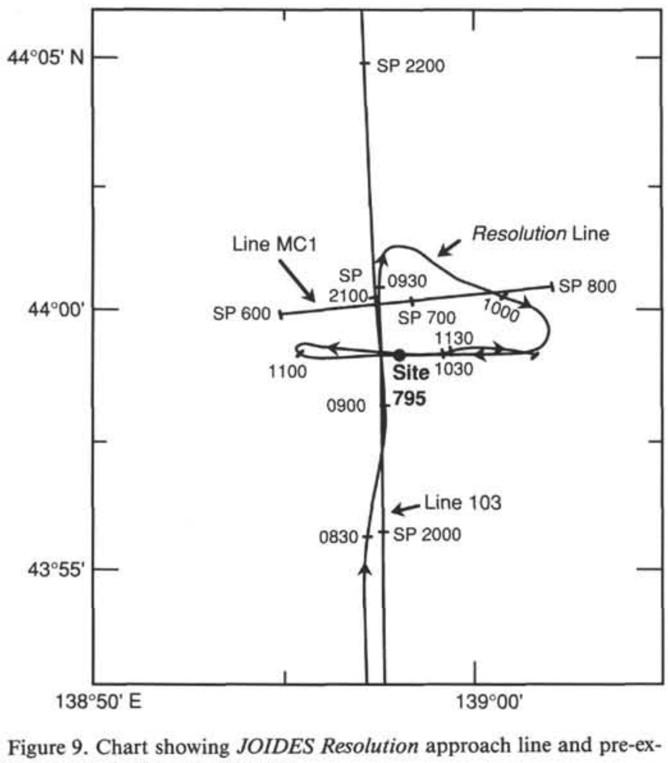

Figure 9. Chart showing *JOIDES Resolution* approach line and pre-existing seismic lines for Site 795.

Drilling and Logging Summary

We planned to drill two adjacent holes at Site 795 to achieve our scientific objectives. Hole 795A was planned as an APC/XCB hole into indurated sediments to recover a complete and relatively undisturbed sedimentary section. *In-situ* temperature measurements were planned for 30 m intervals. Hole 795B was to be an RCB hole beginning at the Hole 795A total depth and carrying 50 m into hard basement rocks. We planned to log the complete sedimentary and basement sections of this hole and perform packer/hydrofracture experiments in the basement interval.

Hole 795A

Hole 795A spudded at 0745 on 13 July (2345 UTC, 12 July 1989) with a mud-line core which established the seafloor depth at 3311.2 m below the driller's datum. Calm seas and almost no current made for good coring conditions. Nineteen cores were taken with a TCI roller cone bit and the APC to a depth of 171.9 mbsf before it became necessary to change to the XCB (Table 1). Except for one interval between 151.8 and 162.4 mbsf, core recovery using the APC was excellent and drilling disturbance was minimal. All APC cores were oriented beginning with Core 127-795A-2H. The temperature probe tool (WSTP) was run for temperature measurements every third to fourth core to a depth of 162.4 mbsf.

Following the APC coring, 20 XCB cores were taken between 171.9 and 365.9 mbsf (Table 1). Recovery was somewhat variable, and many of the cores were broken or fractured. During retrieval of the third XCB core, the coring line parted and the core barrel fell back down the pipe. The core barrel was recovered on the second fishing attempt and it was found that the coring line had parted just above the sinker bar assembly. The next two cores had zero recovery, the latter (Core 127-795A-24X) after encountering some constriction in the pipe. The constriction problem abated and the next two cores had full recovery before hard siliceous claystones were encountered at 327 mbsf. XCB operations continued in Hole 795A to 365.9 mbsf. With recovery decreasing and coring becoming more difficult in the brittle siliceous rocks, a round trip was made to retrieve the BHA for rotary coring in Hole 795B.

Hole 795B

Disaster struck as we lowered the pipe and BHA to begin RCB operations at Hole 795B. After lowering 2100 m, the driller's weight indicator registered a sudden decrease, indicating that a long section of the pipe had somehow come loose and fallen to the seafloor. When the remaining pipe was retrieved, we found that the metal of the threaded connection had failed rather than the joints unscrewed. About 1200 m of pipe were lost and we were down to our last BHA. We made up the final BHA, offset our position 185 m to the west-northwest, and lowered the pipe once again to the seafloor to begin Hole 795B.

Core 127-795B-1R was on deck at 0500 on 17 July (2000 UTC, 16 July 1989). Core 127-795B-2R was cut and being retrieved when we experienced a full power failure due to a fire in the THYRIG "D" transformer. We drifted about 122 m off site

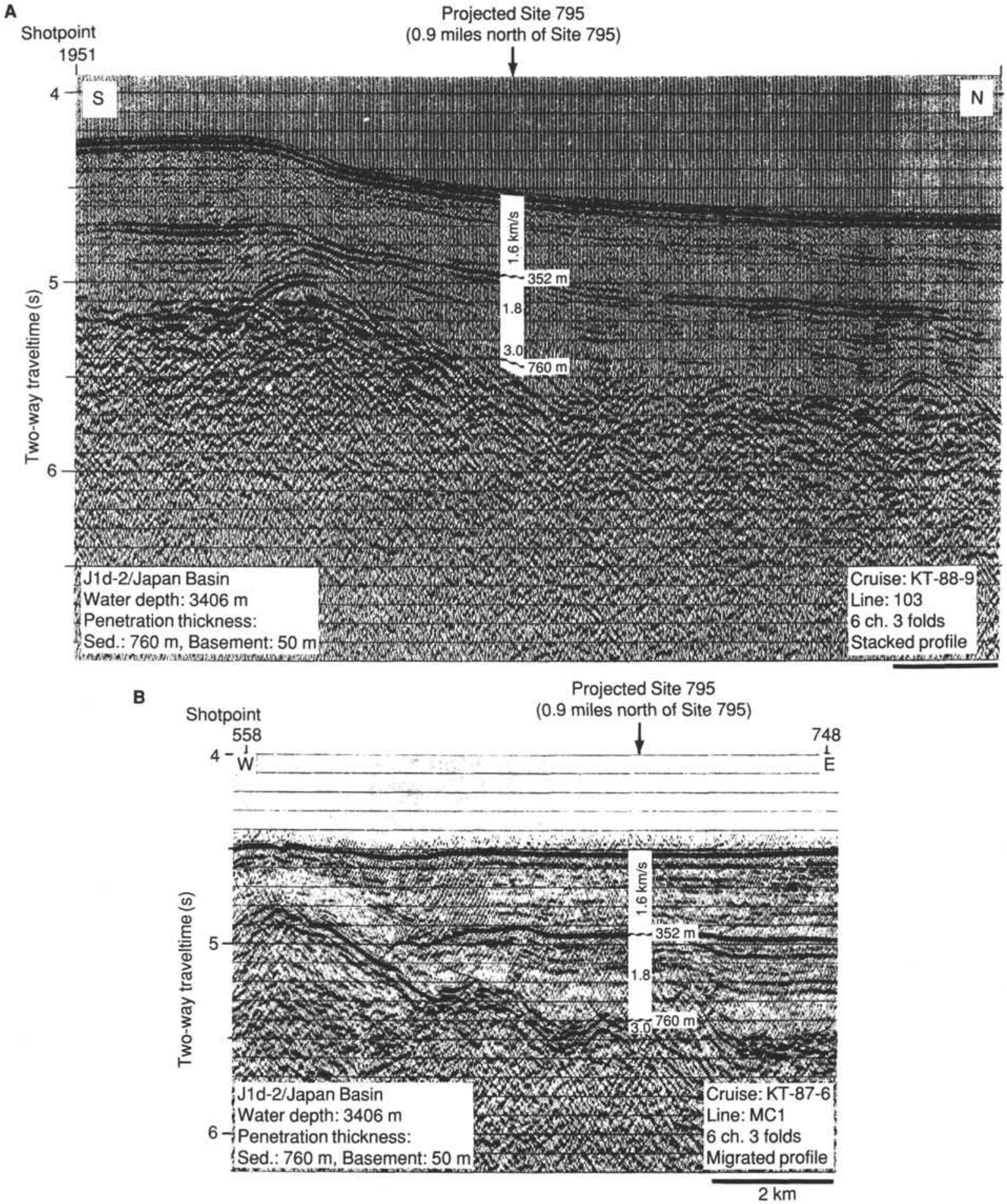

Figure 10. Multichannel seismic lines near Site 795. Locations given in Figure 9. **A.** Ocean Research Institute seismic Line 103. **B.** Ocean Research Institute seismic Line MC1.

before power was restored to the thrusters; calm seas and almost no current kept us out of more serious trouble. Although full power was not restored to the rig until 1715 (0815 UTC) on 17 July 1989, we were able to continue coring at 0730 of that day (2230 UTC 16 July 1989) without difficulty. We recovered a total of 41 RCB cores from this hole, averaging a respectable 47% recovery (Table 1). We completed RCB coring operations in Hole 795B at 1635 (0735 UTC) on 20 July 1989, after taking eight basement cores consisting of altered basalts and basaltic breccias.

Following RCB coring, we conditioned Hole 795B, released the bit, and raised the pipe to 100 mbsf in preparation for logging. The planned logging sequence was: L-DGO magnetometer/susceptibility, BHTV, Schlumberger logs ("Quad Combo" and geochemical log), and the FMS. In addition, we planned to run a packer test followed by an additional BHTV run if hole

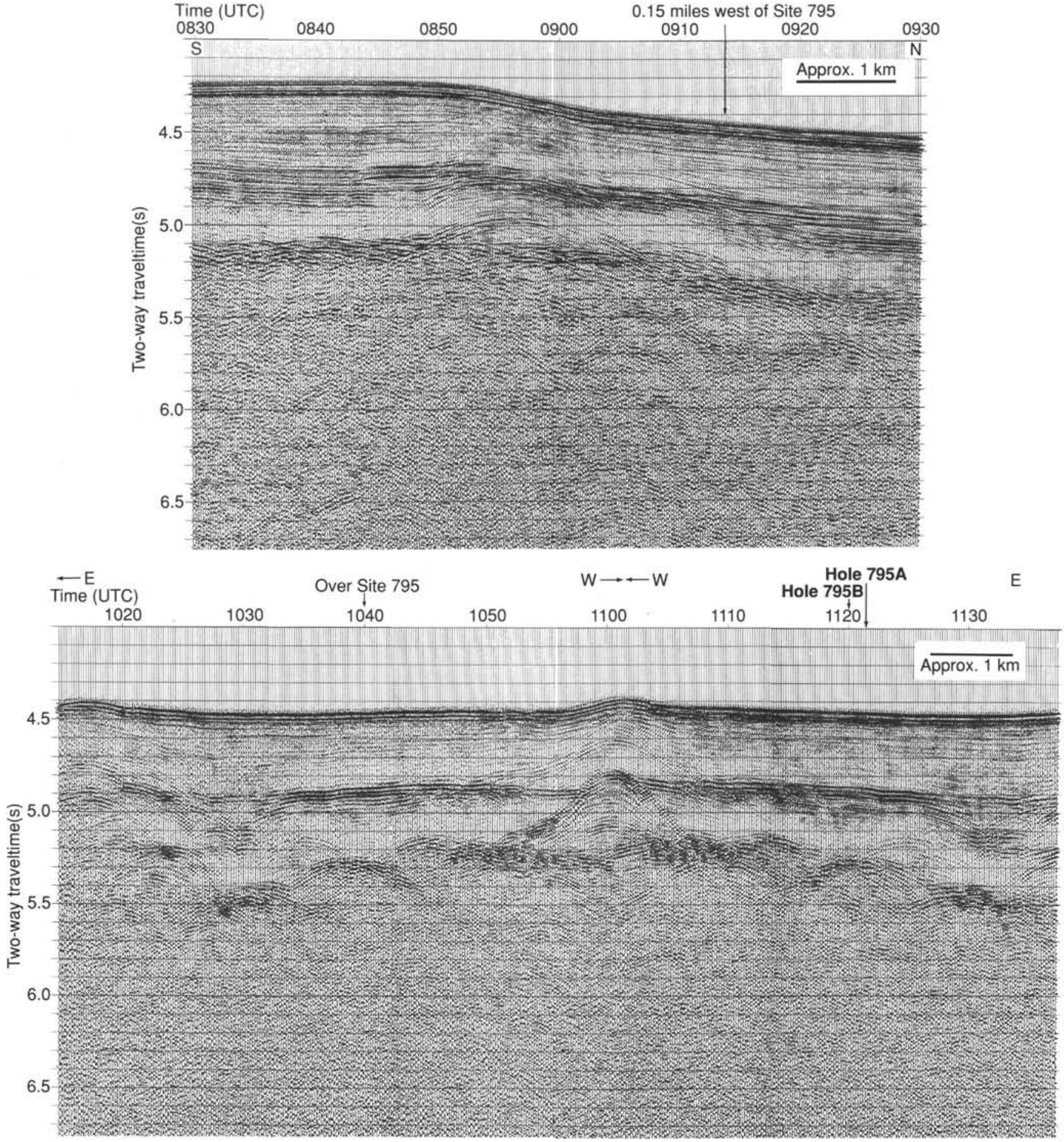

Figure 11. *JOIDES Resolution* single channel seismic line over Site 795. Location on Figure 9. Note course changes.

conditions permitted. The magnetometer was never deployed because of an electrical malfunction; after several hours were spent trying to repair it, we decided to run the BHTV. The tool was lowered to about 231 mbsf, but would not proceed below this point. We recovered the tool and made a short wiper trip to open the congested zone. Some difficulties were encountered during this trip over a 30-m interval (230–260 mbsf), so we decided to deploy the much heavier "Quad Combo" tool on the next run rather than the BHTV. This tool also failed to get past the constriction at about 238 mbsf after several attempts. The cause of the blockage was uncertain. We suspected swelling clays because a lithologic change from diatom ooze to diatomaceous silty clay occurs at about 220 mbsf. Alternatively, slumping of incompetent material in the upper part of the hole may have caused the blockage. We recovered the Schlumberger tool string after logging the short interval between the constriction and the base of the pipe, and continued to work the pipe in the hole over the tight interval, which had grown to encompass 230–280

Table 1. Coring summary, Site 795.

Core no.	Date (July 1989)	Time (UTC)	Depth (mbsf)	Cored (m)	Recovered (m)	Recovery (%)	Age
127-795A-							
1H	12	2315	0.0–9.3	9.3	9.33	100.0	Quaternary
2H	13	0020	9.3–18.8	9.5	9.79	103.0	Quaternary
3H	13	0115	18.8–28.3	9.5	9.94	104.0	Quaternary
4H	13	0340	28.3–37.8	9.5	9.92	104.0	Quaternary
5H	13	0420	37.8–47.3	9.5	10.03	105.6	Quaternary
6H	13	0510	47.3–56.8	9.5	9.95	105.0	Unknown
7H	13	0720	56.8–66.3	9.5	9.70	102.0	Unknown
8H	13	0810	66.3–75.8	9.5	9.90	104.0	Unknown
9H	13	0845	75.8–85.3	9.5	9.86	104.0	Unknown
10H	13	1130	85.3–94.8	9.5	2.70	28.4	Quaternary
11H	13	1215	94.8–104.3	9.5	9.94	104.0	Quaternary
12H	13	1330	104.3–113.8	9.5	9.81	103.0	l. Pliocene
13H	13	1445	113.8–123.3	9.5	9.96	105.0	l. Pliocene
14H	13	1715	123.3–132.8	9.5	10.02	105.5	l. Pliocene
15H	13	1815	132.8–142.3	9.5	9.99	105.0	l. Pliocene
16H	13	2045	142.3–151.8	9.5	5.90	62.1	l. Pliocene
17H	13	2125	151.8–151.9	0.1	0.01	10.0	l. Pliocene
18H	13	2310	152.9–162.4	9.5	9.55	100.0	l. Pliocene
19H	14	0220	162.4–171.9	9.5	10.02	105.5	l. Pliocene
20X	14	0400	171.9–181.6	9.7	0.00	0.0	
21X	14	0445	181.6–191.2	9.6	9.53	99.3	l. Pliocene
22X	14	0825	191.2–200.9	9.7	9.54	98.3	l. Pliocene
23X	14	0945	200.9–210.7	9.8	0.00	0.0	
24X	14	1130	210.7–220.4	9.7	0.00	0.0	
25X	14	1245	220.4–230.1	9.7	9.78	101.0	e. Pliocene
26X	14	1345	230.1–239.9	9.8	9.80	100.0	e. Pliocene
27X	14	1500	239.9–249.7	9.8	9.80	100.0	e. Pliocene
28X	14	1630	249.7–259.5	9.8	1.68	17.1	e. Pliocene
29X	14	1800	259.5–269.3	9.8	4.82	49.2	e. Pliocene
30X	14	1900	269.3–279.1	9.8	6.87	70.1	e. Pliocene
31X	14	2000	279.1–288.8	9.7	8.08	83.3	e. Pliocene
32X	14	2050	288.8–298.6	9.8	0.00	0.0	
33X	14	2140	298.6–307.9	9.3	0.00	0.0	
34X	14	2250	307.9–317.6	9.7	9.76	100.0	e. Pliocene
35X	15	0000	317.6–327.2	9.6	9.34	97.3	e. Pliocene
36X	15	0200	327.2–336.9	9.7	0.58	6.0	
37X	15	0400	336.9–346.6	9.7	1.83	18.8	
38X	15	0615	346.6–356.2	9.6	0.34	3.5	
39X	15	0820	356.2–365.9	9.7	0.19	2.0	
Coring totals				364.9	258.26	70.8	
127-795B-							
1R	16	2000	365.2–375.0	9.8	3.64	37.1	l. Miocene
2R	16	2230	375.0–384.7	9.7	2.42	24.9	
3R	17	0100	384.7–394.4	9.7	1.69	17.4	l. Miocene
4R	17	0235	394.4–404.1	9.7	1.93	19.9	l. Miocene
5R	17	0420	404.1–413.8	9.7	1.13	11.6	
6R	17	0600	413.8–423.1	9.3	0.84	9.0	
7R	17	0730	423.1–432.8	9.7	0.69	7.1	
8R	17	0930	432.8–442.4	9.6	1.45	15.1	l. Miocene
9R	17	1100	442.4–452.0	9.6	4.14	43.1	
10R	17	1300	452.0–461.7	9.7	9.20	94.8	
11R	17	1415	461.7–471.4	9.7	5.43	56.0	
12R	17	1600	471.4–481.0	9.6	6.10	63.5	
13R	17	1800	481.0–490.7	9.7	4.19	43.2	l. Miocene
14R	17	1930	490.7–500.0	9.3	5.23	56.2	
15R	17	2155	500.0–509.7	9.7	2.76	28.4	
16R	17	2250	509.7–519.4	9.7	3.94	40.6	
17R	18	0030	519.4–529.1	9.7	2.55	26.3	
18R	18	0225	529.1–538.7	9.6	6.06	63.1	
19R	18	0415	538.7–548.4	9.7	7.14	73.6	
20R	18	0650	548.4–558.1	9.7	7.48	77.1	
21R	18	0835	558.1–567.7	9.6	9.09	94.7	m. Miocene
22R	18	1030	567.7–577.4	9.7	4.60	47.4	m. Miocene
23R	18	1230	577.4–587.0	9.6	6.04	62.9	
24R	18	1415	587.0–596.7	9.7	7.83	80.7	
25R	18	1600	596.7–606.4	9.7	9.54	98.3	
26R	18	1800	606.4–616.0	9.6	9.07	94.5	m. Miocene
27R	18	1945	616.0–625.7	9.7	7.43	76.6	
28R	18	2115	625.7–635.3	9.6	7.50	78.1	m. Miocene
29R	18	2250	635.3–644.9	9.6	6.57	68.4	m. Miocene
30R	19	0035	644.9–654.5	9.6	8.65	90.1	
31R	19	0315	654.5–664.2	9.7	8.13	83.8	

Table 1 (continued).

Core no.	Date (July 1989)	Time (UTC)	Depth (mbsf)	Cored (m)	Recovered (m)	Recovery (%)	Age
127-795B- (Cont.)							
32R	19	0505	664.2–673.9	9.7	5.85	60.3	
33R	19	0650	673.9–683.5	9.6	3.05	31.8	
34R	19	0915	683.5–693.2	9.7	1.44	14.8	
35R	19	1100	693.2–702.9	9.7	1.37	14.1	
36R	19	1345	702.9–712.6	9.7	1.87	19.3	
37R	19	2100	712.6–722.2	9.6	1.22	12.7	
38R	19	2350	722.2–731.9	9.7	5.31	54.7	
39R	20	0240	731.9–741.6	9.7	1.69	17.4	
40R	20	0450	741.6–751.3	9.7	2.83	29.2	
41R	20	0735	751.3–762.2	10.9	1.85	17.0	
Coring totals				397.0	188.94	47.6	

mbsf. Attempts at circulating only succeeding in packing off the section and pumping fluids into the formation.

At this point, we considered rigging the side-entry sub in order to acquire logs, but with two sites left and 30 days remaining in the leg, we decided not to risk sticking the pipe and losing our last BHA. The logging tools and sheaves were rigged down and we pulled out of the hole without further logging. With all materials secured, we departed Site 795 at 0300 hr on 22 July (1800 UTC, 21 July 1989).

LITHOSTRATIGRAPHY

Lithologic Units

Quaternary to middle Miocene strata penetrated in Holes 795A and 795B at Site 795 consist of 685 m of clay, silty clay, diatomaceous clay, and claystone with minor pyroclastic material. This succession is underlain by basalt breccia and basalt. The sedimentary section is subdivided into five major lithologic units based on mineralogic composition and grain-size (Fig. 12). Further division of subunits is based on more subtle variation in sedimentary structures and composition as described below. The last occurrence of diatoms (opal-A) in fine-grained siliceous sediments is coincident with the first occurrence of opal-CT. This important lithologic boundary also marks a significant increase in the state of lithification, a change in physical properties, and a change in pore fluid chemistry.

Unit I: Cores 127-795A-1H through -13H (0–123 mbsf)

Unit I (Fig. 12) consists of Quaternary to uppermost Pliocene silty clay with subordinate clay, diatomaceous clay, ashy silty clay, clay-diatom mixed sediment, and diatom ooze. Minor calcareous layers with common foraminifers and carbonate (mostly dolomite) nodules are also present. Discrete ash layers (from 2 mm to 10 cm thick) are numerous. Unit I comprises primarily fine-grained, terrigenous sediment. Some silty beds contain normal grading in the fine-silt size fraction. Diatoms are a significant component of some layers. Organic material and pyrite are minor components in many layers, regardless of the dominant lithology. Fine-grained tephra occurs as a minor admixture in much of the section.

Subunit IA: Cores 127-795A-1H through -9H (0–85 mbsf)

Subunit IA comprises mainly silty clay, clay, and diatomaceous clay (Fig. 13). The subunit contains common medium to thin, gradational color-banded bedding with faint internal lamination in darker-colored layers and thick laminae of clay-rich sediment in lighter colored intervals (Fig. 14). Rare beds contain normal size grading in the fine silt- to clay-size fraction (Fig. 15).

Bioturbation is slight and present in less than 25% of the subunit. The paucity of bioturbation in Subunit IA is the main criterion for subdivision of Subunits IA and IB. Color variation and gradational color-banded bedding are apparently related to the variable content of disseminated organic material (including pollen and spores) and pyrite in all major lithologies. Pyrite occurs both as silt-size, disseminated authigenic crystals and as larger nodules. Bioturbation is more common in lighter-colored intervals.

Ash beds are a minor but common component in Subunit IA. Discrete ash beds range from a few millimeters to several centimeters in thickness and commonly contain normally graded bedding. Ash layers are composed mostly of delicate bubble wall shards, pumice, and minor crystals of quartz and plagioclase feldspar. Fine-grained ash is also a common admixture in all sediment types. Other features in Subunit IA include rare, pebble- to cobble-size isolated clasts and rare small normal faults.

Subunit IB: Cores 127-795A-9H through -13H (85–123 mbsf)

Subunit IB is transitional downward from Subunit IA and is defined by a gradual increase in bioturbation, by mottles, and by wispy, discontinuous laminae. More than 50%–70% of the subunit is bioturbated. The mineralogic composition of Subunit IB is similar to the overlying subunit with a small decrease in diatoms concomitant with an increase in clay content (Fig. 13).

Unit II: Cores 127-795A-13H through -26X (123–239 mbsf)

Unit II consists of lower to upper Pliocene diatom ooze and silty clay-diatom mixed sediment with subordinate silty clay and diatomaceous silty clay. Minor dolomicrite and dolomitic nodules, commonly associated with concentrations of foraminifers, are also present. Normally graded ash layers, to several centimeters thick, are rare and occur mainly at the top and bottom of the unit (Cores 127-795A-15H, -16H, and -25H). Unit II is distinguished from Unit I based on a gradational and significant increase in diatom content at the expense of terrigenous sediment downsection (Fig. 13). Indistinct color banding and laminae are present in the upper part of the unit but diminish downward. The unit is moderately to heavily bioturbated and mottled throughout.

Unit III: Core 127-795A-26X through Section 127-795A-35X-5 (239–325 mbsf)

Unit III consists of uppermost Miocene(?) to lower Pliocene silty diatom claystone, diatom-clay-silt mixed sediment, and subordinate diatom clayey siltstone. Minor calcareous intervals and dolomitic nodules are also present. Unit II is transitional downward to Unit III based on decreased diatom content, increased

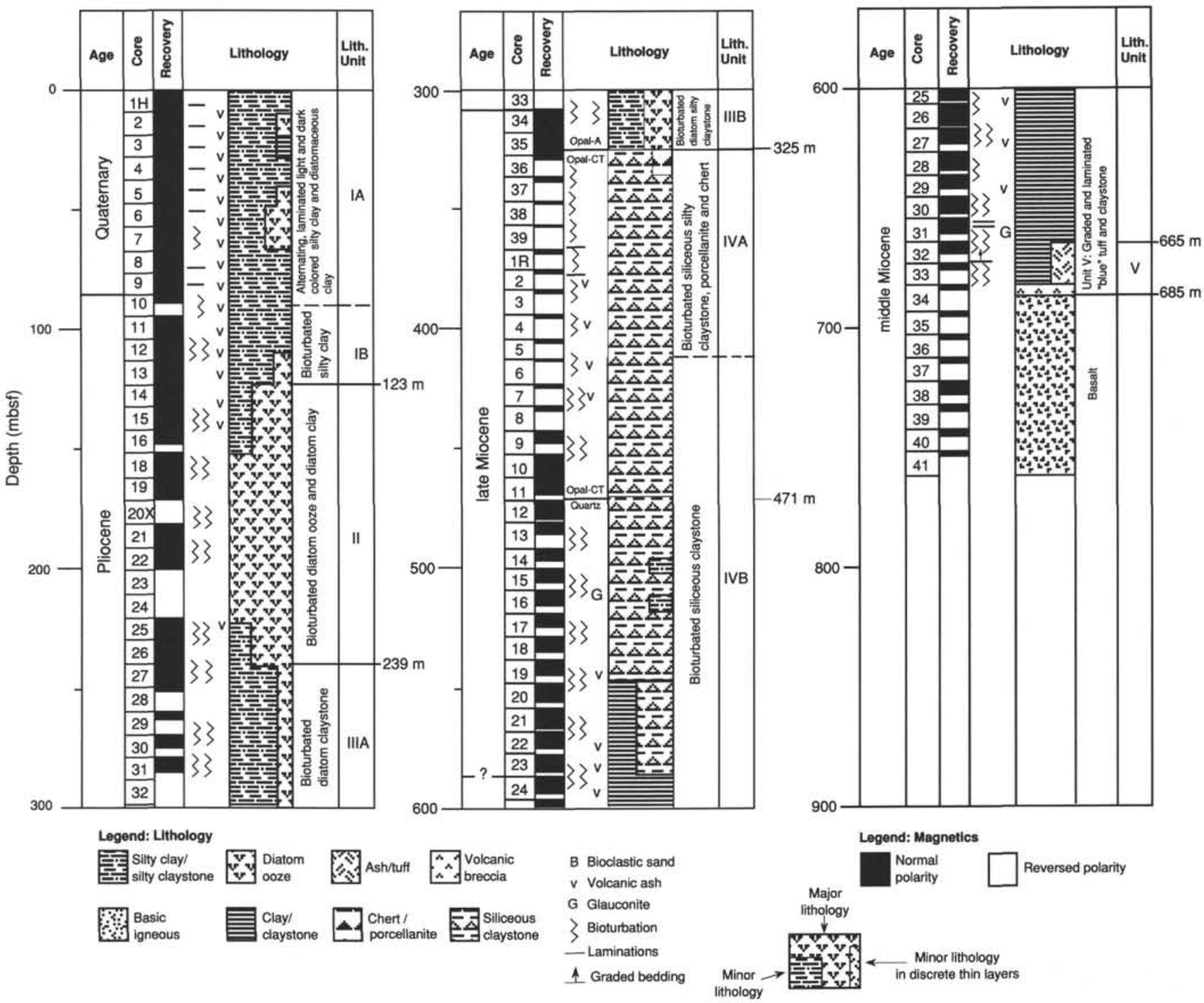

Figure 12. Generalized lithologic column for Site 795. The first lithology column represents the dominant lithology. The second column represents subordinate lithologies. A half column indicates major admixtures in the dominant lithology or interbedded lithologies up to but less than 40%. A full second column indicates mixed sediment or subequal amounts of each lithology in the interval.

silt and clay content, and increased consolidation. Unit III represents a slight to moderate increase in terrigenous sediment at the expense of diatomaceous sediment compared to Unit II. The unit is moderately to heavily bioturbated with a generally homogeneous texture throughout.

Subunit IIIA: Cores 127-795A-26X through -31X (239–288.8 mbsf)

Subunit IIIA consists of diatom claystone and silty diatom claystone. Minor lithologies include very rare ash beds and dolomite nodules. The subunit is faintly mottled to homogeneous due to moderate to intense bioturbation. This subunit is more consolidated than the overlying strata.

Subunit IIIB: Core 127-795A-34X to Section 127-795A-35X-5 (307.9–325 mbsf)

Subunit IIIB comprises diatom-silt-clay mixed sediment, and diatom clayey siltstone. The subunit is distinguished based on increased silt and diatom content at the expense of clay compared to Subunit IIIA. Rare, faint, wispy laminae occur, although the subunit is mostly homogeneously bioturbated.

Unit IV: Section 127-795A-35X-6 through Section 127-795B-32R-1 (325–665 mbsf)

Lithologic Unit IV is an upper Miocene to lower middle Miocene succession of siliceous claystone and silty siliceous claystone with subordinate chert and porcellanite. The unit is moderately to heavily bioturbated throughout. The sharply defined last occurrence of diatom tests (opal-A) and the first occurrence of opal-CT in siliceous sediments at 325 mbsf (Figs. 13 and 16A) coincide with increased lithification, bulk density, grain density, and sonic velocity and decreased porosity (see "Physical Properties" section, this chapter) and significant variation in pore fluid chemistry (see "Inorganic Chemistry" section, this chapter). This sharp lithologic boundary defines the top of Unit IV.

Tuff beds, micrite layers, and calcareous and pyrite nodules are also minor constituents of the section. Dolomite is the main

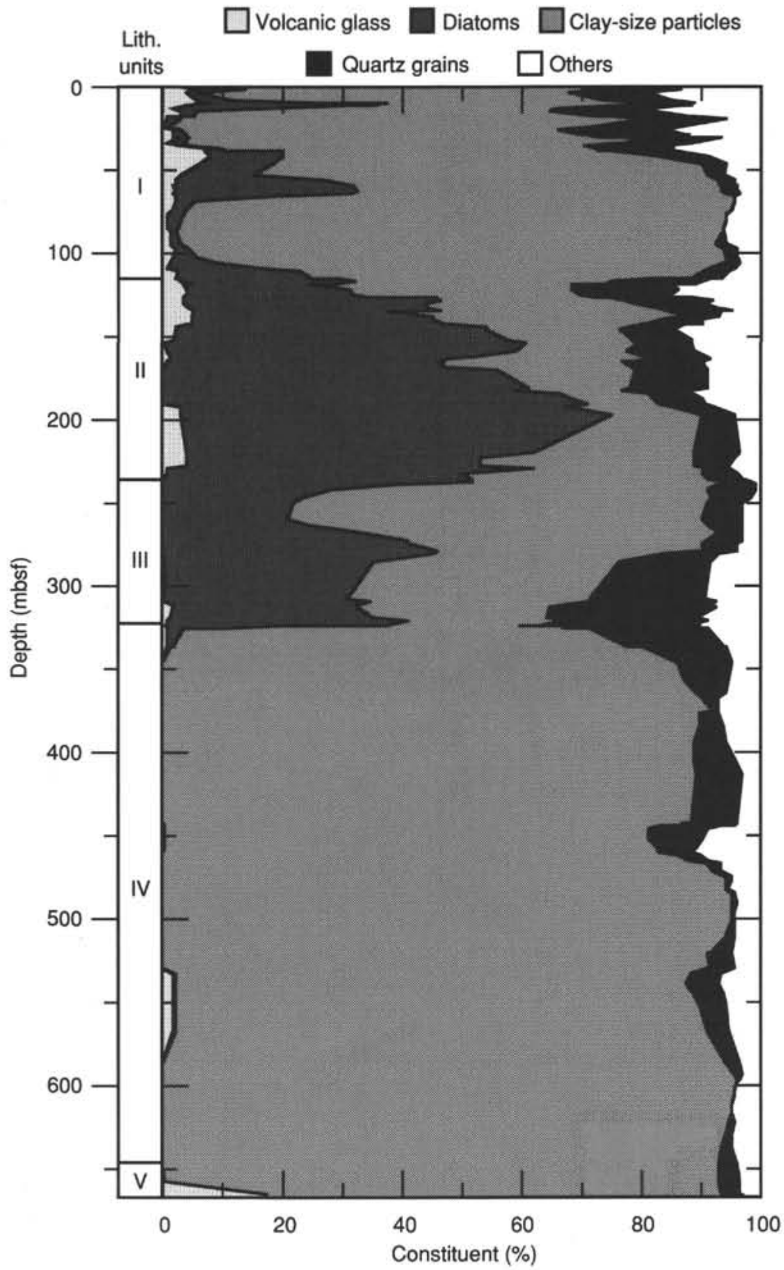

Figure 13. Stack plot of semiquantitative mineralogic data from smear slide analysis vs. depth. Lithologic units are shown.

mineral in calcareous intervals in the upper portion of the unit, whereas, calcite is dominant in the lower portion. Small normal faults are common throughout the succession, and generally increase in abundance downward. Calcite-filled fractures are commonly associated with faulted horizons. Small (several centimeters long by less than a millimeter thick), dark, clay(?)-filled vertical to subvertical and sinuous fluid-escape(?) structures are commonly associated with small faults.

Unit IV comprises predominantly hemipelagic terrigenous sediments with a generally large biogenic silica component that decreases at the base of the section. Original depositional fabric is largely destroyed by bioturbation, compaction, and cementation associated with silica diagenesis. Most primary biogenic silica has been altered by diagenesis.

Subunit IVA: Section 127-795A-35X-6 through Core 127-795B-5R (325–413 mbsf)

Subunit IVA consists of siliceous silty claystone and several porcellanite and chert layers that are highly disturbed by drilling. This interval may contain abundant cherty layers that were not recovered (based on observed drilling conditions and poor recovery). The subunit is moderately bioturbated, with few faint laminae.

Subunit IVB: Core 127-795B-6R through Section 127-795B-32R-1 (413–665 mbsf)

The base of Subunit IVA is defined by the decrease in grainsize from silty siliceous claystone to siliceous claystone and a

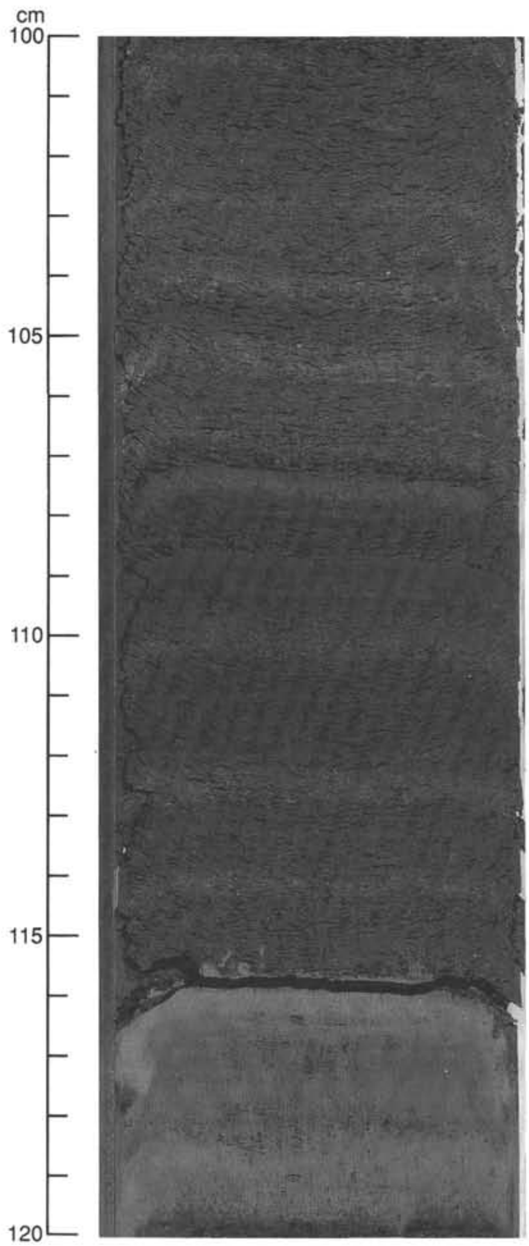

Figure 14. Typical color-banded bedding in dark, internally laminated layers, and lighter layers with thick, clay-rich laminae, Unit I, Interval 127-795A-7H-5, 100–120 cm.

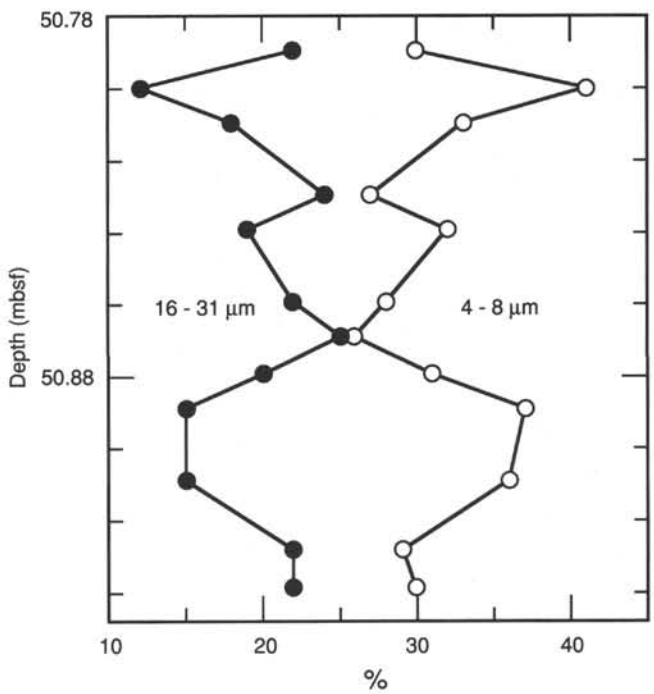

Figure 15. Grain-size profile from a Quaternary succession, Site 795, 50.78–50.94 mbsf.

gradual variation in the style of bioturbation. Subunit IVB is a generally monotonous interval characterized by moderately to heavily bioturbated siliceous claystone, claystone, and subordinate silty siliceous claystone. Disseminated pyrite is common and many intervals contain (agglutinated?) foraminifers. Disseminated sand-size green pellets (glauconite?) are a minor constituent. Green particles are most common at the base of the subunit. Crystal vitric tuff beds, to 42 cm thick, are a minor component but occur in increasing number at the base of the subunit. Tuff beds are normally graded with internal lamination and common bioturbation at the top.

Although bioturbation has rendered much of the subunit essentially homogeneous, a cyclicity in the style of bioturbation is present, especially between approximately 440 and 650 mbsf. Lighter colored layers, generally from 30 to 100 cm thick, are heavily bioturbated and homogeneous with sparse, distinct, dark horizontal, oblique, and subvertical burrows from 1 mm to several centimeters in maximum diameter. Small (< 1 mm) branching forms resembling *Chondrites* are the most obvious burrows, although other traces including probable *Zoophycos* and *Nereites* are present.

Light colored, heavily bioturbated layers alternate with 5–30 cm thick, darker-colored layers. Darker colored layers are slightly to moderately bioturbated and contain a less diverse suite of burrow forms. Pyrite and disseminated organic material are more abundant components in these darker layers. Incipient fissility in these layers is associated with distinct, compacted, mostly ellipse-shaped burrows from several millimeters to 2 cm in maximum diameter. Typical cyclicity in color, style of bioturbation, and texture in this interval is shown in Figures 17A and B.

The last occurrence of opal-CT in Unit IV coincides with an increase in quartz content at approximately 471 mbsf, based on X-ray diffraction analysis (Figs. 16A and B). The quartz content increases downward to 575 mbsf, then decreases. These mineralogic changes suggest diagenetic alteration of biogenic opal-CT to quartz beginning at 471 mbsf and lower initial content of biogenic silica in sediment below 575 mbsf, respectively.

Unit V: Section 127-795B-32R-3 through Section 127-795B-34R-1, 80 cm (665–685 mbsf)

Unit V comprises claystone and altered fine- to coarse-grained tuff. These strata are underlain by basalt breccia and then basalt at 685 mbsf. Tuff beds are commonly graded, laminated, and burrowed sequentially upward in a style similar to overlying tuffaceous layers in Unit IV. Strata at the base of Unit IV and in Unit V dip up to 30°. Small normal faults and fluid escape(?)-fractures are common throughout the unit. Calcite-filled veins are commonly associated with tuff beds. Subangular to subrounded, green, sand-size particles of altered volcanic fragments, glauconite, or both are a common constituent throughout the unit.

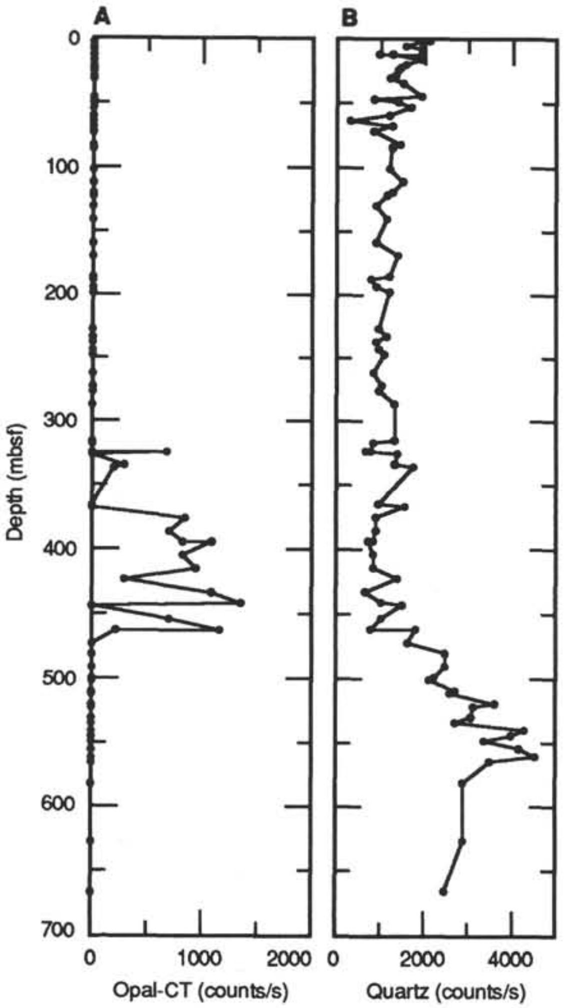

Figure 16. Plot of X-ray intensity (in counts per second) vs. depth. **A.** Main reflection of opal-CT. First and last occurrence are clearly indicated. **B.** Main reflection of quartz. Note the step-wise increase in quartz content indicated below the last occurrence of opal-CT. See text for discussion.

Petrography of Tuffaceous Rocks in Unit V: 665–685 mbsf

The main component of tuffaceous rocks in Cores 127-795B-32R and -33R, based on thin-section petrography, is devitrified glass shards. Strongly altered plagioclase grains and microcrystalline volcanic lithic fragments are minor constituents. Most shards are equant and slightly vesicular with sharp, angular grain boundaries. Grain boundaries cut across vesicles, and particle size is generally larger than the size of component vesicles (Fig. 18). Many fragments are uniform in shape.

Most shards are completely devitrified and altered to zeolite (heulandite), calcite, palagonite(?), and very finely crystalline clay minerals. Rare shards are clear, colorless, nearly isotropic, and suggest an initial sideromelane glass composition.

Distribution of Ash Layers at Site 795

As at Site 794, discrete ash layers were counted and tabulated vs. age, depth, and recovery to relate sedimentation to volcanic activity. Data are presented in Figures 19A and B. The distribution of ash layers at Site 795 is similar to that at Site 794 and DSDP sites on the eastern side of the Japanese archipelago. We recorded two maximums in volcanism at Site 795, one in the Quaternary and latest Pliocene and another in the middle Miocene and early late Miocene. We did not observe a Pliocene maximum in ash layer abundance as we did at in Site 794. This difference may be due to poor recovery in several Pliocene cores (Fig. 19B).

Silica Diagenesis at Site 795

The remarkably sharp last occurrence of diatoms (biogenic opal-A) and the essentially coincident first occurrence of opal-CT (Fig. 16a) at 325 mbsf marks a significant change in the lithology, physical properties (see "Physical Properties" section, this chapter), pore water chemistry (see "Inorganic Geochemistry" section, this chapter), and seismic character (see "Seismic Stratigraphy" section, this chapter) at Site 795. This important horizon occurs in probable uppermost Miocene to lowermost Pliocene strata and is the result of diagenetic transformation of opal-A to opal-CT. A similar lithologic transition, although less sharply defined, occurs at Site 794 at approximately 300 mbsf in slightly older upper Miocene strata (see "Biostratigraphy" section in "Site 794" chapter). Downhole measurements in Sites 794 and 795 indicate temperatures of 36° and 43°, respectively (see "Downhole Measurements" section, this and preceding chapter) at the opal-A to opal-CT transition.

The observations relating to silica diagenesis in Sites 794 and 795 indicate that the lithologic boundary resulting from the diagenetic transformation of opal-A to opal-CT is neither isochronous nor does it represent a sharply defined isotherm. The transformation is the result of a time and temperature dependent diagenetic phenomenon (Mizutani, 1970; Pisciotto, 1981). The position of the opal-A to opal-CT transformation probably represent an approximate isocontour of time-temperature index (Waples, 1980) analogous to isomaturation contours in the alteration of organic material and formation of hydrocarbons.

Depositional History

Basaltic lavas and breccia with a minimum age of 15.5 Ma underlie the stratigraphic section at Site 795. A 20 m thick section of marine hyaloclastite tuff and claystone immediately overlies the basalt breccia. The superjacent middle Miocene through Quaternary section consists of very fine-grained terrigenous and pelagic diatomaceous sediments. Based on study of benthonic foraminifers (see "Biostratigraphy" section, this chapter), the Neogene sedimentary section was apparently deposited in midbathyal and deeper waters. Water depths probably increased upsection.

Pelagic, biogenic sedimentation was dominant during latest middle(?) Miocene to middle late Pliocene. The uppermost Pliocene through Quaternary succession is mostly silty clay with less abundant diatomaceous sediment. The uppermost Pliocene through Quaternary succession in Site 795 is about 40 m thicker and slightly coarser-grained than the same section in Site 794. These relationships are consistent with the more proximal position to terrestrial sediment sources and the more isolated, basinal setting of Site 795.

Middle Miocene Volcaniclastic Rocks: 685–665 mbsf

The composition and textures of tuffaceous strata from 685 to 665 mbsf are consistent with a subaqueous origin, probably at significant water depth. The presence of sideromelane, a quickly quenched basaltic glass, is characteristic of subaqueous extrusion. Minor, small vesicles and the blocky, equant shape of shards are consistent with phreatic (water interaction) eruption and formation of hydroclasts below the volatile fragmentation depth (that depth below which ambient pressure is in excess of the pressure of gas exsolution from the vesiculating magma; Fisher, 1984). The pressure compensation depth for typical basaltic lavas is 200 m or less. Typical, volatile rich alkali basalt

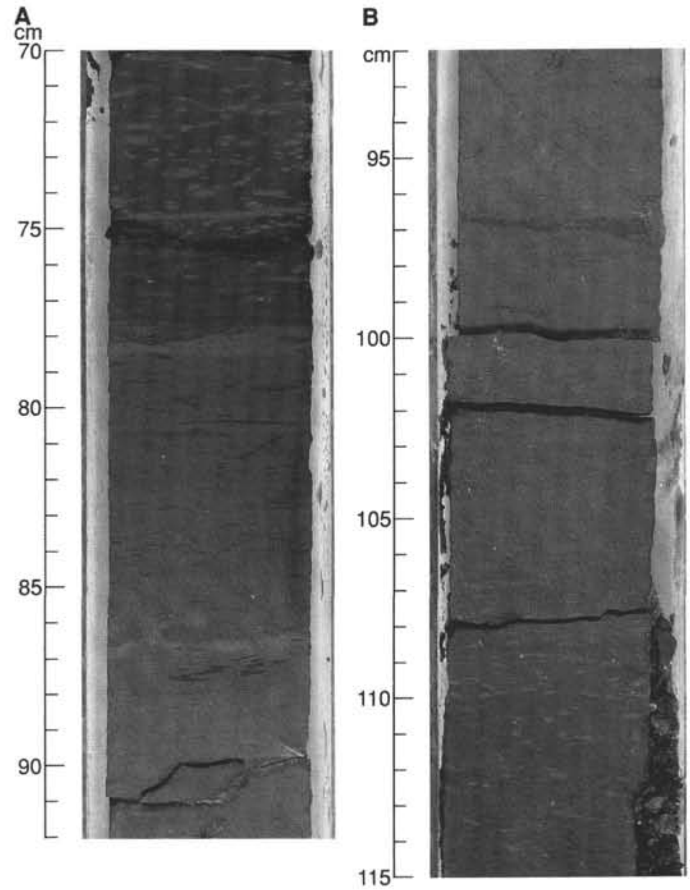

Figure 17. Typical alternation of darker, incipiently fissile, and slightly to moderately bioturbated layers and lighter colored, heavily bioturbated layers in Unit IV. **A.** Interval 127-795B-9R-2, 70–92 cm. **B.** Interval 127-795B-9R-2, 92–115 cm.

probably begins to vesiculate at less than 1800 m. Lavas of intermediate composition may begin to explosively vesiculate at 1000 m water depth or less. Therefore, the water paleodepth during formation of locally derived hyaloclastite tuff at the base of the sedimentary section at Site 795 is estimated to be 200–1800 m.

Middle Miocene Claystone: 665–560 mbsf

Consideration of accumulation rate (see "Sediment Accumulation Rates" section, this chapter) and composition data from X-ray diffraction analysis (Fig. 16B) tentatively suggests that lower silica content in this interval correlates with possible lower sediment accumulation rates (datum 9 or 10 vs. datum 8 accumulation rate: see "Sediment Accumulation Rates" section, this chapter). We tentatively interpret the lower silica content and the probable lower sediment accumulation rate from approximately 665 to 560 mbsf to indicate a generally lower accumulation rate of biogenic silica as compared to that of the overlying section. Clay-rich, heavily bioturbated strata in this interval may have been deposited without a major input of pelagic siliceous sediment in middle bathyal depositional environments (see "Biostratigraphy" section, this chapter) isolated from sources of terrigenous sediment. Bioturbation has removed any evidence of the depositional mechanisms. Cyclicity in the style of bioturbation suggests regularly varying conditions of oxygenation at the sediment water interface between well oxygenated and possibly dysoxic conditions.

Siliceous Claystone and Diatom-Rich Strata: 560–123 mbsf

The accumulation rate for siliceous strata from 560 to 123 mbsf at Site 795 was generally higher than that of subjacent strata (see "Sediment Accumulation Rates" section, this chapter). This difference suggests an increased rate of accumulation of initially diatom-rich(?) sediment. Biogenic silica-rich strata in this interval at Site 795 correlate lithologically with, but are younger than the siliceous Onnagawa and Funakawa formations on the Japanese mainland (Iijima et al., 1988).

Siliceous strata in Site 795 were probably deposited during a period of moderate to high biological productivity. Such oceanographic conditions suggest good overall circulation and exchange with oxygenated, open ocean, intermediate and bottom waters. Upwelling is inferred by both the abundance of diatoms and the presence of upwelling-diagnostic species. Terrigenous sediment accumulation was probably relatively low due to low sediment production rates or isolation of the depositional site from terrestrial sediment sources.

Quaternary to Uppermost Pliocene Clastics: 123–0 mbsf

The significantly greater accumulation rate in the Quaternary and uppermost Pliocene strata from Site 795 as compared to the correlative section in Site 794 (see "Sediment Accumulation Rates" section, this and preceding chapter) suggests a variation in the style of sedimentation. The bathymetric setting of the two sites offers a clue, in that Site 794 is located in a shel-

Figure 18. Hyaloclastite tuff (Interval 127-795B-32R-4, 98–99 cm) with equant, blocky, slightly vesiculated shards suggesting water interaction (phreatic) fragmentation. See text for discussion.

tered environment, isolated from major conduits linking terrigenous sources to the depositional basin. Site 795 is more proximal to terrigenous sources when compared to Site 794. Additional input of terrigenous sediment probably accounts for the enhanced sedimentation rate at Site 795.

Initial grain-size analyses confirm that the mean grain-size of the sediment at Site 795 is greater than that at Site 794 (approximately 13 μm vs. 10 μm). Both sites contain a Quaternary to uppermost Pliocene sequence which is characterized by light-colored (gray), clayey silts interbedded with darker colored (dark olive green/black) layers. These layers are rich in either diatoms, organic debris, ash, or pyrite in various combinations. Dark-colored layers are comparable in number and thickness in both sites based on initial ship-board analyses (C_{org}, grain-size, $CaCO_3$, visual).

Limited data from shipboard grain-size analyses carried out on several light-colored (gray) clayey silt intervals from Site 795 indicate that fine-grained, laminated, silt sequences are present. Individual sequences are approximately 3–5 cm in extent, with two or three sequences present within a 10–15 cm light-colored horizon. Individual sequences show grain size fluctuations, especially within the 4–8 μm and 16–31 μm fractions (Fig. 15). A similar grain size pattern in other studies has been related to the depositional record of turbidity flows (cf. Piper, 1978; Hill, 1984). Chough (1984) reported the presence of similar fine-grained sequences in the Ulleung (Tsushima) back-arc basin southeast of Site 795, and related their deposition to the occurrence of density flows. Fine-grained turbidity current deposits dominated sedimentation in the Ulleung basin during glacial periods when sea level was lower than present. A similar depositional setting may account for deposition of portions of the Quaternary-uppermost Pliocene succession at Site 795.

BIOSTRATIGRAPHY

Introduction

The abundance and preservation of microfossils are variable throughout Holes 795A and 795B (Tables 2 and 3). Diatoms and radiolarians are most abundant in the silty clay and ooze of the Pleistocene and Pliocene. There are also rare to common diatoms and radiolarians in the Miocene claystone unit below the opal-A/opal-CT boundary. Diatoms are moderately preserved in calcareous concretions and layers, and radiolarians are coated with opal-CT and are preserved in the claystone. Calcareous nannofossils are occasionally present in Quaternary, lower Pliocene, and middle Miocene sediments. Planktonic foraminifers are most common in the Quaternary silty clay and are less frequently present in the upper Pliocene silty oozes. Arenaceous benthonic foraminifers are present throughout Holes 795A and 795B and are quite common. In general, they are most abundant in the clay and claystone of the upper and lower Miocene.

Both Holes 795A and 795B are dated by diatom biostratigraphy (Figs. 20 and 21). The radiolarian zonation and several calcareous nannofossil and planktonic foraminifer datum levels are consistent with the age of the cores suggested by the diatom zonation. Poor paleomagnetic resolution of sediments older than 2 Ma at this site precludes comparison with magnetostratigraphy. Extrapolations from a diatom datum in Sample 127-795B-20R-CC, through a calcareous nannofossil datum level in Sample 127-795B-25R-6, 149–150 cm, and a middle Miocene diatom datum level in Sample 127-795B-28R-CC, provide minimum and maximum age estimates of the basement of 13 and 15 Ma.

Diatoms

Samples 127-795A-1H-CC, through 127-795A-13H-CC, consist of clay and silty clay, with minor amounts of diatomaceous ooze, and have diatoms showing variable abundance and preservation. Samples 127-795A-1H-CC, and 127-795A-2H-CC, contain *Neodenticula seminae* but do not have *Rhizosolenia curvirostris* and are, therefore, assigned to the Quaternary *Neodenticula seminae* Zone (Fig. 20). Samples 127-795A-3H-CC, through 127-795A-5H-CC, are assigned to the Quaternary *Rhizosolenia curvirostris* Zone based on the presence of *R. curvirostris* (Fig. 20). Samples 127-795A-6H-CC, through 127-795A-9H-CC, contain a few poorly preserved diatoms but no zonal indicators are present. Samples 127-795-10H-CC, and 127-795-11H-CC, both have *Actinocyclus oculatus* and are assigned to the Quaternary *Actinocyclus oculatus* Zone (Fig. 20), the base of which marks the Quaternary/Pliocene boundary. Six out of eleven Quaternary samples contain reworked upper Miocene diatoms such as *Thalassionema schraderi* and *Denticulopsis praedimorpha* (Fig. 20). Samples 127-795A-12H-CC, and 127-795A-13H-CC, are the lowermost samples from the silty clay of lithologic Unit I. They have common *Neodenticula koizumii* and are assigned to the upper Pliocene *Neodenticula koizumii* Zone (Fig. 20).

Lithologic Unit II is dominated by diatomaceous ooze and includes Samples 127-795A-14H-CC, through 127-795A-26X-CC. These samples have abundant diatoms with excellent to moderate preservation (Table 2). Samples 127-795A-14H-CC, through 127-795A-16H-CC, have common *Neodenticula koizumii* and are assigned to the upper Pliocene *Neodenticula koizumii* Zone

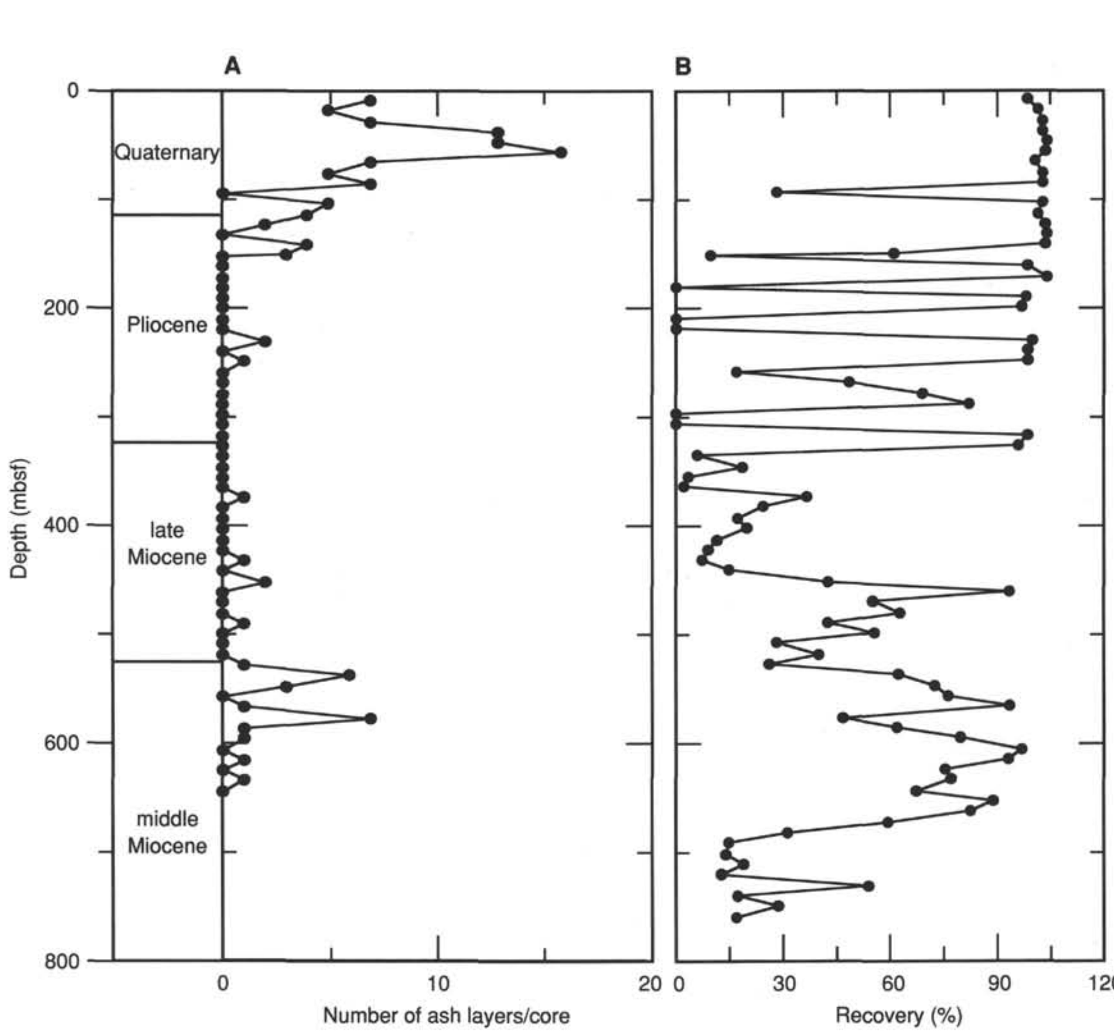

Figure 19. **A.** Plot of discrete ash layers per core vs. depth and age. Note the two maxima, Quaternary-latest Pliocene and early-late Miocene. **B.** Plot of percent core recovery vs. depth. Note sporadic poor core recovery in Pliocene cores. See text for discussion.

(Fig. 20). Samples 127-795A-17H-CC, through 127-795A-22X-CC, have both *Neodenticula koizumii* and *Neodenticula kamtschatica* and belong to the upper Pliocene *Neodenticula koizumii-Neodenticula kamtschatica* Zone (Fig. 20). No sediments were recovered in Cores 127-795A-23X and 127-795A-24X. The lower Pliocene *Thalassiosira oestrupii* Zone occurs in Samples 127-795A-25X-CC, and 127-795A-26X-CC, based on the occurrences of *Thalassiosira oestrupii* and *Neodenticula kamtschatica* and the absence of *Rouxia californica.*

Lithologic Unit III is made up of silty clay, siltstone, and diatomite and includes Samples 127-795A-27X-CC, through 127-795A-35X-CC. This unit contains common to abundant diatoms, with good to moderate preservation (Table 2). The diatom assemblage is characteristic of the lower Pliocene *Thalassiosira oestrupii* Zone. Similar to the Quaternary samples at this hole, 7 of 21 Pliocene core catcher samples have reworked upper and middle Miocene diatoms.

Lithologic Unit IV consists of siliceous silty clay and claystone and lies below the opal-A/opal-CT boundary. Samples 127-795A-36X-CC, through 127-795A-39X-CC, are barren of diatoms (Table 2). In Hole 795B, eight calcareous nodules and layers contain preserved diatoms. Samples 127-795B-1R-1, 88–89 cm, and 127-795B-3R-CC, are assigned to the upper Miocene *Neodenticula kamtschatica* Zone (Fig. 21) based on the presence of *Neodenticula kamtschatica* and *Rouxia californica.* The precise depth of the Miocene/Pliocene boundary at Site 795 is unknown because of the dissolution of diatoms and the lack of authigenic carbonates sediments in Cores 127-795A-36X through -39X. However, extrapolating from the sedimentation rate curve (see "Sediment Accumulation Rates" section, this chapter) the boundary is placed between 325 and 365 m.

A carbonate layer from 127-795B-13R-1, 79–81 cm, has poorly preserved specimens of *Denticulopsis dimorpha* and *Denticulopsis hustedtii* and belongs to the upper Miocene *Denticulopsis dimorpha* Zone (Fig. 21). Carbonate samples from Cores 127-795B-21R, -22R, -26R, and -28R have *Denticulopsis praedimorpha* and are assigned to the middle Miocene *Denticulopsis praedimorpha* Zone (Fig. 21). The middle/late Miocene boundary is tentatively placed at the top of the first sample bearing *Denticulopsis praedimorpha* (Fig. 21). A carbonate layer from 127-795B-29R-1, 139–140 cm, has poorly preserved specimens of *Denticulopsis hustedtii* and is assigned to the *Denticulopsis hustedtii* Zone. Diatoms were not recovered from sediments below Core 127-795B-29R (Table 3). The maximum age of the basement is estimated at about 15 Ma based on extrapolation through the first and last occurrence datum levels of *D. praedimorpha* in the middle and late Miocene (Fig. 21).

Calcareous Nannofossils

Most of the samples studied at Site 795, as at Site 794, do not contain calcareous nannofossils. Nannofossils are found sporadically in the Pleistocene, the middle part of the Pliocene, and

Table 2. Abundance and preservation of microfossils in Hole 795A.

Core	Diatoms		Nannofossils		Planktonic foraminifers		Benthonic foraminifers		Radiolaria	
	Abundance	Preservation	Abundance	Preservation	Abundance	Preservation	Abundance	Preservation	Abundance	Preservation
1H-CC	few	good	barren		rare	poor	barren		rare	good
2H-CC	few	moderate	barren		barren		barren		rare to few	moderate
3H-CC	common	good	barren		barren		barren		abundant	good
4H-CC	rare	poor	abundant	good	abundant	moderate	few	moderate	rare	moderate
5H-CC	abundant	good	barren		common	moderate	barren		abundant	good
6H-CC	rare	poor	barren		barren		barren		few	moderate
7H-CC	few	poor	barren		barren		barren		rare	poor
8H-CC	few	poor	barren		barren		barren		few	moderate
9H-CC	rare	poor	barren		rare	poor	barren		rare	poor
10H-CC	rare	moderate	barren		barren		barren		rare	moderate
11H-CC	common	good	barren		common	moderate	abundant	moderate	few	moderate
12H-CC	abundant	good	barren		few	poor	rare	moderate	common	moderate
13H-CC	abundant	good	barren		barren		rare	moderate	common	moderate
14H-CC	abundant	good	barren		common	moderate	few	moderate	abundant	good
15H-CC	abundant	excellent	barren		barren		few	moderate	abundant	moderate
16H-CC	abundant	good	barren		few	moderate	common	moderate	common	good
17H-CC	abundant	good	barren		barren		barren		common	good
18H-CC	abundant	good	barren		barren		barren		common	moderate
19H-CC	abundant	good	barren		barren		barren		abundant	good
20X-CC					barren		rare	moderate	common	moderate
21X-CC	abundant	good	barren		barren		barren		common	good
22X-CC	abundant	good	barren		rare	poor	few	moderate	common	good
23X-CC										
24X-CC										
25X-CC	abundant	good	barren		barren		few	moderate	abundant	moderate
26X-CC	abundant	moderate	barren		rare	good	few	good	common	moderate
27X-CC	common	moderate	barren		barren		few	moderate	abundant	moderate
28X-CC	common	moderate	few	poor	rare	moderate	few	moderate	common	moderate
29X-CC	common	good	barren		barren		few	moderate	common	good
30X-CC	abundant	good	barren		barren		few	moderate	common	moderate
31X-CC	common	moderate	barren		barren		few	moderate	common	moderate
32X-CC										
33X-CC										
34X-CC	common	moderate	barren		barren		few	moderate	common	moderate
35X-CC	common	moderate	barren		barren		barren		common	moderate
36X-CC	rare	poor	barren		barren		rare	moderate	few	moderate
37X-CC	barren		barren		barren		barren		rare	moderate
38X-CC	barren		barren		barren		barren		rare	poor
39X-CC	barren		barren		barren		barren		common	moderate

in the upper part of the middle Miocene. The assemblages are low in diversity and are almost completely devoid of the tropical and subtropical taxa *Sphenolithus*, *Helicosphaera*, and *Discoaster*.

Of the 34 cores recovered at Hole 795A, only three core catcher samples, 127-795A-4H-CC, 127-795A-10H-CC, and 127-795A-28H-CC, contain nannofossils. A cursory examination of other samples revealed sporadic occurrences of nannofossils from Cores 127-795A-1H through -5H. The preservation of the nannofossils ranges from good to poor, and the abundance ranges from abundant to rare (Table 2). Due to the absence of nannofossils in most of the cores and the absence of the zonal markers, age assignments using nannofossils were not possible for the complete sedimentary sequence. Cores 127-795A-1H through -3H are tentatively assigned to the *Emiliania huxleyi* Zone of the latest Pleistocene to Holocene age (Fig. 20). The assemblage in this zone contains the nominal species, common to few in abundance, with *Braarudosphaera bigelowii*, *Coccolithus pelagicus*, *Calcidiscus leptoporus*, and small *Reticulofenestra* sp., and without any *Gephyrocapsa caribbeanica* or *Gephyrocapsa oceanica*. The absence of the last two species in the latest Pleistocene to Holocene is probably related to adverse surface water conditions related to Northern Hemisphere glaciation and sea level changes. The identification of *E. huxleyi* under the light microscope is difficult due to its very small size. Electron microscopic observation is needed to confirm its presence in the *Emiliania huxleyi* Zone. The upper part of the Core 127-795A-4H is tentatively assigned to the *Gephyrocapsa oceanica* Zone of late Pleistocene age, based on the absence of *E. huxleyi* and *Pseudoemiliania lacunosa*. This zone contains small *Reticulofenestra* and *C. pelagicus*. The lower part of Core 127-795A-4H is assigned to the *Umbilicosphaera sibogae* Zone of early Pleistocene age, based on the presence of *P. lacunosa* and *G. oceanica*. This zone also contains *C. pelagicus*, *G. caribbeanica*, *Helicosphaera carteri*, *Pontosphaera* sp., small *Gephyrocapsa*, *C. leptoporus*, and small *Reticulofenestra*. Sample 127-795A-5H-2, 67–68 cm, contains only *C. pelagicus* and *B. bigelowii* and is not assigned to a zone due to the absence of the marker species. *B. bigelowii* is one of the very few nannofossil species known to live in shelf areas rather than in the open-ocean environment (Perch-Nielsen, 1985). Thus, its presence in the Quaternary sediments probably indicates transport from a nearshore environment. Sample 127-795A-28X-CC, yielded a poorly preserved assemblage of small *Reticulofenestra*, *Sphenolithus abies*, and some questionable remains of *Sphenolithus* sp., which are very difficult to recognize because of strong overgrowth.

Only 3 of the 33 core catcher samples from Hole 795B yielded nannofossils; these are Samples 127-795B-12R-CC, 127-795B-24R-CC, and 127-795B-27R-CC. These samples, and some other samples between the core catchers, contain low diversity assemblages with moderate to poor preservation and specimens few to rare in abundance (Table 3). Sample 127-795B-12R-CC, only contains small *Reticulofenestra*, a condition which precludes zonal or age assignment. Nannofossils occur sporadically within and between Samples 127-795B-25R-6, 149–150 cm, and 127-795B-27R-CC. The assemblage consists of *Reticulofenestra pseudoumbilica*, *Coccolithus pelagicus*, *Cyclicargolithus floridanus*, *Calcidiscus macintyrei*, and small *Reticulofenestra*. The pres-

Table 3. Abundance and preservation of microfossils in Hole 795B.

Core	Diatoms		Nannofossils		Planktonic foraminifers		Benthonic foraminifers		Radiolaria	
	Abundance	Preservation	Abundance	Preservation	Abundance	Preservation	Abundance	Preservation	Abundance	Preservation
1R-CC	barren		barren		barren		barren		common	moderate
2R-CC	barren		barren		barren		barren		few	moderate
3R-CC	common	good	barren		barren		barren		rare to few	moderate
4R-CC	barren		barren		barren		barren		few	moderate
5R-CC	barren		barren		barren		barren		barren	
6R-CC	barren		barren		barren		barren		few	poor
7R-CC	barren		barren		barren		common	poor	common	poor
8R-CC	barren		barren		barren		rare	poor	common	poor
9R-CC	barren		barren		barren		common	moderate	rare	poor
10R-CC	barren		barren		barren		few	moderate	rare	poor
11R-CC	barren		barren		barren		abundant	moderate	barren	
12R-CC	barren		rare	poor	few	poor	abundant	good	barren	
13R-CC	barren		barren		few	poor	abundant	good	barren	
14R-CC	barren		barren		barren		abundant	moderate	barren	
15R-CC	barren		barren		barren		abundant	moderate	barren	
16R-CC	barren		barren		barren		abundant	moderate	barren	
17R-CC	barren		barren		barren		abundant	moderate	barren	
18R-CC	barren		barren		barren		common	moderate	barren	
19R-CC	barren		barren		barren		few	moderate	barren	
20R-CC	barren		barren		barren		rare	poor	barren	
21R-CC	rare	poor	barren		barren		rare	moderate	barren	
22R-CC	rare	poor	barren		barren		barren		barren	
23R-CC	barren		barren		barren		common	moderate	barren	
24R-CC	barren		barren		barren		common	moderate	barren	
25R-CC	barren		rare	poor	barren		few	good	barren	
26R-CC	barren		barren		barren		few	good	barren	
27R-CC	barren		few	moderate	few	moderate	abundant	good	barren	
28R-CC	barren		barren		barren		abundant	good	rare	poor, pyritized
29R-CC	barren		barren		barren		common	poor	barren	
30R-CC	barren		barren		barren		few	poor	barren	
31R-CC	barren		barren		barren		few	poor	barren	
32R-CC	barren		barren		barren		barren		barren	
33R-CC	barren		barren		barren		barren		barren	

ence of *C. floridanus*, the last occurrence of which is reported to be 11.6 Ma (Berggren et al., 1985b) provides a minimum age estimate of Sample 127-795B-25R-6, 149–150 cm. Other nannofossils with last occurrences in the middle Miocene, such as *Sphenolithus moriformis*, *Sphenolithus heteromorphus*, and *Discoaster deflandrea* were found at Site 794 but are completely absent from Hole 795B.

The age of the basement is estimated at about 13 Ma based on extrapolation from the last occurrence of *Cyclicargolithus floridanus* and the diatom datum plane immediately above it in the sedimentary sequence (Fig. 26). The true last occurrence of *C. floridanus* could lie above Sample 127-795B-25R-6, 149–150 cm, because dissolution has removed nannofossils from 127-795B-24R-CC, to 127-795B-12R-CC. A shallower last occurrence of this species would have provided an older age estimate. Therefore, the age estimate of 13 Ma should be considered the minimum age of the basement.

Foraminifers

Carbonate preservation is generally poor at Site 795, and many intervals are barren of calcium carbonate microfossils. In contrast, textularid foraminifers are preserved in most lithologies of the site (Tables 2 and 3). The Quaternary and uppermost Pliocene siltstone, lithologic Unit I, suffers extremes in abundance and preservation of calcite microfossils ranging from barren and no preservation to abundant and moderately well preserved. Textularid microfossils that are strong enough to withstand bioturbation in the mixed layer either do not occur or do not survive post-depositional alteration. Reworked neritic diatoms, *Arachynodiscus* and *Isthmia*, are few to common in the sand-size fraction of core catcher Samples 127-795A-12H-CC, and 127-795A-13H-CC, at the base of lithologic Unit I. The underlying Pliocene diatom ooze, lithologic Unit II, contains common calcite microfossils in the topmost core catcher sample of the unit, Sample 127-795A-14H-CC, but rare or no calcite microfossils in all other samples. In contrast, textularid microfossils are preserved in 6 of 11 core catcher samples in the unit. Reworked, sand-size neritic diatoms occur persistently throughout the unit and are especially abundant in Samples 127-795A-15H and 127-795A-19H. The underlying lower Pliocene siltstone, lithologic Unit III, is essentially barren of calcite microfossils, but bears rare to few textularid taxa. Both calcite and agglutinated microfossils are absent from the underlying late Miocene, silty clay claystone, lithologic Unit IVA, which lies below the opal-A/opal-CT boundary. The basal sedimentary sequence of the site is a claystone, lithologic Units IVB and IVC. Textularids are preserved throughout the late and middle Miocene sequence, and two short intervals bear calcite microfossils beneath the opal-CT/quartz boundary in Core 127-795B-11R.

Planktonic foraminifers were recovered from 11 of 39 core catcher samples in Hole 795A, but were common to abundant in only 4 samples, 127-795A-4H-CC, 127-795A-5H-CC, 127-795A-11H-CC, and 127-795A-14H-CC. Preservation is moderate in samples with common to abundant tests, and preservation is generally poor in samples with rare tests. Species typical of the subarctic Quaternary are found in core catcher Samples 127-795A-1H-CC, to 127-795A-9H-CC, and consist of *Globigerina bulloides*, *Globigerina clarkei*, *Globigerina quinqueloba*, and sinistrally and dextrally coiled varieties of *Neogloboquadrina pachyderma*. Assemblages reflect Pleistocene climatic fluctuations. Sample 127-795A-4H-CC, represents a distinctly warmer climate than does Sample 127-795A-5H-CC, based on the frequency of sinistral to dextral forms of *N. pachyderma*. The former sample bears 100% dextral forms indicating warmer conditions than the latter sample, which bears only 50% dextral forms. Samples 127-795A-11H-CC, to 127-795A-26X-CC, bear species

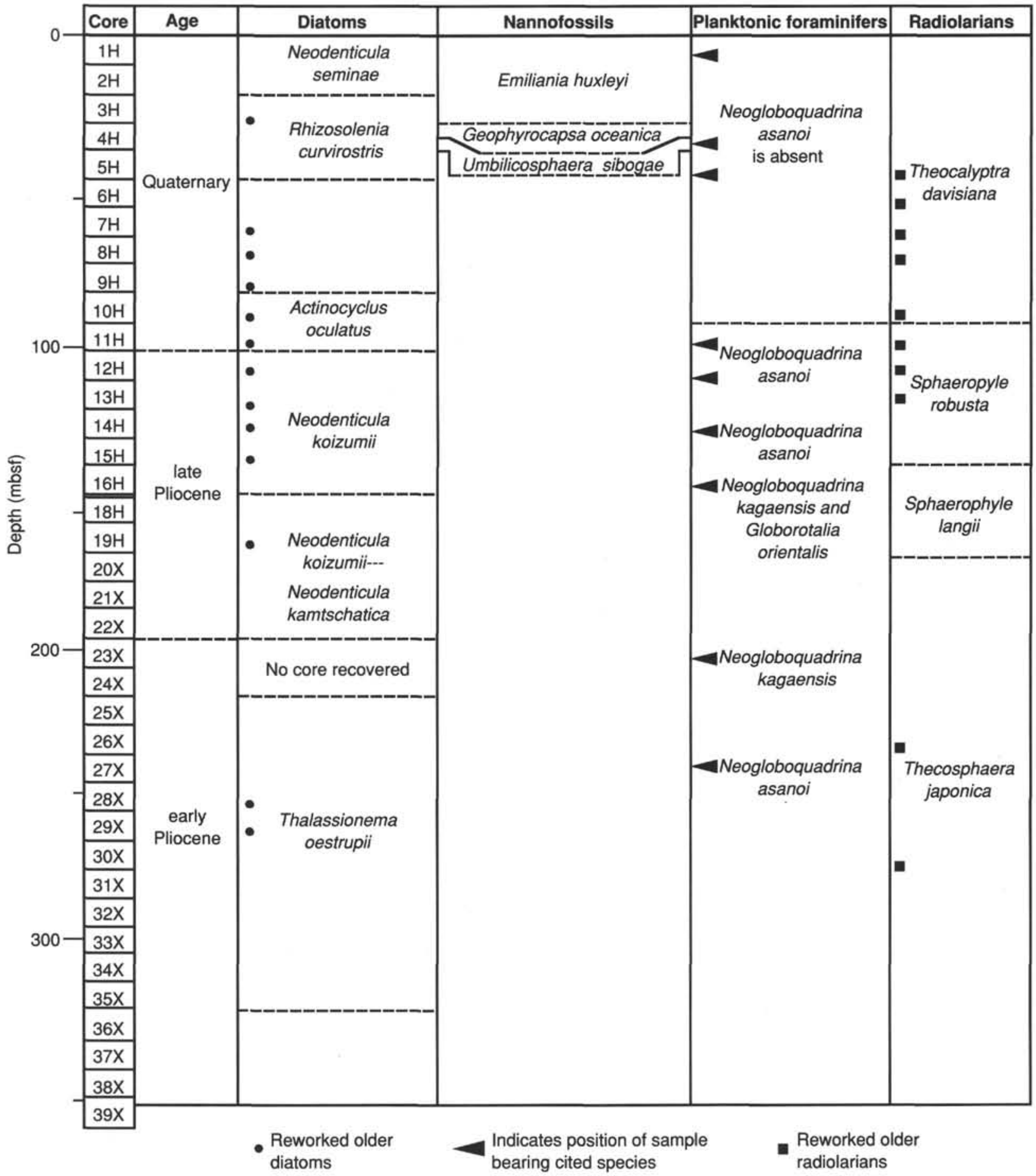

Figure 20. Planktonic microfossil zones in Hole 795A.

typical of the high-latitude North Pacific Ocean during the Pliocene Epoch (Fig. 20). Species include *Neogloboquadrina asanoi*, *Neogloboquadrina kagaensis*, *Neogloboquadrina humerosa*, and *Globorotalia orientalis*, which are limited to the Pliocene and latest Miocene, *Globigerina umbilicata*, which ranges from the Pliocene to the Pleistocene, and *Globigerina bulloides*, *Globigerina quinqueloba*, *Globigerinita* cf. *uvula*, and sinistrally and dextrally coiled varieties of *Neogloboquadrina pachyderma*, which range from the Miocene to the Quaternary.

Planktonic foraminifers are absent from Samples 127-795A-29X-CC, to 127-795A-39X-CC, from Samples 127-795B-1R-CC, to 127-795B-12R-CC, and from Samples 127-795B-14R-CC, to 127-795B-26R-CC. Specimens occur in rare to few numbers in 3 of 31 core catcher samples in Hole 795B, Samples 127-795B-12R-CC, 127-795B-13R-CC, and 127-795B-27R-CC. The assemblages consist of *Globigerina bulloides*, *Globigerina quinqueloba*, *Globigerina woodi*, and *Globigerinita glutinata*, all of which are long-ranging species that are consistent with, but not

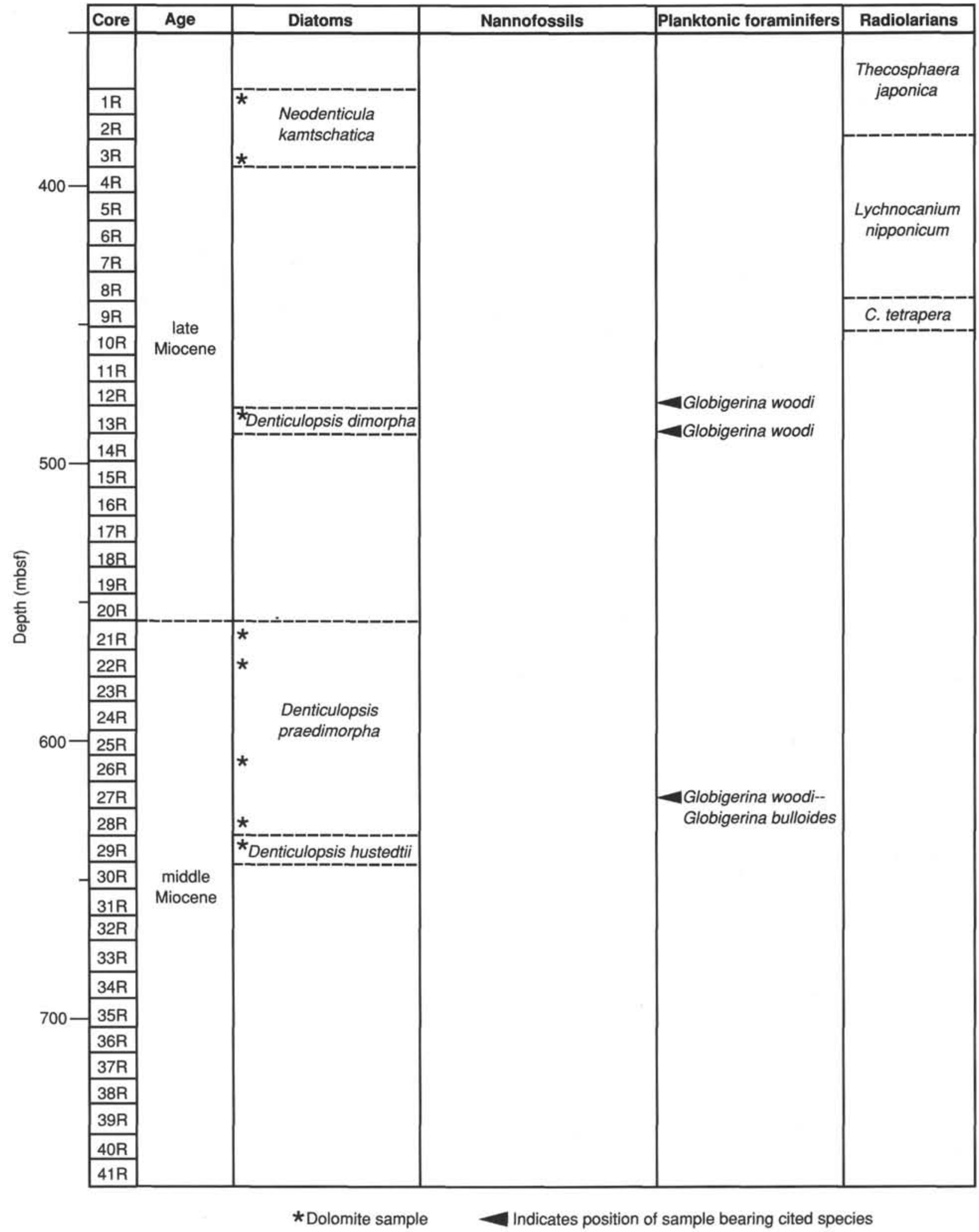

Figure 21. Planktonic microfossil zones in Hole 795B.

diagnostic of, late and middle Miocene ages (Fig. 21). The assemblages are typical of cool, high latitudes in the North Pacific Ocean.

Benthonic foraminifers were recovered from 18 of 39 core catcher samples in Hole 795A. Abundance ranges from rare to few specimens per sample, and most samples from the Quaternary, 9 of 11, are barren. The two fossiliferous samples contain benthonic foraminiferal tests made of calcite and exclude textularids, which bear tests agglutinated with clastic material. Assemblages include *Fursenkoina*, *Epistomaroides*, and *Globocas-*

sidulina with accessory lagenids and *Pyrgo*. A marked change in assemblage occurs in Core 127-795A-12H. Textularids become an important component of the fauna, and feature *Miliamina* and *Martinottiella*. The association, which bears some affinities to that of the Pliocene Funakawa Formation of the Oga Peninsula (Matoba, 1984), persists to Core 127-795A-36X. *Eggerella* becomes an important element of the association in Samples 127-795A-26X-CC, to 127-795A-31X-CC. Foraminifers with calcite tests occur in most samples, and consist of *Cibicides*, *Epistomaroides*, *Fissurina*, *Globobulimina*, *Globocassidulina*, *Lenticulina*, *Melonis*, *Quinqueloculina*, and *Triloculina*, an association consistent with lower middle bathyal depths. Samples from 127-795A-37X-CC, to 127-795A-39X-CC, and from 127-795B-1R-CC, to 127-795B-7R-CC, are barren of all benthonic foraminifers.

Benthonic foraminifers occur in 24 of 31 core catcher samples in Hole 795B, and are limited to the claystone of lithologic unit IV. Many samples contain common and abundant specimens, which are, in general, moderately well preserved. The fauna is dominated by textularids, especially *Martinottiella*, *Cyclammina*, *Haplophragmoides*, and *Ammodiscus*, some of which are greater than 400 μm in diameter. Most samples contain only textularids, but two intervals, from Samples 127-795B-11R-CC, to 127-795B-14R-CC, and from Samples 127-795B-25R-CC, to 127-795B-28R-CC, also bear calcite microfossils. The upper interval contains *Cibicides*, *Fontbotia wuellerstorfi*, *Globobulimina*, *Globocassidulina*, *Gyroidina*, lagenids, *Lenticulina*, *Melonis*, *Pullenia*, *Quinqueloculina*, and *Sphaeroidina bulloides*, all of which are consistent with lower bathyal depths. The lower interval contains the taxa listed above plus *Uvigerina*, *Spirosigmoilinella*, *Oridorsalis*, *Nonionella*, *Fissurina*, *Epistominella*, and *Elphidium*, all of which suggest deposition at a shallower depth, perhaps upper middle bathyal. The association is similar to that above the dolerite at Site 794.

Radiolarians

Radiolarians recovered from Site 795 are generally less abundant and less well preserved than radiolarians found in Site 794 sediments. The poorer preservation is probably caused by the numerous turbiditic mud deposits that were found at this site. These flows have caused significant reworking and destruction of radiolarian tests. The lower abundances of radiolarians at Site 795 have also resulted from greater dilution by detrital components. Radiolarian preservation and abundance for Site 795 are listed in Tables 2 and 3, and the radiolarian zonation is summarized in Figures 20 and 21.

Pleistocene radiolarian assemblages found in the silty clays of Site 795 show variable states of preservation and abundance as well as assemblage composition. Again, as at Site 794, these dramatic changes were probably caused by climatic and oceanographic changes resulting from Northern Hemisphere glaciations and sea level changes. Pleistocene radiolarian datum levels recognized at Site 795 include the FAD of *Lychnocanium* sp. cf. *L. grande* (between Samples 127-795A-2H-CC, and 127-795A-3H-CC) and the LAD of *Clathrocyclas cabrilloensis* (between Samples 127-795A-4H-CC, and 127-795A-5H-CC). Reworked radiolarians are found in Samples 127-795A-4H-CC, 127-795A-5H-CC, 127-795A-6H-CC, 127-795A-7H-CC, 127-795A-8H-CC, and 127-795A-10H-CC (see Fig. 20).

Radiolarian assemblages recovered from the Pliocene diatom oozes and silty clays of Site 795 are slightly different in assemblage composition and generally less abundant with common radiolarians than the Pliocene assemblages of Site 794. The main difference in assemblage composition is the common occurrence of species from the genus *Botryostrobus*, and the variable occurrence of the species *Sphaeropyle robusta* and *Sphaeropyle langii*. It was difficult to select the LAD of *Botryostrobus bramlettei* because numerous unidentifiable *Botryostrobus* species were found having morphologies similar to *Botryostrobus bramlettei*. A significant number of *Thecosphaera akitoensis* were found spanning Samples 127-795A-17H-CC, to 127-795A-30X-CC. The LAD of *Sphaeropyle robusta* did not occur in the Pleistocene sediments of Site 795, but instead was found lower in Hole 795A between Samples 127-795A-13H-CC, and 127-795A-14H-CC, in the upper Pliocene. Both *Sphaeropyle robusta* and *Sphaeropyle langii* displayed different stratigraphic records at Site 795 than at Site 794. Their ranges were not continuous and were found to be shorter with respect to the diatom zonation. Perhaps these species should not be used to define zonal boundaries in the Japan Sea, but more work is necessary to document their true ranges. The top of the *Sphaeropyle robusta* Zone is based mainly on the occurrence of *Druppatractus acquilonius* in this hole, and correlates well to the top of this zone at Site 794. The FAD of *Sphaeropyle langii* lies between Samples 127-795A-19X-CC, and 127-795A-20X-CC. Other datum levels found in the Pliocene of Site 795 include the LAD of *Druppatractus acquilonius* (between Samples 127-795A-10H-CC, and 127-795A-11H-CC), the LAD of *Thecosphaera japonica* (between Samples 127-795A-11H-CC, and 127-795A-12H-CC), the LAD *Theocalyptra davisiana* (between Samples 127-795A-15H-CC, and 127-795A-16H-CC), the LAD of *Stylacontarium* sp. cf. *S. acquilonarium* (between Samples 127-795A-15H-CC, and 127-795A-16H-CC), the LAD of *Lipmanella* sp. aff. *Theocyrtis redondoensis* (between Samples 127-795A-17H-CC, and 127-795A-18H-CC), and the FAD of *Lipmanella* sp. aff. *Theocyrtis redondoensis* (between Samples 127-795A-34H-CC, and 127-795A-35X-CC). The LAD of *Stichocorys peregrina* was difficult to identify because the species occurred sporadically in the samples and was extensively reworked into Pleistocene samples. No specimens of *Stichocorys delmontensis* or *Stichocorys wolfii* were found. Reworked *Stichocorys* species were identified mainly by the dark and robust appearance of fragmented tests. Reworked radiolarians were found in Samples 127-795A-11H-CC, 127-795A-12H-CC, 127-795A-13H-CC, 127-795A-26X-CC, and 127-795A-30X-CC.

Miocene radiolarians are found in sediments composed of silty clay, clay, and claystone that have undergone the transition from opal-A to opal-CT (below Core 127-795A-35X in Hole 795A and in Cores 127-795B-1R through -10R in Hole 795B). The level at which the sediments become barren of radiolarians approximately corresponds to the level where the siliceous sediments have undergone the transition from opal-CT to quartz. In general, Miocene radiolarians recovered from Site 795 are moderately (Samples 127-795A-35X-CC, to 127-795B-4R-CC) to poorly preserved (Samples 127-795B-6R-CC, to 127-795B-10R-CC). One sample (127-795B-28R-CC) contains pyritized radiolarians which are not age diagnostic. It appears that radiolarians did not undergo complete dissolution during the opal-A to opal-CT reactions that completely dissolved the diatoms. The radiolarians preserved below the opal-A/opal-CT boundary are coated with clays and opal-CT, suggesting that radiolarian tests served as nucleation sites for opal-CT precipitation. Because Miocene radiolarians were so poorly preserved, no paleoceanographic interpretations can be made without analysis of additional samples.

Miocene datum levels identified at Site 795 include the FAD of *Thecosphaera japonica* (between Samples 127-795A-35X-CC, and 127-795A-36X-CC), that marks the boundary between the *Thecosphaera japonica* and the *Lychnocanium nipponicum* Zones, the LAD of *Sethocyrtis japonica* (between Samples 127-795A-38X-CC, and 127-795A-39X-CC), and the LAD of *Lychnocanium nipponicum* (between Samples 127-795B-2R-CC, and 127-795B-3R-CC). Sample 127-795B-8R-CC, yielded three specimens of *Lithatractus tochigiensis* and several poorly preserved

Tholospyris species which are unidentifiable to the species level because they are partially dissolved. The *Tholospyris* species are probably either *Tholospyris anthopora* or *Tholospyris mammillaris*, and for this reason the boundary between the *Lychnocanium nipponicum* and *Cyrtocapsella tetrapera* Zones is placed between Samples 127-795B-7R-CC, and 127-795B-8R-CC.

Paleoenvironment

Middle Miocene surface waters were cool in the northern Japan Basin based on the absence of sphenoliths and discoasters from the calcareous nannofossil flora and the presence of a typical, high-latitude assemblage of planktonic foraminifers. The seafloor deepened during the middle Miocene from upper middle bathyal (approximately 500–1,000 m) to lower middle bathyal paleodepth (deeper than 1,500 m) based on assemblages of benthonic foraminifers. The CCD fell below the site at least once during the middle Miocene based on the presence of planktonic foraminifers and calcareous nannofossils in the sequence.

In the late Miocene, surface waters were generally cool based on assemblages of planktonic foraminifers from the lower sequence, and assemblages of diatoms, which occur sporadically throughout the sequence in dolomite nodules. The depth of the CCD fell below the site for a short period during the early late Miocene based on the occurrence of planktonic foraminifers. Poor recovery of all microfossils from the upper sequence, which lies between the opal-A/opal-CT boundary and the opal-CT/quartz boundary, precludes further paleoceanographic and paleodepth assessment.

Pliocene surface waters were subarctic in character based on assemblages of planktonic foraminifers. Surface waters at Site 795 appear environmentally different from those at Site 794 in yet-undefined way based on differences in radiolarian assemblages. Upwelling conditions were strong during the latest early Pliocene and late Pliocene from about 4 to 2 Ma in the northern Japan Basin based on the presence of diatom ooze and the radiolarian, *Spongotrochus glacialis*, whereas similar upwelling conditions persisted from 8 to 4 Ma at Site 794 in the northern Yamato Basin and elsewhere in the Japan Sea and marginal basins of the north Pacific rim. The basin floor remained at bathyal paleodepths during the Pliocene, but deep waters changed environmentally to conditions more oxygenated than during the middle Miocene based on differences in benthonic foraminiferal assemblage composition. Downslope transport is evident at the site throughout the Pliocene based on the presence of Miocene diatoms and radiolarians, and neritic diatoms. The CCD was probably shallow throughout most of the Neogene based on the persistently poor preservation of calcareous microfossils.

Late Pliocene and Quaternary surface waters fluctuated between subarctic and arctic conditions based on assemblages of planktonic foraminifers. Strong changes in water mass character are supported by great variability in radiolarian assemblages in core catcher samples throughout the sequence. The CCD fell below the depth of the site repeatedly through the late Pliocene and Quaternary based on the alternating presence of well preserved, calcareous nannofossils and planktonic foraminifers. Downslope transport is evident throughout the Quaternary based on the presence of Miocene diatoms and radiolarians, neritic diatoms, and a species of shelfal nannofossil.

PALEOMAGNETISM

Introduction

Paleomagnetic measurements were performed on cores from both Holes 795A and 795B at Site 795. Natural Remanent Magnetization (NRM) from the drilled basalts of the basement (from Core 127-795B-33R through -41R) was combined with the volume magnetic susceptibility (K) to calculate the Koenigsberger ratio (Q) of the samples according to the formula $Q = Jr/Ji$ (Jr = Remanent Magnetization; Ji = Induced Magnetization). The Induced magnetization ($Ji = K \times H$, where H is the local magnetic field) was calculated assuming a field value of 46,000 nanotesla (nT).

All the 19 APC cores from Hole 795A were oriented with the multishot camera system, except for the mud-line core. Virtually all of the recovered sedimentary cores were measured at 10 cm intervals with the cryogenic magnetometer and demagnetized in steps of 9 and 15 millitesla (mT). Cores drilled in Hole 795B were demagnetized with an additional step of 4 mT because the weak magnetization (generally below 1 mA/m) sometimes decreased below half of its NRM value after Alternating Field (AF) treatment in a 9 mT field. As at Site 794, the intensity of the sediment magnetization is generally weak, except in the uppermost part of Hole 795A (Fig. 22A) where it reaches values of 10–100 mA/m. A similar trend in the magnetic susceptibility (Fig. 23A and B) suggests a correlation with the presence of ash layers in this part of the section.

The weak magnetization hampered measurements with the Molspin magnetometer. In order to preserve the possibility for working with weakly magnetized specimens onshore with more sensitive instruments, it was decided to use the Molspin magnetometer only for samples with a relatively stronger magnetization. Step-wise AF demagnetizations were possible only on a selected number of discrete samples from the uppermost part of Hole 795A. Two Zijderveld plots of these samples are shown in Figure 24A.

Magnetostratigraphy

A polarity pattern for Hole 795A can be clearly recognized for the first 100 mbsf. The magnetostratigraphy related to this part of the hole is summarized in Figure 25. This figure also shows the correlation with Hole 794A to give an estimation of the sedimentation rates at the two sites during the Quaternary (see also "Sedimentation Accumulation Rates" section, this chapter). A correlation with the Geomagnetic Reference Time Scale (GRTS), in the same figure, is well constrained up to the top of the Olduvai subchron which according to Berggren et al. (1985a) spans from 1.66 to 1.88 m.y. The lower part of the Olduvai could be assigned to the normal polarity interval existing in the first two sections of Core 127-795A-11H. Biostratigraphic data, primarily diatoms (FAD of *A. oculatus*, 1.8 m.y. in Section 127-795A-11H-CC), confirm this correlation.

As noted at the previous site (Site 794) the Brunhes-Matuyama boundary does not seem to be a sharp transition. The magnetic field showed a double reversal occurring over a length of about 80 cm (55 cm R + 25 cm N). An apparent decrease in the intensity of the remanence in the transition zone seems to confirm this behavior of the field. By assuming that the sedimentation rate is 57 m/m.y. (on the basis of the length between the end of the Brunhes and the top of the Jaramillo, and after a correction for the effect of the compaction calculated by the dry bulk density of the sediments), the transition zone corresponds to a period of about 14,000 years (9600 yr R + 4400 yr N).

Multiple reversals in the Brunhes-Matuyama boundary have recently been found by Okada and Niitsuma (1989) in a sedimentary section of the Boso peninsula (Japan), and also by Cisowsky and Koyama at Site 792 in the Izu-Bonin basin (ODP Leg 126).

Below 100 mbsf, the paleomagnetic results are less reliable and warrant further study before interpretations may be made (Fig. 22B). Scattered directions occur below 100 mbsf, and magnetic susceptibilities are low (Fig. 23A and 23B). The absence of discrete sample measurements prevent reliable magnetostrati-

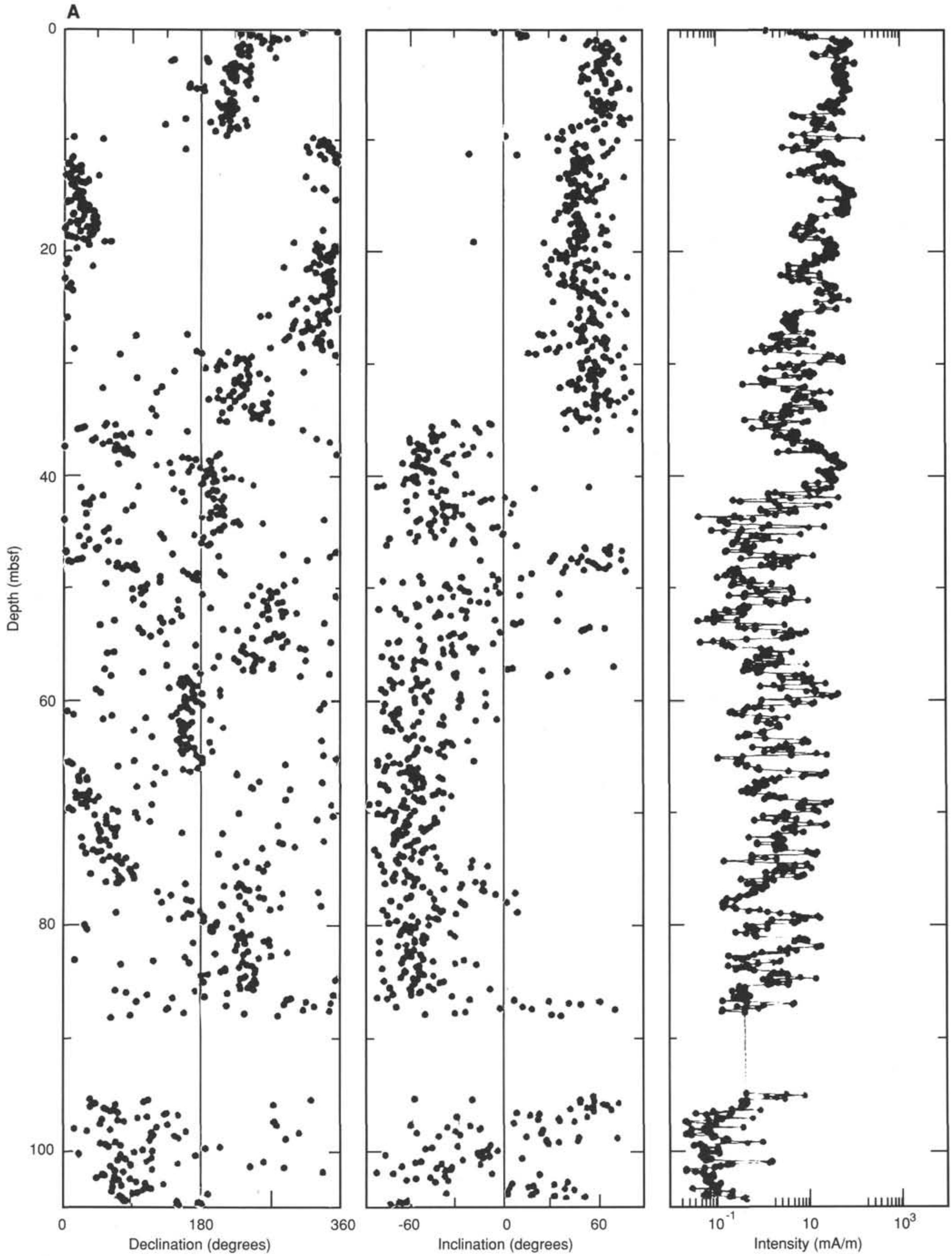

Figure 22. Declination, inclination, and intensity plot after demagnetization with 15 mT. **A.** Results for the first 100 mbsf of Hole 795A. **B.** Results from Core 127-795A-11H through -39X at Hole 795A. **C.** Results for Hole 795B from Core 127-795B-1R through -33R.

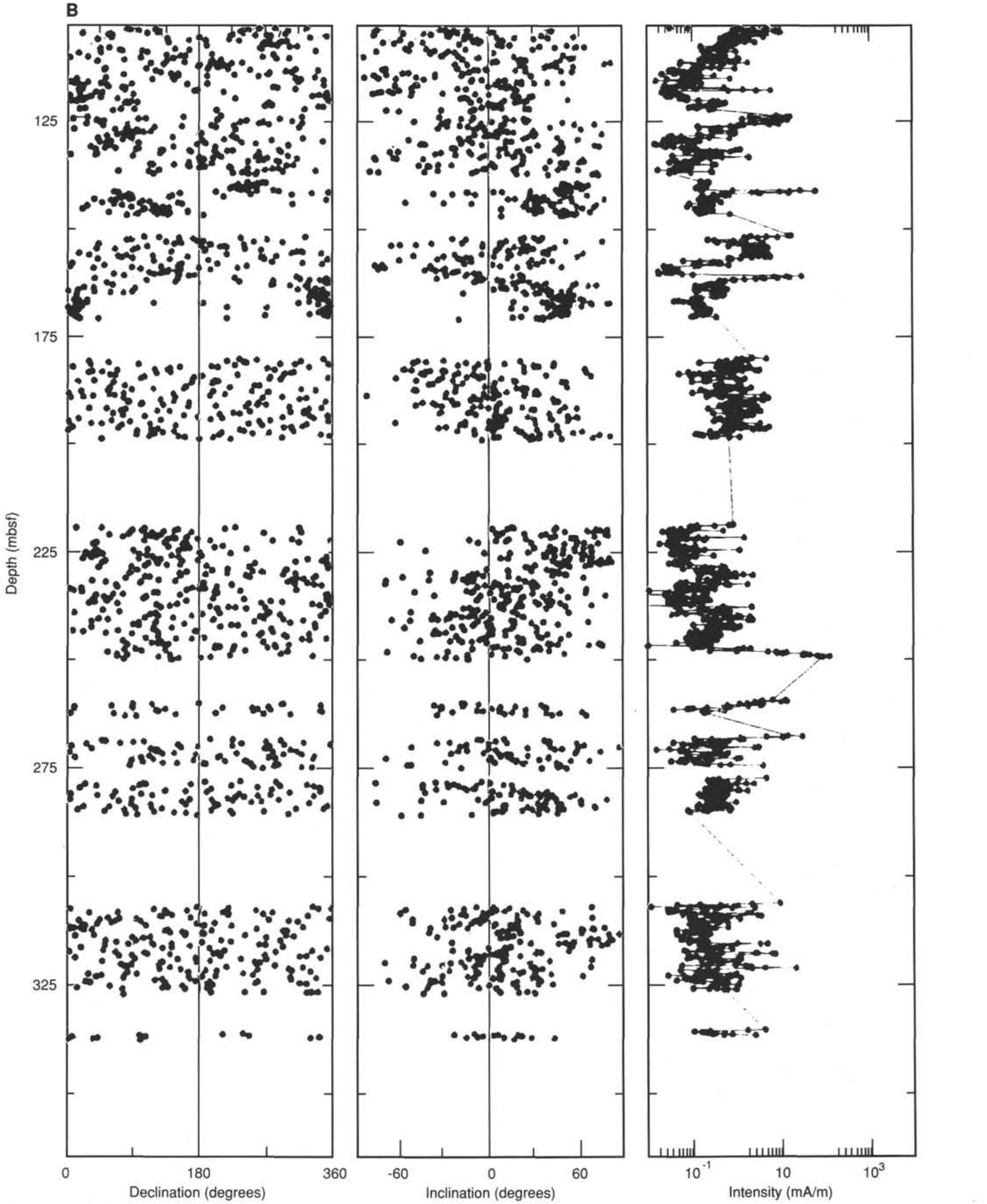

Figure 22 (continued).

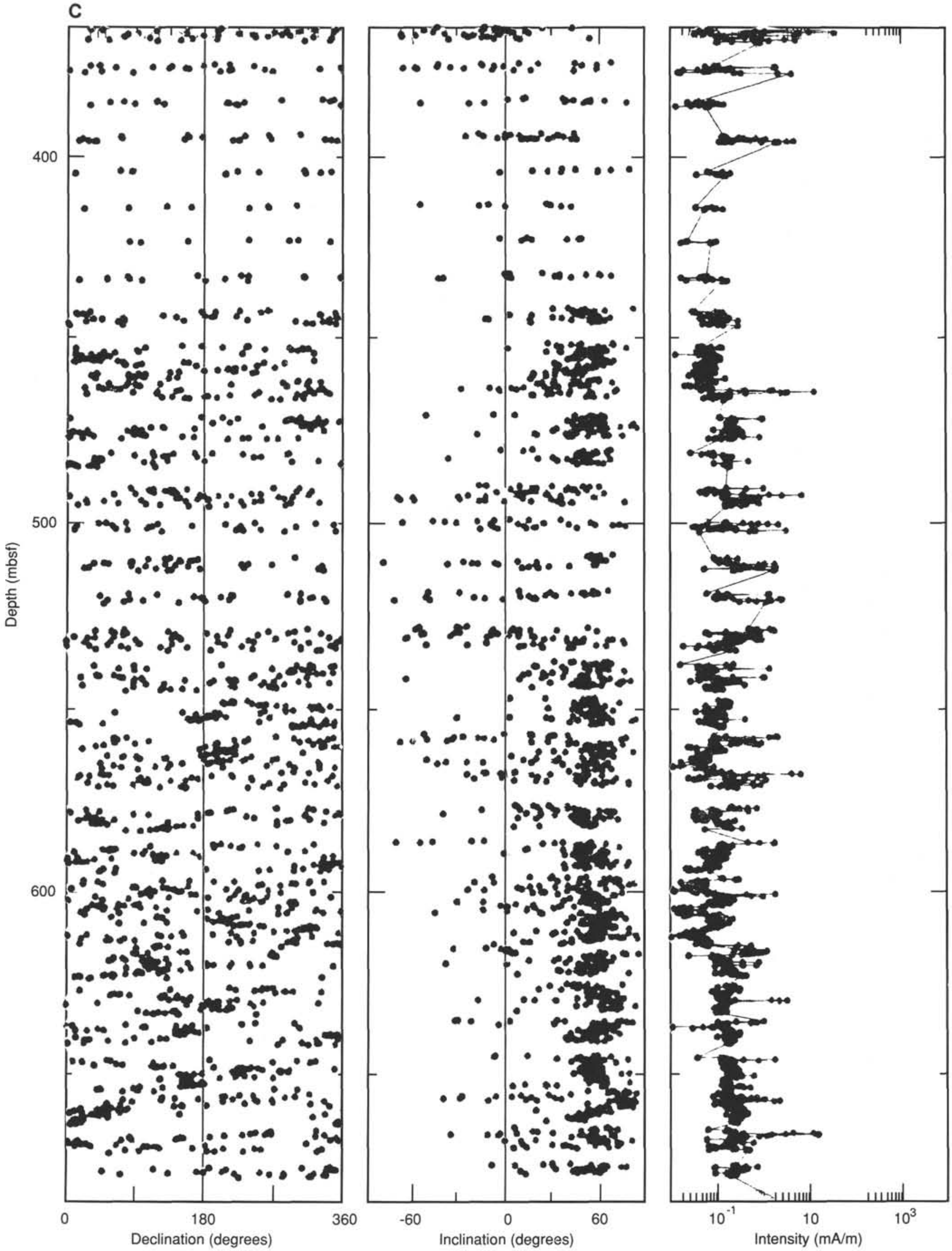

Figure 22 (continued).

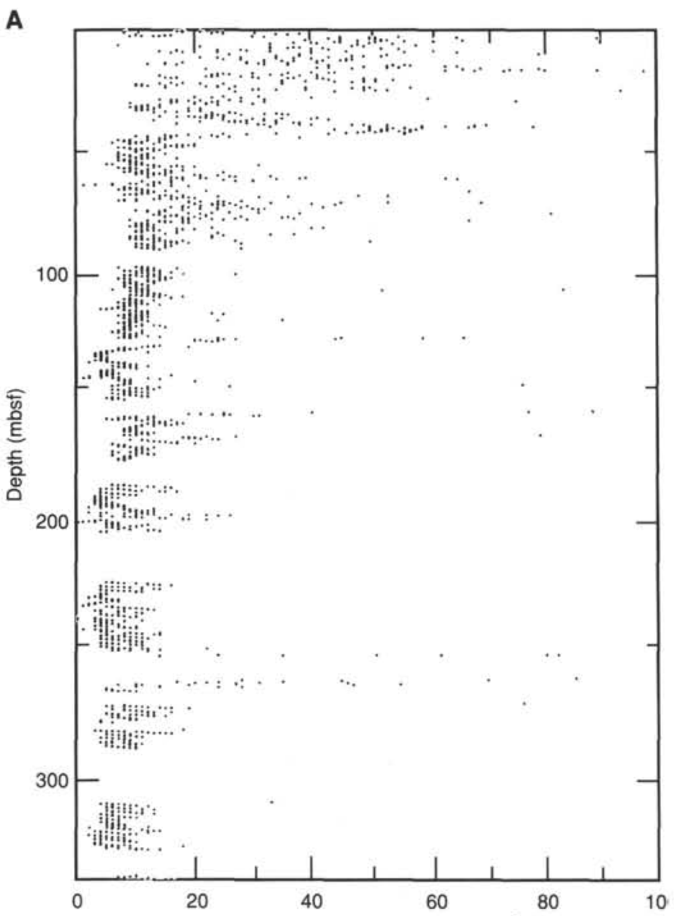

Figure 23. Whole-core volume magnetic susceptibility measurements plotted vs. depth. **A.** Hole 795A sediments. **B.** Hole 795B sediments. **C.** Hole 795B basement from Core 127-795B-34R through -41R.

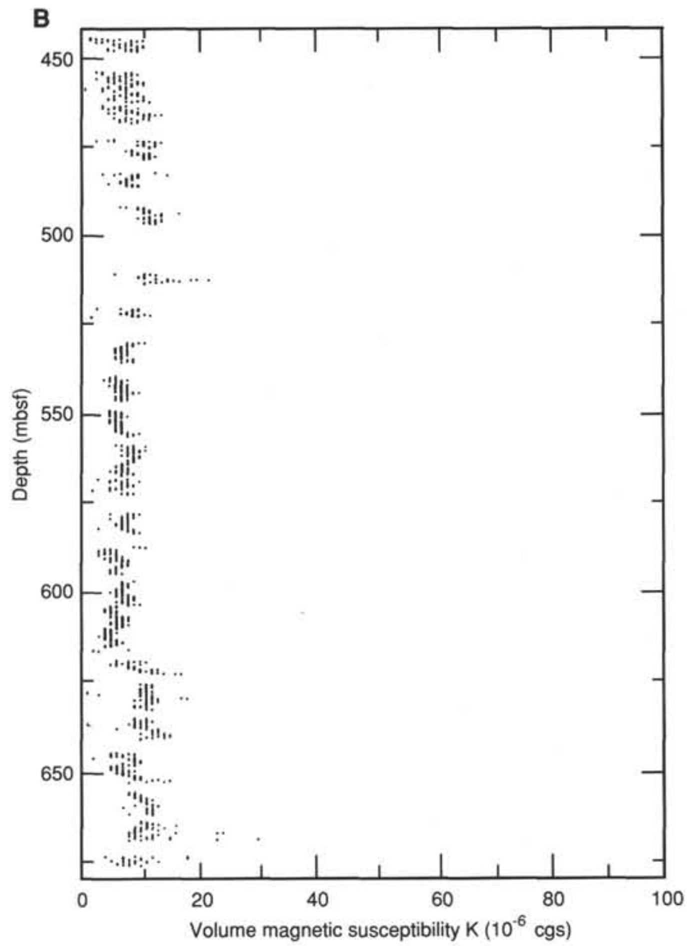

Figure 23 (continued).

graphic interpretation. It is significant that at about 100 mbsf a sharp increase in the diatom content has been noted in the sediments. A similar observation was also noted at Site 794.

Sediments recovered in Hole 795B yield a dominant normal polarity that when compared with the biostratigraphic data cannot be considered primary. Except for the uppermost 12 m (from Core 127-795B-1R through -2R; 365–377 mbsf) and a few short reversed polarity intervals scattered along the section, all sediments from this hole exhibit normal polarity. The downhole plot of paleomagnetic directions after AF cleaning with a peak-field of 15 mT is shown in Figure 22C.

In the uppermost part of the section, the drilling disturbance may account for the remagnetization of the rock; however, an original remagnetization acquired in the present field cannot be excluded. The occurrence of pyrite nodules along the section testifies to the growth of secondary minerals that may be responsible for the remagnetization.

Igneous Rocks

Basalts, basaltic andesites, and volcanic breccias were recovered from the bottom of Hole 795B (from Core 127-795B-34R through -41R). The different degree of alteration between the basalts (moderately altered) and the volcanic breccia (highly altered) influences the magnetic properties of the rock. Both the natural remanent magnetization and the magnetic susceptibility (Fig. 23C) show differences of two orders of magnitude between the fresh and the altered rock that can only partially reflect the lithologies. In spite of this huge difference, the adjacent occurrence of massive flows and breccia hampered the measurements with the cryogenic magnetometer because the overflow of the magnetometer sensors, induced by the strongly magnetic basalt, affected the readings of the more weakly magnetized volcanic breccia.

The natural remanent magnetization before and after cleaning with high peak-field (up to 90 mT) were measured with the Molspin magnetometer on minicores drilled from the basement. The remanent magnetization is predominant with respect to the induced magnetization, such that the Koenigsberger ratio is >1. As reported in Table 4, Q ranges from 6 to 33 with a mean value of 19 for the basaltic rocks. The magnetic coercivity of the NRM of the igneous rocks is low as can be estimated from the Median Destructive Fields (MDF) which range between 4 and 31 mT with a mean value of 14 mT (Table 4). Generally, oceanic basalts show MDF in this range (Furuta and Levi 1983; Pechersky et al., 1983).

The basaltic lithology exhibited a stable component of magnetization with normal polarity as can be seen in the Zijderveld plots of Figure 24B. Samples drilled from the most altered part of the volcanic breccia exhibit a complex paleomagnetic record with two or three magnetic components that only poorly define end-points after demagnetization (Figure 24C). Stable inclinations obtained from the least-squares fit on the Zijderveld diagrams show a mean value of about 64° (Table 4), steeper than the expected value (53°) and attesting to a possible disruption of the basement.

SEDIMENT ACCUMULATION RATES

Estimates of sedimentation rates for Site 795 are based on biostratigraphic datum levels and the paleomagnetic reversal stratigraphy recognized at this site. The data points include the

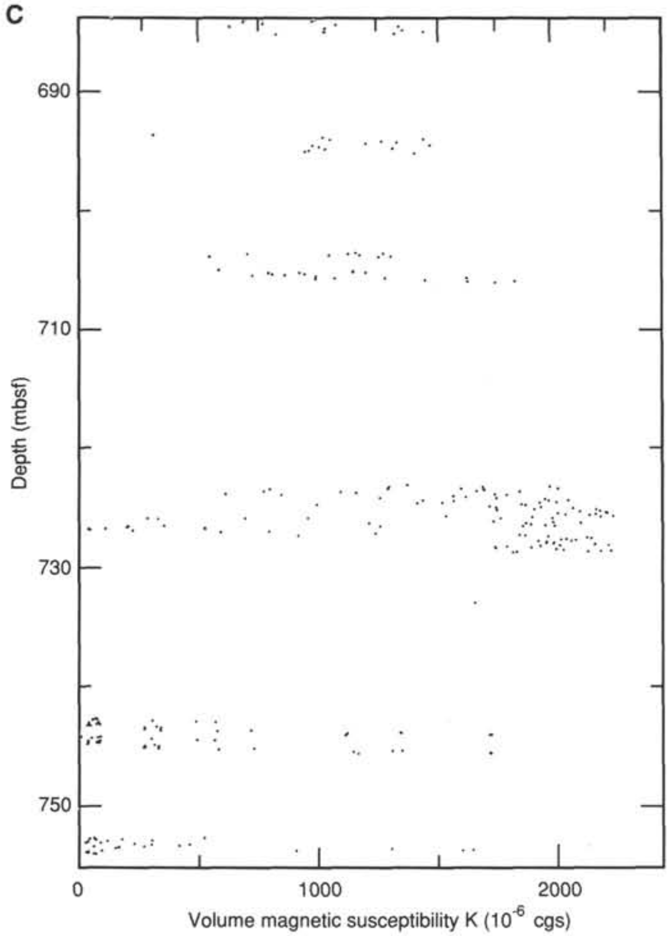

Figure 23 (continued).

depths and ages of two magnetostratigraphic boundaries, seven diatom datum levels, and one calcareous nannofossil datum level (Table 5). A sedimentation rate for each interval was calculated from the age vs. depth relationship (Table 5 and Fig. 26). Large uncertainties in the depths of several diatom datum levels are due to the lack of preserved diatoms below the opal-A/opal-CT boundary (325 mbsf) except in widely spaced carbonate layers. Sediment accumulation rates were also calculated by multiplying the sedimentation rate by the dry bulk density of the sediments. The rate of sediment accumulation ("decompacted sedimentation rate") is then expressed in $g/cm^2/k.y.$ (Table 5). Trends in bulk accumulation rates expressed as $g/cm^2/k.y.$ are similar to trends in the sedimentation rate (m/m.y.) above 327.2 mbsf, which approximates the opal-A/opal-CT boundary (Table 5). Below this boundary the sediment accumulation rates are consistently higher and suggest that the effect of compaction and/or porosity reduction during silica diagenesis may be significant. Caution must still be used in the interpretation of these differences because datum levels below this boundary are more widely spaced and have larger uncertainties.

Sedimentation rates at Site 795 range from 29 to 77 m/m.y., with an average of 53 m/m.y. The lowest rates are in the middle Miocene, whereas the highest rates are in the late Pliocene to late Miocene between 1.66 and 6.4 Ma (Fig. 26). The average sedimentation rate for Site 795 is one and one-half times greater than that of Site 794, which averaged 37 m/m.y. The sedimentation rate estimates for the clay, claystone, and tuff of the middle and early late Miocene is between 29 and 38 m/m.y. (Fig. 26). For the silty clay and diatomaceous ooze of the late Miocene and early Pliocene, the sediment accumulation rate is estimated to be between 49 and 70 m/m.y. The highest sedimentation rates correspond to the diatomaceous ooze and likely reflect the periods of strongest upwelling in the Japan Basin (see "Biostratigraphy" section, this chapter). Silty and ashy clay of the late Pliocene and Quaternary accumulated with an average rate of 52 m/m.y.

Extrapolation from the RDD of *D. praedimorpha* through the LAD of *C. floridanus* estimates the minimum age of basement at 13 Ma, and extrapolation from the RDD of *D. praedimorpha* through its FAD estimates a maximum age of basement at 15 Ma.

INORGANIC GEOCHEMISTRY

Introduction

The shipboard inorganic geochemistry program at Site 795 continued its focus on interstitial water analysis, with whole-round core samples being squeezed by both the standard stainless-steel ODP squeezer (Manheim and Sayles, 1974) and the new plastic-lined Brumsack squeezer (Brumsack et al., in preparation). Samples were gathered from 6.0 to 661.9 mbsf. The Barnes *in-situ* sampler was not used. Major ion data from both squeezers are presented in Table 6.

The pore waters of Site 795 define a chemical zonation over three depth intervals. The upper interval, from 0 to 80 mbsf, is characterized by intense sulfate reduction. The second interval, from 80 to approximately 325 mbsf, is characterized by generally smooth gradients and ends at the opal-A/opal-CT transition. The opal-A to opal-CT transition zone is the most fundamental physical and chemical demarcation at Site 795. The third interval, from 325 to 662 mbsf, is delineated by either steep concentration gradients toward the basement or rather constant values. In most profiles, a deviation from a smooth trend is observed near 500 mbsf, just below the opal-CT/quartz transition.

Sulfate, Alkalinity, and Ammonia

Sulfate, alkalinity, and ammonia concentrations are strongly controlled by the availability of organic matter for bacterial degradation. Sulfate is present only in the interstitial waters in the upper 80 m and exhibits an almost linear decrease from near-surface values of 20.9 mmol/L (mM) to 0 mmol/L at 81.8 mbsf (Fig. 27). At and below this depth, bacterially mediated sulfate reduction processes have completely depleted sulfate in the interstitial waters. A value of 2.1 mmol/L, close to the detection limit of the analytical method, observed at 340 mbsf, may be related to the nearby opal-A/opal-CT transition or might be due to drill water contamination.

Alkalinity (Fig. 27) increases rapidly with depth and attains constant values of approximately 26 mmol/L over the interval 80 to 160 mbsf, coincident with complete sulfate reduction and the onset of methanogenesis. Below 160 mbsf, values decrease nearly linearly to 1.5 mmol/L at 511 mbsf and stay constant to the bottom of the analyzed pore waters. The decrease in alkalinity is due to carbonate precipitation.

Ammonia (Fig. 27) increases from a near surface value of 400 μmol/L to maximum concentrations ranging from 3100 to 3400 μmol/L over the opal-A/opal-CT transition zone at 325 mbsf. Below this transition zone, ammonia concentrations decrease to a relative minimum value of 1050 μmol/L at 662 mbsf. The ammonia increase from the surface sediments to the opal-A/opal-CT transition zone reflects the continuing bacterial degradation of organic matter. The overall decrease from 325 mbsf to the basement indicates uptake of ammonia into diagenetically formed clay minerals.

Silica

Silica in pore waters at Site 795 (Fig. 27) increases from initial values of 615 μmol/L at 6 mbsf to a maximum value of 1450 μmol/L at 325 mbsf, the opal-A/opal-CT boundary. Immediately below 325 mbsf, silica decreases to 700 μmol/L and continues to decrease through the opal-CT zone. Minimum values of 200–100 μmol/L are reached at 511 mbsf, slightly below the opal-CT/quartz boundary.

The silica profile clearly indicates the position of the silicification front at 325 mbsf below which silica is removed from the interstitial waters during precipitation of progressively ordered silica phases. The opal-CT/quartz boundary also affects the silica profile, although to a lesser degree. As will be discussed later, physical changes in the lithology resulting from these chemical processes profoundly affect the profiles of virtually all analyzed constituents.

Phosphate

Phosphate exhibits a general trend from an initial value of approximately 50 μmol/L near the surface to 0 μmol/L at 360 mbsf and below, indicating strong removal into sedimentary phases (Fig. 27).

pH, Salinity, Sodium, and Chloride

The pH at Site 795 (Fig. 27) is highly variable in the first 80 m of sediment, ranging from approximately 7.4 to nearly 7.9. From 138 to 262 mbsf, pH is constant at 7.4 or 7.5. Throughout the opal-A to opal-CT transition, the pH is again quite variable, ranging from 7.50 to 7.74. The pH through the opal-CT zone toward the basement increases slightly yet consistently and exhibits a major increase to 7.9 at the opal-CT/quartz transition.

The salinity of the interstitial waters starts at near-seawater values of 33.5 g/kg and decreases rapidly to 31.8 g/kg in the upper 80 m (Fig. 27). From 80 to 272 mbsf, the concentration stays constant at approximately 32 g/kg, before rapidly decreasing again through the opal-A/opal-CT transition zone from 280 to 330 mbsf. Below 330 mbsf, salinity increases toward basement. Like many other Site 795 profiles, a large concentration change is found from 480 to 510 mbsf, just below the opal-CT/quartz transition.

The salinity decrease in the upper 80 m results from the removal of sulfate due to bacterial reduction and carbonate precipitation. The increase toward basement (Fig. 27) reflects the extreme calcium enrichment discussed below.

Sodium and chloride are both essentially constant from the surface of the sediment column to the bottom of the opal-CT zone, with Na ranging between 440 and 460 mmol/L and Cl between 520 and 540 mmol/L (Fig. 27). Beneath the zone, starting at approximately 500 mbsf, Cl shows a slight increase from 510 to about 560 mmol/L, which is probably due to the net uptake of water from the basaltic basement.

Immediately below the opal-A to opal-CT transition at 325 mbsf, Na decreases to a near-basement value of approximately 260 mmol/L. Again, a large concentration change occurs near the opal-CT/quartz boundary. The overall large decrease in Na content indicates removal of Na during low temperature basement alteration.

Potassium and Rubidium

At Site 795, potassium and rubidium are both removed from pore waters, but, in contrast to Site 794, exhibit distinctive profiles. Potassium (Fig. 27) decreases virtually linearly throughout the entire column from a concentration slightly higher than average seawater to a minimum value near zero just above the basalt. This indicates large-scale removal of K into clay minerals that are forming within the sediments and during basalt alteration.

The Rb profile (Fig. 27), generally mimics the K profile, but differs in that the overall gradient is not as smooth. First, the Rb content decreases rapidly throughout the upper 80 m, indicating removal from the pore waters over this clay-rich interval. From 80 mbsf to the opal-A/opal-CT boundary at 325 mbsf, the Rb content is approximately constant, at values near 1.10 μmol/L. Beneath the opal-A/opal-CT boundary, Rb decreases due to basement alteration and removal into clay minerals.

Lithium

As at Site 794, the Li profile (Fig. 27) can be related to the biogenic silica content. The general increase from near-surface concentrations of 27 to approximately 165 μmol/L indicates release of Li during diatom dissolution. High values continue through the opal-CT interval. Again, near 500 mbsf a change occurs in the profile, with a relative increase in dissolved Li, perhaps reflecting further release during opal-CT dissolution and quartz precipitation. Lithium values decrease rapidly toward basement, due to alteration reactions.

Calcium, Magnesium, and Strontium

Calcium, magnesium, and strontium are commonly involved in carbonate formation and basement alteration. At Site 795, dolomite is the dominant carbonate phase above 400 mbsf, with calcite dominant below 400 mbsf (see "Lithology" section, this chapter). The basement rocks show evidence of significant water circulation (see "Basement Rocks" section, this chapter). Consistent with these lithologic occurrences, the Ca, Mg, and Sr profiles indicate that both carbonate formation and basement alteration processes control their interstitial water concentrations.

Magnesium exhibits a linear profile, decreasing from an initial value of 50 mmol/L at 6 mbsf to 0 mmol/L at 662 mbsf (Fig. 27), indicating that the basaltic basement is the final sink for Mg. Calcium concentrations initially decrease to a depth of 65 mbsf, due to carbonate precipitation resulting from the buildup of alkalinity during sulfate reduction and methanogenesis. Calcium increases slightly toward the opal-A/opal-CT interface at 325 mbsf (Fig. 27). Below this depth, Ca in the interstitial waters greatly increases to 145 mmol/L just above basement, indicating diffusive transport from basement alteration reactions. The relationship between Ca and Mg concentrations and depth are summarized in Figure 27.

These trends of Ca and Mg concentrations in the upper sediments can be related to the occurrence and formation of carbonate. In the upper 60–80 m, where the Ca profile decreases and dolomite is found, the Mg concentrations in the interstitial water also decrease. A portion of this Mg decrease must be caused by dolomite formation.

Interestingly, calcareous nannofossils and foraminifers are scarcely found in the upper 80 m of Site 795 (see "Biostratigraphy" section, this chapter) and when present appear to be partially dissolved. The observed Ca decrease in these upper sediments clearly illustrates that this dissolution is not occurring in the sediments, and thus occurred either in the water column or at the sediment/water interface.

Strontium is constant throughout the first 80 m of the sediment column, with seawater-like values of approximately 80 or 90 μmol/L (Fig. 27). From 80 to 100 mbsf, the Sr concentrations increase to nearly 120 μmol/L and remain constant thereafter until 340 mbsf, just below the opal-A/opal-CT transition of 325 mbsf. Within the opal-CT zone, Sr increases to 285–340 μmol/L. From 450 to 662 mbsf, Sr values are relatively constant, varying about an average of 310 μmol/L.

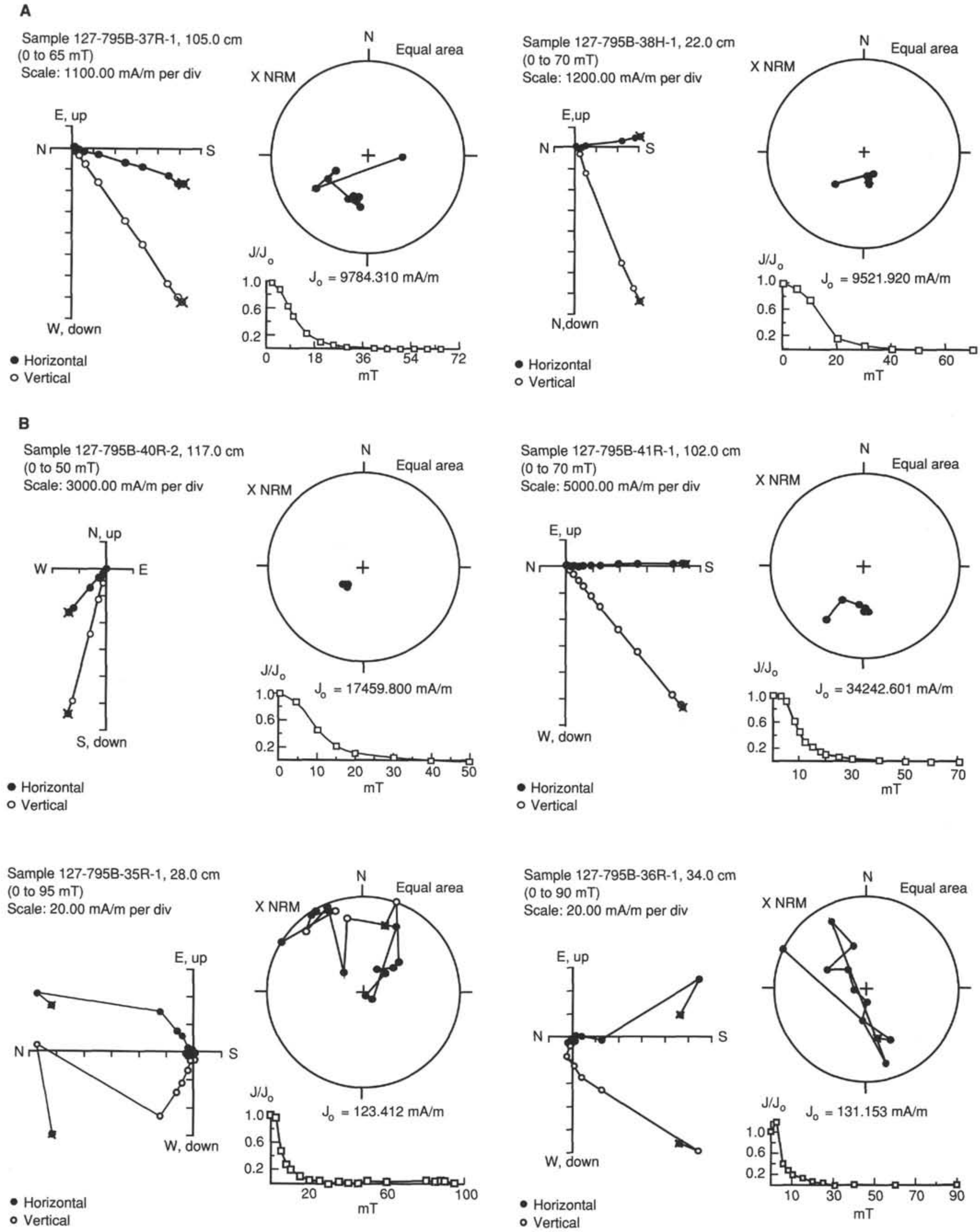

Figure 24. Zijderveld, equal area, and intensity decay plot as function of AF demagnetization. **A.** Sediments. **B.** Basaltic rocks. **C.** Altered volcanic breccia.

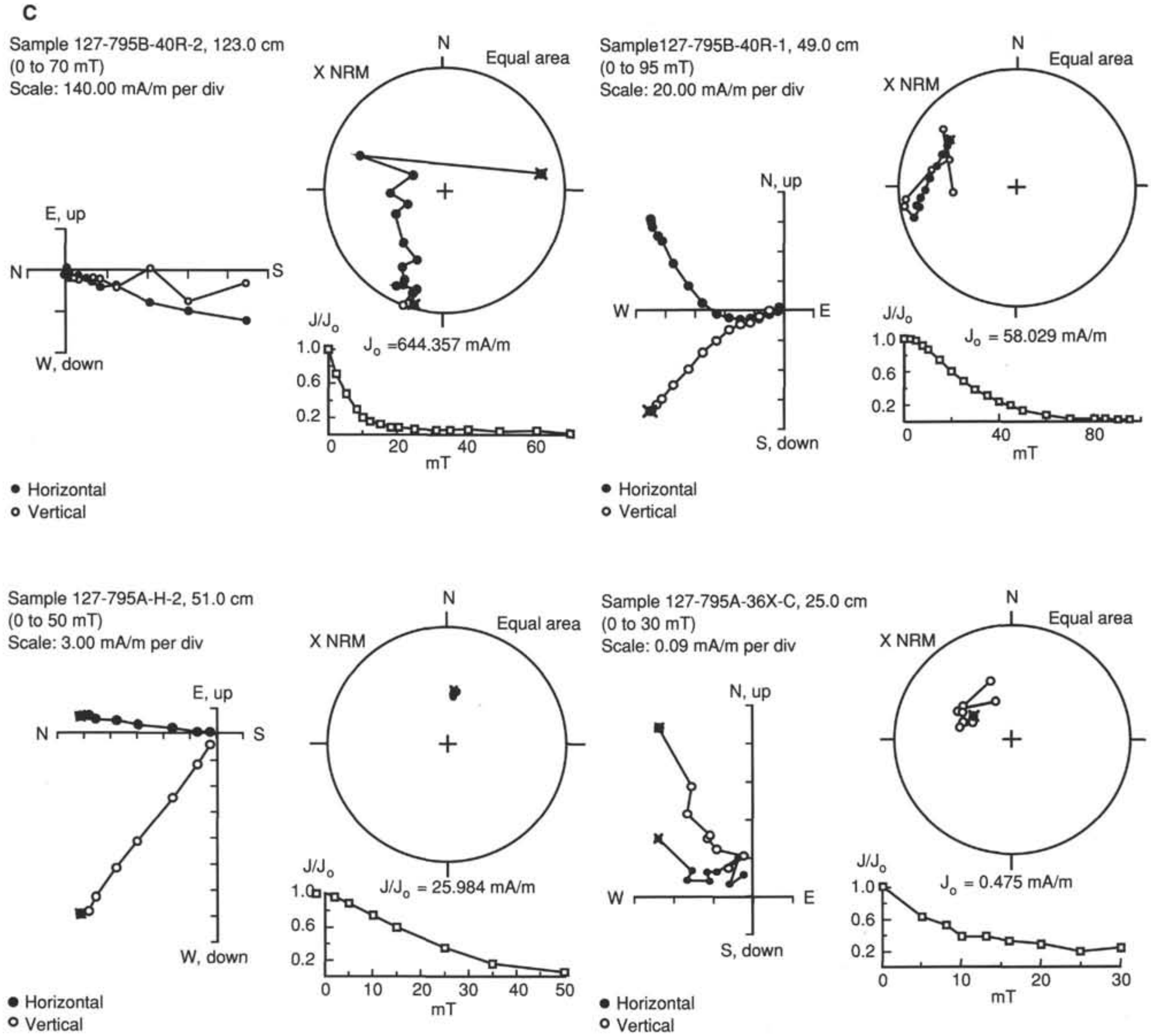

Figure 24 (continued).

This Sr profile does not indicate a strong control by carbonate formation. For example, strontium concentrations are constant throughout the zone of dolomite and calcite formation from 0 to 80 mbsf. The strontium profile may indicate an overall basement source, as Sr values are relatively high at depth.

Discussion

As mentioned briefly in the Introduction to this section, and as is evident from profiles of the individual chemical constituents, Site 795 possesses a well-defined chemical zonation. The three depth intervals can be distinguished in the profiles of almost all the constituents. Variations in pH also occur between the three intervals, but due to the sometimes severe sampling artifacts (e.g., Gieskes and Peretsman, 1986) can not be confidently correlated. The opal-A/opal-CT transition is the most important demarcation at Site 795.

The first interval, from the sediment/water interface to approximately 80 mbsf, is characterized by bacterially mediated degradation of organic matter in the sediments by sulfate reduction and methanogenesis. The depth of total sulfate depletion depends on the organic matter content and the sedimentation rate. At Site 795, the sedimentation rate is the dominant control, with the organic matter content being of secondary importance. This is evidenced by Site 795 having only slightly more organic matter than is found at Site 794, but twice the sedimentation rate. Furthermore, heterogeneity in the sedimentary lithology (see "Lithostratigraphy" section, this chapter) and the organic matter content (see "Organic Geochemistry" section, this chapter) in the uppermost 80 m results in variations of Si, phosphate, Ca, Rb, K, and perhaps pH.

The second interval, from 80 to 325 mbsf, is characterized by essentially constant chemical trends. Constantly increasing (e.g., ammonia, Si, Li) and decreasing (e.g., phosphate, K) concentration gradients both occur, yet a majority of profiles exhibit no change over this interval. Sediments throughout this second interval consist of highly porous diatom oozes and are also extensively bioturbated. The opal-A to opal-CT transition zone at approximately 325 mbsf marks the end of this second interval, and is a sharp boundary in virtually all the profiles.

The third interval, from 325 mbsf to the last interstitial water sample at 662 mbsf, is characterized by steep gradients toward the basement. With the exception of the influence of the opal-

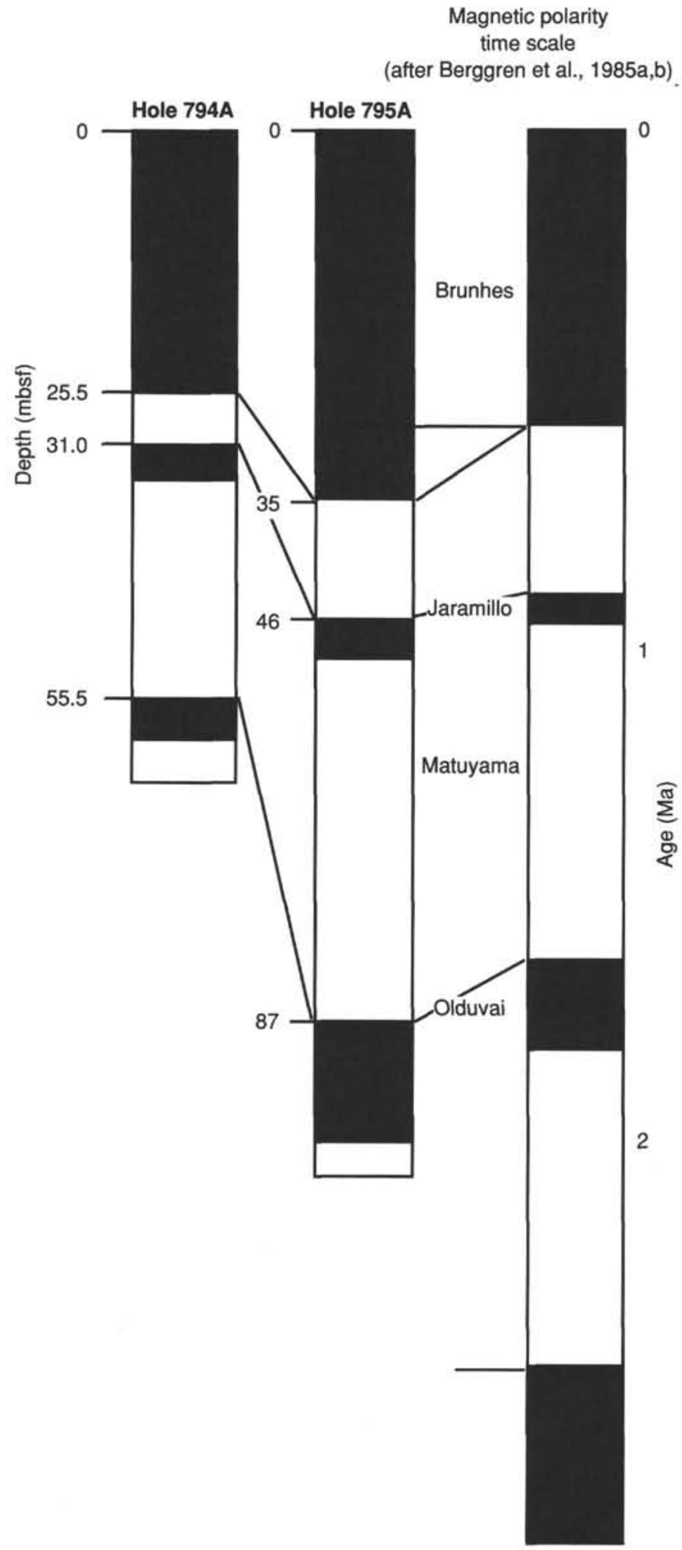

Figure 25. Magnetostratigraphic correlation between Hole 795A with Hole 794A and the magnetostratigraphic time scale of Berggren et al. (1985a, b).

Table 4. Paleomagnetic results from the basement of Hole 795B. MDF = Median Destructive Field; values are given in mT. Q = Koenigsberger Ratio. I = Characteristic inclinations determined from orthogonal vector projections.

Sample	MDF	Q	I
Basalt			
127-795B-			
37R-1, 105	9	14	54
38R-1, 22	14	10	68
38R-5, 4	11	6	68
40R-1, 31	11	—	77
40R-2, 117	9	22	68
41R-1, 85	28	30	64
41R-1, 102	9	33	50
Volcanic breccia			
35R-1, 28	5	—	—
36R-1, 34	4	—	—
38R-1, 23	5	—	—
40R-1, 49	28	—	—
40R-2, 123	5	—	—
41R-1, 86	31	—	—
41R-1, 87	27	—	—
Mean value	14	19	64

CT/quartz transitional zone, gradients through this final interval are all constant, and reflect alteration reactions in the basement.

The opal-A to opal-CT transition at 325 mbsf profoundly influences the chemistry of the interstitial waters below by impeding fluid transport and more or less isolating the lower 350 m of sediment from the upper 320 m of sediment. This boundary acts as a new surface and end-point from which diffusional gradients can develop. Both Na and Ca, for example, exhibit marked changes in their profiles above and below the opal-A/opal-CT boundary, each profile below 325 mbsf indicating strong chemical exchange with the basal basalt (Fig. 27). Na is incorporated into clay minerals during alteration, and Ca is being released from the basement.

Summary

The chemistry of the interstitial waters at Site 795 is controlled by the sedimentary history of the northern Japan Basin. The higher sedimentation rate than in the Yamato Basin enhanced the preservation of organic matter which in turn assisted bacterially mediated sulfate reduction. The bulk composition of the sediments, recording the paleoceanographic variations of the region, strongly controls the interstitial water chemistry and the extent to which diffusive transport of the dissolved constituents may occur. Overall, the chemical zonation at Site 795 reveals behavioral variations that can be directly correlated with sedimentological changes. The most important of these stratigraphic controls is the position of the silicification front at 325 mbsf which isolates the uppermost pore waters from those currently involved in low temperature basement alteration.

ORGANIC GEOCHEMISTRY

The shipboard organic geochemical analyses of sediment samples from Holes 795A and 795B included inorganic carbon, total carbon, nitrogen, sulfur, Rock-Eval, and volatile hydrocarbon analyses. The procedures used for these determinations are outlined in the "Explanatory Notes" chapter (this volume), while background and detailed descriptions are given in Emeis and Kvenvolden (1986).

Carbon, Nitrogen, and Sulfur

The concentrations of inorganic, total, and organic carbon in the sediments recovered from Site 795 are presented in Table 7. The percentage of calcium carbonate ($CaCO_3$) was calculated from the inorganic carbon concentrations by assuming that all carbonate is in the form of calcite. Nitrogen and sulfur concentrations are also given in Table 7. Carbonates range from 0.1% to 20.7% although most of the samples contain less than 1%

Table 5. Magnetostratigraphic and biostratigraphic datum levels used to determine sedimentation rates for Site 794. The depths of zonal boundaries and datums in core-catcher samples are taken from the top or bottom of the cored interval rather than from the base of the recovered sediment.

Datum	Age (Ma)	Depth (mbsf)	Sedimentation rate (m/m.y.)	Sedimentation rate (cm/k.y.)	Mean dry bulk density (g/cm^3)	Accumulation rate (g/cm^2 k.y.)
Seafloor	0	0				
			48	4.8	0.96	4.6
1. Brunhes/Matuyama	0.73	35.0				
			56	5.6	0.94	5.3
2. Top of Olduvai	1.66	87.0				
			77	7.7	0.93	7.2
3. LAD of *N. kamtschatica*	2.50	151.9				
			49	4.9	0.90	4.4
4. FAD of *N. koizumii*	3.50	200.9				
			70	7.0	0.94	6.6
5. Base of *T. oestrupii* Zone	5.30	327.2				
			61	6.1	1.38	8.4
6. FAD of *N. kamtschatica*	6.40	394.4				
			34	3.4	1.47	5.0
7. FAD of *D. dimorpha*	9.00	481.1				
			46	4.6	1.65	7.6
8. RDD of *D. praedimorpha*	10.70	560.5				
			38	3.8	1.73	6.6
9. LAD of *C. floridanus*	11.60	605.7				
			29	2.9	1.73	5.0
10. FAD of *D. praedimorpha*	13.30	635.3				

LAD = last appearance datum. FAD = first appearance datum. RDD = rapid decrease datum.

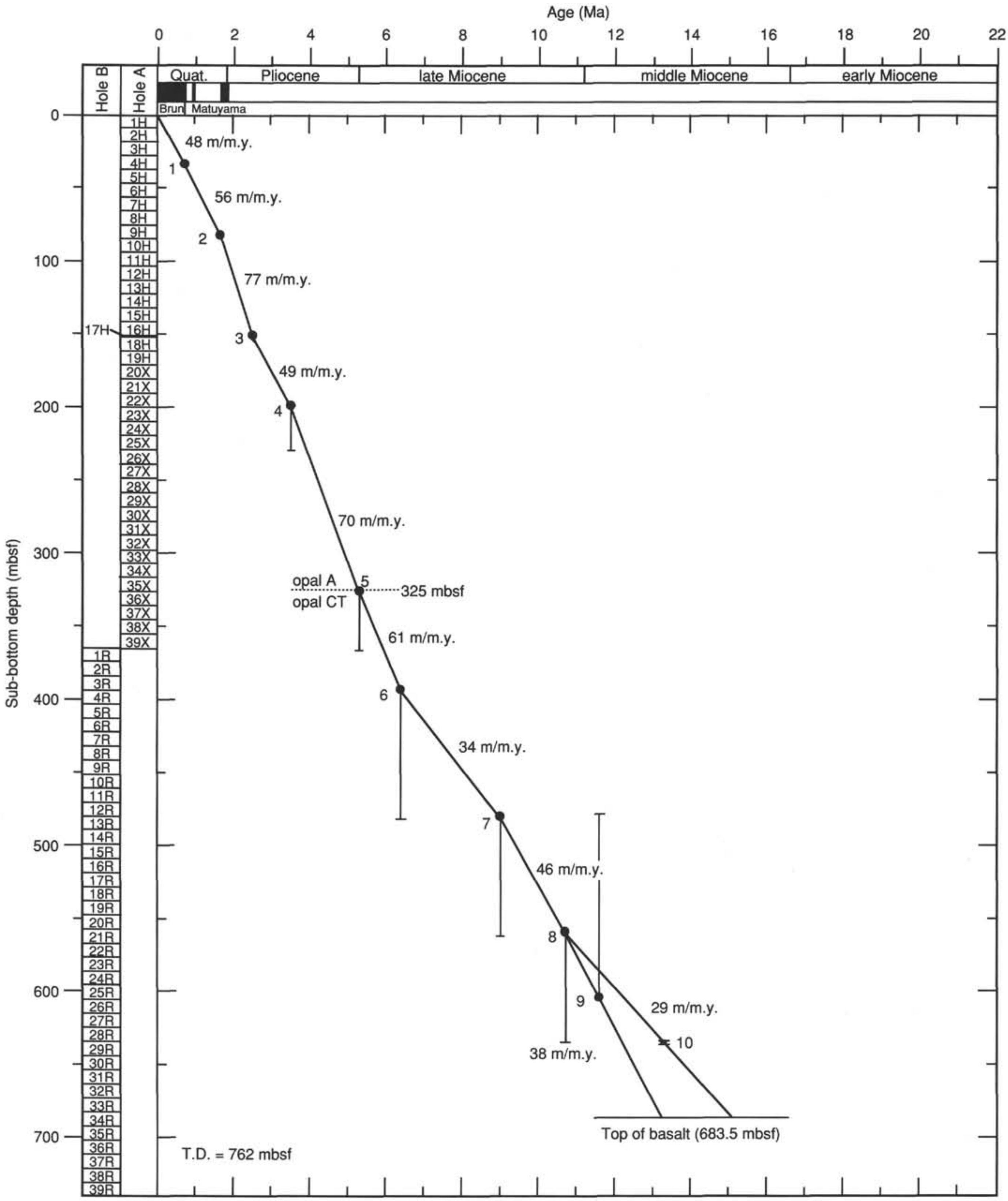

Figure 26. Age vs. depth relationship at Site 795. Error bars indicate uncertainties in the precise age and depth of the datum levels.

Table 6. Interstitial water geochemistry data, Site 795.

Core, section, interval (cm)	Depth (mbsf)	Vol. (mL)	pH	Alk. (mM)	Sal. (g/kg)	Mg (mM)	Ca (mM)	Cl (mM)	SO_4 (mM)	PO_4 (μM)	NH_4 (μM)	SiO_2 (μM)	Mg/Ca
795A-													
1H-4, 145–150	5.95	5	7.40	7.250	33.5	49.50	9.80	529.00	20.90	50.00	400	615	5.05
2H-4, 145–150	15.25	5	7.50	11.650	33.0	45.70	9.10	529.00	17.20	54.00	750	780	5.02
3H-4, 145–150	24.75	35	7.86	16.140	32.5	44.90	8.50	523.00	13.10	43.00	980	700	5.28
4H-4, 145–150	34.25	45	7.68	18.010	32.5				9.40	44.00	1390	900	
5H-4, 145–150	43.75	4	7.69	21.310	32.5	41.60	7.60	524.00	6.40			775	5.47
6H-4, 145–150	53.25	100	7.44	23.013	32.0	40.80	7.50	525.00	4.30	51.00	1560	820	5.44
7H-4, 145–150	62.75	5	7.65	24.110	32.0	38.20	7.30	527.00	2.40	17.00	1870	735	5.23
8H-4, 145–150	72.25	5	7.85	23.575	31.8				1.00			870	
9H-4, 145–150	81.75	70	7.48	25.246	31.5	37.30	7.60	530.00	0.00	32.00	1850	830	4.91
10H-1, 145–150	86.75	5	7.77	25.802	32.0				0.00				
12H-4, 140–145	110.20	5											
12H-4, 145–150	110.25	60	7.63	25.715	31.9	35.40	8.30	532.00	0.00	24.00	2200	1055	4.27
15H-4, 140–145	138.70	5											
15H-4, 145–150	138.75	59	7.45	25.114	32.0	33.80	8.90	537.00	0.00	12.00	2390	1150	3.80
18H-4, 140–145	158.80	5											
18H-4, 145–150	158.85	5	7.40	25.356	32.0	33.20	9.40	531.00	0.00	23.00	2570	1290	3.53
21X-4, 140–145	187.50	5											
21X-4, 145–150	187.55	50	7.48	21.342	32.0	31.40	9.80	529.00	0.60	10.00	2600	1275	3.20
25X-3, 140–145	224.80	5											
25X-3, 145–150	224.85	25	7.40	19.197	32.1	28.80	10.70	525.00	0.50	8.00	2680	1340	2.69
29X-2, 145–150	262.45	5	7.47	18.595	31.7	26.00	11.90	527.00	0.50	3.00	2820	1460	2.19
30X-2, 145–150	272.25	5	7.74	15.868	31.3	23.80	11.90	525.00	0.00		3130	1415	2.00
31X-4, 145–150	285.05	5	7.60	15.040	30.8	23.50	12.30	524.00	0.20		3160	1375	1.91
34X-5, 140–145	315.30	5											
34X-5, 145–150	315.35	5	7.74	14.102	30.3	22.50	13.40	522.00	0.20	16.00	2840	1380	1.68
35X-2, 145–150	320.55	5	7.54	12.440	30.3	22.70	13.90	520.00	0.40	8.00	3380	1452	1.63
37X-1, 138–143	338.28	5	7.67	8.685	30.0	19.90	13.60		2.10		3280	700	1.46
795B-													
1R-1, 140–145	366.60	5			29.7						2650		
1R-1, 145–150	366.65	5	7.50	6.933	29.7	19.70	22.70			0.00	2650	810	0.87
10R-4, 140–145	457.90	5			30.0								
10R-4, 145–150	457.95	7	7.52	3.188	30.0	11.30	43.70	513.00	0.00	0.00	2080	340	0.26
13R-2, 140–145	483.90	5			30.0								
13R-2, 145–150	483.95	12	7.92	2.386	31.5	9.90	49.60	522.00	0.00	0.00	2220	210	0.20
16R-1, 140–145	511.10	5			28.5								
16R-1, 145–150	511.15	5	7.84	1.476	30.3	9.50	59.40	514.00	0.00		1880	105	0.16
19R-1, 140–145	540.10	5			31.8								
19R-1, 145–150	540.15	11	7.62	1.443	31.8	7.50	71.20	526.00	0.40	0.00	2280	180	0.11
22R-2, 84–89	570.04	4			32.8	8.10	86.50	539.00	0.90	0.00	1830	145	0.09
25R-1, 140–145	598.10	5											
25R-1, 145–150	598.15	6	7.62	1.443	33.7	6.50	99.50	546.00	0.00	0.00	1200	150	0.07
28R-2, 140–145	628.60	5											
28R-2, 145–150	628.65	5			34.0	0.00	123.40	544.00	0.00	0.00	1230	120	0.00
31R-5, 136–143	661.86	5			36.3		143.40				1050		
31R-5, 143–150	661.93	5	7.75	0.726	36.3	0.00	143.40	557.00		0.00	1110	105	0.00

Note: Samples with no reported data were analyzed for trace elements.

$CaCO_3$. These low values and the poor preservation of biogenic carbonate detritus (see "Biostratigraphy" section, this chapter) suggest that sediment deposition generally occurred below the carbonate compensation depth (CCD) or that subsurface carbonate dissolution occurred. The concentrations of organic carbon (%C_{org}) in the whole sediments range from 0.15% to 4.31%, with most of the sediments containing less than 1.0% on a dry weight basis. The total nitrogen contents range from 0.03% to 0.33% of whole sediments on the same basis. The ratio of organic carbon to total nitrogen (C/N) ranges from 2.83 to 15.28, with most of the sediments having values between 5 and 12.

The %$CaCO_3$, %C_{org}, and C/N ratio values are plotted against the sub-bottom depth in Figure 28. Carbonates are generally present at less than 2% but there are some higher levels (7%–20%) in the uppermost 90 m. These occurrences of increased carbonate content over narrow intervals in the top 90 m may be authigenic in nature, although increased preservation of biogenic carbonate must also be considered. There is very little carbonate preservation below 90 mbsf (approximately the base of the Quaternary), but minor amounts are present between 100–150 mbsf (upper Pliocene), and 370–410 mbsf and 435–490 mbsf (both upper Miocene). Conditions were unfavorable for carbonate preservation in the Pliocene and Miocene.

The downhole distribution of organic carbon in the sediments at Site 795 is characterized by predominantly low values of organic carbon (less than 1%). Organic carbon concentrations vary markedly (0.2%–4.2%) in the Quaternary and the uppermost Pliocene (0%–165 mbsf) with occasional increases to between 3% and 4% in the upper 70 m of the Quaternary. The highest organic contents are found in the Quaternary in the darkest colored samples, many of which contain pyrite (see below) or are rich in foraminifers. The latter are often concentrated at the bases of dark layers. Total organic carbon (TOC) levels decrease to about 0.6% in the silty claystones observed in sediments at the base of the upper Pliocene, the lower Pliocene, and the uppermost Miocene (165–400 mbsf). Organic carbon concentrations are generally higher (about 0.8%) in the upper Miocene claystones (approximately 400–600 mbsf) with a maxi-

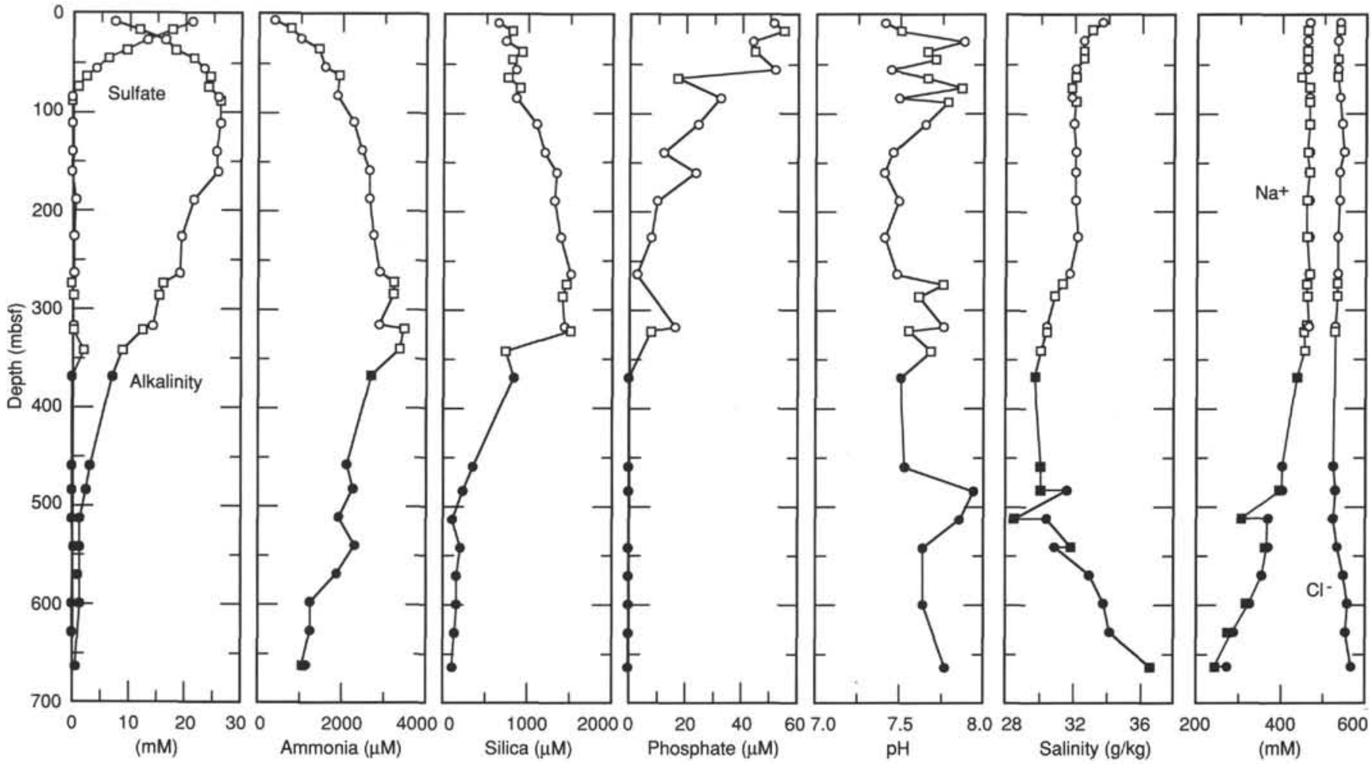

Figure 27. Depth profiles of sulfate, alkalinity, ammonia, silica (opal-A/opal-CT transition is at 325 mbsf), phosphate, pH (some of the pH variability may be caused by CO_2 loss during sample handling (Gieskes and Peretsman (1986)), salinity, sodium, chloride, potassium, rubidium, lithium, calcium, magnesium, calcium vs. magnesium, and strontium. Circles: ODP squeezer. Squares: Brumsack squeezer. Open symbols for Hole 795A, solid symbols for Holes 795B.

mum concentration of 2.02% observed at 521 mbsf. The oldest claystones recovered (middle Miocene; 600–670 mbsf) consistently show TOC levels of about 0.5%.

The top 80 m of Hole 795A are characterized by an abundance of both laminated and unlaminated or massive intervals containing clays, silty clays, diatoms, and foraminifers (see "Lithostratigraphy" section, this chapter). The generally low organic content at Site 795 attests to conditions which were unfavorable for the preservation of organic matter. Mottling of sediments due to bioturbation is commonly observed at Site 795, which implies oxygenated conditions at the sediment/water interface. The occurrence of the dark, organic-rich layers represent conditions in which productivity was enhanced and/or that conditions for the preservation of organic matter were more favorable. Such a situation may be due to the short-term formation of anoxic bottom waters associated with the restriction of deep water circulation in the Japan Sea during the Quaternary. Alternatively, these sediments may derive from organic rich sediments originally deposited upslope and transported downslope by slumping and turbidity flows, with rapid burial preventing oxidative degradation of the organic matter.

The ratio of organic carbon to total nitrogen in the sediments is also plotted in Figure 28. The nitrogen component includes both organic and inorganic nitrogen. Nitrogen concentrations (Table 7) are highly variable (0.03%–0.33%) in the silty clays of the Quaternary and the uppermost Pliocene (0–140 mbsf) and are generally low (about 0.07%) in the silty clay/claystones and diatomaceous oozes of the Pliocene and upper Miocene (140–410 mbsf). Nitrogen concentrations increase (to about 0.1%) in the claystones of the upper Miocene and uppermost middle Miocene (410–600 mbsf), and fall (to about 0.06%) in the deeper (600–670 mbsf) samples of the middle Miocene.

In the Quaternary, several pairs of light and dark bands which are immediately adjacent to each other have been analyzed. The dark bands show C/N ratios between 10 and 16, with a mean of 12.5. The light bands show C/N ratios between 4 and 11, with a mean of 7. Organic carbon often increases by an order of magnitude from a light- to a dark-colored band (see Fig. 29). Nitrogen increases also but not to the same extent, hence there is an increase in the C/N ratio from a lighter to a darker band. It is generally accepted that C/N values are higher for terrestrial- than for marine-sourced organic matter (e.g., Calvert, 1983). The implication here is that the organic matter in the dark bands contains a higher contribution of terrestrially sourced organic matter than do the lighter colored samples. However, modern marine sediments have C/N ratios in the range of 9 to 18 (Müller, 1977; Stevenson and Cheng, 1972) and diagenesis can alter C/N values (Müller, 1977; Waples and Sloan, 1980).

The mean concentration of total sulfur shows maximum concentrations (up to 9%) in the upper 110 m of the Quaternary and falls (to about 1%) in the diatom oozes of the upper Pliocene (150–250 mbsf). The concentration of sulfur again falls (below 1%) in the silty clay siltstones and claystones of the lower Pliocene and upper Miocene (250–450 mbsf), and is approximately 1% in the Miocene claystones (450–670 mbsf).

Sulfate in pore waters is fairly rapidly depleted at this site (see "Inorganic Geochemistry" section, this chapter) and is absent below 80 m. Some of the sulfate in the upper 80 m may be due to downward diffusion of seawater. Sulfate reduction has been significant at this site, as has methanogenesis (see discussion of volatile hydrocarbons below), but the smell of hydrogen sulfide was usually absent or faint. Presumably the sulfide has reacted with iron to form pyrite which was commonly observed at Site 795 and probably accounts for the higher (>2%) sulfur

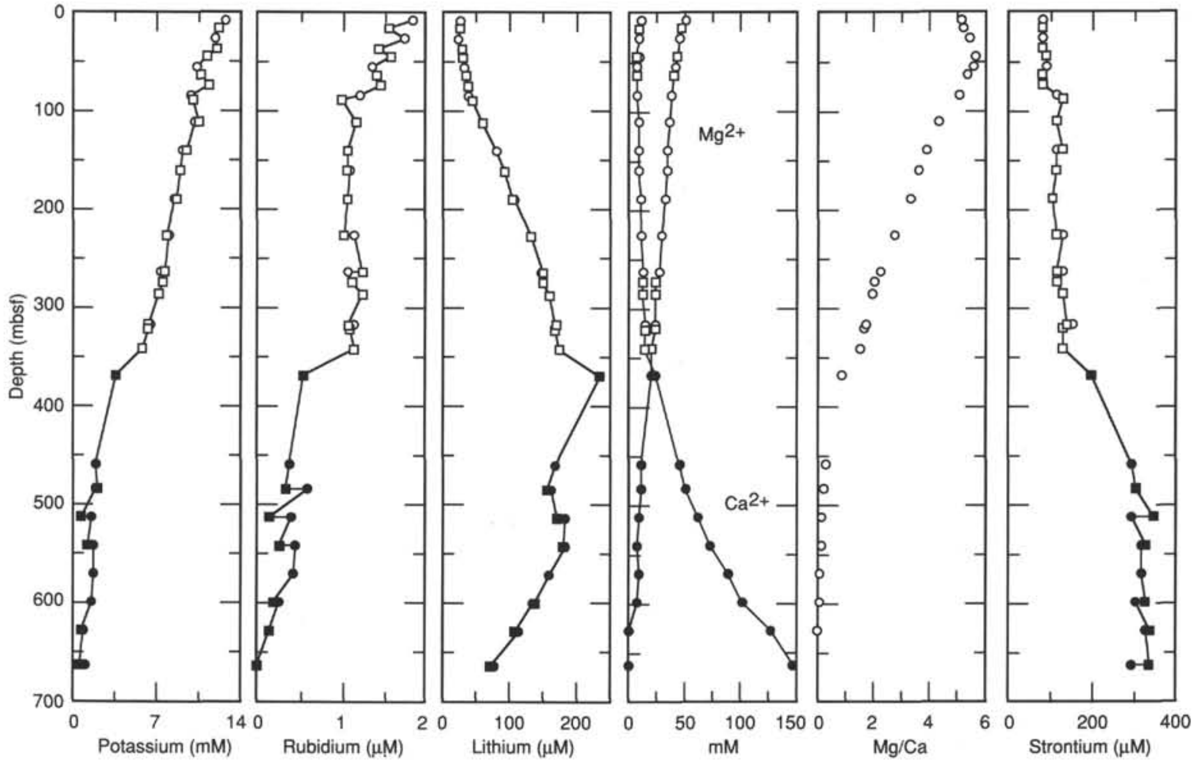

Figure 27 (continued).

concentrations reported in these sediments. The results are complex as some organic rich samples contain little sulfur while some organic poor sediments contain significantly high sulfur concentrations. The transfer of hydrogen sulfide through the sedimentary column may also be a controlling factor in the distribution of pyrite.

Rock-Eval Analysis

Samples from Site 795 were analyzed for TOC, source character, and thermal maturity and hydrocarbon potential using the Rock-Eval instrument. The resulting values are presented in Table 8. The measurement of the parameter S_3 is inconsistent at this site (see "Organic Geochemistry" section in "Site 794" chapter, this volume) and interpretations based solely upon this parameter are unwarranted. However, general trends in the composition of the organic matter can be inferred.

Total Organic Carbon Concentrations

The sediment concentrations of TOC determined by Rock-Eval range from 0.23% to 4.84%. These values are comparable to the $\%C_{org}$ values determined by difference (cf. Tables 7 and 8). When the organic carbon content of the sediments are fairly low, the TOC values are often underestimated. As the Rock-Eval TOC determinations are conducted by pyrolysis at only 600°C, the underestimations may be due to incomplete combustion as can occur with very mature samples (Emeis and Kvenvolden, 1986; Peters, 1986). This inference is supported by the high T_{max} values (see following discussion and Table 8).

Source Character

The S_2 and S_3 values represent the amount of hydrocarbons and carbon dioxide, respectively, that can be released from the kerogen (i.e., insoluble organic matter) during pyrolysis or thermal maturation of whole sediments. When normalized to the amount of organic carbon in the sediments, the new parameters of hydrogen index (HI) and oxygen index (OI) provide an estimate of the organic type (Espitalié et al., 1977). For the sediments at Site 795, these indices were determined using the TOC values from the Rock-Eval analysis.

The hydrogen and oxygen indices approximate the H/C and O/C ratios of the kerogen. A Van Krevelen-type plot of the HI and OI values for sediments at Site 795 is presented in Figure 30; some samples exhibit OI values above 300 and are not included on this plot. Based on the sample distributions in this plot, the organic contents of these sediments are primarily mixtures of Type II and Type III organic matter, with the latter type of terrestrial origin usually dominant in samples which are richer in organic matter (greater than 1%). The few samples which plot within the range of immature Type I and Type II organic matter suggest occasional episodes of increased marine/algal productivity or preservation, or a low input of terrestrially sourced organic matter. In general, the oxygen indices above 150 suggest substantial inputs of highly oxidized and reworked/recycled organic matter to the sediments of the area. Contributions of marine organic matter, though, are also suggested by the high hydrogen indices. It is interesting to note that for the dark- and light-colored adjacent samples of the Quaternary, all of the dark, organic rich samples contain Type III/II material, while the respective lighter-colored, organic poor layers always plot more toward the Type II/I region, indicative of a marine input.

Volatile Hydrocarbons

As part of the shipboard safety and pollution monitoring program, the hydrocarbon gases were continuously measured in the sediments at Site 795 using the headspace technique. Significantly high levels of volatile hydrocarbons, predominantly methane, were detected. The results are presented in Table 9. Methane concentrations in the headspace volumes ranged between 5 and 68,000 ppm, ethane concentrations ranged between 1 and 107 ppm, and propane concentrations ranged between 1 and 22

Table 7. Concentrations of inorganic and organic carbon, and total nitrogen and sulfur at Site 795.

Core, section, interval (cm)	Depth (mbsf)	Total carbon (%)	Inorganic carbon (%)	Organic carbon (%)	$CaCO_3$ (%)	Nitrogen (%)	Sulfur (%)	OrgC/N	OrgC/S
127-795A-									
1H-1, 17–19	0.17	0.60	0.01	0.59	0.1	0.08	0.20	7.40	2.90
1H-1, 102–104	1.02	3.11	0.48	2.63	4.0	0.26	0.38	10.10	6.92
1H-1, 110–112	1.10	1.30	0.08	1.22	0.7	0.13	0.24	9.38	5.08
1H-2, 44–46	1.94	1.38	0.21	1.17	1.8	0.12	3.03	9.75	0.39
1H-4, 17–19	4.67	3.26	0.07	3.19	0.6	0.29	2.00	11.00	1.59
1H-4, 145–150	5.95	0.62	0.04	0.58	0.3	0.07	0.56	8.30	1.00
1H-5, 0–5	6.00	0.60	0.04	0.56	0.3	0.08	0.29	7.00	1.90
1H-5, 32–38	6.32	3.54	0.06	3.48	0.5	0.30	4.44	11.60	0.78
1H-5, 38–44	6.38	0.71	0.07	0.64	0.6	0.06	1.05	10.00	0.61
1H-5, 61–63	6.61	4.70	1.94	2.76	16.2	0.25	2.39	11.00	1.15
2H-1, 61–67	9.91	0.52	0.11	0.41	0.9	0.05	0.11	8.20	3.70
2H-1, 67–73	9.97	2.38	0.09	2.29	0.8	0.19	3.50	12.00	0.65
2H-3, 25–27	12.55	1.67	0.06	1.61	0.5	0.13	4.58	12.40	0.35
2H-3, 103–105	13.33	2.65	0.12	2.53	1.0	0.22	3.72	11.50	0.68
2H-5, 0–5	15.30	1.21	0.08	1.13	0.7	0.10	0.27	11.30	4.18
2H-7, 36–38	18.66	0.77	0.15	0.62	1.3	0.06	2.58	10.00	0.24
3H-2, 99–101	21.29	1.44	1.29	0.15	10.8	0.04	0.21	3.70	0.71
3H-3, 43–49	22.23	3.65	0.07	3.58	0.6	0.29	4.20	12.30	0.85
3H-3, 56–62	22.36	0.25	0.02	0.23	0.2	0.04	2.91	5.70	0.08
3H-4, 140–145	24.70	1.42	0.05	1.37	0.4	0.13	0.55	10.50	2.49
3H-5, 0–5	24.80	1.57	0.08	1.49	0.7	0.13	0.55	11.40	2.71
4H-1, 104–106	29.34	1.79	0.14	1.65	1.2	0.13	2.89	12.70	0.57
4H-2, 83–86	30.63	4.38	1.25	3.13	10.4	0.25	0.71	12.50	4.41
4H-2, 86–92	30.66	0.38	0.10	0.28	0.8	0.06	0.87	4.60	0.32
4H-2, 93–94	30.73	0.27	0.09	0.18	0.8	0.04	0.12	4.50	1.50
4H-3, 127–129	32.57	0.85	0.19	0.66	1.6	0.07	3.26	9.40	0.20
4H-4, 106–108	33.86	2.86	0.15	2.71	1.3	0.23	1.95	11.80	1.39
4H-5, 0–5	34.30	0.39	0.08	0.31	0.7	0.05	1.06	6.20	0.29
4H-5, 25–27	34.55	2.75	0.06	2.69	0.5	0.23	1.50	11.70	1.79
4H-6, 143–145	37.23	4.05	0.20	3.85	1.7	0.32	4.18	12.00	0.92
5H-1, 100–101	38.80	0.83	0.34	0.49	2.8	0.06	0.14	8.10	3.50
5H-2, 100–101	40.30	0.42	0.01	0.41	0.1	0.05	0.09	8.20	4.50
5H-3, 59–61	41.39	4.14	1.06	3.08	8.8	0.26	3.74	11.80	0.82
5H-5, 0–5	43.80	0.48	0.04	0.44	0.3	0.05	0.12	8.80	3.60
5H-5, 74–76	44.54	2.64	0.15	2.49	1.3	0.19	3.40	13.10	0.73
5H-6, 63–65	45.93	1.42	0.03	1.39	0.3	0.13	1.70	10.70	0.82
5H-6, 77–79	46.07	1.11	0.06	1.05	0.5	0.10	0.36	10.50	2.91
5H-7, 36–42	47.16	4.00	0.19	3.81	1.6	0.29	3.30	13.10	1.15
5H-7, 42–48	47.22	0.76	0.13	0.63	1.1	0.07	1.63	9.00	0.39
6H-4, 145–150	53.25	1.14	0.08	1.06	0.7	0.09	1.18	11.80	0.90
6H-5, 0–5	53.30	2.35	0.06	2.29	0.5	0.16	2.63	14.30	0.87
6H-5, 83–89	54.13	4.40	0.09	4.31	0.8	0.33	4.36	13.00	0.99
6H-5, 89–95	54.19	0.37	0.08	0.29	0.7	0.05	2.27	5.80	0.13
7H-4, 8–14	61.38	0.29	0.03	0.26	0.3	0.04	0.07	6.50	3.70
7H-4, 14–20	61.44	2.77	0.02	2.75	0.2	0.18	0.96	15.30	2.86
7H-5, 0–5	62.80	0.41	0.05	0.36	0.4	0.06	0.11	6.00	3.30
7H-5, 101–107	63.81	2.40	0.37	2.03	3.1	0.14	3.62	14.50	0.56
8H-5, 0–5	72.30	0.26	0.02	0.24	0.2	0.05	0.06	4.80	4.00
9H-2, 100–102	78.30	0.20	0.01	0.19	0.1	0.04	0.10	4.70	1.90
9H-3, 32–38	79.12	2.40	0.15	2.25	1.3	0.19	0.67	11.80	3.36
9H-3, 38–44	79.18	0.36	0.07	0.29	0.6	0.05	0.15	5.80	1.90
9H-4, 145–150	81.75	3.28	2.48	0.80	20.7	0.12	0.77	6.60	1.00
9H-5, 0–5	81.80	0.33	0.14	0.19	1.2	0.04	0.13	4.70	1.40
10H-1, 127–133	86.57	0.46	0.06	0.40	0.5	0.06	0.05	6.60	8.00
10H-2, 0–5	86.80	0.21	0.02	0.19	0.2	0.05	0.06	3.80	3.10
10H-2, 50–52	87.30	0.19	0.01	0.18	0.1	0.04	0.05	4.50	3.60
11H-2, 100–102	97.30	0.80	0.03	0.77	0.3	0.09	0.14	8.50	5.50
11H-4, 32–34	99.62	1.58	0.01	1.57	0.1	0.14	0.14	11.20	11.20
11H-5, 0–5	100.80	0.22	0.02	0.20	0.2	0.05	0.25	4.00	0.80
11H-7, 0–5	103.85	1.41	0.19	1.22	1.6	0.11	9.34	11.10	0.13
12H-2, 100–101	106.80	0.91	0.02	0.89	0.2	0.06	1.14	15.00	0.78
12H-4, 145–150	110.25	0.92	0.10	0.82	0.8	0.09	0.23	9.10	3.50
12H-5, 0–5	110.30	0.51	0.04	0.47	0.3	0.07	0.24	6.70	1.90
13H-2, 99–101	116.29	0.65	0.14	0.51	1.2	0.07	0.38	7.30	1.30
13H-5, 0–5	119.80	0.33	0.03	0.30	0.3	0.07	0.94	4.30	0.32
14H-2, 99–100	125.79	0.70	0.03	0.67	0.3	0.08	0.98	8.40	0.68
14H-5, 0–5	129.30	0.93	0.21	0.72	1.8	0.09	0.95	8.00	0.76
15H-2, 8–10	134.38	1.72	0.09	1.63	0.8	0.16	2.03	10.20	0.80
15H-2, 100–101	135.30	0.81	0.04	0.77	0.3	0.09	0.67	8.50	1.10
15H-4, 145–150	138.75	0.50	0.01	0.49	0.1	0.07	0.21	7.00	2.30
15H-5, 0–5	138.80	0.42	0.02	0.40	0.2	0.06	0.16	6.60	2.50
16H-1, 63–65	142.93	0.25	0.02	0.23	0.2	0.05	0.15	4.60	1.50
16H-2, 0–5	143.80	0.64	0.03	0.61	0.3	0.08	0.42	7.60	1.40
16H-2, 100–101	144.80	1.01	0.23	0.78	1.9	0.08	0.59	9.70	1.30
16H-4, 77–79	147.57	0.55	0.02	0.53	0.2	0.06	0.46	8.80	1.10

Table 7 (continued).

Core, section, interval (cm)	Depth (mbsf)	Total carbon (%)	Inorganic carbon (%)	Organic carbon (%)	$CaCO_3$ (%)	Nitrogen (%)	Sulfur (%)	OrgC/N	OrgC/S
127-795A- (Cont.)									
18H-1, 110–112	154.00	0.63	0.06	0.57	0.5	0.07	1.27	8.10	0.45
18H-2, 100–101	155.40	0.23	0.08	0.15	0.7	0.03	0.29	5.00	0.52
18H-4, 145–150	158.85	0.76	0.02	0.74	0.2	0.09	0.82	8.20	0.90
18H-5, 0–5	158.90	0.73	0.02	0.71	0.2	0.09	0.56	7.90	1.20
19H-2, 100–101	164.90	0.40	0.04	0.36	0.3	0.06	0.20	6.00	1.80
19H-5, 0–5	168.40	0.50	0.03	0.47	0.3	0.07	0.44	6.70	1.00
21X-2, 100–102	184.10	0.42	0.03	0.39	0.3	0.06	0.75	6.50	0.52
21X-4, 145–150	187.55	0.58	0.02	0.56	0.2	0.07	0.79	8.00	0.71
21X-5, 0–5	187.60	0.60	0.03	0.57	0.3	0.07	0.75	8.10	0.76
22X-2, 101–102	193.71	0.56	0.01	0.55	0.1	0.07	0.54	7.80	1.00
22X-5, 0–5	197.20	0.48	0.02	0.46	0.2	0.06	1.25	7.60	0.37
22X-6, 41–48	199.11	0.54	0.04	0.50	0.3	0.06	0.54	8.30	0.92
25X-2, 100–102	222.90	0.46	0.01	0.45	0.1	0.06	0.80	7.50	0.56
25X-3, 145–150	224.85	0.71	0.02	0.69	0.2	0.09	1.42	7.60	0.49
25X-4, 0–3	224.90	0.71	0.03	0.68	0.3	0.08	1.32	8.50	0.52
26X-2, 100–102	232.60	0.43	0.01	0.42	0.1	0.08	0.60	5.20	0.70
26X-5, 0–3	236.10	0.51	0.01	0.50	0.1	0.07	0.62	7.10	0.80
27X-2, 100–102	242.40	0.58	0.01	0.57	0.1	0.07	0.76	8.10	0.75
27X-5, 0–5	245.90	0.61	0.01	0.60	0.1	0.07	0.78	8.60	0.77
29X-2, 100–102	262.00	0.46	0.01	0.45	0.1	0.06	0.76	7.50	0.59
29X-2, 145–150	262.45	0.42	0.01	0.41	0.1	0.06	0.78	6.80	0.52
29X-3, 0–5	262.50	0.41	0.01	0.40	0.1	0.06	0.97	6.60	0.41
30X-2, 100-102	271.80	0.53	0.01	0.52	0.1	0.07	0.71	7.40	0.73
30X-3, 0–5	272.30	0.40	0.02	0.38	0.2	0.06	0.80	6.30	0.47
31X-1, 50–64	279.60	0.55	0.02	0.53	0.2	0.07	0.63	7.60	0.84
31X-2, 99–101	281.59	0.46	0.01	0.45	0.1	0.06	0.69	7.50	0.65
31X-5, 0–5	285.10	0.67	0.02	0.65	0.2	0.08	0.88	8.10	0.74
34X-2, 100–102	310.40	0.59	0.02	0.57	0.2	0.07	0.63	8.10	0.90
34X-5, 145–150	315.35	0.57	0.01	0.56	0.1	0.08	0.71	7.00	0.79
34X-6, 0–5	315.40	0.60	0.01	0.59	0.1	0.08	0.59	7.40	1.00
35X-2, 100–102	320.10	0.45	0.01	0.44	0.1	0.09	0.49	4.90	0.90
35X-3, 0–5	320.60	0.57	0.01	0.56	0.1	0.07	0.62	8.00	0.90
35X-5, 103–117	324.63	0.56	0.02	0.54	0.2	0.06	0.42	9.00	1.30
35X-6, 59–73	325.69	0.47	0.02	0.45	0.2	0.06	0.57	7.50	0.79
37X-1, 133–138	338.23	0.51	0.03	0.48	0.3	0.07	0.89	6.80	0.54
127-795B-									
1R-2, 48–54	367.18	0.45	0.04	0.41	0.3	0.09	0.87	4.50	0.47
1R-2, 48–49	367.18	0.19	0.02	0.17	0.2	0.06	4.24	2.80	0.04
5R-1, 0–3	404.10	0.83	0.10	0.73	0.8	0.09	0.71	8.10	1.00
6R-1, 81–84	414.61	0.71	0.06	0.65	0.5	0.10	0.88	6.50	0.74
7R-1, 0–3	423.10	0.61	0.03	0.58	0.3	0.08	0.56	7.20	1.00
8R-1, 0–3	432.80	0.30	0.01	0.29	0.1	0.05	0.47	5.80	0.62
9R-2, 92–95	444.82	0.98	0.12	0.86	1.0	0.11	1.09	7.80	0.79
10R-4, 145–150	457.95	1.17	0.05	1.12	0.4	0.14	1.27	8.00	0.88
10R-5, 0–3	458.00	1.02	0.06	0.96	0.5	0.12	1.02	8.00	0.94
11R-2, 0–3	463.20	1.25	0.05	1.20	0.4	0.14	1.22	8.57	0.98
11R-2, 92–98	464.12	0.71	0.10	0.61	0.8	0.09	0.75	6.80	0.81
12R-3, 0–3	474.40	0.88	0.05	0.83	0.4	0.11	1.03	7.50	0.81
13R-2, 145–150	483.95	0.79	0.06	0.73	0.5	0.10	1.33	7.30	0.55
13R-2, 147–150	483.97	1.06	0.03	1.03	0.3	0.13	0.88	7.92	1.17
14R-2, 22–28	492.42	1.17	0.08	1.09	0.7	0.12	1.48	9.08	0.74
14R-3, 0–3	493.70	0.61	0.04	0.57	0.3	0.09	0.78	6.30	0.73
15R-2, 0–3	501.50	0.73	0.02	0.71	0.2	0.10	0.56	7.10	1.20
16R-1, 145–150	511.15	0.71	0.03	0.68	0.3	0.09	1.45	7.50	0.47
16R-1, 147–150	511.17	0.65	0.04	0.61	0.3	0.09	0.93	6.80	0.65
17R-2, 0–3	520.90	2.04	0.02	2.02	0.2	0.17	1.17	11.90	1.72
18R-3, 0–3	532.10	0.74	0.01	0.73	0.1	0.08	0.66	9.10	1.10
19R-1, 145–150	540.15	0.64	0.01	0.63	0.1	0.08	0.81	7.90	0.78
19R-2, 0–3	540.20	0.77	0.01	0.76	0.1	0.09	0.83	8.40	0.91
20R-1, 147–150	549.87	0.72	0.02	0.70	0.2	0.09	1.15	7.80	0.61
21R-6, 0–3	565.60	0.73	0.01	0.72	0.1	0.08	1.16	9.00	0.62
22R-2, 84–89	570.04	0.55	0.02	0.53	0.2	0.05	0.48	10.00	1.10
22R-3, 0–3	570.14	0.54	0.01	0.53	0.1	0.07	0.63	7.60	0.84
23R-2, 0–3	578.90	0.75	0.01	0.74	0.1	0.09	0.91	8.20	0.81
23R-2, 145–147	580.35	0.59	0.02	0.57	0.2	0.07	0.61	8.10	0.93
24R-4, 71–77	591.15	1.03	0.01	1.02	0.1	0.09	1.17	11.30	0.87
24R-5, 111–113	593.05	0.74	0.01	0.73	0.1	0.08	0.96	9.10	0.76
24R-6, 0–3	593.44	0.67	0.01	0.66	0.1	0.08	1.44	8.20	0.46
25R-1, 145–150	598.15	0.84	0.02	0.82	0.2	0.08	1.12	10.00	0.73
25R-1, 147–150	598.17	0.87	0.02	0.85	0.2	0.09	1.21	9.40	0.70
25R-2, 141–146	599.61	0.44	0.04	0.40	0.3	0.05	2.74	8.00	0.15
26R-4, 0–3	610.90	0.50	0.01	0.49	0.1	0.05	0.87	9.80	0.56
27R-3, 0–3	619.00	0.60	0.03	0.57	0.3	0.07	1.00	8.10	0.57
28R-2, 145–150	628.65	0.49	0.04	0.45	0.3	0.06	0.72	7.50	0.62

Table 7 (continued).

Core, section, interval (cm)	Depth (mbsf)	Total carbon (%)	Inorganic carbon (%)	Organic carbon (%)	$CaCO_3$ (%)	Nitrogen (%)	Sulfur (%)	OrgC/N	OrgC/S
127-795B- (Cont.)									
28R-2, 147–150	628.67	0.50	0.04	0.46	0.3	0.06	0.72	7.60	0.64
29R-3, 0–3	638.30	0.43	0.04	0.39	0.3	0.06	0.61	6.50	0.64
29R-4, 40–44	640.20	0.46	0.03	0.43	0.3	0.06	2.30	7.10	0.19
30R-3, 0–3	647.90	0.58	0.02	0.56	0.2	0.06	0.73	9.30	0.77
31R-5, 143–150	661.93	0.48	0.01	0.47	0.1	0.06	0.82	7.80	0.57
31R-6, 0–3	662.00	0.47	0.02	0.45	0.2	0.06	1.01	7.50	0.45
32R-3, 0–3	667.20	0.50	0.02	0.48	0.2	0.05	1.39	9.60	0.35
33R-1, 0–3	673.90	0.52	0.01	0.51	0.1	0.05	0.30	10.00	1.70

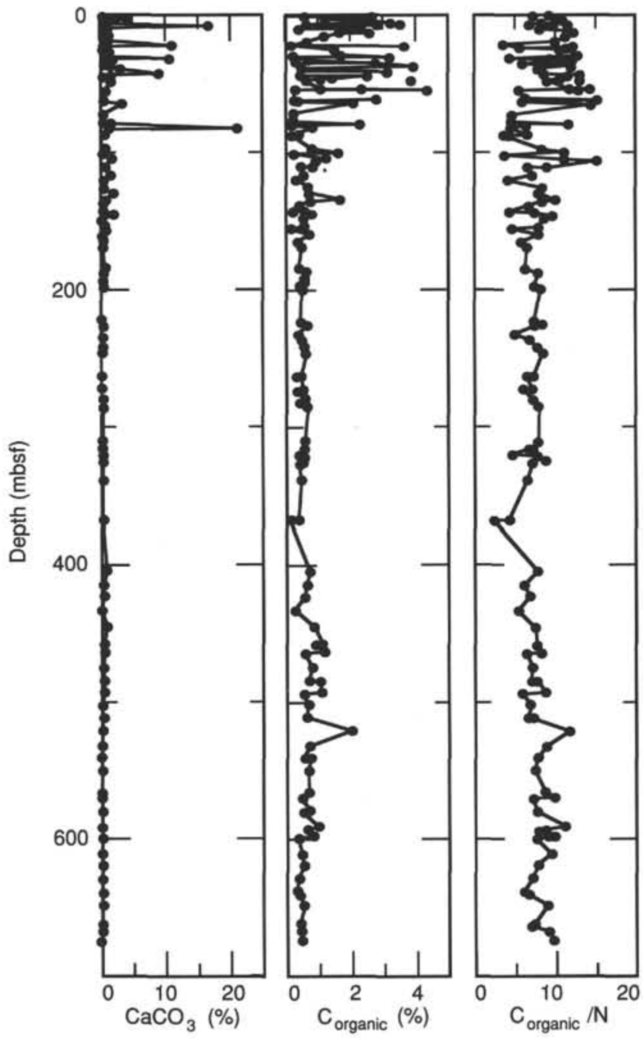

Figure 28. Downhole distributions of calcium carbonate and organic carbon concentrations as percentages of whole dry sediments and ratio of organic carbon to total nitrogen in sediments at Site 795.

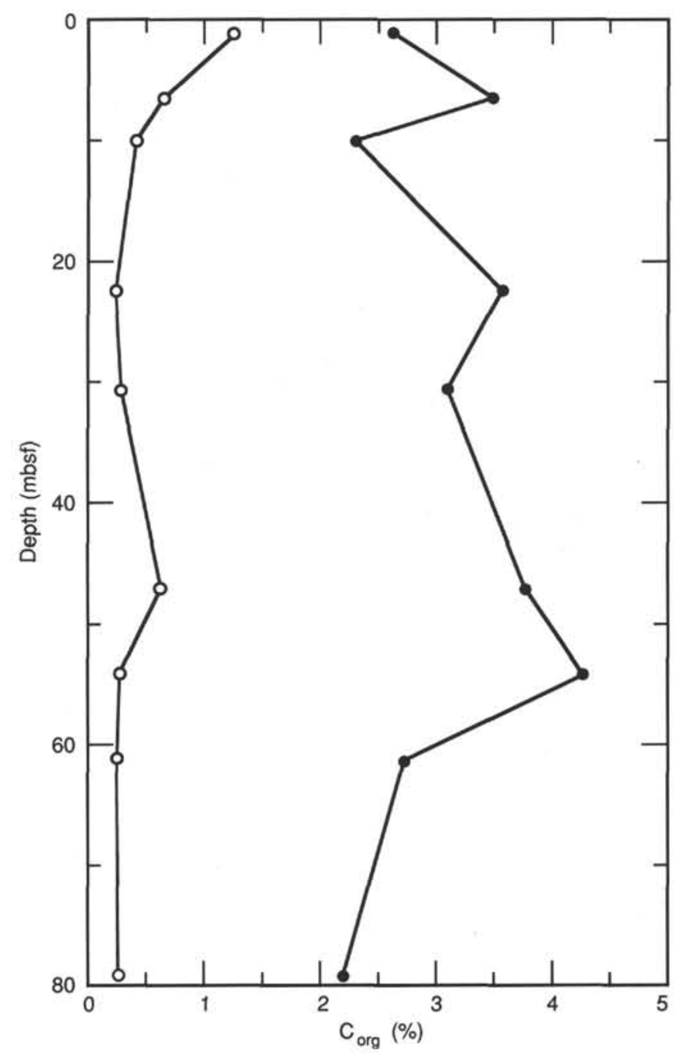

Figure 29. Downhole concentration of organic carbon in Quaternary samples; solid circles = organic-rich samples; open circles = organic-poor samples.

ppm. The high overall content of methane in the sediments, coupled with the depleted sulfate levels, suggests that considerable methanogenesis has occurred at Site 795. The necessary conditions to initiate and sustain methanogenesis are significant concentrations of organic matter in oxygen low sedimentary environments, particularly when the available sulfate has been utilized (Oremland and Taylor, 1978). The downhole concentrations of methane and the ratio of methane to ethane is shown in Figure 31. The presence of ethane and propane (see Table 9) between 445 and 647 mbsf indicates a thermogenic origin, in part, for the methane at this site. It is possible that the thermogenically generated hydrocarbons may have migrated as bottom hole temperatures are about 80°C (see "Downhole Measurements" section, this chapter).

Conclusions

Preservation of organic matter at Site 795 is generally poor. The sediments may have been initially laid down in oxic bottom waters, which allowed the organic matter to be recycled by aerobic respiration. This, coupled with subsequent sulfate reduction and methanogenesis as the sediments progressively became anoxic, led to considerable biodegradation of the organic matter. Deposition of thin, dark, organic-rich sediments occurred periodically, particularly during the Quaternary. These sediments may have been laid down during short periods of time when the bottom waters were anoxic due to restricted or sluggish water circulation in the Japan Basin. On the other hand, these organic-rich sediments appear to contain significant amounts of terrestrial material, so another scenario for their formation could be by deposition of downslope turbidites. The material comprising these turbidites would have been deposited in shallower water, perhaps where the oxygen-minimum layer impinged upon the slope, which should have enhanced the preservation of organic matter. The development of anoxia (Tissot et al., 1979; Waples, 1985;) in either of the above models will be related to climatic and tectonic factors (e.g., changes in sea-bottom topography, sea level, productivity and circulation). A fundamental question is why do these organic-rich bands appear to be exclusive to the Quaternary. The answer must relate to the continental upthrust which occurred during the Pliocene (see "Lithostratigraphy" section in "Site 796" chapter, this chapter). In the Miocene, Site 795 would have been more distant from slopes which could project into an oxygen-minimum zone, and basins nearer to these slopes would have acted as traps for turbidites.

BASEMENT ROCKS

Introduction

A sequence of massive to brecciated, vesicular, sparsely to moderately phyric basalt and basaltic andesite was cored at Site 795, between 683.5 and 762.2 mbsf. A total of 17.6 m of volcanic rock was recovered from 78.7 m cored, an average core recovery of 22%. The volcanic rocks lie beneath claystone sediments whose age is estimated to be early middle Miocene, 13–15 Ma (see "Biostratigraphy" section, this chapter). Three units were defined on the basis of variations in phenocryst mineralogy. All three units are brecciated, either throughout, or in zones separated by more massive portions. Unit 3 was further divided into two subunits using variations in geochemical characteristics and macroscopic textures. The lithological characteristics of the units are described below, and a summary lithostratigraphic diagram is presented as Figure 32.

Lithology

Unit 1: Brecciated Sparsely Plagioclase Pyroxene Phyric Basaltic Andesite

This unit is defined from Section 127-795B-34R-1, 5 cm, to Section 127-795B-36R-1, Piece 1c (683.5–703.3 mbsf). The unit is overlain by claystone interbedded with minor tuffs, but no contact between the sediments and the volcanics was recovered. The unit consists of brecciated, vesicular, moderately plagioclase pyroxene magnetite phyric basaltic andesite clasts, which range in size from 1 mm to 15 cm and are set in a matrix dominantly composed of dark green clay minerals with subordinate zeolite and blue-green siliceous material (mixed cryptocrystalline silica and zeolite, identified by X-ray diffraction (XRD) analysis). Identification of the primary matrix composition is impossible due to its total alteration to secondary phases. The breccia is primarily clast-supported and often exhibits jigsaw-fit texture, although a few pieces are matrix-supported, where the matrix content is up to 30% (Fig. 33). Phenocrysts within the basaltic andesite clasts are euhedral, tabular plagioclase (5%, <1 mm), subhedral clinopyroxene (5%, 1 mm), and euhedral magnetite (2%, <0.5 mm), all of which occur both singly and as glomerophenocrysts. The groundmass has microcrystalline interstitial texture, composed of euhedral plagioclase laths (<0.3 mm) and scattered fine (<0.03 mm) magnetite grains within an altered mesostasis. Elongate vesicles, up to 10 mm in length, are rimmed with green celadonite(?) and filled with zeolite. The direction of elongation of the vesicles defines a weak fabric in many of the breccia clasts (Fig. 34). The clasts have a 10 mm thick outer rim of high alteration (Fig. 33), where phenocrysts and mesostasis are mostly and totally altered to clay minerals, respectively. The centers of clasts greater than 3 cm in diameter are moderately altered, with some pyroxene phenocrysts and all the mesostasis replaced by clays.

Unit 2: Silicified Brecciated Moderately Plagioclase Phyric Basalt

This unit is defined from Section 127-795-36R-1, Piece 1c, 42 cm, to Piece 11 (703.3–704 mbsf). Intense alteration and the presence of many siliceous veins characterize this unit, and the incoming of these features marks the upper boundary with Unit 1. The phenocryst assemblage is plagioclase (7%, <1 mm) and a mafic mineral (tentatively identified as pyroxene) which has been totally replaced by clays. The breccia clasts appear petrographically similar to those in Unit 1, indicating that this may be a very highly altered basal section to Unit 1.

Unit 3: Sparsely Pyroxene Plagioclase Phyric Basalt

This unit is defined from Section 127-795-36R-1, Piece 12, to Section 127-795-41R-2, Piece 10, 704–762.2 mbsf, bottom of hole. No upper contact with Unit 2 was recovered. Unit 3 was further divided into two subunits on the basis of macroscopic texture and geochemical data.

Subunit 3A is predominantly massive, sparsely pyroxene plagioclase phyric basalt with minor fractured to brecciated zones. It extends from Section 127-795-36R-1, Piece 12, to Section 127-795-39R-2, Piece 1b (704–733.7 mbsf). The basalt contains subhedral clinopyroxene (<2%, <2 mm) and euhedral, tabular plagioclase (<2%, <2 mm) phenocrysts set in a microcrystalline interstitial groundmass of euhedral plagioclase laths and altered mesostasis. The degree of alteration is high, with plagioclase phenocryst cores and the mesostasis altered to clay minerals. The subunit contains 5%–20% round to lobate vesicles which range up to 10 mm in diameter and are rimmed with greenish-brown clays and partially to totally filled with bright green celadonite(?). Irregularly shaped and heterogeneously distributed vugs and fracture-bound cavities are lined with botryoidal green clay and clear, tabular heulandite as identified by XRD analysis. In the massive portions, fractures are randomly oriented, generally <1 mm thick, and are filled with greenish-black clays and minor zeolite. In the upper part of the subunit, an earlier generation of fractures, <10 mm thick, is filled with blue-green mixed cryptocrystalline silica and zeolite (identified by XRD analysis), and is cross-cut by the second generation clay- and/or zeolite-filled fractures. Brecciated portions have angular basalt clasts ranging in size from 10 cm to <1 mm within a matrix of greenish-black clay and subordinate zeolite. The matrix composes up to 10% of the brecciated zones.

Subunit 3B is composed principally of brecciated sparsely pyroxene plagioclase phyric basalt with a lesser amount of massive basalt to basaltic andesite, and is defined from Section 127-795-39R-2, Piece 2, to Section 127-795-41R-2, Piece 10 (733.7–762.2 mbsf), bottom of hole. Phenocrysts in the basalt are subhedral to anhedral clinopyroxene (1%–2%, 1 mm), which often occur as glomerophenocrysts, and euhedral, tabular plagioclase

Table 8. Results of Rock-Eval analysis for Site 795.

Core, section, interval (cm)	Depth (mbsf)	S_1 (mg/g)	S_2 (mg/g)	S_3 (mg/g)	TOC (%)	PC	HI	OI	T_{max} (°C)	PI	S_2/S_3
127-795A-											
1H-1, 102–103	1.02	1.08	5.71	11.00	2.98	0.56	191	369	380	0.16	0.51
1H-1, 110–112	1.10	0.28	4.86	3.13	1.60	0.42	303	195	475	0.05	1.55
1H-2, 44–46	1.94	0.22	3.56	1.68	1.27	0.31	280	132	378	0.06	2.11
1H-4, 17–19	4.67	1.32	11.09	8.17	3.90	1.03	284	209	401	0.11	1.35
1H-4, 145–150	5.95	0.17	2.07	1.51	0.66	0.18	313	228	465	0.08	1.37
1H-5, 61–63	6.61	0.81	5.91	14.21	3.54	0.56	166	401	427	0.12	0.41
2H-3, 25–27	12.55	0.52	5.93	1.19	1.62	0.53	366	73	410	0.08	4.98
2H-3, 103–105	13.33	0.73	7.47	5.42	3.11	0.68	240	174	390	0.09	1.37
2H-7, 36–38	18.66	0.19	1.51	0.96	0.64	0.14	235	150	514	0.11	1.57
3H-3, 43–49	22.23	1.96	13.16	6.00	4.07	1.26	323	147	396	0.13	2.19
3H-3, 56–62	22.36	0.07	1.69	0.03	0.32	0.14	528	9	586	0.04	56.33
3H-4, 140–145	24.70	0.30	1.99	2.87	1.38	0.19	144	207	425	0.13	0.69
4H-1, 104–106	29.34	0.53	5.55	3.30	2.04	0.50	272	161	409	0.09	1.68
4H-2, 83–86	30.63	0.65	3.73	11.39	2.72	0.36	137	418	413	0.15	0.32
4H-2, 86–92	30.66	0.00	1.76	2.26	0.23	0.14	765	982	524	0.00	0.77
4H-3, 127–129	32.57	0.21	2.19	1.19	0.77	0.20	284	154	490	0.09	1.84
4H-4, 105–108	33.85	0.78	6.77	6.99	3.33	0.62	203	209	423	0.10	0.96
4H-5, 25–27	34.55	0.65	7.51	5.65	3.43	0.68	218	164	424	0.08	1.32
4H-6, 143–145	37.23	1.73	12.75	9.99	4.84	1.20	263	206	403	0.12	1.27
5H-3, 59–61	41.39	0.97	7.68	10.97	3.81	0.72	201	287	417	0.11	0.70
5H-5, 74–76	44.54	0.86	7.43	5.52	2.67	0.69	278	206	397	0.10	1.34
5H-6, 63–65	45.93	0.32	4.23	2.75	1.89	0.37	223	145	416	0.07	1.53
5H-6, 77–79	46.07	0.17	2.66	2.65	1.34	0.23	198	197	546	0.06	1.00
5H-7, 36–42	47.16	1.37	7.59	7.08	3.85	0.74	197	183	405	0.15	1.07
5H-7, 42–48	47.22	0.17	1.97	2.56	0.67	0.17	294	382	587	0.08	0.76
6H-4, 145–150	53.25	0.24	2.78	1.12	1.28	0.25	217	87	423	0.08	2.48
6H-5, 83–89	54.13	1.22	10.96	7.48	4.68	1.01	234	159	405	0.10	1.46
6H-5, 89–95	54.19	0.00	1.67	0.19	0.36	0.13	463	52	570	0.00	8.78
7H-4, 8–14	61.38	0.11	3.30	0.00	0.47	0.28	702	0	487	0.03	
7H-4, 14–20	61.44	0.59	11.87	2.97	3.18	1.03	373	93	427	0.05	3.99
7H-5, 101–107	63.81	0.61	4.27	3.88	1.73	0.40	246	224	406	0.12	1.10
8H-5, 0–5	72.30	0.05	3.98	0.00	0.48	0.33	829	0	574	0.01	
9H-3, 32–38	79.12	0.47	5.31	4.33	2.43	0.48	218	178	425	0.08	1.22
9H-3, 38–44	79.18	0.14	2.38	0.07	0.48	0.21	495	14	553	0.06	34.00
9H-4, 145–150	81.75	0.20	1.77	11.66	1.46	0.16	121	798	403	0.10	0.15
10H-1, 127–133	86.57	0.17	2.37	0.02	0.53	0.21	447	3	586	0.07	
11H-4, 32–34	99.62	0.31	5.94	1.72	2.28	0.52	260	75	412	0.05	3.45
11H-7, 3–5	103.83	0.26	2.61	2.78	0.93	0.23	280	298	399	0.09	0.93
12H-4, 145–150	110.25	0.14	1.40	2.36	1.06	0.12	132	222	533	0.09	0.59
15H-2, 8–10	134.38	0.38	4.03	2.08	1.68	0.36	239	123	471	0.09	1.93
15H-4, 145–150	138.75	0.09	1.74	0.00	0.52	0.15	334	0	511	0.05	
16H-1, 63–65	142.93	0.09	2.94	0.00	0.40	0.25	735	0	561	0.03	
16H-4, 77–79	147.57	0.10	3.26	0.07	0.65	0.28	501	10	493	0.03	46.57
18H-1, 110–112	154.00	0.13	2.79	0.64	0.64	0.24	435	100	577	0.04	4.35
18H-4, 145–150	158.85	0.15	1.76	0.17	0.79	0.15	222	21	531	0.08	10.35
21X-4, 145–150	187.55	0.15	1.31	1.57	0.59	0.12	222	266	564	0.10	0.83
22X-6, 41–48	199.11	0.05	2.77	0.27	0.74	0.23	374	36	534	0.02	10.25
25X-3, 145–150	224.85	0.14	0.88	0.00	0.59	0.08	149	0	455	0.14	
29X-2, 145–150	262.45	0.11	1.98	0.00	0.45	0.17	440	0	523	0.05	
31X-1, 50–64	279.60	0.09	2.52	0.01	0.66	0.21	381	1	492	0.03	
34X-5, 145–150	315.35	0.03	1.35	0.00	0.52	0.11	259	0	550	0.02	
35X-5, 103–117	324.63	0.05	2.46	0.00	0.65	0.20	378	0	473	0.02	
35X-6, 59–73	325.69	0.06	2.03	0.02	0.63	0.17	322	3	562	0.03	
127-795B-											
1R-2, 48–54	367.18	0.04	1.07	0.00	0.39	0.09	274	0	576	0.04	
5R-1, 2–3	404.12	0.03	2.42	0.01	0.88	0.20	275	1	455	0.01	
6R-1, 81–84	414.61	0.03	1.68	0.02	0.63	0.14	266	3	505	0.02	84.00
7R-1, 0–3	423.10	0.03	1.38	0.00	0.55	0.11	250	0	480	0.02	
8R-1, 0–3	432.80	0.01	0.92	0.00	0.29	0.07	317	0	587	0.01	
9R-2, 92–95	444.82	0.02	2.11	0.02	0.85	0.17	248	2	508	0.01	
10R-4, 145–150	457.95	0.03	1.57	0.02	0.87	0.13	180	2	414	0.02	78.50
10R-5, 0–3	458.00	0.03	1.90	0.00	0.93	0.16	204	0	417	0.02	
11R-2, 0–3	463.20	0.02	1.61	0.28	1.16	0.13	138	24	421	0.01	5.75
11R-2, 92–98	464.12	0.00	1.46	0.00	0.64	0.12	228	0	471	0.00	
12R-3, 0–3	474.40	0.02	1.27	0.01	0.77	0.10	164	1	480	0.02	
13R-2, 145–150	483.95	0.00	1.12	0.01	0.66	0.09	169	1	453	0.00	
14R-2, 22–28	492.42	0.02	1.75	0.26	1.04	0.14	168	25	417	0.01	6.73
14R-3, 0–3	493.70	0.00	0.00	0.00	0.42	0.00	0	0	307		
15R-2, 0–3	501.50	0.00	2.04	0.03	0.73	0.17	279	4	427	0.00	68.00
16R-1, 145–150	511.15	0.00	1.23	0.00	0.60	0.10	205	0	494	0.00	
17R-2, 0–3	520.90	0.07	4.42	0.08	2.03	0.37	217	3	422	0.02	55.25
18R-3, 0–3	532.10	0.01	2.22	0.00	0.81	0.18	274	0	425	0.00	
19R-1, 145–150	540.15	0.00	1.62	0.00	0.64	0.13	253	0	426	0.00	

Table 8 (continued).

Core, section, interval (cm)	Depth (mbsf)	S_1 (mg/g)	S_2 (mg/g)	S_3 (mg/g)	TOC (%)	PC	HI	OI	T_{max} (°C)	PI	S_2/S_3
127-795B- (Cont.)											
20R-1, 145–150	549.87	0.01	1.94	0.00	0.71	0.16	273	0	415	0.01	
21R-6, 0–3	565.60	0.01	1.75	0.00	0.66	0.14	265	0	420	0.01	
22R-2, 84–89	570.04	0.00	1.45	0.00	0.58	0.12	250	0	426	0.00	
23R-2, 0–3	578.90	0.01	1.53	0.00	0.71	0.12	215	0	499	0.01	
24R-4, 71–77	591.15	0.02	2.55	0.00	1.12	0.21	227	0	423	0.01	
25R-1, 145–150	598.15	0.00	1.41	0.00	0.78	0.11	180	0	425	0.00	
25R-2, 145–150	599.65	0.00	1.08	0.05	0.39	0.09	276	12	560	0.00	21.60
26R-4, 0–3	610.90	0.01	1.65	0.00	0.57	0.13	289	0	417	0.01	
27R-3, 0–3	619.00	0.00	0.83	0.00	0.53	0.06	156	0	564	0.00	
28R-2, 145–150	628.65	0.00	0.91	0.00	0.42	0.07	216	0	564	0.00	
29R-4, 40–44	640.20	0.00	1.28	0.01	0.41	0.10	312	2	511	0.00	
30R-3, 0–3	647.90	0.00	1.09	0.01	0.54	0.09	201	1	514	0.00	
31R-5, 143–150	661.93	0.00	1.01	0.01	0.44	0.08	229	2	516	0.00	
32R-3, 0–3	667.20	0.01	1.40	0.01	0.47	0.11	297	2	498	0.01	
33R-1, 0–3	673.90	0.00	1.47	0.00	0.55	0.12	267	0	420	0.00	

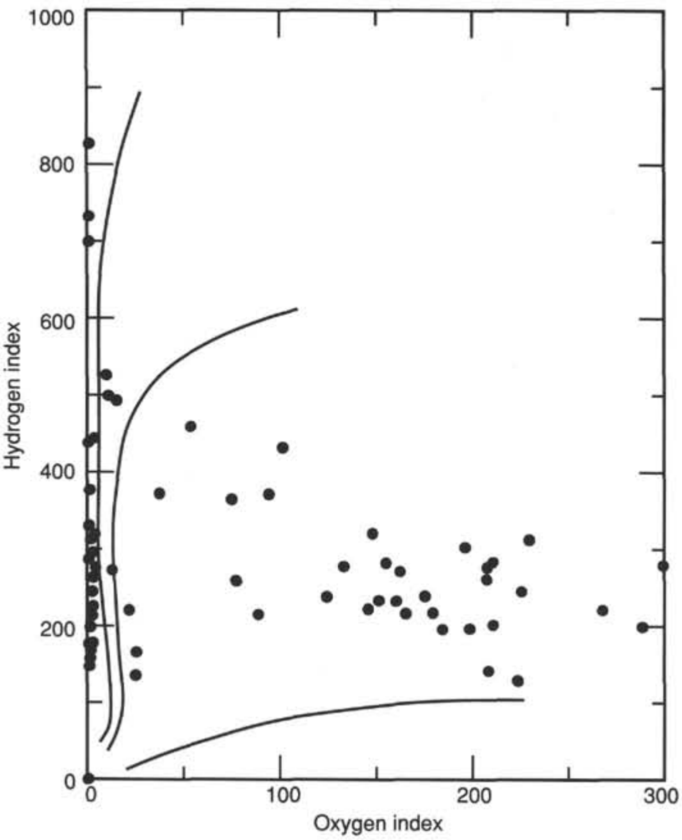

Figure 30. van Krevelen-type diagram of the hydrogen vs. oxygen indices of sediments from Site 795.

(1%, 2 mm). The groundmass is microcrystalline interstitial, and is composed of euhedral plagioclase laths and altered mesostasis. Alteration of the basalt varies from moderate in the massive portions and large (>5 cm) breccia clasts to high in the smaller clasts and rims of larger clasts. The breccia is mostly clast-supported, and has some areas of jigsaw-fit brecciation as seen in Figure 35. Nevertheless, the matrix, which comprises greenish-black clays and zeolite, can form up to 20% of the rock in some pieces.

Geochemistry

X-ray fluorescence (XRF) whole rock analyses of 14 basement samples from Hole 795B are presented in Table 10. The measured loss on ignition (LOI) of these samples, which is related to the degree of alteration, varies from 2.8% to nearly 6%. There appears to be no consistent correlation between the concentration of any element analyzed and LOI. The extreme mobility of the large-ion lithophile elements (LILE), particularly K, Rb, and Ba, during alteration (e.g., Saunders and Tarney, 1984) make the reliability of the values for these elements in altered rocks questionable. In these analyses, however, the low values of K, Rb, and Ba correspond with low values for the less-mobile LILE Sr and Ce. For this reason we believe that the analyses may approximate original magma compositions. The samples analyzed fall into three groups, which correspond to Unit 1 and Subunits 3A and 3B of Unit 3. Unit 1 is basaltic andesite, and has higher SiO_2, Al_2O_3, Nb, and Zr and lower FeO, MgO, CaO, Ni, and Cr contents than Unit 3. Subunit 3A is basaltic and has lower SiO_2 and MgO, and higher Al_2O_3, CaO, Zr, and Ni contents than Subunit 3B, which ranges compositionally from basalt to basaltic andesite. Cr, Ni, and MgO values indicate that the volcanics from Site 795 are relatively evolved. The volcanics exhibit chemical characteristics which distinguish them from mid-ocean ridge basalts (MORB) and tholeiitic back-arc basin basalts (BABB). For a given MgO content in the Site 795 lavas, FeO_{total} and TiO_2 are low and Al_2O_3 is high in comparison with typical values for MORB and tholeiitic BABB. The ratio of LILE to HFSE (high-field-strength elements) in the Site 795 lavas is also higher than that observed in MORB's and BABB's (Fig. 36). The lack of a significant iron enrichment trend with differentiation, the high Al_2O_3 content, and the relatively high LILE/HFSE ratios of the Site 795 lavas are definitive features of calc-alkaline basic volcanics associated with volcanic arcs and subduction zones (Wilson, 1989). The high Al_2O_3 content of the lavas may be due to a high water content of the magma delaying plagioclase crystallization. The low contents of LILE and Ce suggest that the magmas underwent little or no interaction with continental crust during their genesis.

Summary

The basalts and basaltic andesites recovered by drilling at Site 795 are interpreted as lavas erupted in a subaqueous environment. The vesicularity of the volcanics does not provide a precise determination of the water depth beneath which the ba-

Table 9. Hydrocarbon gas data for Site 795.

Core, section interval (cm)	Depth (mbsf)	C_1 (ppm)	C_2 (ppm)	C_3 (ppm)	C_1/C_2
127-795A-					
1H-5, 0–5	6.00	5	1		5.00
2H-5, 0–5	15.30	6			
3H-5, 0–5	24.80	8			
4H-5, 0–5	34.30	5			
5H-5, 0–5	43.80	5			
6H-5, 0–5	53.30	5			
7H-5, 0–5	62.80	6			
8H-5, 0–5	72.30	11			
9H-5, 0–5	81.80	1300			
10H-2, 0–5	86.80	5507	1		5507.00
11H-5, 0–5	100.80	7502	2		3751.00
12H-5, 0–5	110.30	9388	5		1877.60
13H-5, 0–5	119.80	14947	24		622.79
14H-5, 0–5	129.30	67565	13		5197.31
15H-5, 0–5	138.80	46665	9		5185.00
16H-2, 0–5	143.80	32471	6		5411.83
18H-5, 0–5	158.90	24609	15		1640.60
19H-5, 0–5	168.40	67952	12	1	5662.67
21X-5, 0–5	187.60	21487	5		4297.40
25X-4, 0–3	224.90	10379	7		1482.71
26X-5, 0–3	236.10	61499	9		6833.22
27X-5, 0–5	245.90	21260	6		3543.33
29X-3, 0–5	262.50	43808	10		4380.80
30X-3, 0–5	272.30	24139	7		3448.43
31X-5, 0–5	285.10	24598	14		1757.00
34X-6, 0–5	315.40	30000	13		2307.69
127-795B-					
6R-1, 81–84	414.61	87588	37		2367.24
7R-1, 0–3	423.10	60720	226		268.67
8R-1, 0–3	432.80	25154	16		1572.13
9R-2, 92–95	444.82	74049	358	1	206.84
10R-5, 0–3	458.00	25286	22	1	1149.36
11R-2, 0–3	463.20	149200	146	3	1021.92
12R-3, 0–3	474.40	32274	30	2	1075.80
13R-2, 147–150	483.97	103573	76	5	1362.80
14R-3, 0–3	493.70	71715	39	3	1838.85
15R-2, 0–3	501.50	89923	69	9	1303.23
16R-1, 147–150	511.17	89622	55	6	1629.49
17R-2, 0–5	520.90	92924	107	22	868.45
18R-3, 0–3	532.10	9774	31	5	315.29
19R-2, 0–3	540.20	9768	25	4	390.72
20R-1, 147–150	549.87	35640	32	4	1113.75
21R-6, 0–3	565.60	35206	38	4	926.47
22R-3, 0–3	570.14	7889	17	2	464.06
23R-2, 0–3	578.90	50472	38	5	1328.21
24R-6, 0–3	593.44	32250	34	6	948.53
25R-1, 147–150	598.17	55520	53	9	1047.55
27R-3, 0–3	619.00	63430	42	7	1510.24
29R-3, 0–3	638.30	8485	15	3	565.67
30R-3, 0–3	647.90	6939	10	3	693.90
31R-6, 0–3	662.00	3691	3		1230.33
32R-3, 0–3	667.20	6713	1		6713.00
33R-1, 0–3	673.90	6174	1		6174.00

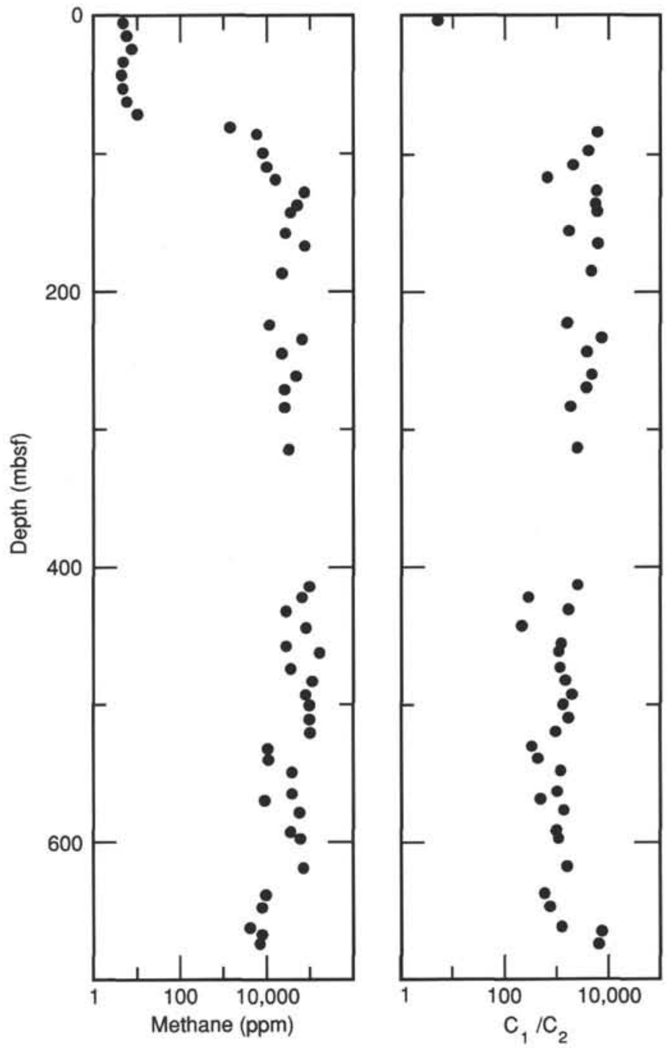

Figure 31. Downhole concentration of methane (ppm) and ratio of methane to ethane (C_1/C_2) at Site 795.

salts were erupted. However, a range estimate of between wave-base (100–200 mbsl) and 1000 mbsl is consonant with constraints imposed by the vesicularity and the character of the overlying sediments (see "Lithostratigraphy" section, this chapter). Brecciated zones occur within the volcanic sequence, and the style of brecciation, with common jigsaw-fit textures, indicates that autobrecciation occurred upon extrusion. Middle Miocene volcanic complexes consisting of massive to autobrecciated basalts and pillow basalts have been described from the back-arc side of northeast Honshu (e.g., Ohguchi et al., 1989; Tsuchiya, 1988, 1989) and southwest Hokkaido (Ishida and Hata, 1989). Basalt breccia and basalt fragments have also been dredged from the Okushiri Ridge near Site 795 (Tamaki et al., 1988b; Ishii et al., 1988). The lavas recovered from Site 795 have calc-alkaline chemical characteristics which are consistent with eruption within a subduction-related volcanic arc, perhaps at an early stage of arc rifting during back-arc basin formation (Ewart, 1982; Saunders and Tarney, 1984). The deep bathymetry of the site and the lack of LILE and Ce enrichment in the lavas suggest that Site 795 overlies oceanic rather than continental crust.

PHYSICAL PROPERTIES

Introduction

A full program of physical property measurements was conducted on Site 795 cores that included magnetic susceptibility, GRAPE density and *P*-wave velocity measurements on the multisensor track (MST), index properties, thermal conductivity, *P*-wave velocity using the Hamilton Frame, and the formation factor. All of the physical property results for discrete samples and selected values from the *P*-wave logger are presented in Table 11 for Holes 795A and 795B.

Methods and Data Quality

To allow cross-correlation of the results, index properties, thermal conductivity, and the formation factor were measured at a single location in each section, usually 100 cm from the top. In addition, two of the index property samples from each APC core and one for each XCB and RCB core were analyzed for

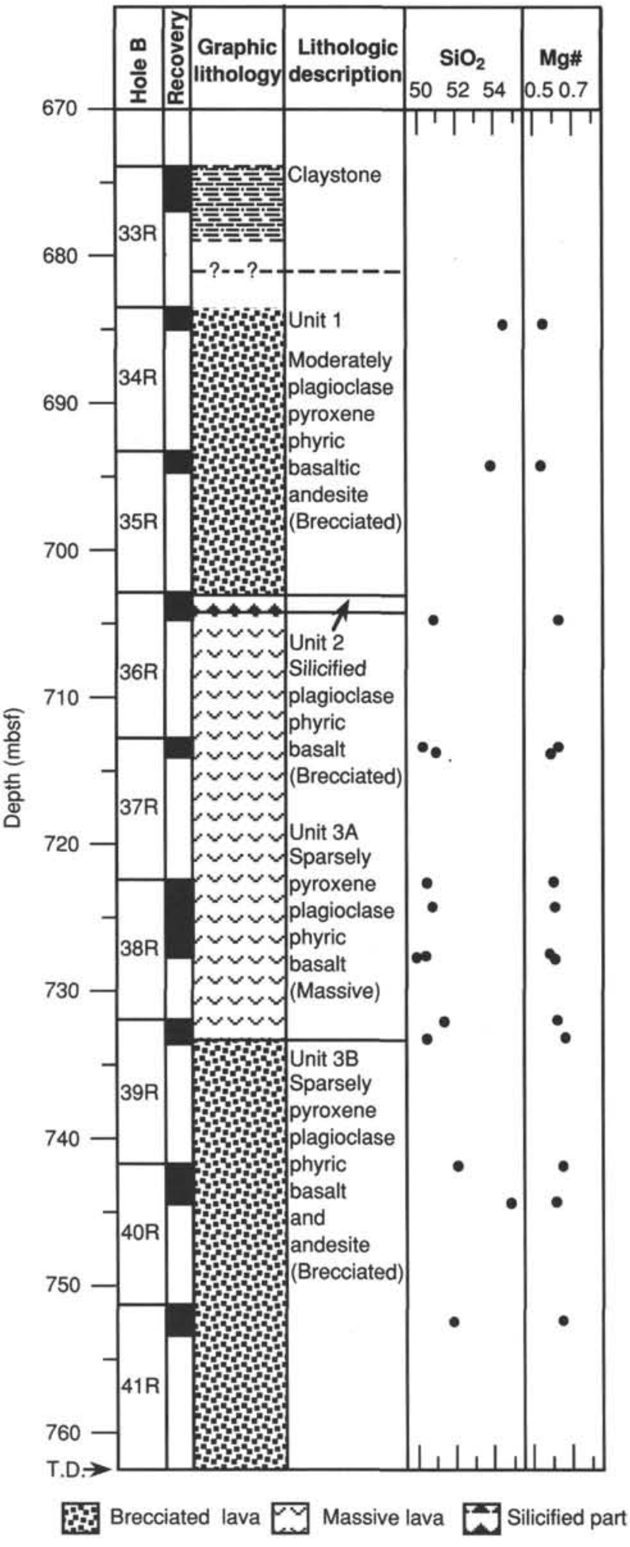

Figure 32. Lithostratigraphic diagram of basement at Site 795 showing core recovery, unit boundaries, and representative geochemical variation.

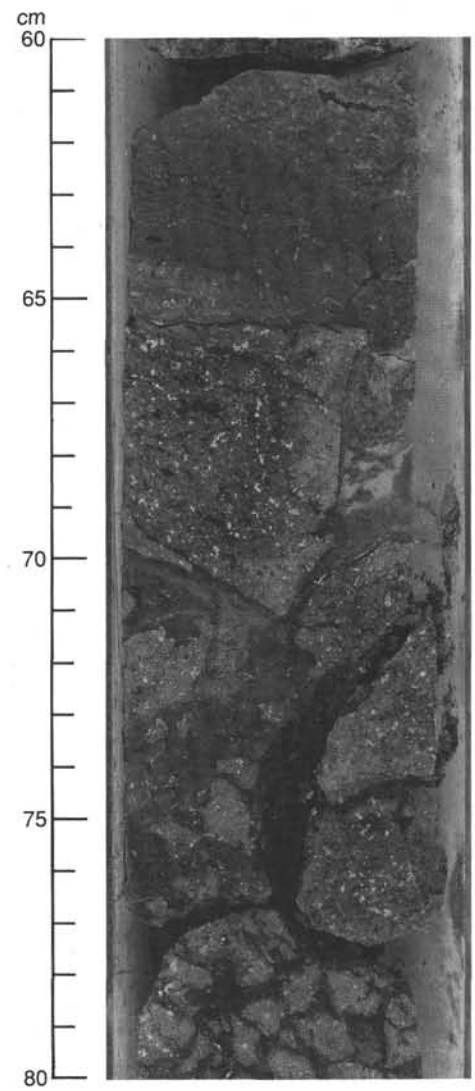

Figure 33. Brecciated basaltic andesite of Unit 1. Note high proportion of matrix at 73–80 cm and alteration rind on clast at 64–70 cm.

grain size, carbonate content, and total organic carbon content. The *P*-wave logger on the MST could only be used reliably on APC cores, i.e., to a depth of about 160 mbsf. Deeper in the section (>300 mbsf), where the strength of the cored material allowed, a sample from each section was cut into a cube and the velocity measured using the Hamilton Frame apparatus. As a consequence almost no velocity measurements were made between 180 and 350 mbsf. Unfortunately, downhole logging in Hole 795B was limited to the shallowest part of the hole (see "Downhole Measurements" section, this chapter) and no results are available to fill the data gap or for comparison with the shipboard measurements.

As described in the Site 794 physical properties summary, the cores taken at Hole 795A using the XCB are disturbed to such a degree that some of the physical properties are altered from their *in-situ* condition. The XCB disturbance appears to decompact the sediments by the formation of small fractures throughout the cores (also see "Lithostratigraphy" section, this chapter). The effects on the physical properties are to bias the bulk density and thermal conductivity toward lower values, and the water content toward higher values.

The accuracy of the thermal conductivity values in Table 11 is estimated to be ±5%. The individual thermal conductivity measurements show less variability than was observed at Site 794. This is due in large part to improvements in reduction methods and standardization of the measurement technique.

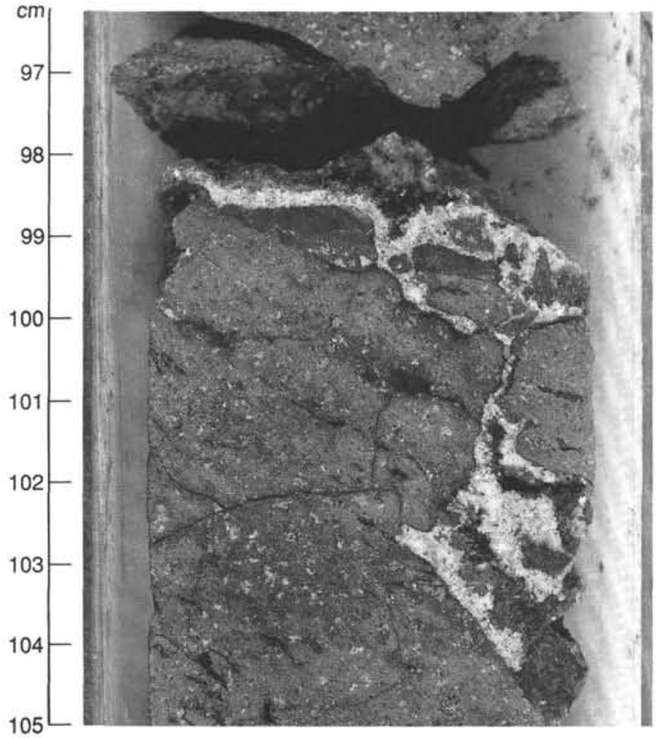

Figure 34. Brecciated basaltic andesite of Unit 1 showing fabric weakly defined by elongation of vesicles. Note the fracture/cavity filling by white zeolite.

The scatter in values for all of the discrete measurements decreased due to increased familiarity with and standardization of measurement techniques.

The formation factor determinations involve measurements of the resistivity of the sediments parallel and perpendicular to the axis of the core, preceded and followed closely by a resistivity measurement of surface seawater. The seawater was contained in a half core liner to duplicate the geometry of the sediment measurements. As at Site 794, the seawater resistivity measurements gave variable results, which added to the uncertainty of each measurement of the formation factor. The variation in the resistivity of the seawater reference was about 10%, leading to an estimated error of about 20% in the formation factor. Resistivity measurements could only be made in unconsolidated sediments and consequently were only made in the interval from 0 to 320 mbsf.

Physical Properties of the Sedimentary Section

In this section we use the lithostratigraphic units as a framework for discussing the magnitude and variation of the physical property measurements. Plots of the principal physical properties vs. depth are presented in Figures 37–43. The first-order statistics for each of the major lithostratigraphic units are presented in Tables 12–17. The general patterns and trends are similar to those observed at Site 794.

Unit I (0–123 mbsf) is comprised of an unconsolidated silty clay with zones of diatomaceous ooze and frequent occurrences of thin layers of tephra. The index properties and thermal conductivity in this unit show a relatively high variability, but the mean value shows no significant trend with depth. The variability is primarily due to alternating zones of high and low diatom abundance and infrequent measurements in ash layers. The acoustic velocity exhibits low scatter and values close to that of seawater (1519 m/s).

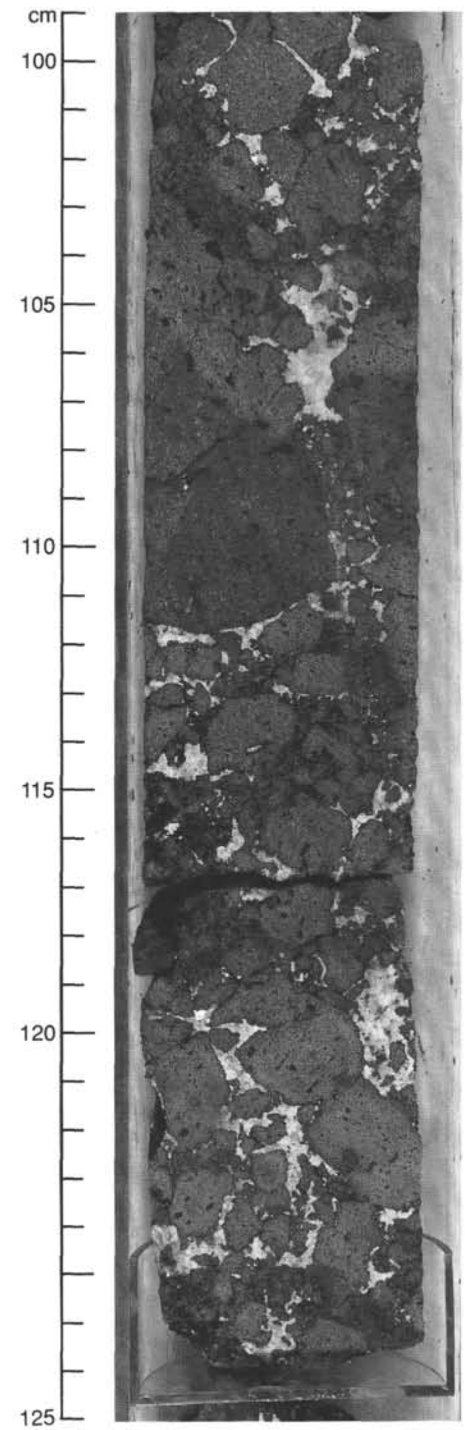

Figure 35. Basaltic breccia of Subunit 3B. Matrix is composed of white zeolite and dark green clays. Alteration rinds can be seen on some larger clasts.

Unit II (123–239.9 mbsf) is mainly diatomaceous ooze. All of the physical parameters we measured are remarkably uniform with depth and exhibit low variability. The mean value of bulk density, 1.43 g/cm^3, is the lowest measured in the entire sedimentary section.

Unit III (239.9–325 mbsf) sediments are a mixture of silt, silty clay, and diatomaceous ooze. The physical properties have about the same mean value as Unit II but variability with depth

Table 10. Whole rock and trace element chemistry of basement samples from Hole 795B as determined by X-ray fluorescence. Mg# refers to molecular Mg/(Mg + Fe^{2+}), where Fe^{2+} = Fe^{total} × 0.9. (Nb/Zr)n represents the chondrite-normalized ratio of these elements (Sun et al., 1979).

Hole	795B	795B	795B	795B	795B	795B	795B	795B	795B	795B	795B	795B	795B	795B
Core, section	34R-1	35R-1	36R-2	37R-1	37R-1	38R-1	38R-2	38R-4	38R-5	39R-1	39R-1	40R-1	40R-2	41R-1
Interval (cm)	121–123	95–97	49–51	62–64	105–107	23–25	51–53	99–100	4–6	9–11	131–133	15–17	123–125	107–109
Unit	1	1	3A	3A	3A	3A	3A	3A	3A	3A	3A	3B	3B	3B
SiO_2	54.50	53.84	50.89	50.32	51.04	50.51	50.86	50.49	50.01	51.46	50.60	52.13	54.82	51.97
TiO_2	0.99	1.01	0.96	0.92	0.99	1.00	0.98	0.90	0.95	0.99	0.92	0.84	0.93	0.83
Al_2O_3	21.16	21.34	19.36	19.09	19.58	19.25	19.38	19.07	19.06	19.15	18.90	17.06	17.79	17.13
FeO	6.75	6.21	7.19	7.30	7.00	7.76	7.46	7.81	7.59	6.99	7.74	8.56	6.96	8.43
MnO	0.14	0.14	0.23	0.17	0.23	0.24	0.17	0.18	0.24	0.22	0.14	0.14	0.17	0.16
MgO	4.08	3.72	6.35	6.76	5.28	6.01	6.04	5.91	6.10	6.02	7.70	8.32	5.83	8.04
CaO	7.21	7.56	9.79	9.76	10.27	9.84	9.95	10.40	10.62	9.73	9.46	8.67	8.92	9.00
Na_2O	3.95	3.93	3.13	3.35	3.46	3.05	3.14	3.35	2.77	3.45	2.76	2.69	3.36	2.68
K_2O	0.36	0.27	0.41	0.45	0.54	0.49	0.44	0.52	0.30	0.30	0.28	0.23	0.22	0.27
P_2O_5	0.33	0.34	0.22	0.30	0.32	0.26	0.20	0.18	0.17	0.27	0.30	0.20	0.34	0.22
Total	99.47	98.36	98.53	98.42	98.71	98.41	98.62	98.81	97.81	98.58	98.80	98.84	99.34	98.73
LOI	4.75	5.99	4.17	4.56	3.46	2.84	3.41	4.69	2.84	3.04	4.82	5.88	3.49	5.50
Nb	7.7	8.2	3.4	2.4	3.1	3.7	3.3	2.9	2.8	2.9	3.4	3.2	2.8	2.6
Zr	159	162	65	63	68	69	69	64	67	67	62	57	63	56
Y	29.5	40.5	19.5	23.9	26.6	20.4	18.3	18.0	19.7	22.1	37.7	22.9	27.5	21.9
Sr	336	343	249	296	259	259	246	240	243	243	226	231	223	212
Rb	5.1	2.7	7.3	7.6	13.3	11.3	10.9	11.4	5.6	4.1	2.4	3.2	5.3	5.6
Zn	98	105	96	81	103	91	87	74	76	98	99	89	91	99
Cu	8	6	49	48	48	51	53	52	61	58	51	53	43	48
Ni	5	3	32	31	26	26	29	28	31	29	28	31	24	32
Cr	ND	ND	15	24	23	25	24	18	23	25	16	16	19	17
V	103	93	304	292	318	324	312	280	298	296	284	258	225	227
Ce	30	39	16	18	19	16	17	16	13	19	29	21	27	16
Ba	89	98	79	114	84	79	64	59	60	53	46	47	—	52
Mg#	0.545	0.543	0.636	0.647	0.599	0.605	0.616	0.600	0.614	0.630	0.663	0.658	0.624	0.654
(Nb/Zr)n	0.69	0.72	0.74	0.54	0.65	0.76	0.69	0.65	0.60	0.61	0.78	0.80	0.64	0.66

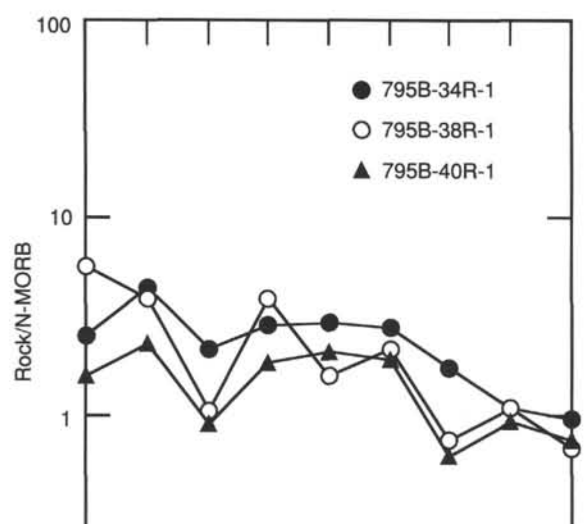

Figure 36. Multielement plot of selected samples representing Unit 1 and Subunits 3A and 3B, normalized to N-type MORB. Normalization factors from Pearce et al. (1981), with the order of elements from Sun et al. (1979).

is slightly greater due to the varying content of silt, clay, and diatoms.

The most remarkable feature of the section from the seafloor to 325 mbsf (Units I, II, and III) is the uniformity of all parameters that depend on water content. The profile at Site 795 is similar to that at Site 794 and suggests that there is virtually no consolidation of the sediments with depth of burial over this interval. As we proposed for the Site 794 observations, this behavior is attributable to the extraordinary strength of sediments whose framework is made up predominantly of diatoms. Ostensibly, it can support the lithostatic load to a depth of 325 m (about 143,000 kg/m^2) with very little compression. The great compressive strength of diatom oozes has been demonstrated by laboratory consolidation tests (Lee, 1973).

The boundary between Unit III and IV at 325 mbsf is the transition from opal-A to opal-CT. All of the measured physical properties, with the exception of grain density, show an abrupt and relatively large change at this boundary. Bulk density and thermal conductivity increase and there are complementary decreases in porosity and water content. The velocity measurements on discrete samples are too sparse across this transition to define the variation.

Unit IV (325–665 mbsf) is claystone with porcellanite zones and occasional dolomite concretions. The variability of all properties in Unit IV is greater than in the two overlying units. Some of the values that appear as outliers in the plots of Figures 37–43 were made on carbonate concretions.

The velocity measurements define a zone of significantly higher values between 380 and 440 mbsf (Fig. 39). Thermal conductivity and bulk density also show elevated values in this zone, which is composed of siliceous silty claystone and porcellanite with greater hardness than other sediments in the section. The formation of porcellanite has apparently given the sediments higher elastic moduli.

The transition from opal-CT to quartz occurs at about 470 mbsf. From this depth to the base of Unit IV the physical properties show a nearly linear variation with depth as result of increasing compaction. The gradients of the various parameters are given in Table 15. The gradient in the bulk density is 0.14 g/cm^3 per 100 m, and the gradient in acoustic velocity measured

Table 11. Summary of Site 795 physical properties data.

Core, section, interval (cm)	Depth (mbsf)	Density: Wet bulk (g/cm³)	Density: Dry bulk (g/cm³)	Density: Grain (g/cm³)	Porosity (%)	Water content (%)	Void ratio	Water ratio	Velocity: A	Velocity: B[a]	Velocity: C	Thermal conductivity (W/m · K)	Formation factors: H	Formation factors: V	Formation factors: Mean	Anisotropy
127-795A-																
1H-1, 116–118	1.16	1.42	0.41	2.63	98.4	71.1	61.50	2.46		1518		0.679				
1H-2, 100–102	2.50	1.58	0.63	2.54	93.2	60.4	13.71	1.53		1507		0.871	1.67	1.60	1.63	0.98
1H-3, 111–113	4.11	1.58	0.69	2.52	86.9	56.5	6.63	1.30		1509		0.757	1.52	1.59	1.55	1.02
1H-4, 98–100	5.48	1.58	0.68	2.50	87.7	56.7	7.13	1.31		1507		0.826	2.50	2.68	2.59	1.04
1H-5, 62–64	6.62	1.42	0.58	2.49	81.4	58.9	4.38	1.43		1524						
1H-5, 100–102	7.00									1513		0.853	1.84	1.89	1.86	1.01
1H-6, 100–102	8.50	1.70	1.01	2.65	67.5	40.6	2.08	0.68		1516		1.026	2.20	2.24	2.22	1.01
2H-1, 100–102	10.30	1.44	0.64	2.66	78.6	55.8	3.67	1.26		1447		0.854	1.72	1.72	1.72	1.00
2H-2, 100–102	11.80	1.33	0.42	2.51	88.3	68.2	7.55	2.14		1522		0.815	1.94	2.01	1.97	1.02
2H-3, 100–102	13.30	1.51	0.71	2.61	78.0	53.1	3.55	1.13		1513		0.852	2.05	2.12	2.08	1.02
2H-4, 98–100	14.78	1.44	0.63	2.58	79.2	56.4	3.81	1.29		1523		0.922	1.87	1.97	1.92	1.03
2H-5, 100–102	16.30	1.53	0.75	2.66	76.1	50.9	3.18	1.04		1520		0.968	2.18	2.21	2.19	1.01
2H-6, 100–102	17.80	1.38	0.49	2.54	86.3	64.2	6.30	1.79		1523		0.843	1.80	1.93	1.86	1.04
2H-7, 50–52	18.80	1.61	0.86	2.73	72.8	46.5	2.68	0.87								
3H-1, 100–102	19.80	1.39	0.53	2.52	84.1	61.8	5.29	1.62		1515		0.807	1.76	1.84	1.80	1.02
3H-2, 100–102	21.30	1.45	0.63	2.65	80.7	56.9	4.18	1.32		1504		0.866	1.72	1.88	1.80	1.05
3H-3, 100–102	22.80	1.40	0.53	2.55	85.5	62.5	5.90	1.67		1513		0.880	1.72	1.84	1.78	1.03
3H-4, 100–102	24.30	1.36	0.44	2.82	89.6	67.4	8.67	2.07		1513		0.833	1.66	1.75	1.70	1.03
3H-5, 100–102	25.80	1.46	0.62	2.68	81.9	57.3	4.52	1.34		1509		0.903	1.93	2.03	1.98	1.03
3H-6, 100–102	27.30	1.44	0.58	2.25	83.9	59.8	5.21	1.49		1523		0.812	1.90	1.88	1.89	0.99
4H-1, 93–95	29.23	1.64	0.92	2.79	70.1	43.8	2.34	0.78		1508		0.916	2.36	2.38	2.37	1.00
4H-2, 93–95	30.73	1.59	0.85	2.86	72.6	46.7	2.65	0.88		1515		0.991	1.77	1.77	1.77	1.00
4H-3, 94–96	32.24	1.53	0.73	2.65	77.6	52.0	3.46	1.08		1508		0.866	2.16	2.14	2.15	1.00
4H-4, 91–93	33.71	1.55	0.78	2.73	75.1	49.7	3.02	0.99		1517		0.891	2.30	2.47	2.38	1.04
4H-5, 93–95	35.23	1.47	0.64	2.61	80.9	56.5	4.24	1.30		1511		0.813	1.92	2.43	2.16	1.13
4H-6, 93–95	36.73	1.34	0.43	2.53	89.5	68.2	8.52	2.14		1518		0.830	2.04	2.14	2.09	1.02
4H-7, 40–42	37.70									1512			1.85	1.89	1.87	1.01
4H-7, 50–52	37.80	1.46	0.59	2.57	84.4	59.3	5.41	1.46		1516		0.883				
5H-1, 99–101	38.79	1.49	0.66	2.74	80.7	55.5	4.18	1.25				0.904	1.91	2.01	1.96	1.03
5H-2, 100–102	40.30	1.49	0.70	2.67	77.6	53.3	3.46	1.14				0.827	2.58	2.77	2.67	1.04
5H-3, 100–102	41.80	1.48	0.68	2.58	78.1	53.9	3.57	1.17		1531		0.928	2.47	2.54	2.50	1.01
5H-4, 100–102	43.30	1.50	0.70	2.48	77.8	53.3	3.50	1.14		1536		0.867	2.70	2.63	2.66	0.99
5H-5, 100–102	44.80	1.52	0.75	2.55	75.5	50.9	3.08	1.04		1538		0.812	2.74	2.72	2.73	1
5H-6, 100–102	46.30	1.44	0.61	2.58	80.5	57.4	4.13	1.35		1526		0.816	2.29	2.26	2.27	0.99
5H-7, 19–21	46.99	1.54	0.79	2.49	73.1	48.6	2.72	0.95		1587			3.36	3.37	3.36	1
6H-1, 100–102	48.30	1.43	0.58	2.85	82.9	59.5	4.85	1.47				0.820	1.85	1.94	1.89	1.02
6H-2, 100–102	49.80	1.42	0.60	2.44	80.1	57.6	4.03	1.36				0.815	2.02	2.94	2.44	1.21
6H-3, 100–102	51.30	1.57	0.81	2.79	74.4	48.4	2.91	0.94		1546		0.971	2.19	2.21	2.2	1
6H-4, 100–102	52.80	1.37	0.52	2.40	83.5	62.4	5.06	1.66		1530		0.803				
6H-5, 100–102	54.30	1.54	0.77	2.66	75.9	50.3	3.15	1.01		1524		0.990	2.57	2.49	2.53	0.98
6H-6, 100–102	55.80	1.54	0.79	2.60	73.8	49.0	2.82	0.96		1531		0.814	1.36	1.36	1.36	1
6H-7, 20–22	56.50	1.56	0.79	2.61	75.1	49.3	3.02	0.97		1532						
6H-7, 30–32	56.60									1531			2.23	2.20	2.21	0.99
6H-7, 40–42	56.70									1527		0.869				
7H-1, 100–102	57.80	1.49	0.71	2.65	76.4	52.4	3.24	1.10		1521		0.982	2.07	2.06	2.06	1
7H-2, 100–102	59.30	1.41	0.53	2.90	85.4	62.2	5.85	1.65		1510		0.827	1.84	1.90	1.87	1.02
7H-3, 100–102	60.80	1.36	0.47	2.55	86.6	65.1	6.46	1.87		1508		0.773	1.79	1.82	1.80	1.01
7H-4, 80–82	62.10									1503			1.88	2	1.94	1.03
7H-4, 100–102	62.30	1.48	0.69	2.57	76.7	53.1	3.29	1.13		1506		0.937				
7H-5, 100–102	63.80	1.27	0.35	2.14	90.3	72.8	9.31	2.68		1553		0.699	1.65	1.73	1.69	1.02
7H-6, 100–102	65.30	1.43	0.60	2.48	81.4	58.4	4.38	1.40		1514		0.901	2.03	2.31	2.17	1.07
7H-7, 20–22	66.00	1.42	0.57	2.69	83.1	60.0	4.92	1.50								
8H-1, 100–102	67.30	1.54	0.74	2.80	77.4	51.6	3.42	1.07		1496		0.917	2.01	2.04	2.02	1.01
8H-2, 100–102	68.80	1.42	0.56	2.73	84.0	60.5	5.25	1.53		1509		0.815	1.86	1.95	1.9	1.02
8H-3, 100–102	70.30	1.43	0.58	2.86	83.2	59.5	4.95	1.47		1510		0.811	1.91	1.94	1.92	1.01
8H-4, 100–102	71.80	1.49	0.69	2.67	77.9	53.7	3.52	1.16		1511		0.940	2.00	1.97	1.98	0.99
8H-5, 100–102	73.30	1.46	0.64	2.52	80.4	56.4	4.10	1.29		1538		0.893	2.35	3.36	2.81	1.2
8H-6, 100–102	74.80	1.43	0.59	2.63	81.9	58.6	4.28	1.41		1518		0.844	2.27	2.81	2.53	1.11
8H-7, 20–22	75.50	1.51								1517						
8H-7, 50–52	75.80									1520		0.937				
9H-1, 100–102	76.80	1.42	0.59	2.67	81.3	58.6	4.35	1.42		1527		0.877	1.81	1.86	1.83	1.01
9H-2, 100–102	78.30	1.43	0.58	2.76	82.7	59.2	4.80	1.45		1518		0.858	2.00	2.07	2.03	1.02
9H-3, 100–102	79.80	1.46	0.63	2.64	81.1	56.9	4.29	1.32		1518		0.793	2.11	2.18	2.14	1.02
9H-4, 100–102	81.30	1.54	0.76	2.69	75.8	50.4	3.13	1.02		1517		0.889	2.43	2.52	2.47	1.02
9H-5, 100–102	82.80	1.49	0.68	2.65	79.4	54.7	3.85	1.21		1519		0.896	2.10	2.15	2.12	1.01
9H-6, 100–102	84.30	1.53	0.75	2.86	76.0	50.9	3.17	1.04		1523		0.991	2.34	2.59	2.46	1.05
9H-7, 50–52	85.30	1.59	0.86	2.62	71.3	45.9	2.48	0.85		1528		1.112				
10H-1, 100–102	86.30	1.45	0.64	2.59	79.3	56.1	3.83	1.28				0.843	1.97	1.99	1.98	1.01
10H-2, 50–52	87.30	1.55	0.78	2.74	75.2	49.9	3.03	1.00				0.985	2.16	2.22	2.19	1.01
11H-1, 100–102	95.80	1.44	0.63	2.58	79.4	56.5	3.85	1.30		1511		0.864	2.09	2.22	2.15	1.03
11H-2, 100–102	97.30	1.45	0.60	2.83	83.2	58.9	4.95	1.43		1505		0.818	1.89	1.91	1.9	1.01
11H-3, 100–102	98.80	1.45	0.62	2.72	81.1	57.3	4.28	1.34		1513		0.829	2.07	2.11	2.09	1.01
11H-4, 100–102	100.30	1.43	0.57	2.78	83.4	59.9	5.02	1.49		1505		0.812	1.97	2.08	2.02	1.03
11H-5, 100–102	101.80	1.44	0.60	2.63	81.7	58.1	4.46	1.39		1517		0.920	2.01	2.06	2.03	1.01
11H-6, 100–102	103.30	1.58	0.72	2.73	84.2	54.4	5.33	1.19		1520		0.924	2.20	2.12	2.16	0.98
11H-7, 50–52	104.30	1.50	0.66	2.60	81.3	55.7	4.35	1.26		1516		0.915				
12H-1, 100–102	105.30	1.53	0.69	2.68	81.5	54.8	4.41	1.21				0.859	2.35	2.38	2.36	1.01
12H-2, 100–102	106.80	1.48	0.65	2.73	81.1	56.0	4.29	1.27		1528		0.929	2.48	2.54	2.51	1.01
12H-3, 100–102	108.30	1.47	0.58	2.72	87.4	60.8	6.94	1.55				0.820	2.06	2.19	2.12	1.03
12H-4, 100–102	109.80	1.53	0.71	2.55	80.2	53.7	4.05	1.16		1531		0.857	2.34	2.54	2.44	1.04
12H-5, 100–102	111.30	1.53	0.69	2.69	81.6	54.7	4.43	1.21		1522		0.901	2.16	2.29	2.22	1.03
12H-6, 100–102	112.80	1.57	0.71	2.79	83.9	54.7	5.21	1.21				0.850	2.25	2.42	2.33	1.04
12H-7, 40–42	113.70									1545		0.921				

Table 11 (continued).

Core, section, interval (cm)	Depth (mbsf)	Density: Wet bulk (g/cm^3)	Density: Dry bulk (g/cm^3)	Density: Grain (g/cm^3)	Porosity (%)	Water content (%)	Void ratio	Water ratio	Velocity: A	Velocity: B[a]	Velocity: C	Thermal conductivity (W/m · K)	Formation factors: H	Formation factors: V	Formation factors: Mean	Anisotropy
127-795A- (Cont.)																
13H-1, 100–102	114.80	1.59	0.73	2.80	83.8	54.0	5.17	1.17		1536		0.851	2.42	2.42	2.42	1.00
13H-2, 100–102	116.30	1.53	0.71	2.57	80.1	53.5	4.03	1.15		1530		0.854	2.04	2.13	2.08	1.02
13H-3, 100–102	117.80	1.48	0.63	2.69	82.6	57.4	4.75	1.35		1532		0.872	2.52	3.69	3.05	1.21
13H-4, 100–102	119.30	1.45	0.64	2.55	79.2	56.0	3.81	1.27		1541		0.918	2.11	2.34	2.22	1.05
13H-5, 100–102	120.80	1.41	0.59	2.54	79.9	57.9	3.98	1.38		1542		0.867	2.23	2.31	2.27	1.02
13H-6, 100–102	122.30	1.45	0.64	2.53	79.4	56.1	3.85	1.28		1540		0.845	2.08	2.25	2.16	1.04
13H-7, 45–47	123.25	1.46	0.66	2.49	78.0	54.7	3.55	1.21		1482						
14H-1, 13–15	123.43	1.31	0.41	2.64	88.4	69.0	7.62	2.23								
14H-2, 99–101	125.79	1.45	0.62	2.61	80.8	56.9	4.21	1.32		1464		0.833	2.39	2.56	2.47	1.03
14H-3, 99–101	127.29	1.48	0.66	2.49	80.1	55.5	4.03	1.25		1541		0.855	2.54	3.25	2.87	1.13
14H-4, 99–101	128.79	1.43	0.57	2.46	83.3	59.8	4.98	1.49		1472			1.90	2.01	1.95	1.03
14H-5, 99–101	130.29	1.42	0.57	2.52	82.3	59.5	4.65	1.47		1533		0.812	1.87	1.92	1.89	1.01
14H-6, 99–101	131.79	1.41	0.58	2.54	81.0	58.8	4.26	1.43		1532		0.843	1.99	2.11	2.05	1.03
14H-7, 30–32	132.60	1.42	0.59	2.46	80.7	58.2	4.17	1.39		1538			1.94	2.1	2.02	1.04
15H-1, 100–102	133.80	1.52	0.74	2.47	76.1	51.2	3.18	1.05		1542		0.887	2.34	2.34	2.34	1
15H-2, 100–102	135.30	1.45	0.63	2.54	80.5	56.8	4.13	1.31		1533		0.866	1.94	2.05	1.99	1.03
15H-3, 100–102	136.80	1.50	0.67	2.49	80.6	55.2	4.15	1.23		1542		0.860	2.33	2.46	2.39	1.03
15H-4, 100–102	138.30	1.37	0.51	2.46	83.8	62.6	5.17	1.67		1537		0.748	2.35	2.64	2.49	1.06
15H-5, 100–102	139.80	1.47	0.67	2.54	78.0	54.2	3.55	1.18		1551		0.891	2.72	2.79	2.75	1.01
15H-6, 100–102	141.30	1.44	0.61	2.62	80.9	57.6	4.24	1.36		1538		0.841	2.25	2.58	2.41	1.07
15H-7, 50–52	142.30	1.42	0.60	2.50	80.2	57.8	4.05	1.37		1556			2.44	2.64	2.54	1.04
16H-1, 100–102	143.30	1.38	0.53	2.36	82.7	61.4	4.78	1.59		1545		0.827	2.17	2.25	2.21	1.02
16H-2, 100–102	144.80	1.43	0.62	2.42	79.6	56.9	3.90	1.32		1548		0.845	2.23	2.25	2.24	1.00
16H-3, 100–102	146.30	1.45	0.60	2.53	82.5	58.3	4.71	1.40		1541		0.837	2.18	2.24	2.21	1.01
16H-4, 100–102	147.80	1.42	0.58	2.26	81.9	59.2	4.52	1.45				0.828	2.38	2.54	2.46	1.03
18H-1, 100–102	153.90	1.39	0.55	2.47	81.8	60.2	4.49	1.51				0.846	1.81	1.84	1.82	1.01
18H-2, 100–102	155.40	1.41	0.57	2.58	81.8	59.3	4.49	1.46				0.790	2.05	2.19	2.12	1.03
18H-3, 100–102	156.90	1.39	0.53	2.57	84.2	61.9	5.33	1.62		1543			1.78	1.77	1.77	1.00
18H-4, 100–102	158.40	1.41	0.57	2.48	81.7	59.5	4.46	1.47		1545		0.848	1.87	2.04	1.95	1.04
18H-5, 100–102	159.90	1.42	0.59	2.53	80.7	58.2	4.18	1.39		1539		0.893	1.87	1.90	1.88	1.01
18H-6, 100–102	161.40	1.45	0.64	2.55	79.1	55.8	3.78	1.26		1538		0.922	1.98	2.10	2.04	1.03
18H-7, 20–22	162.10	1.48	0.67	2.62	78.9	54.5	3.74	1.20					2.05	2.06	2.05	1.00
19H-1, 100–102	163.40	1.45	0.62	2.61	81.2	57.5	4.32	1.35		1542		0.824	2.13	2.29	2.21	1.04
19H-2, 100–102	164.90	1.45	0.62	2.47	81.6	57.5	4.43	1.35		1565		0.773	2.55	2.92	2.73	1.07
19H-3, 100–102	166.40	1.44	0.59	2.47	82.8	58.8	4.81	1.43		1543		0.760	2.12	2.26	2.19	1.03
19H-4, 100–102	167.90	1.44	0.58	2.43	84.0	59.6	5.25	1.48		1542		0.851	2.10	2.17	2.13	1.02
19H-5, 100–102	169.40	1.55	0.70	2.58	83.2	55.2	4.95	1.23		1547		0.895	2.17	2.31	2.24	1.03
19H-6, 100–102	170.90	1.51	0.69	2.65	80.4	54.5	4.10	1.20				0.885	2.28	2.54	2.41	1.06
19H-7, 41–43	171.81	1.52	0.67	2.79	82.7	55.8	4.78	1.26					2.58	2.85	2.71	1.05
21X-1, 100–102	182.60	1.42	0.60	2.46	80.6	58.0	4.15	1.38				0.832	2.35	2.61	2.48	1.05
21X-2, 100–102	184.10	1.41	0.57	2.45	81.8	59.3	4.49	1.46				0.744	2.14	2.14	2.14	1.00
21X-3, 100–102	185.60	1.39	0.55	2.32	81.8	60.3	4.49	1.52				0.784	2.17	2.24	2.20	1.02
21X-4, 100–102	187.10	1.39	0.54	2.40	83.3	61.3	4.99	1.58				0.779	2.36	2.74	2.54	1.08
21X-5, 100–102	188.60	1.36	0.50	2.26	83.8	63.1	5.17	1.71				0.770	2.19	2.24	2.21	1.01
21X-6, 100–102	190.10	1.40	0.55	2.54	82.7	60.6	4.78	1.54				0.890	2.06	2.19	2.12	1.03
21X-7, 20–22	190.80	1.43	0.57	2.65	83.8	60.0	5.17	1.50								
22X-1, 80–82	192.00	1.38	0.54	2.44	82.3	61.1	4.65	1.57					2.01	2.65	2.31	1.15
22X-1, 100–102	192.20											0.705				
22X-2, 100–102	193.70	1.42	0.57	2.57	83.5	60.2	5.06	1.51				0.788	2.62	2.41	2.51	0.96
22X-3, 100–102	195.20	1.43	0.60	2.47	81.0	58.0	4.26	1.38				0.696	2.34	2.49	2.41	1.03
22X-4, 100–102	196.70	1.40	0.57	2.47	80.7	59.0	4.18	1.44				0.747	2.13	2.25	2.19	1.03
22X-5, 100–102	198.20	1.44	0.59	2.60	83.5	59.3	5.06	1.46				0.795	2.24	2.55	2.39	1.07
22X-6, 110–112	199.80	1.41	0.57	2.54	81.7	59.5	4.46	1.47				0.778	2.11	2.32	2.21	1.05
22X-7, 25–27	200.45											0.815				
25X-1, 100–102	221.40	1.38	0.55	2.55	81.8	60.5	4.49	1.53				0.747	2.44	2.26	2.35	0.96
25X-2, 100–102	222.90	1.39	0.57	2.50	79.9	59.0	3.98	1.44				0.771	2.56	2.67	2.61	1.02
25X-3, 100–102	224.40	1.45	0.63	2.63	80.0	56.6	4.00	1.30				0.781	2.37	2.53	2.45	1.03
25X-5, 100–102	226.31	1.44	0.61	2.58	81.1	57.6	4.29	1.36				0.783	2.51	2.77	2.64	1.05
25X-6, 100–102	227.81	1.39	0.56	2.49	81.2	59.6	4.32	1.48				0.754	2	2.35	2.17	1.08
25X-7, 100–102	229.31	1.44	0.63	2.47	79.3	56.3	3.83	1.29				0.837	2.29	2.38	2.33	1.02
26X-1, 100–102	231.10	1.44	0.64	2.49	78.2	55.7	3.59	1.26				0.764	2.55	2.91	2.72	1.07
26X-2, 100–102	232.60	1.38	0.56	2.46	79.8	59.3	3.95	1.46				1.028	2.35	2.3	2.32	0.99
26X-3, 100–102	234.10	1.41	0.57	2.65	81.8	59.3	4.49	1.46				0.740	2.23	1.92	2.07	0.93
26X-4, 100–102	235.60	1.39	0.57	2.39	80.4	59.3	4.10	1.46				0.666				
26X-5, 100–102	237.10	1.39	0.56	2.43	80.9	59.7	4.24	1.48				0.642	2.27	2.39	2.33	1.03
26X-6, 100–102	238.60	1.46	0.64	2.51	80.4	56.3	4.10	1.29				0.883	2.52	2.61	2.56	1.02
26X-7, 22–24	239.32	1.45	0.60	2.66	82.8	58.3	4.81	1.40								
27X-1, 100–102	240.90	1.49	0.66	2.69	81.1	55.7	4.29	1.26				0.840	2.8	2.68	2.74	0.98
27X-2, 100–102	242.40	1.43	0.61	2.42	79.8	57.2	3.95	1.34				0.824	2.17	2.16	2.16	1
27X-3, 100–102	243.90	1.46	0.66	2.38	77.8	54.5	3.50	1.20				0.975				
27X-4, 100–102	245.40	1.39	0.56	2.48	81.4	59.9	4.38	1.49				0.814				
27X-5, 110–112	247.00	1.44	0.64	2.49	78.1	55.6	3.57	1.25				0.905	2.14	2.33	2.23	1.04
27X-6, 100–102	248.40	1.52	0.69	2.80	81.7	54.9	4.46	1.22				0.858	2.28	2.39	2.33	1.02
27X-7, 28–30	249.18	1.49	0.66	2.50	81.1	55.6	4.29	1.25								
29X-2, 100–102	262.00	1.35	0.50	2.40	83.3	63.1	4.99	1.71				0.798				
29X-3, 100–102	263.50	1.51	0.69	2.34	79.8	54.1	3.95	1.18				0.795				
30X-1, 100–102	270.30	1.50	0.71	2.50	77.2	52.7	3.39	1.11				0.844				
30X-2, 100–102	271.80	1.48	0.63	2.76	83.2	57.4	4.95	1.35				0.851				
30X-3, 100–102	273.30	1.47	0.66	2.49	79.0	55.2	3.76	1.23				0.816				
30X-4, 100–102	274.80	1.45	0.62	2.38	80.5	57.0	4.13	1.33				0.765				
30X-5, 50–52	275.80											0.802				
30X-5, 71–73	276.01	1.45	0.61	2.53	81.4	57.6	4.38	1.36								
31X-1, 99–101	280.09	1.45	0.64	2.51	78.6	55.6	3.67	1.25				0.848				
31X-2, 99–101	281.59	1.43	0.62	2.33	79.4	56.7	3.85	1.31				0.784				
31X-3, 99–101	283.09	1.50	0.69	2.52	79.0	54.0	3.76	1.17				0.793				

Table 11 (continued).

Core, section, interval (cm)	Depth (mbsf)	Density			Porosity (%)	Water content (%)	Void ratio	Water ratio	Velocity			Thermal conductivity (W/m · K)	Formation factors			Anisotropy
		Wet bulk (g/cm³)	Dry bulk (g/cm³)	Grain (g/cm³)					A	B[a]	C		H	V	Mean	
127-795A- (Cont.)																
31X-4, 99-101	284.59	1.57	0.78	2.58	77.0	50.4	3.35	1.02				0.800				
31X-5, 99-101	286.09	1.50	0.73	2.56	75.2	51.3	3.03	1.05				0.797				
34X-1, 100-102	308.90	1.46	0.64	2.47	79.8	56.1	3.95	1.28					2.25	2.35	2.3	1.02
34X-2, 100-102	310.40	1.49	0.66	2.60	81.6	56.0	4.43	1.27				0.830	2.23	2.25	2.24	1
34X-3, 100-102	311.90	1.51	0.70	2.45	78.9	53.6	3.74	1.16				0.845	2.29	2.32	2.3	1.01
34X-3, 144-146	312.34	1.52	0.76	2.57	73.6	49.7	2.79	0.99	1604		1604					
34X-4, 100-102	313.40	1.48	0.67	2.42	78.8	54.6	3.72	1.20				0.848	2.36	2.41	2.38	1.01
34X-5, 100-102	314.90	1.49	0.65	2.52	82.2	56.7	4.62	1.31				0.830	2.37	2.41	2.39	1.01
34X-6, 100-102	316.40	1.51	0.69	2.57	79.9	54.4	3.98	1.19				0.823				
34X-7, 39-41	317.29	1.53	0.77	2.56	74.0	49.7	2.85	0.99					2.47	3.04	2.74	1.11
35X-1, 9-11	317.69	1.49	0.73	2.42	74.0	51.0	2.85	1.04	1620	1601	1601					
35X-1, 99-101	318.59	1.46	0.68	2.28	76.3	53.4	3.22	1.15				0.804				
35X-2, 99-101	320.09	1.45	0.65	2.44	78.4	55.4	3.63	1.24				0.740	2.37	2.48	2.42	1.02
35X-3, 99-101	321.59	1.40	0.58	2.34	80.0	58.4	4.00	1.40				0.802	2.25	2.34	2.29	1.02
35X-4, 99-101	323.09	1.48	0.70	2.42	76.5	52.9	3.26	1.12				0.820	2.4	2.42	2.41	1
35X-5, 99-101	324.59	1.42	0.56	2.43	83.5	60.3	5.06	1.52				0.785	2.05	2.27	2.16	1.05
35X-6, 13-15	325.23	2.14	1.86	2.24	27.6	13.2	0.38	0.15								
35X-6, 80-82	325.90												2.62	2.52	2.57	0.98
35X-6, 99-101	326.09	1.67	0.95	2.60	70.3	43.2	2.37	0.76	1.019							
36X-CC, 25-27	327.67	1.71	1.40	1.84	30.0	18.0	0.43	0.22			6770					
37X-1, 65-67	337.55											1.049				
37X-1, 99-101	337.89	1.72	1.11	2.45	59.5	35.4	1.47	0.55				0.949				
37X-1, 126-127	338.16	1.72	0.92	2.53	63.8	38.0	1.77	0.61								
38X-CC, 22-24	346.82	2.20	1.84	1.96	35.0	16.3	0.54	0.19	2559	2960	2688					
127-795B-																
1R-1, 86-88	366.06	2.95	2.82	2.86	12.7	4.4	0.15	0.05		6025						
1R-1, 90-94	366.10	1.66	0.95	2.44	68.9	42.6	2.22	0.74	1566		1756					
1R-2, 69-72	367.39	1.83	1.19	2.83	62.3	34.9	1.65	0.54		1588	1603					
1R-3, 8-10	368.28	1.85	1.32	2.45	51.6	28.6	1.07	0.40	1698		1911	1.174				
2R-1, 145-147	376.45	1.61	0.87	2.52	72.0	45.8	2.57	0.85	1686	1785	1812	0.979				
3R-1, 57-59	385.27	1.92	1.38	2.49	52.4	28.0	1.10	0.39	2085	2248	2254	1.253				
4R-1, 72-74	395.12	1.92	1.43	2.40	47.8	25.5	0.92	0.34	2211	2399	2357	1.152				
4R-1, 143-145	395.83								2831	2788	2749					
5R-1, 87-89	404.97	1.87	1.34	2.38	51.6	28.2	1.07	0.39	1970	2153	2129	1.323				
6R-1, 38-40	414.18	1.88	1.36	2.42	50.8	27.7	1.03	0.38	2174	2303	2881	1.213				
7R-1, 31-33	423.41	1.91	1.33	2.73	56.8	30.6	1.32	0.44								
8R-1, 112-114	433.92	1.91	1.42	2.40	47.5	25.5	0.90	0.34	2304	2420	2538	1.347				
9R-1, 104-106	443.44	1.90	1.33	2.57	55.2	29.8	1.23	0.42	1671			1.213				
9R-2, 93-95	444.83								1783							
9R-2, 111-113	445.01	1.96	1.45	2.44	50.1	26.1	1.00	0.35	2292	2292	2412	1.289				
10R-1, 137-139	453.37	1.77	1.17	2.54	58.9	34.0	1.43	0.52	2404	1847	2043	1.106				
10R-3, 120-122	456.20	1.74	1.13	2.50	59.3	34.9	1.46	0.54	1739	1831	1814	1.128				
10R-5, 41-43	458.41	1.94	1.36	2.59	56.3	29.8	1.29	0.42	1743	1830	1865	1.157				
11R-1, 97-99	462.67	1.79	1.20	2.48	57.7	33.0	1.36	0.49	1937	2015	2015	1.169				
11R-2, 81-83	464.01	1.79	1.16	2.47	61.7	35.3	1.61	0.55	1782	1816	1803	1.101				
11R-3, 120-122	465.90	1.97	1.45	2.62	50.5	26.3	1.02	0.36	1807	1914	1882	1.159				
12R-1, 105-107	472.45	2.05	1.50	2.73	53.3	26.6	1.14	0.36	1778	1908	1865	0.996				
12R-3, 96-98	475.36	2.04	1.55	2.68	48.2	24.2	0.93	0.32	1892	1987	1928	1.262				
13R-1, 86-88	481.86	2.11	1.60	2.58	50.2	24.3	1.01	0.32	1883	1991	2016	1.221				
13R-3, 64-66	484.64	1.87	1.31	2.65	54.8	30.1	1.21	0.43	1695	1814	1775					
14R-1, 64-66	491.34	1.96	1.41	2.78	53.3	27.8	1.14	0.39	1782	1874	1810	1.264				
14R-3, 127-129	494.97	1.96	1.35	2.67	59.2	31.0	1.45	0.45	1780	1852	1832					
15R-1, 18-20	500.18	1.99	1.45	2.71	52.3	26.9	1.10	0.37	1740	1816	1769	1.262				
15R-1, 30-32	500.30	2.19	1.61	2.52	57.0	26.6	1.32	0.36	1748	1803	1844					
16R-1, 30-32	510.00	2.02	1.46	2.65	54.3	27.5	1.19	0.38	1726	1871	1848	1.338				
16R-2, 26-28	511.46	1.98	1.41	2.62	55.6	28.8	1.25	0.41	1735	1833	1831	1.279				
17R-1, 94-96	520.34	2.09	1.59	2.66	49.2	24.1	0.97	0.32	1798	1913	2013	1.391				
17R-2, 25-27	521.15								1754	1845	1795					
17R-2, 48-50	521.38	2.20	1.63	2.51	55.9	26.1	1.27	0.35	1748	1812	1779	1.333				
18R-1, 100-102	530.10	2.05	1.53	2.83	50.4	25.2	1.02	0.34	1785	1858	1841					
18R-2, 101-103	531.61	2.09	1.65	2.66	42.5	20.8	0.74	0.26	1967	2113	2124					
18R-3, 49-52	532.59								1768	1847						
18R-3, 115-117	533.25	2.06	1.56	2.68	48.6	24.2	0.94	0.32	1854	1974	1950					
18R-4, 106-108	534.66	2.03	1.52	2.71	49.3	24.9	0.97	0.33	1843	1987	1940					
19R-1, 70-72	539.40	2.06	1.52	2.68	52.5	26.1	1.11	0.35	1740	1800	1759	1.406				
19R-1, 126-128	539.96								1866	1985	2001					
19R-2, 74-76	540.94	2.15	1.61	2.68	52.2	24.9	1.09	0.33	1776	1866	1853	1.352				
19R-3, 100-102	542.70	2.08	1.61	2.64	46.1	22.7	0.85	0.29	1844	2067	2054	1.367				
19R-4, 100-102	544.20	2.02	1.52	2.67	48.7	24.7	0.95	0.33	1873	1888	1882					
19R-5, 49-51	545.19	2.08	1.60	2.58	47.2	23.2	0.89	0.30								
20R-1, 65-67	549.05	2.08	1.59	2.72	47.8	23.5	0.92	0.31	1744	1848	1821	1.328				
20R-2, 10-12	550.00	2.07	1.59	2.62	47.1	23.3	0.89	0.30	1821	1933						
20R-3, 98-100	552.38	2.19	1.78	2.66	39.8	18.6	0.66	0.23	1961	2109	2122	1.434				
20R-4, 98-100	553.88	2.17	1.70	2.65	45.8	21.6	0.85	0.28	1856	1977	2055					
20R-5, 88-90	555.28	2.13	1.65	2.66	46.8	22.5	0.88	0.29	1858	2035	2096	1.472				
21R-2, 115-117	560.75	2.26	1.74	2.72	50.8	23.0	1.03	0.30	1808	1908	1901	1.403				
21R-3, 114-116	562.24	2.14	1.76	2.68	36.8	17.6	0.58	0.21	1859							
21R-5, 91-93	565.01	2.08	1.67	2.64	39.9	19.7	0.66	0.25	1804	1920	1923	1.435				
21R-6, 37-39	565.97	2.20	1.76	2.67	42.5	19.8	0.74	0.25		1824	1809	1.531				
22R-1, 38-40	568.08	2.09	1.65	2.64	43.0	21.1	0.76	0.27	1861	2014	1944	1.403				
22R-1, 120-122	568.90	1.78	1.14	2.55	62.8	36.1	1.69	0.57	1812	1922						
22R-2, 29-31	569.49	2.08	1.62	2.70	45.2	22.2	0.83	0.29	1861	1977	1927	1.404				

Table 11 (continued).

Core, section, interval (cm)	Depth (mbsf)	Density			Porosity (%)	Water content (%)	Void ratio	Water ratio	Velocity			Thermal conductivity (W/m · K)	Formation factors			Anisotropy
		Wet bulk (g/cm³)	Dry bulk (g/cm³)	Grain (g/cm³)					A	B[a]	C		H	V	Mean	
127-795B- (Cont.)																
23R-1, 111-113	578.51	2.06	1.61	2.66	43.7	21.8	0.78	0.28	1830	1993	1943					
23R-2, 145-147	580.35	2.00	1.50	2.67	48.6	24.9	0.94	0.33	1789	1905	1880	1.198				
23R-3, 89-91	581.29	2.08	1.63	2.63	43.8	21.6	0.78	0.28	1838	1913	1937					
23R-4, 74-76	582.64	2.16	1.74	2.73	41.0	19.4	0.69	0.24	1922	2033	2019	1.478				
24R-1, 11-13	587.11	2.12	1.67	2.73	44.2	21.4	0.79	0.27	1806	1936						
24R-3, 127-129	590.21	1.99	1.48	2.66	50.2	25.9	1.01	0.35	1775	1834	1809	1.365				
24R-5, 111-113	593.05	2.12	1.65	2.72	45.6	22.0	0.84	0.28	1820	1887	1916	1.458				
25R-1, 71-73	597.41	2.11	1.66	2.77	43.7	21.2	0.78	0.27	1843	1922	1900	1.443				
25R-3, 59-61	600.29	2.13	1.71	2.66	40.9	19.7	0.69	0.25	1936	2081	1961	1.584				
25R-5, 125-127	603.95	1.96	1.46	2.64	48.5	25.4	0.94	0.34	1794	1882	1878	1.494				
26R-2, 64-66	608.54	2.10	1.67	2.67	41.8	20.4	0.72	0.26	1931	2035	1942	1.534				
26R-4, 22-24	611.12	2.06	1.59	2.67	46.2	23.0	0.86	0.30	1841	1925	1877	1.478				
26R-6, 51-53	614.41	2.08	1.63	2.75	44.1	21.7	0.79	0.28	1832	1925	1920	1.409				
27R-1, 92-94	616.92	2.20	1.78	2.73	40.6	18.9	0.68	0.23	1944	2079		1.554				
27R-3, 139-141	620.39	2.14	1.70	2.65	43.2	20.6	0.76	0.26	1884	1968	1965	1.582				
27R-5, 37-39	622.37	2.13	1.70	2.72	42.4	20.4	0.74	0.26				1.300				
28R-1, 13-15	625.83	2.16	1.74	2.66	40.7	19.3	0.69	0.24	1871	1950	1954	1.549				
28R-3, 60-62	629.30	2.17	1.76	2.74	40.4	19.1	0.68	0.24	1779	1960	1905	1.553				
28R-5, 66-68	632.36	2.16	1.75	2.70	39.8	18.9	0.66	0.23	1915	1968	1982	1.595				
29R-1, 80-82	636.10	2.10	1.66	2.69	42.7	20.9	0.75	0.26	1869	1958	1897	1.438				
29R-3, 80-82	639.10	2.16	1.74	2.70	41.3	19.6	0.70	0.24								
29R-5, 11-13	641.41	2.18	1.75	2.65	41.9	19.7	0.72	0.25	1810	1977	1950	1.585				
30R-1, 52-54	645.42	2.16	1.72	2.69	43.2	20.4	0.76	0.26	1820	1936	1940	1.554				
30R-1, 122-124	646.12								1823	1975	1998					
30R-3, 135-137	649.25	2.16	1.71	2.71	43.4	20.6	0.77	0.26	1879	1974	1948	1.669				
30R-5, 35-37	651.25	2.18	1.74	2.68	42.6	20.0	0.74	0.25	1873	1980	1986	1.527				
31R-2, 133-135	657.33	2.22	1.82	2.66	39.5	18.2	0.65	0.22	1933	2070	2077	1.484				
31R-4, 33-35	659.33	2.23	1.80	2.69	41.7	19.2	0.71	0.24	1889	2045	1908	1.563				
32R-1, 85-87	665.05	2.17	1.74	2.65	41.7	19.6	0.71	0.24	1902	2030	1970					
32R-3, 84-86	668.04	2.34	1.78	2.66	55.2	24.1	1.23	0.32	1959	2120	2104	1.479				
33R-1, 47-49	674.37	2.18	1.75	2.55	42.3	19.9	0.73	0.25	2189	2353	2327	1.340				
33R-2, 92-94	676.32	2.09	1.61	2.60	46.7	23.0	0.88	0.30								
34R-1, 14-16	683.64	2.41	1.98	2.83	41.7	17.8	0.72	0.22	2396	2417	2418	1.180				
35R-1, 28-30	693.48	2.19	1.84	2.70	34.6	16.2	0.53	0.19			2566	1.189				
36R-1, 34-36	703.24	2.21	1.85	2.69	34.9	16.2	0.54	0.19			2452	1.218				
36R-2, 49-51	704.89	2.45	2.21	2.78	24.0	10.0	0.32	0.11			3528	1.255				
36R-2, 49-51	704.89										3605					
37R-1, 105-107	713.65	2.44	2.19	2.81	24.5	10.3	0.32	0.12			3475	1.308				
37R-1, 105-107	713.65										3758					
38R-1, 22-24	722.42	2.39	2.12	2.83	26.4	11.3	0.36	0.13			3374	1.265				
38R-2, 42-44	723.72	2.48	2.25	2.79	22.0	9.1	0.28	0.10			3658	[b]1.305				
38R-2, 42-43	723.72											[c]1.260				
38R-3, 47-49	725.27	2.46	2.21	2.82	24.6	10.2	0.33	0.11			3556	1.300				
38R-4, 100-102	727.22	2.54	2.32	2.83	21.4	8.6	0.27	0.09			3673	1.354				
38R-5, 3-5	727.47	2.53	2.33	2.81	19.8	8.0	0.25	0.09			3903					
39R-1, 9-11	731.99	2.44	2.2	2.77	23.1	9.7	0.30	0.11			3299	1.322				
39R-2, 22-24	733.62	2.37	2.12	2.71	24.8	10.7	0.33	0.12			3067					
40R-1, 49-51	742.09	2.19	1.81	2.67	36.7	17.1	0.58	0.21			2628	1.166				
40R-2, 117-119	744.27	2.35	2.07	2.76	27.7	12.0	0.38	0.14			3278	1.388				
41R-1, 20-22	751.50	2.45	2.22	2.70	22.2	9.3	0.29	0.10			3768	1.315				
41R-2, 28-30	753.01	2.30	1.99	2.99	30.0	13.3	0.43	0.15			2996	1.335				
41R-2, 28-30	753.01										3040					

[a] All velocities for APC cores are taken from the *P*-wave logger record.
[b] Reading taken perpendicular to bedding.
[c] Reading taken parallel to bedding.

normal to the bedding is 54 m/s per 100 m. The sediments in Unit IV become less siliceous with depth. As a consequence, the quartz is probably disseminated too sparsely through the sediment to form chert or to affect the elastic moduli as was observed above the opal-CT/quartz boundary.

Unit V (665–685 mbsf) is a tuff overlying a basaltic breccia. The basalts in the breccia are highly altered. Relatively few measurements were made in this unit. The *P*-wave velocity and thermal conductivity show large changes in this unit from those in Unit IV. The velocity increases with depth and the conductivity decreases.

Physical Properties of the Igneous Units

A 70 m section of basalt and basaltic breccia was cored at Hole 795B. The recovered rocks are highly altered and vesicular. The vesicles were either clay-filled or open. Open vesicles were frequently several millimeters in diameter and lined with zeolite crystals. Recovery was poor in these units and only 15 discrete measurements of physical properties were made. The mean values for the main physical properties for Unit 3, which makes up most of the igneous section cored, are given in Table 17. The mean grain density of 2.79 g/cm³ is slightly higher than the overlying claystone. The low bulk density of 2.41 g/cm³ is indicative of the high porosity of these rocks (20%–25%). The average acoustic velocity for the whole igneous section is 3.31 km/s. The scatter is very large as can be seen in Figure 39. Two measurements in a thin layer near the top of the igneous section have a very low mean of 2.50 km/s. The mean of the remainder of the igneous unit is 3.41 km/s; a typical value for altered and porous igneous rocks of basic composition.

The average value of thermal conductivity in the igneous section (1.2 W/m · K) is significantly lower than in the overlying claystones, even though the claystones have higher porosities (40% as opposed to 25%). Figure 44 shows the conductivity values plotted vs. porosity. The basement values (solid dots) are best fit by a solid component conductivity of 1.7 W/m · K, which is typical for basaltic rocks (e.g., Hyndman et al, 1977). On the other hand, Figure 44 suggests that the thermal conduc-

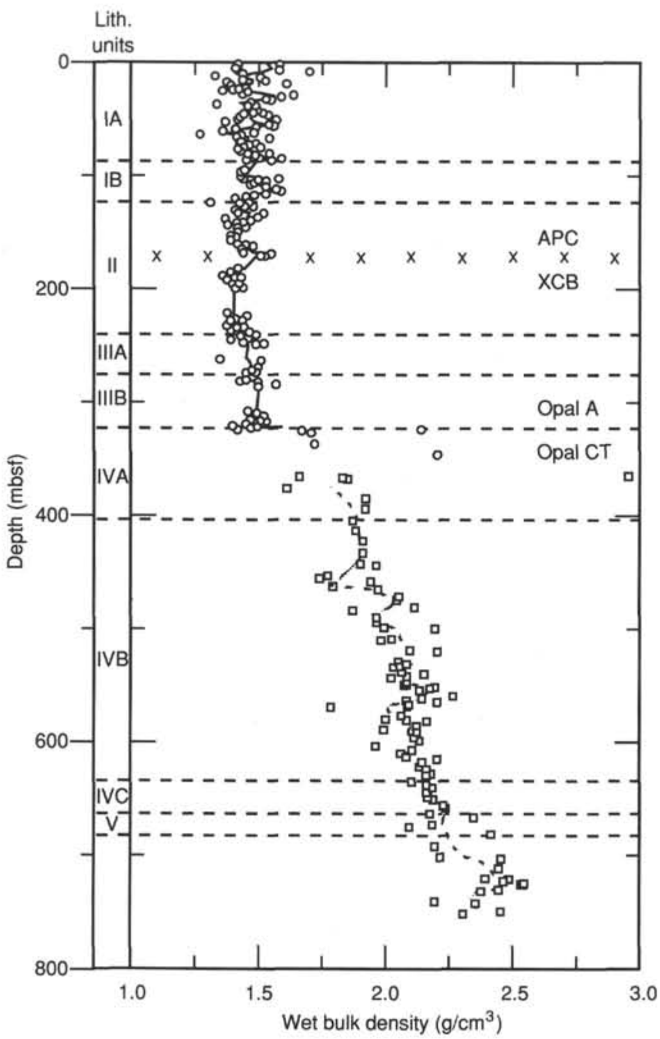

Figure 37. Wet bulk density vs. depth for Holes 795A (circles and solid curve) and 795B (squares and dashed curve). The curves are five-point tapered running means. The boundaries of lithostratigraphic units cited in the text are shown by dashed lines.

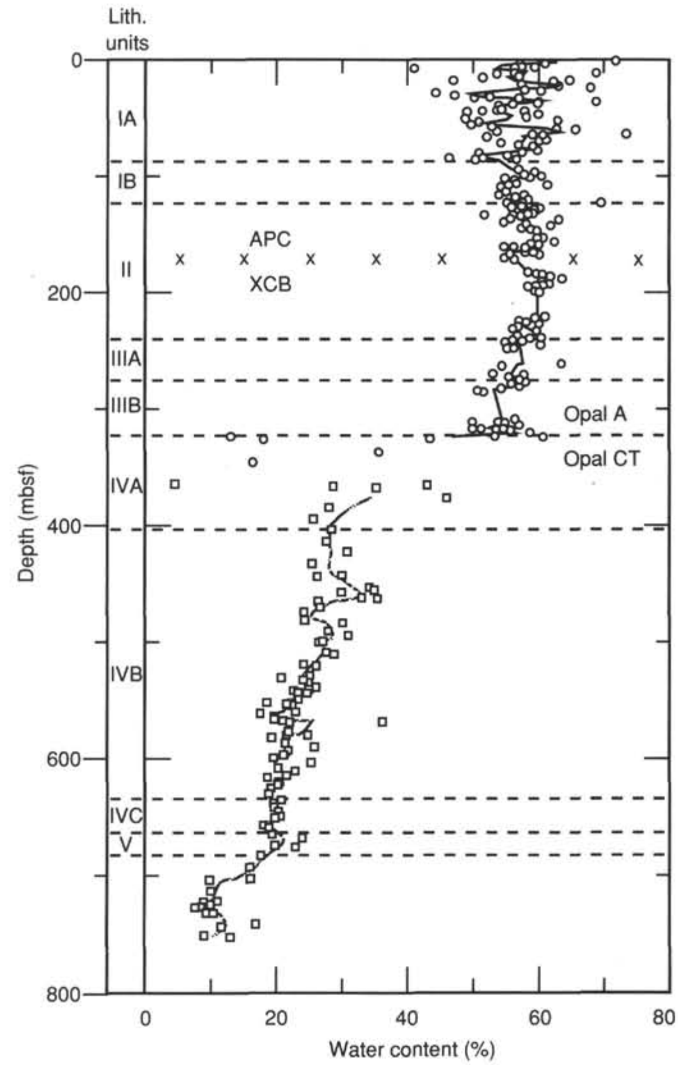

Figure 38. Water content vs. depth for the sedimentary section. Symbols as in Figure 37.

tivity of the solid component of the silty claystone is 3–4 W/m · K, indicating that these sediments may contain significant amounts of quartz and/or carbonates, which are common rock-forming minerals with high conductivities. In the downhole measurements section we show that the relatively high conductivity of the sedimentary rocks in the lower part of the section reduces the temperature gradient significantly below the opal A/opal-CT transition.

Discussion

Comparison with Site 794 Results

The variation of physical properties with depth at Site 795 mimics the major features of the Site 794 profiles. Figure 45 shows the wet bulk density and the grain density profiles from both sites. The uniformity of the bulk density in the upper 300 m and the pronounced effects of the opal-A/opal-CT transformation are clearly seen in both profiles. Along many sections of the profiles the small scale variations match if the differences in sedimentation rate are taken into account. There are some important differences between the two sites; for example at Site 794 there is a negative gradient in the bulk density with depth that is much smaller or absent at Site 795. The difference between the two profiles is caused by lower grain densities in the interval from 100 to 300 mbsf at Site 794 (see Fig. 45). The lower grain densities reflect the higher abundance of diatoms in Hole 794A in this interval.

The Accuracy of Wet Bulk Density and Porosity Measurements

The wet bulk densities measured on cores from Sites 794 and 795 are not in good accord with the grain density determinations. This is illustrated by the plot in Figure 46 of bulk density vs. water content for Site 795 samples. The distribution is compared with curves calculated with an equation that relates wet bulk density (D_b) to water content in percent wet weight (W), grain density (D_g), and the density of seawater (D_w). Specifically,

$$D_b = D_g \times D_w/(W \times (D_g - D_w) + D_w)/100 \quad (1)$$

Curves for three different grain densities are shown. The best fit to the data is for a grain density of 3.0 g/cm^3. The mean grain

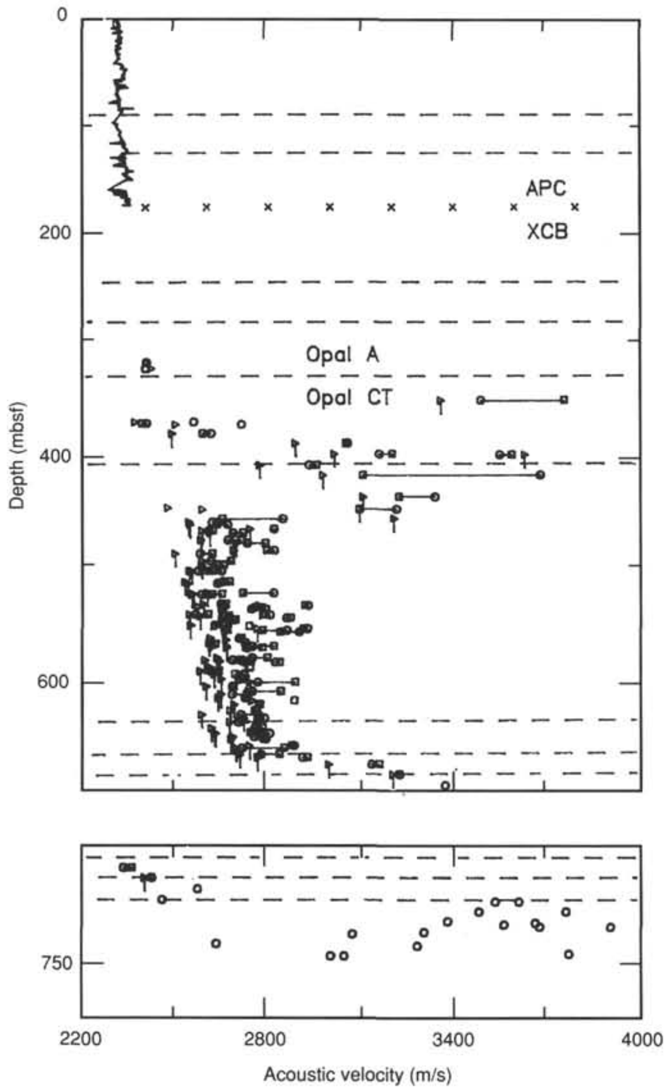

Figure 39. Compressional wave velocities vs. depth. The solid curve between 0 and 160 mbsf shows results from the *P*-wave logger on the MST. The symbols on the Hamilton Frame values represent three orthogonal measurements. The thin horizontal lines connect values in the B (square) and C (circle) direction. The velocity in the A direction, normal to the bedding, is marked by a triangle and a short vertical line.

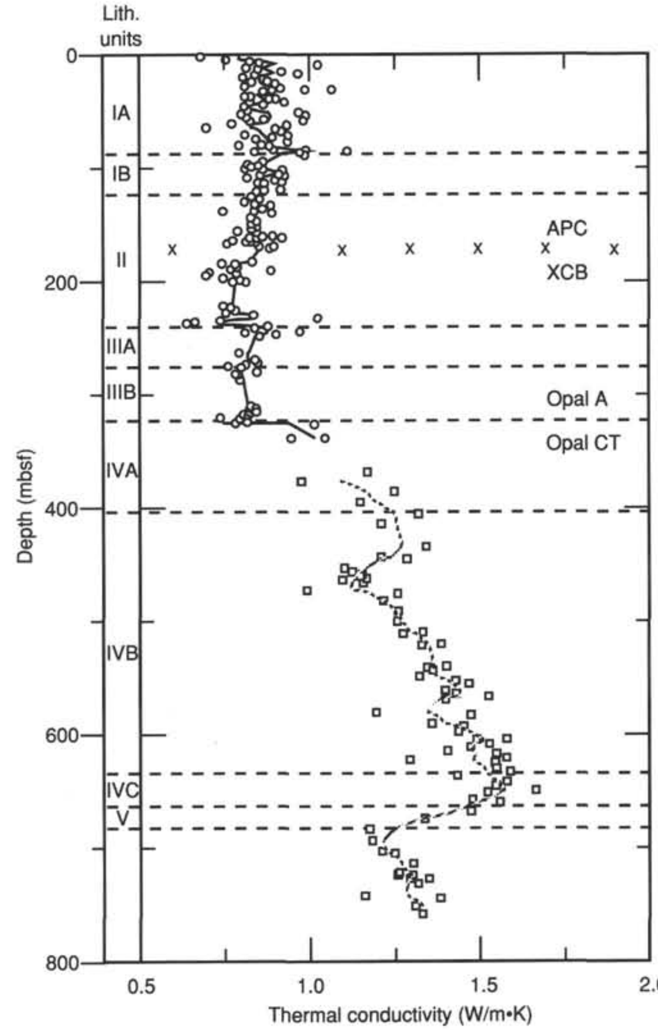

Figure 40. Thermal conductivity vs. depth for Site 795. Individual measurements are shown as squares, and the solid curve is a five-point tapered mean.

density for all Site 795 measurements is 2.55 g/cm^3, which is slightly less than values reported for marine sediments by other investigators (see, e.g., Horai, 1982).

Similarly, porosity determinations are not in accord with reasonable grain densities. In Figure 47, porosities are plotted vs. water content for all Site 795 data and compared with predicted curves of porosity vs. water content for three different grain densities. The curves are derived from the equation:

$$P = W \times D_g/(W \times (D_g - D_w)/100 + D_w) \quad (2)$$

Where P is porosity in percent. Here again the best fit is for a grain density of about 3.0 g/cm^3. The cross-plots of Figures 46 and 47 suggest that density and porosity measurements are systematically biased toward values that are too high, and that the grain densities may be systematically too low. The discrepancy between the two is about 5%–8%.

We have used water content as the independent variable in Figures 46 and 47 because it is derived solely from measurements of weight. The accuracy of the calibration of the balance was verified at least twice during the course of measurements on Site 794 and Site 795 samples, consequently systematic errors of weight measurement are considered less likely than for volume measurements. We believe the sources of this apparent error are volume determinations that are systematically in error, but currently we do not know the cause of this bias. The reader should be advised that the values of density and porosity will probably be revised slightly in the future.

Anisotropy

With a few exceptions, orthogonal velocity measurements on discrete samples indicate a clear anisotropy in the claystones and siltstones from below the opal-A/opal-CT transition (Fig. 39). Velocities measured parallel to the bedding are generally 5% higher than when measured normal to the bedding planes. This result is expected because of the preferential alignment of the long axis of grains parallel with the seafloor during deposition and subsequent compaction. In Unit IV, V_p averages 1830 m/s normal to bedding and 1925 m/s parallel to bedding.

Individual observations of resistivity on the unconsolidated sediment cores often showed an anisotropy, but the calculated mean anisotropy of 3% in the formation factor is not statistically significant.

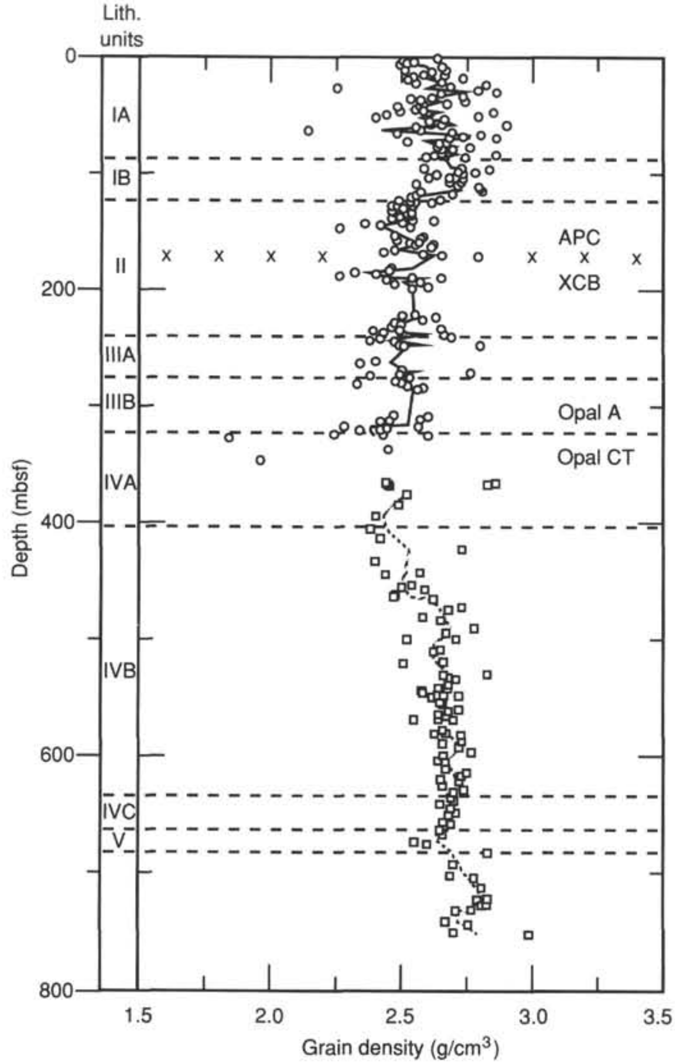

Figure 41. Grain density vs. depth for Site 795. Symbols as in Figure 37.

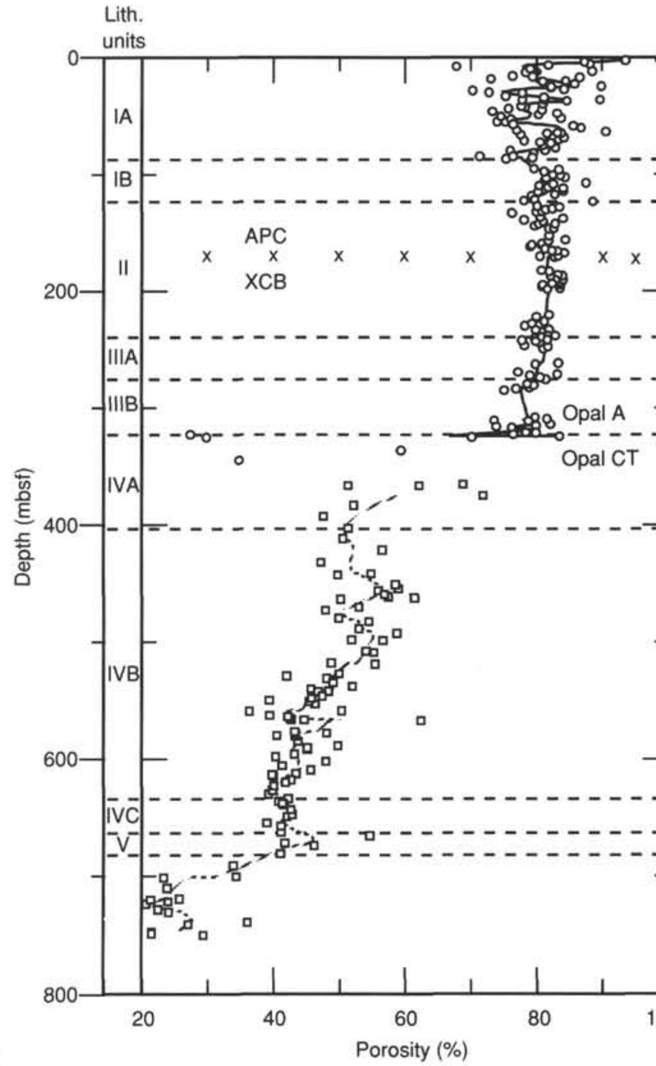

Figure 42. Porosity vs. depth for the sedimentary section. Symbols as in Figure 37.

DOWNHOLE MEASUREMENTS

Operations

Downhole measurements were made in both holes drilled at Site 795. In Hole 795A, six measurements of temperature ahead of the bit were attempted using the Barnes/Uyeda instrument. In Hole 795B, the geophysical/lithodensity logging combination was run, but poor hole conditions precluded attempts to run the geochemistry tool string and formation microscanner. A planned packer/hydrofracture experiment and supporting runs of the borehole televiewer also had to be abandoned because of hole conditions.

Temperature Measurements

Four of the downhole temperature runs yielded valid formation temperatures, while a fifth (run 1) shows evidence of a small disturbance while in the mud. On run 4, the probe apparently did not penetrate into the sediment ahead of the bit. The virgin formation temperatures for all of the runs for which valid data were obtained are shown in Table 18 and plotted vs. depth in Figure 48. The temperatures describe a nearly uniform increase of the temperature with depth with a best fit gradient of 132°C/km, which is 6% higher than at Site 794.

Equilibrium temperatures in the sediment for each run were estimated by extrapolating the temperature history after penetration to equilibrium using plots of temperature vs. 1/time. These temperature histories are shown in Figure 49. The trace for the first run shows evidence of disturbance in the first few cycles. The equilibrium temperature measured on this run falls below the best-fit line of all five measurements. This leads us to believe that on this run the probe only partially penetrated the sediment and consequently the measurement is biased low by cold water in the hole. The temperatures recorded at the seafloor before penetration are 0.17°C, a value which agrees well with hydrographic measurements of deep water temperatures in the Japan Sea, and indicates that the thermistor probe held its calibration throughout this series of measurements as successfully as at Site 794.

Thermal conductivity measurements were made on cores from Holes 795A and 795B using the needle probe technique in unconsolidated and semiconsolidated sediments and the "half-space" technique for indurated sediments and igneous rock samples. These measurements are presented in more detail in the section on "Physical Properties" (this chapter). The heat flow associated with the thermal gradient measured in Hole 795A was determined using the conductivity measurements corrected to *in-situ* conditions using the Ratcliffe relations (1960). The *in-situ* conductivity vs. depth profile (Fig. 50) was used to determine the thermal resistance of the sedimentary section between the seafloor and the depth of each temperature measurement (Table 18). A plot of formation temperatures versus thermal resistance

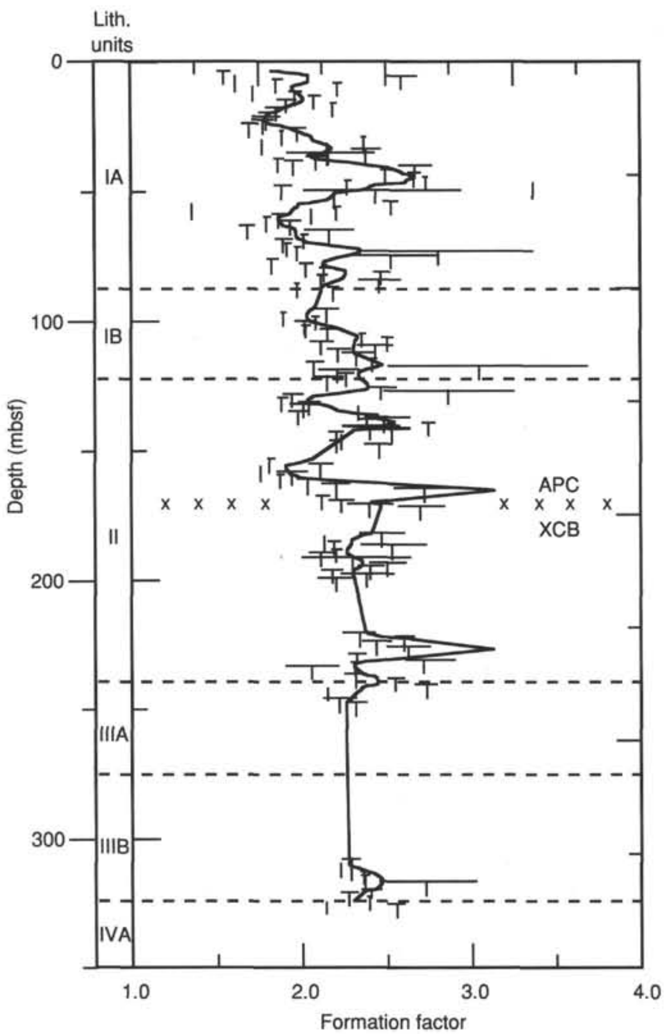

Figure 43. Apparent formation factor vs. depth for Hole 795A. The horizontal lines connect values measured across the core axis and along the axis.

Table 12. Physical properties of Unit I, Site 795.

	Units	Mean	Standard deviation	Maximum	Minimum
Wet-bulk density	g/cm^3	1.48	0.08	1.70	1.27
Dry-bulk density	g/cm^3	0.65	0.12	1.01	0.35
Grain density	g/cm^3	2.62	0.14	2.90	2.14
Water content	%	56.1	5.7	72.8	40.6
Porosity	%	80.6	5.0	98.4	67.5
Thermal conductivity	W/m · K	0.872	0.069	1.112	0.679
Acoustic velocity	m/s	1519	25	1587	1447
Mean formation factor		2.14	0.34	3.36	1.36
Formation anisotropy		1.03	0.04	1.21	0.98

is shown in Figure 51. The slope $\Delta T/\Delta R$ of the linear regression to the temperature points gives the best estimate of the heat flow through the upper 160 m of sediment at Site 795. The good fit to the temperature points shown in Figure 51 indicates a conductive thermal regime and a heat flow of 113 mW/m^2. The error associated with this heat flow determination is estimated to be $\pm 5\%$.

Because of the larger interval and greater depth of the temperature measurements, the heat flow measurement at Site 795 is considered more accurate and representative than standard seafloor measurements. Previous measurements in the northeastern corner of the Japan Sea in the area between the Bogorov Seamounts and the Okushiri Ridge (the region between 42° and 45°N and 137° and 140°E) average 106 $\pm$ 9 mW/m^2 (Yasui et al., 1968; Tamaki et al., 1986; Yamano and Uyeda, 1988). The

Table 13. Physical properties of Unit II, Site 795.

	Units	Mean	Standard deviation	Maximum	Minimum
Wet-bulk density	g/cm^3	1.43	0.04	1.55	1.31
Dry-bulk density	g/cm^3	0.59	0.05	0.74	0.41
Grain density	g/cm^3	2.52	0.13	3.18	2.26
Water content	%	58.5	2.6	69.0	51.2
Porosity	%	81.5	1.9	88.4	76.1
Thermal conductivity	W/m · K	0.812	0.068	1.028	0.642
Acoustic velocity	m/s	1535	51	1564	1464
Mean formation factor		2.29	0.25	2.87	1.77
Formation anisotropy		1.03	0.04	1.15	0.93

Table 14. Physical properties of Unit III, Site 795.

	Units	Mean	Standard deviation	Maximum	Minimum
Wet-bulk density	g/cm^3	1.47	0.04	1.57	1.35
Dry-bulk density	g/cm^3	0.66	0.06	0.78	0.50
Grain density	g/cm^3	2.49	0.12	2.80	2.25
Water content	%	55.2	2.9	63.1	49.7
Porosity	%	79.1	2.6	83.5	73.6
Thermal conductivity	W/m · K	0.823	0.043	0.975	0.740
Acoustic velocity	m/s	1519	25	1620	1601
Mean formation factor		2.37	0.17	2.74	2.16
Formation anisotropy		1.02	0.04	1.11	0.98

Table 15. Physical properties of Unit IV, Site 795.

	Units	Mean	Gradient (/100 m)
Wet-bulk density	g/cm^3	2.04	0.14 ± 0.01
Dry-bulk density	g/cm^3	1.54	0.20 ± 0.02
Grain density	g/cm^3	2.64	
Water content	%	24.9	−5.3 ± 0.5
Porosity	%	48.8	−6.7 ± 0.7
Thermal conductivity	W/m · K	1.345	0.17 ± 0.01
Acoustic velocity, A	m/s	1826	54 ± 13
Acoustic velocity, B	m/s	1934	64 ± 17
Acoustic velocity, C	m/s	1916	59 ± 21

Table 16. Physical properties of Unit V, Site 795.

	Units	Mean	Maximum	Minimum
Wet-bulk density	g/cm^3	2.20	2.34	2.09
Dry-bulk density	g/cm^3	1.72	1.78	1.61
Grain density	g/cm^3	2.62	2.66	2.55
Water content	%	21.6	24.1	19.6
Porosity	%	46.5	55.2	41.7
Thermal conductivity	W/m · K	1.332	1.480	1.340
Acoustic velocity, A	m/s	2112	2189	1902
Acoustic velocity, B	m/s	2230	2353	2030
Acoustic velocity, C	m/s	2205	2327	1970

Table 17. Physical properties of Igneous Unit 3.

	Units	Mean	Standard deviation	Maximum	Minimum
Wet-bulk density	g/cm^3	2.41	0.09	2.54	2.19
Dry-bulk density	g/cm^3	2.16	0.13	2.33	1.81
Grain density	g/cm^3	2.79	0.08	2.99	2.67
Water content	%	10.7	2.3	19.8	17.1
Porosity	%	25.2	4.2	36.7	8.0
Thermal conductivity	W/m · K	1.298	0.061	1.388	1.166
Acoustic velocity, C	m/s	3413	332	3903	2628

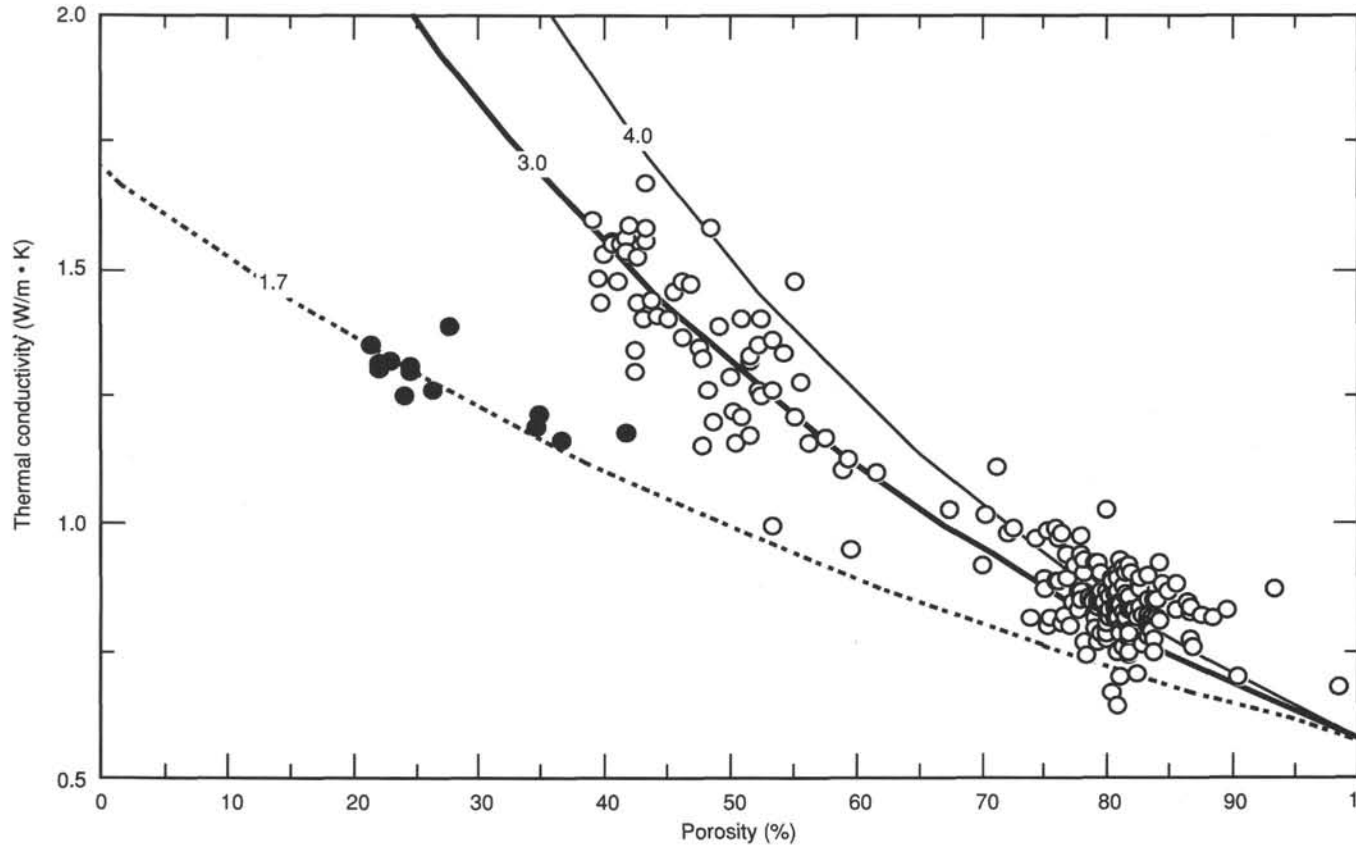

Figure 44. Thermal conductivity vs. porosity. Measurements in the igneous units are shown as solid circles. The curves are derived from the geometric mean relation between conductivity vs. porosity. Curves for three different grain conductivities are shown.

value at Site 795 is at the higher end of the range of seafloor values and lends strong support to the earlier measurements. The heat flow in this region is higher than in the western part of the Japan Basin and the Yamato Basin.

The thermal conductivity profile in the section deeper than 160 m and the Hole 795A heat flow value allow temperatures at deeper levels in the crust to be estimated by extrapolation. The estimated temperature profile in Figure 52, shows that the temperature at the opal-A/opal-CT boundary is 43°C and 72°C at the top of the igneous unit.

Logging

The geophysical/lithodensity tool string was the only tool string run at Hole 795B. The Lamont-Doherty temperature tool was also attached to the bottom of this tool string. Logging runs were conducted from 0 to 227 mbsf. A summary of logging depths reached for the tool string is presented as Table 19.

The drill pipe was lowered to a depth of 124 mbsf. Because of the length of the tool string, not all logs were recorded to 227 mbsf. Only the Natural Gamma Ray tool (NGT) of the geophysical/lithodensity tool string records measurements behind drill pipe which can be corrected for drill pipe effects. A factor bearing on the use of the NGT tool was the use of KCl drilling mud at a 2% concentration.

Caving and infilling created bridges which were impassable at about 238 mbsf. Because of this, the logging measurements could not be made over the most significant diagenetic horizon, the opal-A/opal-CT transition at 325 mbsf.

Log Quality and Processing

The quality of the logging data was very good. Tension was normal and except for the bridge that impeded further progress, the logged interval had few bridges. The unprocessed sonic log showed only minor noise problems.

Density, Resistivity, Sonic Velocity

Figure 53 shows the density, induction (resistivity), and sonic velocity logs acquired in Hole 795B. In general, the resistivity and sonic curves show more variability at Site 795 than at Site 794, a variability that is mostly attributable to a decrease in average log-determined porosity from 65% to 55%.

As at Site 794, the resistivity log at Site 795 shows a negative gradient which cannot be accounted for by temperature and salinity changes alone. The most likely cause of this gradient is an increase in permeability downhole. The density log for Unit II indicates values between 1.5 and 1.6 g/cm^3 higher than at Site 794 (see "Downhole Measurements" section in "Site 794" chapter, this volume). The sonic log shows a rather uniform value of 1600 m/s.

A sharp, brief increase in resistivity at 158 mbsf is manifested as a noisy interval in the sonic log and a peak in the density log. Because this interval is substantially above the opal-A/opal-CT transition, this anomaly probably corresponds to a calcite-cemented or dolomite zone. To test this idea, Figure 54 shows the sonic velocity and photoelectric cross section (PEF) log plotted on the same scale. The photoelectric cross section is roughly proportional to the elemental atomic number (Doveton, 1986), and is measured in Barns per electron (e.g., Si has a PEF of about 4 and Ca a PEF of about 12 (Schlumberger, 1987)). Sharp increases in the velocity and PEF log are coincident and nearly identical at 158 and 205 mbsf. We therefore suggest that the increase in PEF may reflect increased calcium and magnesium in a possible calcite-cemented or dolomite zone. The increase in sonic velocities would also coincide with an increase in

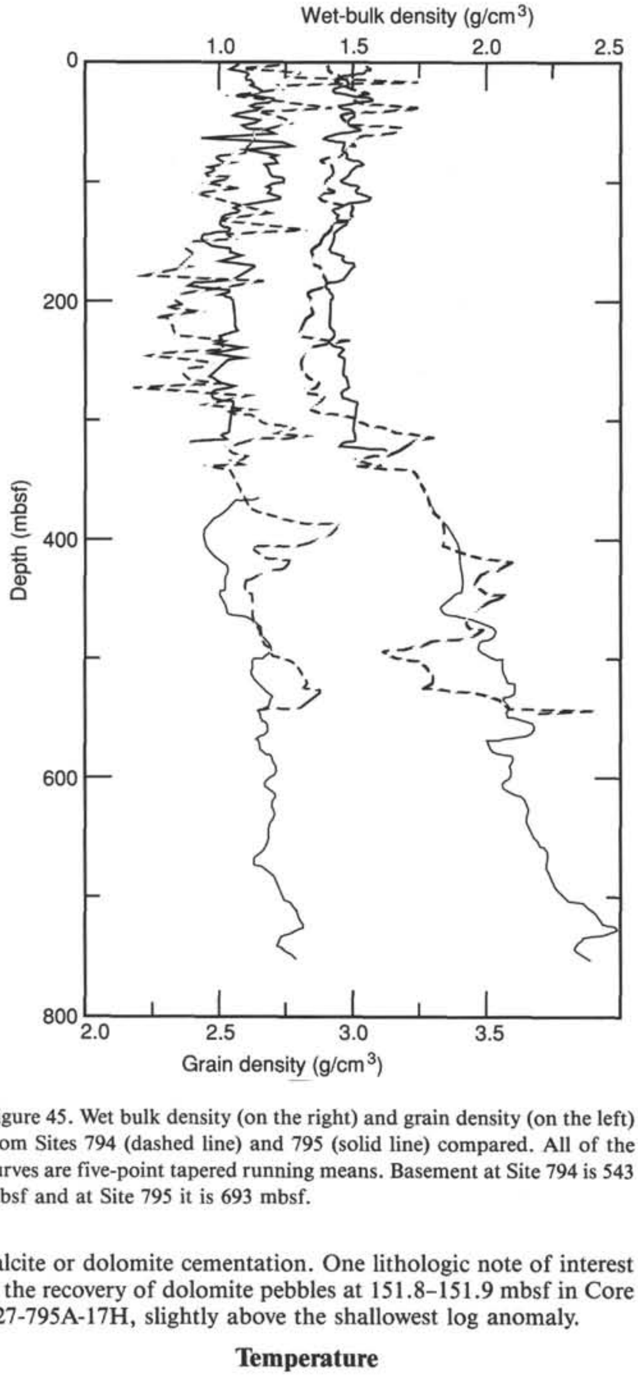

Figure 45. Wet bulk density (on the right) and grain density (on the left) from Sites 794 (dashed line) and 795 (solid line) compared. All of the curves are five-point tapered running means. Basement at Site 794 is 543 mbsf and at Site 795 it is 693 mbsf.

calcite or dolomite cementation. One lithologic note of interest is the recovery of dolomite pebbles at 151.8–151.9 mbsf in Core 127-795A-17H, slightly above the shallowest log anomaly.

Temperature

Since the geophysical tool string was exclusively run at Site 795, only one run of the temperature tool was made at this site. Unfortunately, these data were lost during a computer failure.

SEISMIC STRATIGRAPHY

Available Data

The original proposal for Site 795 was made on the basis of single channel seismic reflection data of the Geological Survey of Japan (Tamaki et al., 1985). The data were obtained by systematic single channel seismic reflection surveys that were carried out in 1977 at an interval of 15 nmi over a wide area of the Japan Sea (Honza, 1978). Two site survey cruises for Site 795 were carried out since the proposal was submitted. A single track line of seismic reflection line was acquired during the

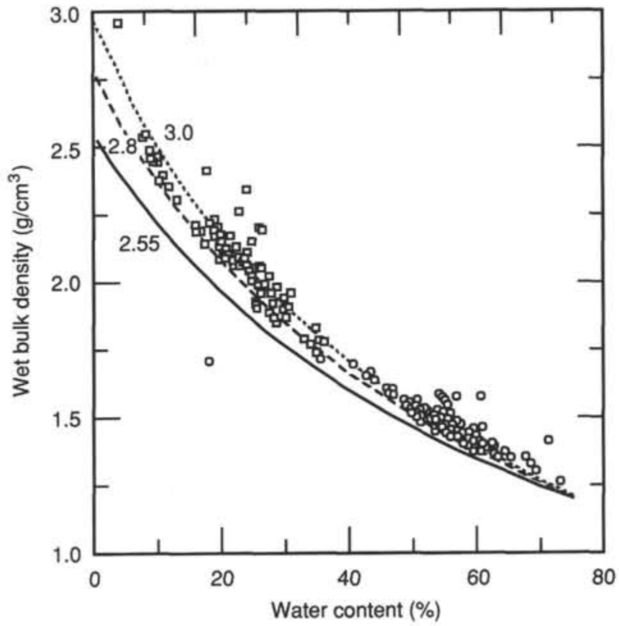

Figure 46. Bulk density vs. water content for Site 795 index property measurements. The curves are density-water content calculated by Eq. 1, for grain densities of 3.0, 2.8, and 2.55 g/cm^3. The mean grain density of Site 795 samples is 2.55.

KT87-6 research cruise in 1985 (Tamaki et al., 1988b), and two north-south seismic reflection survey lines were obtained by the KT88-9 research cruise in 1988. Both cruises were conducted by *Tansei-maru* of Ocean Research Institute, University of Tokyo. A 6-channel seismic reflection system was used on both cruises. Two single channel digital seismic reflection profiles were obtained during the approach of the *JOIDES Resolution* to Site 795 (see "Operations" section, this chapter).

Seismic Stratigraphy

The seismic stratigraphy of the northernmost Japan Basin is characterized by a rather thinner and more acoustically transparent sedimentary section than the main part of the Japan Basin. Site 795 is located on the flank of an east-trending small bathymetric ridge. During the approach to Site 795 from the south by the *JOIDES Resolution*, a densely stratified seismic interval in the upper sedimentary column of the Japan Basin, which is correlated to the turbidite deposits, was confirmed to be continuous over this ridge. The reflectivity of this stratified interval, however, diminishes appreciably to the north, suggesting less contribution of terrigenous matter to the sediments. This situation is different from that of Site 794 where the densely stratified layer of turbidite deposits is completely absent over a much broader bathymetric high of low relief.

Four major seismic intervals (Intervals 1–4) and acoustic basement are recognized in the area around Site 795 (Figs. 10, 11, 55, and 56). From top to bottom they are: Interval 1, an upper moderately-stratified interval; Interval 2, an upper weakly-stratified interval; Interval 3, a middle well-stratified interval; Interval 4, a lower transparent interval; and an unstratified, acoustically-opaque zone corresponding to acoustic basement. Each seismic interval does not necessarily correlate to the seismic intervals of Site 794 although the same nomenclature is used.

The thickness of Interval 1 in the area around Site 795 varies between 0.15 and 0.20 s (two-way traveltime, hereafter, all thicknesses are in two-way traveltime). The boundary between Interval 1 and Interval 2 is slightly disconformable. Interval 2 is a generally weakly stratified layer. The reflectors in Interval 2 are

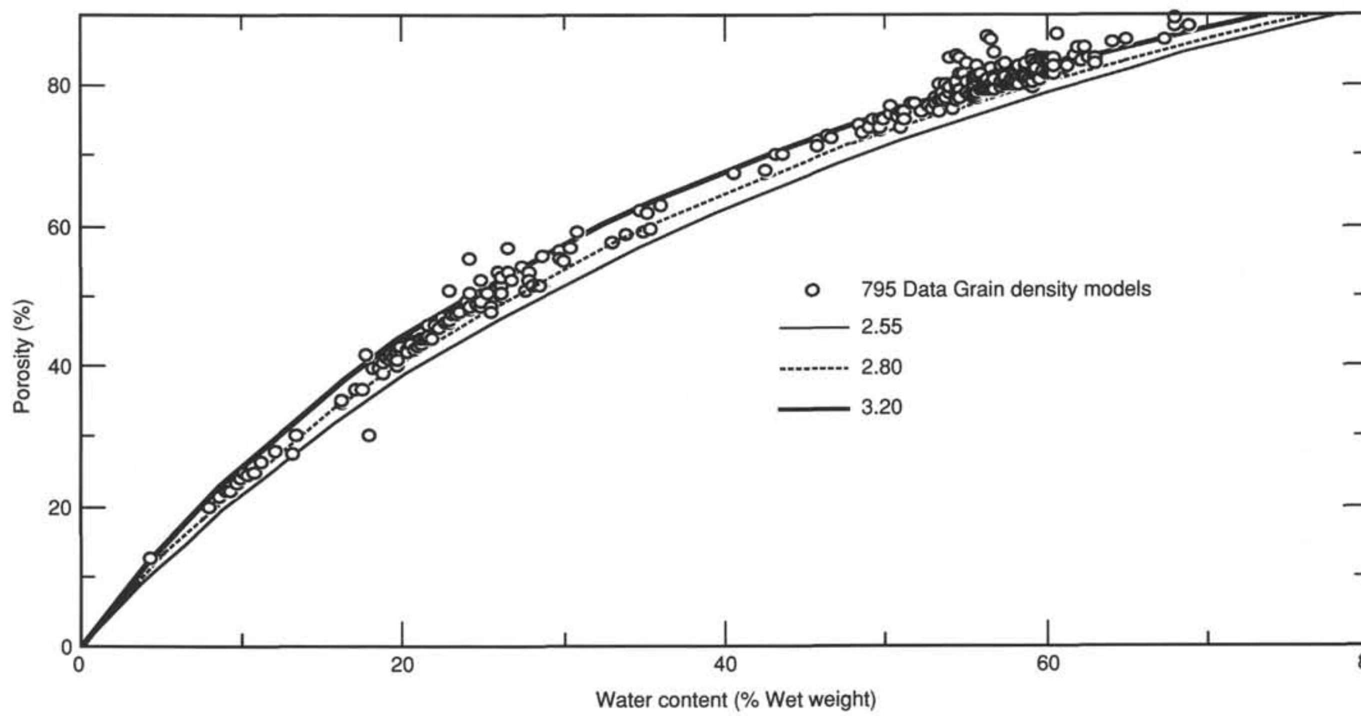

Figure 47. Porosity vs. water content for Site 795 index properties measurements. Curves are porosity-water content calculated by Eq. 2 for grain densities of 2.55, 2.8, and 3.2 g/cm^3.

Table 18. Downhole temperature measurements, Hole 795A.

Measurement no.	Next core no.	Depth (mbsf)	Temperature (°C)	Thermal resistivity (m^2-K/W)
0	1	0.0	0.2	0.0
1	4	29.3	[a]3.18	34.56
2	7	57.8	7.93	67.42
3	10	86.3	11.83	100.23
4	13	114.3	—	—
5	16	143.5	18.85	169.62
6	19	163.4	21.54	189.90

[a] The probe appears to have only partially penetrated the sediment at the bottom of the hole.

very faint but are continuous horizontally. The thickness of Interval 2 is an almost constant 0.22–0.25 s within the area. At Site 795 the lower part of Interval 2 is better stratified than the upper part. Interval 3 is the most stratified interval occurring in the seismic sections in the area. The reflectors of Interval 3 onlap basement highs. The top of Interval 3 makes a remarkable reflector that is continuous over the area surrounding the site. The thickness of this interval is highly variable, ranging from 0.12 to 0.35 s in the area. Interval 4 is generally transparent but contains some faint, hummocky reflectors. It has a rather constant thickness of 0.20–0.25 s, and covers the acoustic basement conformably. Interval 4 appears to be disconformable with the overlying Interval 3.

The thicknesses of each interval determined from the seismic reflection data acquired by the *JOIDES Resolution* during the Site 795 approach are: 0.18 s for Interval 1; 0.22 s for Interval 2; 0.17 s for Interval 3; and 0.23 s for Interval 4.

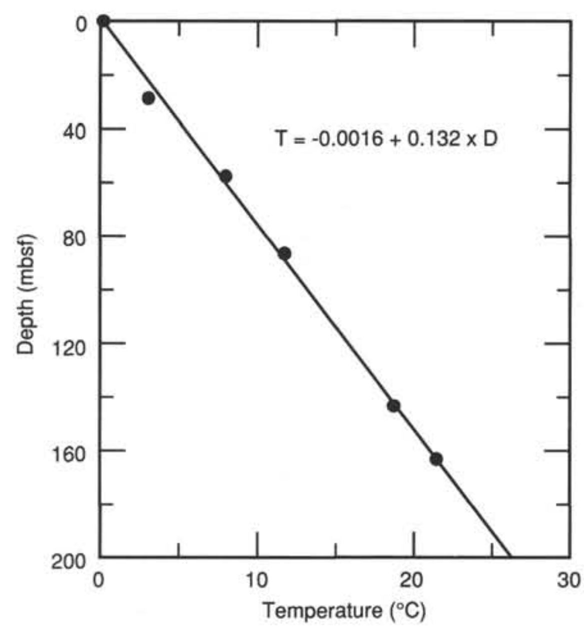

Figure 48. Downhole temperatures plotted vs. depth. The line is a linear regression showing a nearly uniform gradient of 132°/km.

Correlation between Seismic Stratigraphy and Lithology of Site 795

Correlation between seismic stratigraphy and lithostratigraphy was done by using physical property velocity data and two unequivocal reflectors that represent the opal-A/opal-CT bound-

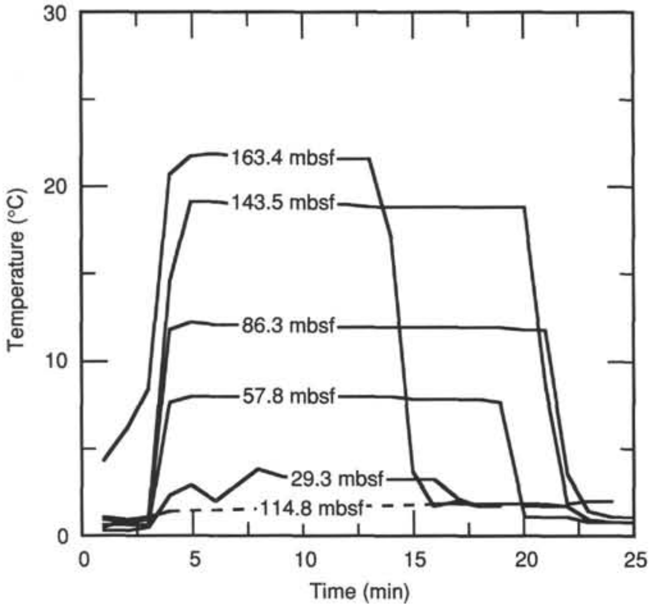

Figure 49. A multiple plot of six temperature records in Hole 795A showing the history just before, during, and after penetration into sediment at the bottom of the hole. Run 4 (the dashed trace) behaves as though the probe never penetrated the sediments at the bottom of the hole, but instead remained in slowly warming water.

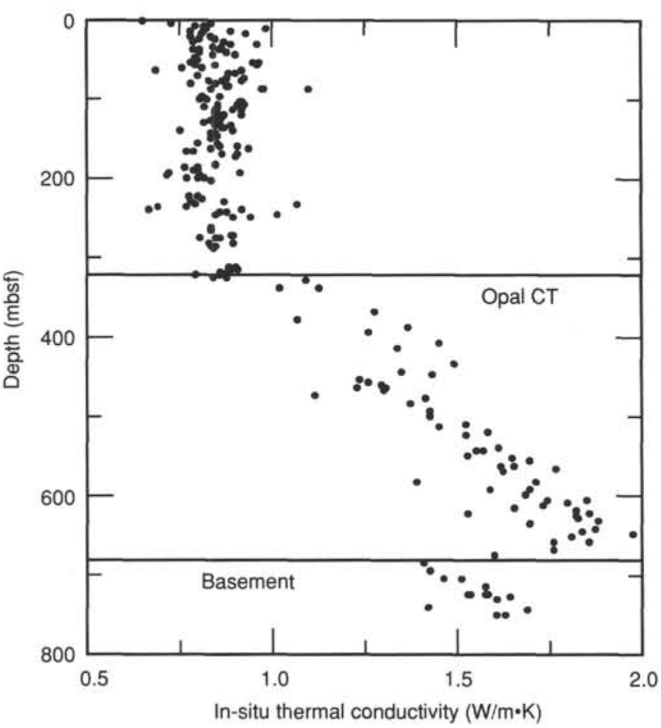

Figure 50. Thermal conductivity values vs. depth in Holes 795A and 795B corrected to *in-situ* conditions.

ary and the top of the igneous rocks. Logging at Site 795 was unfortunately terminated at 231 mbsf and was used only for the estimation of the interval velocity of Interval 1.

The opal-A/opal-CT transition and the top of the igneous rocks provide key markers for the correlation of seismic intervals with lithostratigraphy. The top of the igneous rocks at

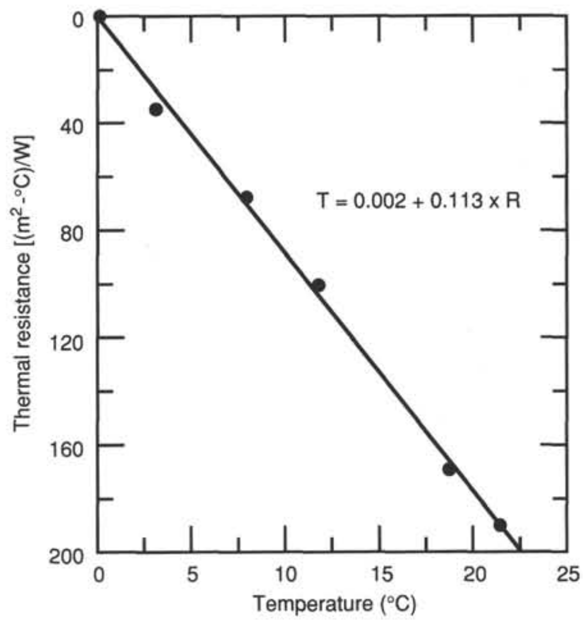

Figure 51. Downhole temperatures plotted vs. thermal resistance of the interval between the seafloor and the measurement. The slope of the linear regression gives the heat flow as 113 mW/m^2.

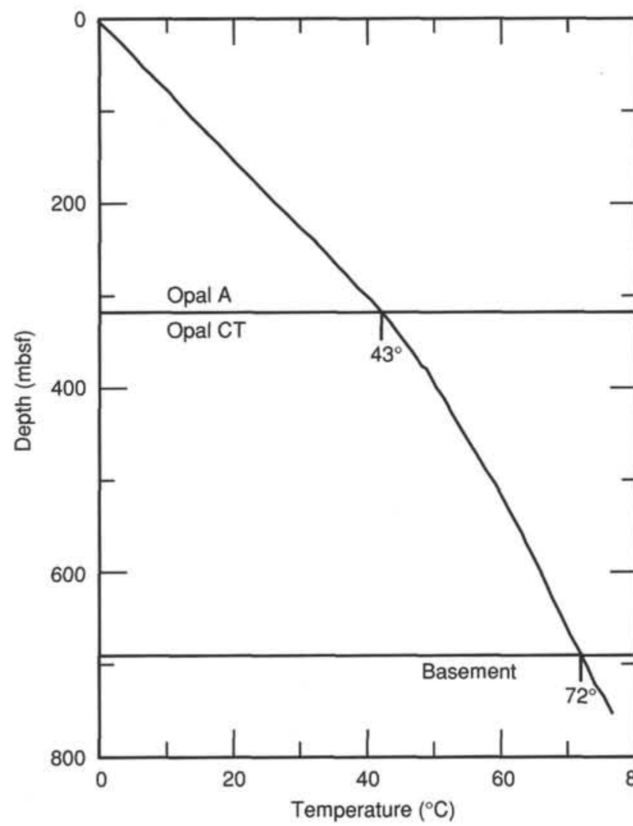

Figure 52. An extrapolated temperature profile based on the observed heat flow of 113 mW/m^2 and the conductivity profile of Figure 50.

Table 19. Summary of logging depths reached by geophysical/lithodensity tool string at Hole 795B.

Seafloor[a] (m)	Seafloor measured from rig floor (m)	Rig floor height (m)	Total depth drilled (m)	Deepest log (m)	Basement depth (m)
3298.9	3310.0 (10,859.6 ft)	11.1	762.2	227	684

Tool	Depths: Shallowest (mbsf)	Shallowest (fbrf)	Deepest (mbsf)	Deepest (fbrf)	Upgoing (y/n)	Hole condition	KCl mud	Side-entry sub
Geophysical	−34.9	10,745.0	227	11,661.5	y	open hole drill pipe 0–124 m	2%	n

[a] From "Introduction" chapter, "Principal Results" section, Table 1, this volume.

684 mbsf was correlated with the top of acoustic basement *a priori*. The opal-A/opal-CT transition at 325 mbsf is well constrained by major changes in almost all of the physical properties (see "Physical Properties" and "Downhole Measurements" sections, this chapter) and correlates unequivocally with the top of Interval 3. The boundaries between Intervals 1 and 2 and Intervals 3 and 4 are rather ambiguous, showing more transitional acoustic natures.

Results of the correlation between the seismic stratigraphy and the lithostratigraphy are summarized in Figure 57. Interval 1 correlates to the silty clay and clay of Unit I and the diatom ooze composing the uppermost part of Unit II. The interval velocity of Interval 1 (1550 m/s) is an estimation based on *P*-wave logger and logging sonic velocity data. The interval velocity is slightly higher than the uppermost interval of Site 794, suggesting a greater contribution of terrigenous components.

Interval 2 correlates to the lower part of Unit II and all of Unit III. Units II and III consist of diatom ooze and silty diatom claystone. The boundary between Intervals 1 and 2 is gradual. As the lithologic transition from Unit I to Unit II is gradual as well, the boundary between Intervals 1 and 2 may roughly correlate to the lithologic boundary between Units I and II. The change of lithology from silty clay to diatom ooze appears to be consistent with the change from the stratified character of Interval 1 to the less stratified character of Interval 2, the diatom ooze having a more transparent acoustic nature. The lower part of Interval 2, slightly more stratified than the upper part, may correlate to lithologic Unit III, which consists of silty diatom claystone. An increase in the terrigenous component of the diatom ooze is probably the cause of this stratification. The acoustic velocity of Interval 2 is estimated to be 1680 m/s. As there are no physical property velocity data nor logging velocity data in this interval, this estimation is less confident than the interval velocities of the other intervals. If this interval velocity is correct, the velocity of Interval 2 is appreciably higher than that of the comparable zone at Site 794 (Interval 2, 1580 m/s). This higher acoustic velocity also may reflect larger amount of terrigenous materials in this interval as compared to that at Site 794.

Interval 3 corresponds to the upper part of Unit IV; its top is coincident with the opal-A/opal-CT transition at 325 mbsf. The well stratified character of Interval 3 reflects the abundant occurrence of hard siliceous layers within this unit. This is supported by the acoustic velocity data which shows correspondingly high variability, suggesting intercalation of layers with different physical properties (see "Physical Properties" section, this chapter). The interval velocity of Interval 3 is 1750 m/s and is comparable with that of the same zone of Site 794 (1750 m/s). The interval velocity of Interval 3 of Site 795 is consistent with the physical property velocity data.

Interval 4 corresponds to the siliceous claystone of the lower part of Unit IV, and to the claystone and tuff of Unit V. This part of the acoustic velocity profile shows less variability than the above interval, which is consistent with its more transparent nature (see "Physical Properties" section, this chapter). The interval velocity of Interval 4 is 1825 m/s, slightly slower than that of the same interval of Site 794 (1850 m/s). This interval velocity is consistent with physical property velocity data.

The acoustic basement correlates to basalts and basaltic andesite. No strong reflectors are observed at this site, unlike the strongly reflective horizon, Interval 5, which was observed above the acoustic basement at Site 794. This observation is well explained by the slower acoustic velocity of the igneous rocks at Site 795 (3410 m/s) (see "Physical Properties" section, this chapter) than those of the basaltic sills at Site 794 (4000–4700 m/s). This slower acoustic velocity of the basement rocks at Site 795 sometimes obscures the boundary between the basement and sediments.

Discussion

As the opal-A/opal-CT reflector is a bottom-simulating reflector, the reflector does not always coincide with the stratigraphic boundaries. At Site 795, the strong opal-A/opal-CT reflector at the top of Interval 3 intersects weak reflectors of original lithological stratification (Figs. 55 and 56). Figure 58 clearly shows this relationship between the opal-A/opal-CT reflector and the stratification of deposits. Three geological seismic units can be discriminated and defined in this profile and are denoted as Units A, B, and C (Fig. 58); they do not correspond to the regional lithofacies described in the introduction of this volume. The geological seismic units used here closely approximate the syndepositional strata in the region, whereas the seismic intervals described above are purely dependent on the seismic character of a limited area around the site.

Interval 1 and Interval 4 are identical with Units A and C, respectively, whereas Interval 2 and Interval 3 are together correlated with Unit B (Fig. 58). Siliceous deposits comprising lithologic Units II, III, and the upper part of IV are denoted as Unit B. These sediments were originally deposited as diatom oozes and clays, but have been altered by burial diagenesis to hard siliceous claystones and porcellanites. Unit B below the opal-A/opal-CT reflector (Interval 3) comprises siliceous claystone while Unit B above the opal-A/opal-CT reflector (Interval 2) represents diatom ooze or clay. This process is confined to the diatom-rich sediments only, where opal A, which comprises diatom frustules, alters to opal-CT. This process is controlled by time and temperature and gives rise to a sharp diagenetic front which is parallel to the seafloor and migrates upward through the stratigraphic section with continued burial. Figure 58 shows the

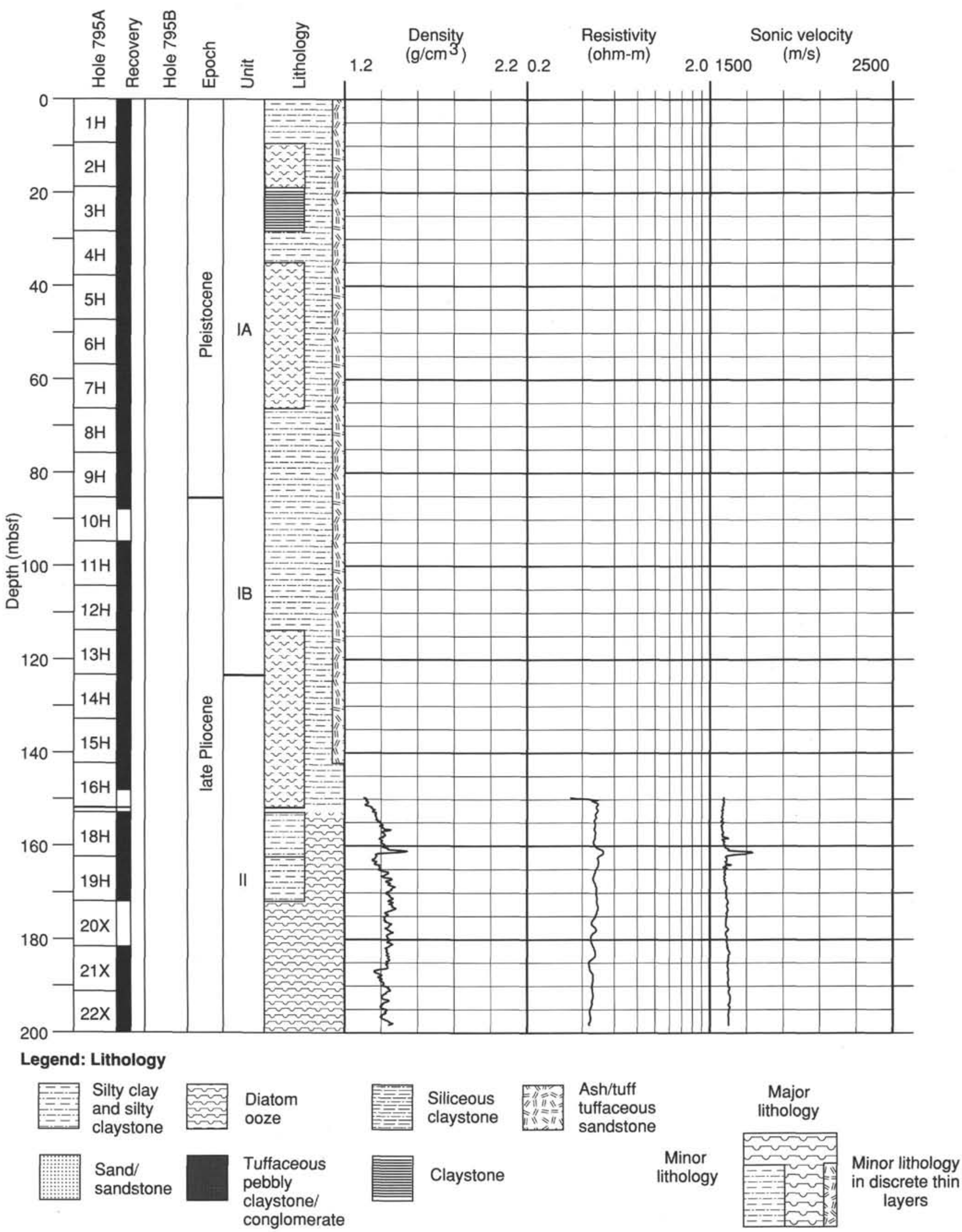

Figure 53. Resistivity (IDPH—ohmmeters), sonic velocity (VELO—m/s), density (g/cm^3) vs. depth below seafloor, Hole 795B.

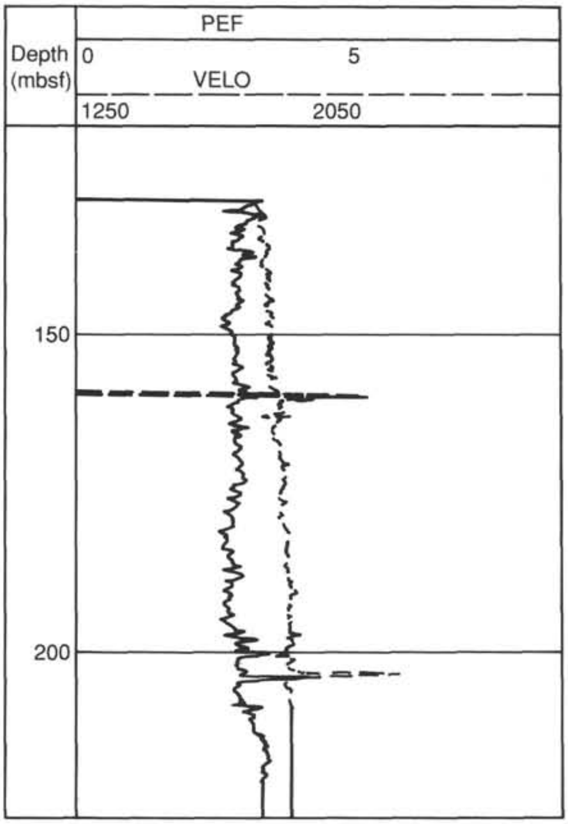

Figure 54. Sonic velocity (VELO—m/s) and photoelectric cross section (PEF—barns/electron) logs plotted vs. depth below seafloor, Hole 795B.

present position of this diagenetic front as it migrates through the diatomaceous sediments denoted by Unit B.

The opal-A/opal-CT reflector that is distributed commonly in the Japan Sea is thus neither a synchronous horizon nor a syndepositional horizon. As the syndepositional horizons principally intersect the opal-A/opal-CT reflector, the siliceous parts of lithological units as well as the seismic intervals do not correlate to syndepositional strata nor to synchronous layers. To complete a seismic stratigraphy of the Japan Sea, the effect of opal-A/opal-CT diagenesis must be carefully accounted for.

CONCLUSIONS

We accomplished two of our three main objectives at Site 795, namely: (1) to gain information on the style and dynamics of rifting through a determination of the age and nature of basement; and (2) to characterize the sedimentation, subsidence, and oceanographic history of the northern Japan Sea. Because of hole problems, we were unable to reach our third goal, a measurement of the magnitude and direction of the present stress field. A detailed summary of the results and conclusions for Site 795 can be found at the beginning of this chapter. For emphasis, we highlight the key findings as they relate to our principal objectives in the sections below.

Style and Dynamics of Rifting

Submarine basalt, basaltic andesite, and basaltic breccia constitute acoustic basement at Site 795 and range in age from 13 to 15 Ma, based on the age of the overlying sediments. These basaltic rocks are chemically distinct from both mid-ocean ridge basalts and tholeiitic back-arc basin basalts in that they lack a significant iron enrichment trend with differentiation, have a high Al_2O_3 contents, and have a relatively high ratio of light ion lithophile elements to high-field-strength elements. These characteristics are typical of calc-alkaline volcanism associated with volcanic arcs and subduction zones. Based on the low contents of both large ion lithophile elements and large rare earth elements, especially Ce, the parental magmas underwent little interaction with continental crust during their genesis and ascent. These results, coupled with the deep bathymetry (3300 m), suggest that this part of the Japan Basin is underlain by oceanic-type crust and that it was formed by subduction-related magmatism at 13–15 Ma.

Oceanographic and Sedimentation History

The stratigraphic succession encountered at Site 795 indicates at least three principal stages in the oceanographic and depositional history of this area. Sedimentation began with middle Miocene submarine volcanism and deposition of upper middle bathyal marine claystone and gravity-flow tuffs on a slope or basin in cool, well oxygenated to mildly dysoxic water. By late Miocene and early Pliocene time, climate and water temperatures cooled further and diatomaceous sedimentation prevailed in a well oxygenated environment as the basin subsided to lower middle bathyal depths. Conditions changed again in the late Pliocene and Quaternary when diatomaceous sedimentation shut down, terrigenous input increased, and climate oscillated between arctic and subarctic conditions. The combination of these factors produced complex interbedding of amalgamated, light-colored, laminated, and graded clayey silts alternating with dark-layered diatomaceous and pyritic layers containing abundant, terrestrially-derived organic materials. Except for parts of the Quaternary, this sequence was largely deposited below the CCD.

The sedimentary strata at this site has been overprinted by significant diagenetic changes, the most striking of which is the wholesale alteration of the opaline diatomaceous sediments to hard siliceous claystones containing opal-CT. These siliceous sediments, which were originally deposited as diatom ooze and clay, now comprise two distinct lithologic units: diatoms ooze and clay above the opal-A/opal-CT transition and siliceous claystone and intercalated cherts and porcellanites below this boundary. As the opal-A/opal-CT transition is not a depositional boundary, these two lithofacies, diatomaceous ooze and harder, siliceous claystones, constitute diagenetic equivalents of a single depositional unit. The alteration of opal-A occurs along a migrating diagenetic front which is parallel to the seafloor and is manifested in seismic reflection records as a prominent bottom simulating reflector that cuts across stratal reflectors.

REFERENCES

Abe, K., and Kanamori, H., 1970. Mantle structure beneath the Japan Sea as revealed by surface wave. *Tokyo Daigaku Jishin Kenkyusho Iho,* 48:1011–1021.

Berggren, W. A., Kent, D. V., Flynn, J. J., and Van Couvering, J. A., 1985a. Cenozoic geochronology. *Geol. Soc. Am. Bull.,* 96:1407–1418.

Berggren, W. A., Kent, D. V., and Van Couvering, J. A., 1985b. The Neogene: Part 2. Neogene geochronology and chronostratigraphy. *In* Snelling, N. J. (Ed.), *The Chronology of the Geological Record:* Geol. Soc. London Mem., 10:211–260.

Calvert, S. E., 1983. Geochemistry of Pleistocene sapropels and associated sediments from the Eastern Mediterranean. *Oceanol. Acta,* 6: 225–267.

Chough, S. K., 1984. Fine-grained turbidites and associated mass-flow deposits in the Ulleung (Tsushima) Back-arc Basin, East Sea (Sea of Japan). *In* Stow, D.V.A., and Piper, D.J.W. (Eds.), *Fine-Grained Sediments: Deep-Water Processes and Facies.* Geol. Soc. Spec. Publ. London, 185–196.

Cisowski, S. M., and Koyama, M., in press. Site 792. *In* Taylor, B., Fujioka, K., et al., *Proc. ODP, Init. Repts.,* 126: College Station, TX (Ocean Drilling Program).

Davis, E. E., and Lister, C.R.B., 1977. Heat flow measured over the Juan de Fuca Ridge: evidence for widespread hydrothermal circulation in a highly heat transportive crust. *J. Geophys. Res.*, 82:4845-4860.

Doveton, J. H., 1986. *Log Analysis of Subsurface Geology-Concepts and Computer Methods:* New York (Wiley).

Emeis, K.-C. and Kvenvolden, K. A., 1986. Shipboard organic geochemistry on JOIDES Resolution. *ODP Tech. Note,* 7.

Espitalié, J., Madec, M., Tissot, B., Mennig, J. J., and Leplat, P., 1977. Source rock characterization method for petroleum exploration. *Proc. 9th Ann. Offshore Technology Conf.,* 3:439-448.

Ewart, A., 1982. The mineralogy and petrology of Tertiary-Recent orogenic volcanic rocks: with special reference to the andesitic-basaltic compositional range. *In* Thorpe, R.S. (Ed.), *Andesites: Orogenic Andesites and Related Rocks:* Chichester (Wiley), 26-87.

Fisher, R. V., 1984. Submarine volcaniclastic rocks. *In* Kokelaar, B. P., and Howells, M. F. (Eds.), *Marginal Basin Geology: Volcanic and Associated Sedimentary Processes in Modern and Ancient Basins.* Geol. Soc. Spec. Publ. London, 16:5-28.

Fukao, Y., and Furamoto, M., 1975. Mechanism of large earthquakes along the margin of the Japan Sea. *Tectonophysics,* 25:247-266.

Furuta, T., and Levi, S., 1983. Basement paleomagnetism of Hole 504B. *In* Cann, J. R., Langseth, M. G., Honnorez, J., Von Herzen, R. P., White, S. M., et al., *Init. Repts. DSDP,* 69: Washington (U.S. Govt. Printing Office), 697-703.

Geological Survey of Japan, 1982. Geologic atlas of Japan. *Geol. Surv. Jpn.*

Gieskes, J. M., and Peretsman, G., 1986. Water chemistry procedures aboard JOIDES Resolution—some comments. *ODP Tech. Note,* 5.

Gnibidenko, H., 1979. The tectonics of the Japan Sea. *Mar. Geol.,* 32: 71-87.

Hamilton, E. L., 1976. Variations in density and porosity with depth in deep sea sediments. *J. Sediment. Petrol.,* 46:280-300.

Hill, P. R., 1984. Facies and sequence analysis of Nova Scotia Slope muds: turbidite vs 'hemipelagic' deposition. *In* Stow, D.V.A. and Piper, D.J.W. (Eds.), *Fine-Grained Sediments: Deep-Water Processes and Facies.* Geol. Soc. Spec. Publ. London, 15:311-318.

Honza, E. (Ed.), 1978. Geological investigation of the Okhotsk and Japan Seas off Hokkaido. June-July 1977 (GH77-3 Cruise). *Cruise Rep., Geol. Surv. Jpn.,* 11:1-72.

Horai, K., 1982. Thermal conductivity of sediments and igneous rocks recovered during Deep Sea Drilling Project, Leg 60. *In* Hussong, D. M., Uyeda, S., et al., *Init. Repts. DSDP,* 60: Washington (U.S. Govt Printing Office), 807-834.

Hyndman, R. D., Von Herzen, R. P., Erickson, A. J., and Jolivet, J., 1977. Heat-flow measurements, DSDP Leg 37. *In* Aumento, F., Melson, W. G., et al., *Init. Repts.DSDP,* 37: Washington (U.S. Govt. Printing Office), 347-362.

Iijima, A., Tada, R., and Watanabe, Y., 1988. Development of Neogene sedimentary basins in the northeastern Honshu arc with emphasis on Miocene siliceous deposits. *J. Fac. Sci., Univ. Tokyo,* 21:417-446.

Isezaki, N., 1986. A magnetic anomaly map of the Japan Sea. *J. Geomagn. Geoelectr.,* 38:403-410.

Ishida, M., and Hata, M., 1989. The geologic development in the Oshima Peninsula, southwestern Hokkaido, Japan. *Chishitsugaku Ronshu,* 32:29-56.

Ishii, J., Takami, M., Miyashita, S., Sakamoto, I., Shin, G., Iikura, S., and Iizuka, 1988. A preliminary report on the third cruise to the Okushiri submarine ridge by the R/V Bosei Maru II of Tokai University. *Proc. Hokkaido Tokai Univ.,* 1:39-68.

Kobayashi, K. (Ed.), 1988. Geophysical and geological investigation of the northeastern part of the Japan Sea and Japan Trench. Preliminary Report of the Hakuho Maru Cruise KH 86-2 (April 21-May 15, 1986), with annex for preliminary report of the Tansei Maru Cruise KT-87-6, May 29-June 4, 1987. *Ocean Res. Inst., Univ. Tokyo,* 1-130.

Lee, H., 1973. Measurements and estimates of engineering and other physical properties, Leg 19. *In* Creager, J. S., Scholl, D. W., et al., *Init. Repts. DSDP,* 19: Washington (U.S. Govt. Printing Office), 701-719.

Ludwig, W. J., Murauchi, S., and Houtz, R. E., 1975. Sediments and structure of the Japan Sea. *Geol. Soc. Am. Bull.,* 86:651-664.

Manheim, F. T., and Sayles, F. L., 1974. Composition and origin of interstitial waters of marine sediments, based on deep sea drill cores. *In* Goldberg, E. D. (Ed.), *The Sea* (Vol. 5): New York (Wiley Interscience), 527-568.

Matoba, Y., 1984. Paleoenvironment of the Sea of Japan. *In Benthos '83, 2nd Intern. Symp. Benthic Foraminifera,* 409-415.

Melankholina, Y. N., and Kovylin, V. M., 1977. Tectonics of the Sea of Japan. *Tectonics,* 10:273-281.

Miyashita, S., Tsuchiya, N., Watanabe, Y., Ishii, J., Yamazaki, T., Sagayama, T., Izu, S., and Iwashita, M., 1987. Basaltic pillow lavas dredges from the Kaiyo-kaizan, northeast margin of the Japan Sea. *Bull. Coll. Arts Sci. Sapporo, Tokai Univ.,* 6:11-21.

Mizutani, S., 1970. Silica minerals in thee early stages of diagenesis. *Sedimentology,* 15:259-272.

Müller, P. J., 1977. C/N ratios in Pacific deep sea sediments: effect of inorganic ammonium and organic nitrogen compounds sorbed by clays. *Geochim. Cosmochim. Acta,* 41:765-776.

Ohguchi, T., Yoshida, T., and Okami, K., 1989. Historical change of the Neogene and Quaternary volcanic field in the Northeast Honshu Arc, Japan. *Chishitsugaku Ronshu,* 32:431-455.

Okada, H., and Niitsuma, N., 1989. Detailed paleomagnetic records during the Brunhes-Matuyama geomagnetic reversal, and a direct determination of depth lag for magnetization in marine sediments. *Phys. Earth Planet. Inter.,* 56:133-150.

Oremland, R. S., and Taylor, B. F., 1978. Sulfate reduction and methanogenesis in marine sediments. *Geochim. Cosmochim. Acta.,* 42: 209-214.

Parsons, B., and Sclater, J. G., 1977. An analysis of the variation of ocean floor bathymetry and heat flow with age. *J. Geophys. Res.,* 82:803-827.

Pearce, J. A., Alabaster, T., Shelton, A. W., and Searle, M P., 1981. The Oman ophiolite as a Cretaceous arc-basin complex: evidence and implications. *Philos. Trans. R. Soc. London,* A300:299-317.

Pechersky, D. M., Tikhonov, L. V., and Pertsev, N. N., 1983. Magnetic properties of basalts, Deep Sea Drilling Project Legs 69 and 70. *In* Cann, J. R., Langseth, M. G., Honnorez, J., Von Herzen, R. P., White, S. M., et al., *Init. Repts. DSDP,* 69: Washington (U.S. Govt. Printing Office), 705-710.

Perch-Nielsen, K., 1985. Cenozoic calcareous nannofossils. *In* Bolli, H. M., Saunders, J. B., and Perch-Nielsen, K. (Eds.), *Plankton Stratigraphy:* Cambridge (Cambridge Univ. Press), 427-554.

Peters, K. E., 1986. Guidelines for evaluating petroleum source rock using programmed pyrolysis. *AAPG Bull.,* 70:318-329.

Piper, D.J.W., 1978. Turbidite muds and silts on deep sea fans and abyssal plains. *In* Stanley, D. J., and Kelling, G. (Eds.), *Sedimentation in Submarine Canyons, Fans, and Trenches:* Stroudsberg, PA (Dowden, Hutchinson and Ross), 163-176.

Pisciotto, K. S., 1981. Distribution, thermal histories, isotopic compositions, and reflection characteristics of siliceous rocks recovered by the Deep Sea Drilling Project. *In* Arme, J. E., Douglas, R. G., and Winterer, E. L. (Eds.), *The Deep Sea Drilling Project: A Decade of Progress.* Soc. Econ. Paleontol. Mineral. Spec. Publ., 32:129-148.

Ratcliffe, E. H., 1960. The thermal conductivity of ocean sediments. *J. Geophys. Res.,* 65:1535-1541.

Sagayama, T., Hoyanagi, K., and Ishii, J., 1988. Diatom assemblage of sediments collected from Kaiyo-kaizan (seamount) off the Shakotan Peninsula. *Proc. Hokkaido Univ.,* 1:17-21.

Saunders, A. D., and Tarney, J., 1984. Geochemical characteristics of basaltic volcanism within back-arc basins. *In* Kokelaar, B. P., and Howells, M. F. (Eds.), *Marginal Basin Geology:* Oxford (Blackwell), 59-76.

Schlumberger, 1987. *Log Interpretation Principles/Applications:* New York (Schlumberger).

Stevenson, F. J., and Cheng, C. N., 1972. Organic geochemistry of the Argentine Basin sediments: carbon-nitrogen relationships and Quaternary correlations. *Geochim. Cosmochim. Acta,* 36:653-671.

Sun, S.-S., Nesbitt, R. W., and Sharaskin, A. Y., 1979. Geochemical characteristics of mid-ocean ridge basalts. *Earth Planet Sci. Lett.,* 44:119-138.

Tamaki, K., 1986. Age estimation of the Japan Sea on the basis of stratigraphy, basement depth, and heat flow data. *J. Geomagn. Geoelectr.,* 38:427-446.

________, 1988. Geological structure of the Japan Sea and its implications. *Chishitsu Chosasho Geppo,* 39:269-365.

Tamaki, K., and Honza, E., 1985. Incipient subduction and obduction along the eastern margin of the Japan Sea. *Tectonophysics,* 119: 381–406.

Tamaki, K., Kagami, H., Honza, E., and Kobayashi, K., 1985. ODP drilling proposal: tectonics of the Japan Sea. ODP proposal (manuscript).

Tamaki, K., Kobayashi, K., Isezaki, N., Sayanagi, K., Nakanishi, N., and Park, C. H., 1988a. Measurement of geomagnetic total force by a proton precession magnetometer. *In* Kobayashi, K. (Ed.), *Geophysical and Geological Investigation of the Northeastern Part of the Japan Sea and Japan Trench. Preliminary Report of the Hakuho Maru Cruise KH 86-2 (April 21–May 15, 1986).* Ocean Res. Inst., Univ. Tokyo, 7-9.

Tamaki, K., Tokuyama, H., Miyashita, S., Tsukui, M., Furukawa, K., Sayanagi, K., Kuramoto, S., Nakanishi, M., Uno, I., Yamashita, S., and Itoda, C., 1988b. An annex for Preliminary report of the Tansei maru cruise KT87-6 (ODP site survey). *In* Kobayashi, K. (Ed.), *Geophysical and Geological Investigation of the Northeastern Part of the Japan Sea and Japan Trench. Preliminary Report of the Hakuho Maru Cruise KH86-2.* Ocean Res. Inst., Univ. Tokyo, 112–130.

Tissot, B., Deroo, G., and Herbin, J. P., 1979. Organic matter in Cretaceous sediments of the North Atlantic: contribution to sedimentology and paleogeography. *In* Talwani, M., Hay, W., and Ryan, W.B.F. (Eds.), *Deep Drilling Results in the Atlantic Ocean: Continental Margins and Paleoenvironments:* Washington (Am. Geophys. Union), 362–374.

Tsuchiya, N., 1988. Distribution and chemical composition of the middle Miocene basaltic rocks in Akita-Yamagata oil fields of northeastern Japan. *Chishitsugaku Zasshi,* 94:591–608.

Tsuchiya, N., 1989. Submarine basalt volcanism of Miocene Aosawa Formation in the Akita-Yamagata oil field basin, back-arc region of Northeast Japan. *Chishitsugaku Ronshu,* 32:399–408.

Waples, D. W., 1985. A reappraisal of anoxia and richness of organic material with emphasis on the Cretaceous North Atlantic. *In* de Graciansky, P. C., Poag, C. W., et al., *Init. Repts. DSDP,* 80: Washington (U.S. Govt. Printing Office), 999–1016.

Waples, D. W., and Sloan, J. R., 1980. Carbon and nitrogen diagenesis in deep sea sediments. *Geochim. Cosmochim. Acta,* 44:1463–1470.

Waples, J. R., 1980. Time and temperature in petroleum formation: application of Lopatin's method to petroleum exploration. *AAPG Bull.,* 64:916–926.

Wilson, M., 1989. *Igneous Petrogenesis:* London (Unwin Hyman).

Yamano, M., and Uyeda, S., 1988. Heat flow in the ocean basins and margins. *In* Nairn, A.E.M., Stehli, F. G. (Eds.), *The Ocean Basins and Margins* (Vol. 7): New York (Plenum).

Yasui, M., Kishii, T., Watanabe, T., and Uyeda, S., 1968. Heat flow in the Sea of Japan, *In* Knopoff, L., et al. (Eds.), *Crust and Upper Mantle of the Pacific Area,* Am. Geophys. Union Monograph, 12: 3–16.

Yasui, M., and Watanabe, T., 1965. Studies of the thermal state of the Earth: the 16th paper: terrestrial heat flow in the Japan Sea (1). *Tokyo Daigaku Jishin Kenkyusho Iho,* 43:549–563.

Yoshii, T., and Yamano, M., 1983. Digital heat flow data file around the Japan islands. Unpublished Data Files, Ocean Res. Inst., Univ. Tokyo.

Yuasa, M., Tamaki, K., Nishimura, K., and Honza, E., 1978. Welded tuff dredged from Musashi Bank, northern Japan Sea and its K-Ar age. *Chishitsugaku Zasshi,* 84:375–377.

Ms 127A-105

NOTE: All core description forms ("barrel sheets") and core photographs have been printed on coated paper and bound as Section 3, near the back of the book, beginning on page 425.

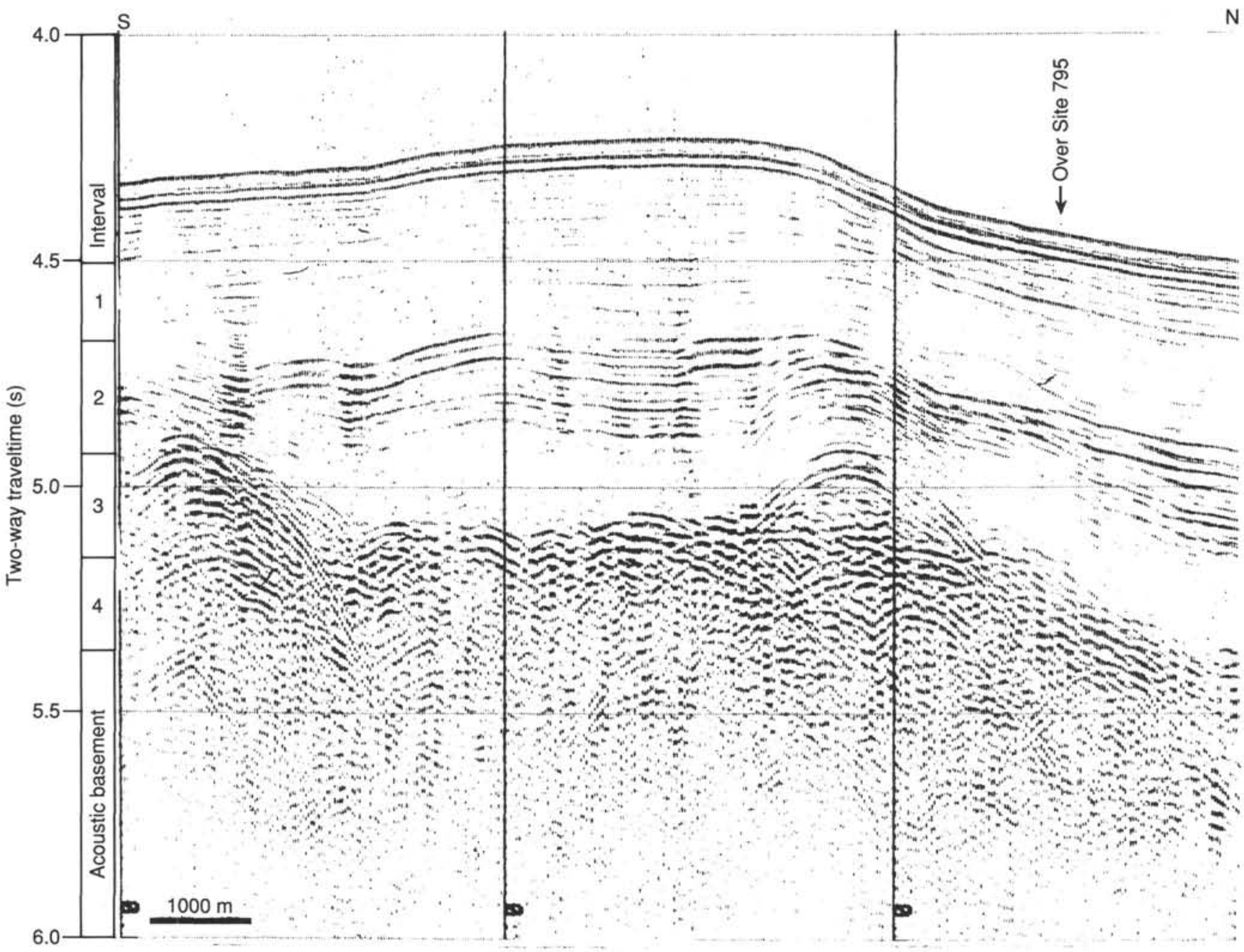

Figure 55. North-south single channel *JOIDES Resolution* seismic reflection record obtained during the approach to Site 795 with an assignment of acoustic intervals and the approximate site location (see "Operations" section, this chapter for track lines).

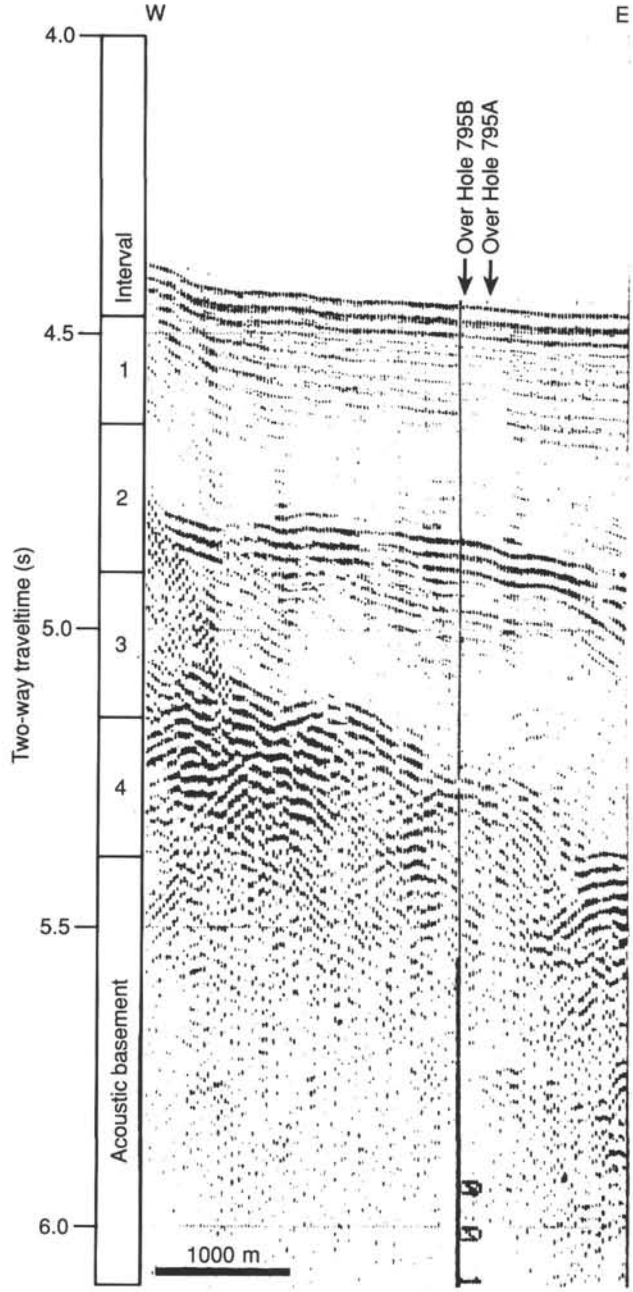

Figure 56. East-west single channel *JOIDES Resolution* seismic reflection record obtained during the approach to Site 795 with an assignment of acoustic intervals and the precise hole locations (see "Operations" section, this chapter for track lines).

Time	Seismic Interval	Acoustic Character	Interval velocity (mk)	Thickness (two-way time) (s)	Thickness (distance-m)	Simplified lithology	Lithologic Unit	Age	Depth
0									0
	1	Moderately stratified	1550	0.18	140	Silt clay and clay with minor ash	I	Pleist.	
0.18									140
	2	Weakly stratified	1680	0.22	185	Diatom ooze	II	Pliocene	
						Silty diatom claystone	III		
0.40						Opal A/CT			325
	3	Well stratified	1750	0.17	149	Hard siliceous layers	IV	late Miocene	
0.57									474
	4	Transparent	1825	0.23	210	Siliceous claystone		middle Miocene	
						Claystone and tuff	V		
0.80									684
	Acoustic basement	Nonstratified reflective	3410	?	?	Basaltic andesite and basalts	Basement	?	

Figure 57. Summary of the seismic stratigraphy of Site 795 and its correlation with lithostratigraphy.

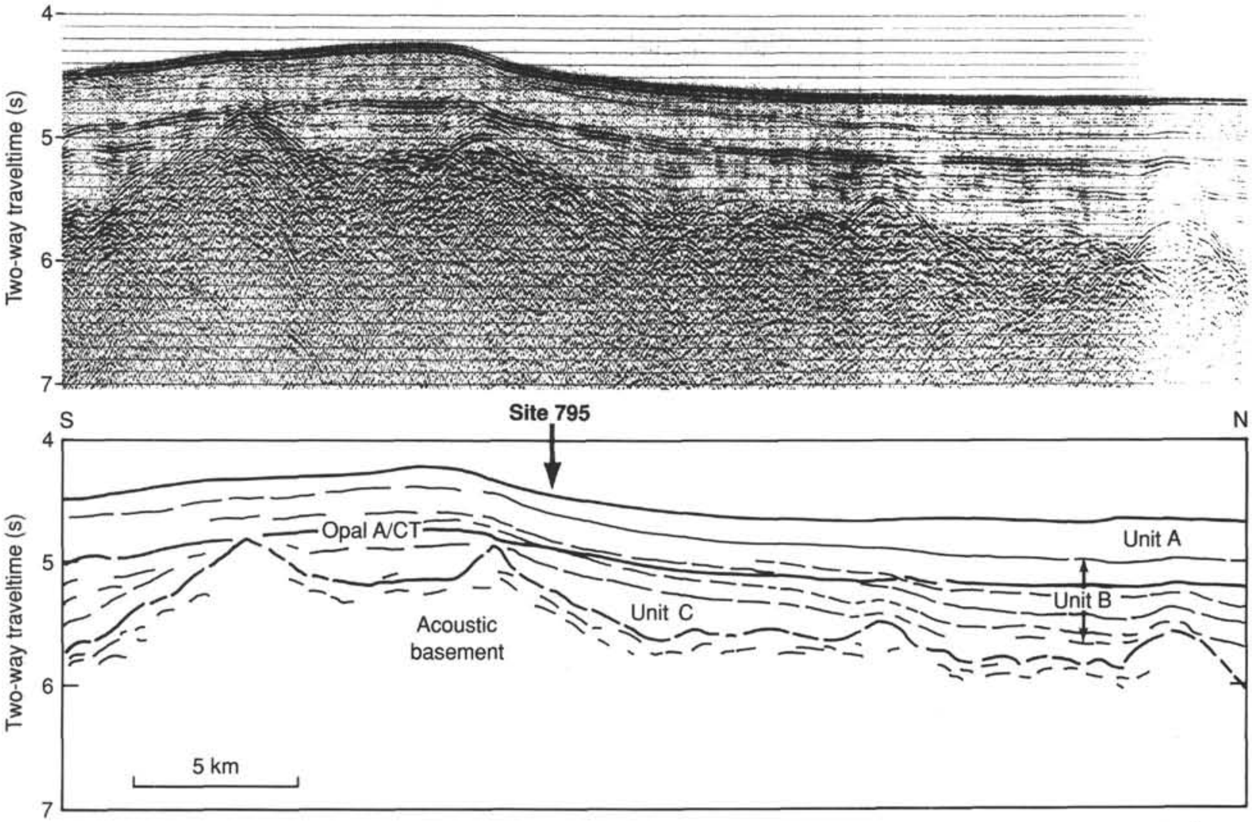

Figure 58. Multichannel seismic profile of Line 103 and its interpretation. The opal-A/opal-CT reflector simulates a sea-bottom reflector and intersects stratified, lithological units. See text for explanation of Units A, B, and C.

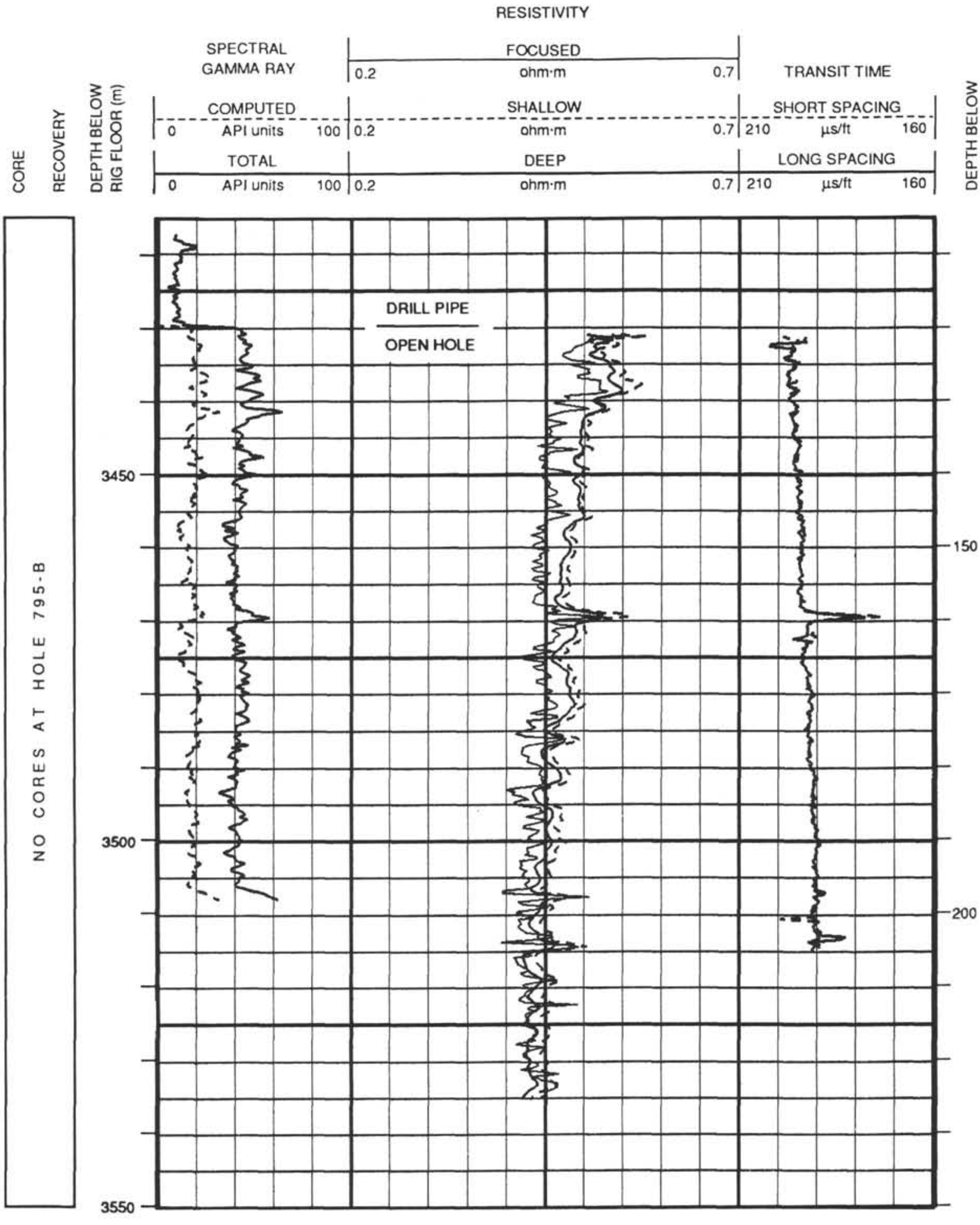
RESISTIVITY
SPECTRAL GAMMA RAY
FOCUSED
0.2 ohm·m 0.7
TRANSIT TIME
COMPUTED
0 API units 100
SHALLOW
0.2 ohm·m 0.7
SHORT SPACING
210 µs/ft 160
TOTAL
0 API units 100
DEEP
0.2 ohm·m 0.7
LONG SPACING
210 µs/ft 160
CORE
RECOVERY
DEPTH BELOW RIG FLOOR (m)
DEPTH BELOW SEA FLOOR (m)
DRILL PIPE
OPEN HOLE
NO CORES AT HOLE 795-B
3450
3500
3550
150
200

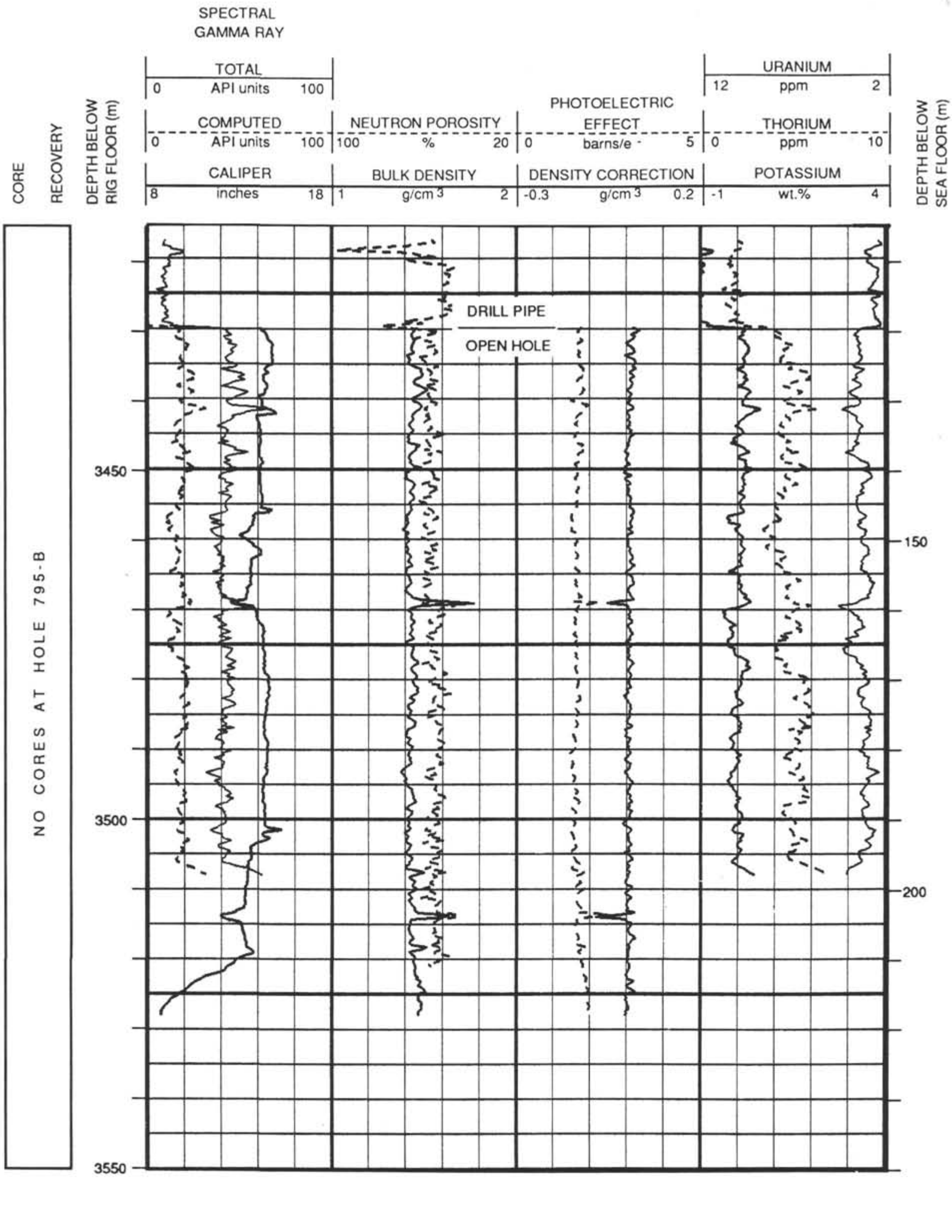
SPECTRAL
GAMMA RAY
TOTAL
0 API units 100
COMPUTED
0 API units 100
CALIPER
8 inches 18
NEUTRON POROSITY
100 % 20
BULK DENSITY
1 g/cm3 2
PHOTOELECTRIC
EFFECT
0 barns/e- 5
DENSITY CORRECTION
-0.3 g/cm3 0.2
URANIUM
12 ppm 2
THORIUM
0 ppm 10
POTASSIUM
-1 wt.% 4
CORE
RECOVERY
DEPTH BELOW
RIG FLOOR (m)
DEPTH BELOW
SEA FLOOR (m)
DRILL PIPE
OPEN HOLE
NO CORES AT HOLE 795-B
3450
3500
3550
150
200